

Self-assembly of Au-Fe₃O₄ dumbbell nanoparticles

Von der Fakultät für Mathematik, Informatik und Naturwissenschaften der RWTH Aachen
University zur Erlangung des akademischen Grades einer Doktorin der
Naturwissenschaften genehmigte Dissertation
vorgelegt von

Nileena Nandakumaran, Master of Science

aus

Bangalore, India

Berichter: *Prof. Dr. Thomas Brückel*
Prof. Dr. Joachim Mayer

Tag der mündlichen Prüfung: *Montag* Datum: *26.09.2022*

Diese Dissertation ist auf den Internetseiten der Universitätsbibliothek verfügbar.

Abstract

A dumbbell nanoparticle (DBNP) system consists of an optically active Au seed particle on which a magnetic iron oxide nanoparticle (IONP) is heterogeneously grown. Control and manipulation of these multi-functional hetero-structures have applications as a dual-probe for biomedical imaging, in catalysis, sensing, optics, photonics and electronics. This thesis investigates the magnetic field-induced self-assembly in diverse DBNPs, with different sizes of Au and IONPs coated with oleic acid and oleylamine and dispersed in toluene. The effects of DBNPs' complex morphology are compared and contrasted to self-assembly studies on the IONPs', which are single-phase spherical counterparts. Direct comparison simplifies the understanding of broad parameter space, including the size of the Au seed and the grown IONP, their size distribution, the thickness of surfactant coating around the nanoparticle, concentration in a dispersion, composition, magnetic structure, and strength of the magnetic field. A multiscale experimental approach is adopted to analyze the structure and magnetic properties to link it to the self-assembly phenomenon. Microscopy combined with local atomic structure obtained from synchrotron x-ray pair distribution function (xPDF) is used to reveal local crystal structure, crystallinity, size and distortion induced at the surface. Macroscopic magnetic measurements along with polarized neutron scattering reveal the magnetic behavior. Small-angle x-ray and neutron scattering (SAXS/SANS) measurements are exploited to observe and analyze self-assembling patterns. Real-space analysis of such patterns is achieved through reverse Monte Carlo (RMC) simulations. Spherical IONPs reversibly form 1D chains that align, straighten with magnetic field. On the other hand, 1D and 2D chains are observed with DBNPs in an applied magnetic field. The assemblies are classified into three categories based on the anisotropy in the 2D scattering pattern. Moreover, due to the unique morphology and orientation effects, the chains formed by DBNPs within these categories have head-to-tail or side-by-side arrangement. Shape-induced mechanisms governed by a dimensionless parameter are suggested to play a vital role in determining assembly formation.

Zusammenfassung

Ein „Dumbbell“-Nanopartikel (DBNP) besteht aus einem optisch aktiven Au-Keimpartikel, auf dem magnetische Eisenoxid-Nanopartikel (IONP) heterogen gezüchtet werden. Die Kontrolle und Manipulation dieser multifunktionalen Heterostrukturen finden Anwendung als Doppelsonde für biomedizinische Bildgebung sowie in der Katalyse, der Sensorik, der Optik, der Photonik und der Elektronik.

Die vorliegende Dissertation untersucht die Magnetfeld-induzierte Selbstorganisation in verschiedenen DBNPs, wobei Au-Partikel und IONPs unterschiedlicher Größe verwendet werden, die mit Ölsäure und Oleylamin beschichtet und in Toluol dispergiert werden. Die Auswirkungen der komplexen Morphologie von DBNPs werden mit Selbstorganisationsstudien an den IONPs verglichen, die einphasige sphärische Gegenstücke darstellen. Der direkte Vergleich vereinfacht das Verständnis des breiten Parameterraums, einschließlich der Größe des Au-Keims und des gezüchteten IONP, ihrer Verteilung, der Dicke der Tensidbeschichtung um das NP, der Konzentration, der Zusammensetzung, der magnetischen Struktur und der Stärke des Magnetfelds. Zur Analyse des Zusammenhangs zwischen der Struktur und magnetischer Eigenschaften und dem Selbstorganisationsphänomen wird ein mehrstufiger experimenteller Ansatz gewählt. Mikroskopie kombiniert mit der aus der Synchrotron-Röntgenpaar-Verteilungsfunktion (xPDF) ermittelten lokalen Atomstruktur wird verwendet, um die lokale Kristallstruktur, die Kristallinität, die Größe und die an der Oberfläche induzierte Verzerrung aufzudecken. Makroskopische magnetische Messungen in Verbindung mit polarisierter Neutronenstreuung zeigen das magnetische Verhalten. Kleinwinkelröntgen- und Kleinwinkelneutronenstreuungsmessungen (SAXS/SANS) werden ergänzend genutzt, um Muster in der Selbstorganisation zu beobachten und zu analysieren. Die Realraumanalyse solcher Muster wird durch umgekehrte Monte-Carlo-Simulationen (RMC) erreicht. Sphärische IONPs bilden reversible 1D-Ketten, die sich mit einem Magnetfeld ausrichten und begradigen. Andererseits werden bei DBNPs bei angelegtem Magnetfeld 1D- und 2D-Ketten beobachtet. Aufgrund der Anisotropie in 2D-Streuungsmustern werden die beobachteten Ketten in drei Kate-

gorien eingeteilt. Darüber hinaus weisen die von DBNPs gebildeten Ketten innerhalb dieser Kategorien aufgrund ihrer einzigartigen Morphologie und Orientierungseffekten „Kopf-zu-Fuß“- bzw. „Seite-an-Seite“-Anordnungen auf. Es wird vermutet, dass forminduzierte Mechanismen, die von einem dimensionslosen Parameter bestimmt werden, eine wichtige Rolle bei der Bestimmung der Anordnungszusammensetzung spielen.

Acknowledgements

"This thesis indeed had one writer, but it took many wonderful people to shape the writer and the story itself"

First and foremost, I like to acknowledge Prof. Thomas Brückel for giving me this opportunity to take on this project, reviewing the thesis carefully and encouraging me to find my true potential. Your insightful feedback always pushed me to sharpen my thinking about a subject. Thank you for the courses you taught with such enthusiasm. It helped solidify the basics of magnetism and neutron scattering. I would like to thank Prof. Joachim Mayer for agreeing to be my second referee and reviewing this thesis. I am incredibly grateful to Dr. Mikhail Feygenson, who has been an ideal mentor for me. Apart from offering valuable insights for the project, you have always supported my personal growth as a researcher by finding me new opportunities and exciting collaborations. Thank you for your care, insight and humor. Without Dr. Lester Barnsley, I would not have discovered my love for python. Thank you for improving my technical skills and your bright optimism always cheered me. I would like to thank Dr. Artem Feoktystov, who always asked the right questions and gave me so much room for learning, experimenting, and thinking out loud. I am also grateful to both Lester and Artem for assisting me during several experiments at KWS-1, MLZ. This project would not have taken off without the dumbbell samples provided by Prof. Francesco Pinieder and Dr. Elvira Fantechi, collaborators from the University of Pisa. Your keen curiosity through scientific discussions and constant support led to an enjoyable collaboration. I also like to thank our collaborators, Dr. Dale Huber from Sandia National Laboratories and Dr. Sergie A. Ivanov from Los Alamos National Laboratories, for the excellent quality and large quantity of single-phase iron oxide samples. I would like to thank Sebastian Sievers, who collected part of the magnetometry data on single-phase iron oxide particles. Thank you to Dr. Sascha Ehlert for his constant help with microscopy and TGA experiments. I am very grateful to Dr. Lisa Fruhner and Dr. Margarita Kruteva for training me in sample preparation, collection and treatment of SAXS data. In this regard, I also

express my sincere gratitude to Dr. Emmanuel Kentzinger. You are always so kind to offer me assistance, even when experiments went on up to midnight. I am grateful to Dr. Oleg Petravic for his discussions on magnetometer data and the excitement to discuss general challenging problems in physics. I thank Dr. Shibabrata Nandi for his support during magnetometry measurements. I thank Dr. Asmaa Qdemat and Dr. Wenhai Ji for their friendship, constant help with SEM measurements and introduction to lab. Special thanks to Dr. Tobias Köhler for his assistance during beamtime experiments and several illuminating discussions. I am thankful to all the instrument scientists at various beamlines worldwide, especially Dr. Antonio Cervellino (PSI-Switzerland), Dr. Leighanne C Gallington (APS-USA), Prof. Dr. Eliot Gilbert (ANSTO-Australia), Dr. William T Heller (SNS-Oakridge-USA) for their patience, time, and invaluable comments during the experiment. I am indebted to several inspiring discussions during conferences on scattering and magnetism with Dr. Sabrina Disch, Dr. Philipp Bender, Prof. Andreas Michels, Dr. Dirk Honecker, Dr. Dominika Zákutná and Dr. Kathryn Krycka. I have to mention special thanks to the BornAgain team, whose workshops on python and simulations were beneficial. I thank our other nanoparticle group members Amal Nasser and Mikhail Smik for facilitating open discussions during nanoparticle meetings or outside. Thank you, Berthold Schmitz, for your constant assistance with the magnetometer. Special thanks to Micha Hölzle for helping me resolve my technical problems ever so kindly and always with a smile. I am very grateful for the generous and perfect administrative assistance from Mrs. Barbara Daegener at every point. I express my sincere thanks to office colleagues Paul Doege, Alexander Schwab, and Qi Ding for making a lively and fun work environment. Special thanks to Alex for proofreading the German version of the abstract. During my time as a Ph.D. student, I thank Dr. Annika Stellhorn, Dr. Anirban Sarkar, Dr. Tanvi Bhatnagar-Schöffman, Dr. Patrick Schöffmann, Mathias Strothmann, Dr. Mohammad Ait Haddouch, Dr. Marco Meixner, Dr. Kelvin Acerborn for stimulating discussions as well as happy distraction from work to help me reset my mind. Further, I express my special thanks to Suqin He and Venus Rai for your invaluable friendship and the joy during stressful pandemic times. I thank my dearest friend Dr. Shyni P. C. for proofreading and encouraging me to keep going during stressful writing times. I am forever indebted to my brothers Vishnu, Varun and friends back home for their humor and constant presence in my life. This would not have been possible without the infinite patience and love from my best friend and husband, Vivek. Thanks for staying awake during those sleepless nights to help with editing or to listen to some

mad new idea. Finally, no words can express my deepest love and gratitude to my parents. Without the inspiration, love and support you gave me, I might not be the person I am today.

Contents

Abstract	i
Zusammenfassung	ii
Acknowledgements	v
1. Introduction	1
1.1. Thesis outline	2
2. Theoretical framework	4
2.1. Magnetism	4
2.1.1. Atomic magnetic moment	4
2.1.2. Magnetic moment due to electrons	7
2.1.3. Magnetism in a solid	10
2.1.4. Macroscopic parameters	12
2.1.5. Types of magnetic order	13
2.1.6. Magnetic anisotropy	14
2.1.6.1. Magnetocrystalline anisotropy	15
2.1.6.2. Shape anisotropy	16
2.1.6.3. Surface anisotropy	17
2.1.6.4. Other anisotropic contributions	18
2.2. Nanomagnetism	19
2.2.1. Magnetic nanoparticles	19
2.2.2. Single Domain	20
2.2.3. Stoner-Wohlfarth (SW) model	22
2.2.4. Superparamagnetism (SPM)	24
2.2.5. Blocking temperature (T_B)	26
2.2.5.1. Langevin function	26
2.3. Interparticle interactions in colloid	26
2.3.1. van der Waals (vdW) forces	27

2.3.2.	Electrostatic (ES) forces	28
2.3.3.	Steric force	30
2.3.4.	Magnetic forces	31
2.3.5.	Gravitational force	32
2.4.	Scattering	33
2.4.1.	Elastic scattering experiment	33
2.4.2.	Scattering cross-section	34
2.4.3.	Quantum scattering theory	35
2.4.3.1.	Lippman-Schwinger equation	35
2.4.3.2.	Born approximation	37
2.4.4.	Types of scattering probes: scattering length	38
2.4.4.1.	Nuclear scattering length	39
2.4.4.2.	X-ray scattering length	39
2.4.4.3.	Magnetic scattering	40
2.4.5.	Coherent and incoherent nuclear scattering	40
2.5.	Small-angle scattering (SAS)	41
2.5.1.	SAS fundamentals	41
2.5.2.	Form and structure factors	43
2.5.3.	Behaviour at low Q: Guinier regime	45
2.5.4.	Behaviour at high Q: Porod regime	46
2.5.5.	Guinier-Porod model	46
2.5.6.	Contrast variation using neutrons	47
2.5.7.	Polarized neutrons: SANS POL	49
2.5.8.	Experimental aspects: data treatment	53
2.6.	Wide angle scattering	54
2.6.1.	Fundamentals: Bragg's Law	55
2.6.2.	Atomic planes and Ewald sphere	56
2.6.3.	Powder diffraction: Bragg peaks	58
2.6.4.	Total scattering experiments: Bragg and diffuse peaks	59
2.6.5.	Experimental aspects: data treatment	60
3.	Review of magnetic dumbbells nanoparticles	64
3.1.	Single phase nanoparticles	64
3.1.1.	Gold nanoparticles	64
3.1.2.	Iron-oxide nanoparticles	65

3.2. Types of dumbbell	66
3.3. Review of current synthesis methods	67
3.4. Emergence of novel properties	68
3.5. Previous observation of assemblies	69
3.6. Applications	70
3.7. Conclusion	72
4. Experiments: Instruments, Methods and Simulations	73
4.1. Samples	73
4.2. Electron Microscope (EM)	73
4.2.1. TEM	75
4.2.1.1. Working principle	75
4.2.1.2. Sample preparation	76
4.2.2. SEM	76
4.2.2.1. Working principle	76
4.2.2.2. Sample preparations	77
4.3. Magnetometer	77
4.3.1. Working principle and setup	77
4.3.2. Sample preparation	78
4.3.3. Data acquisition	79
4.3.4. Elemental analysis	80
4.4. Thermogravimetric Analysis (TGA)	80
4.5. Total scattering experiments-xPDF	80
4.5.1. Setup	80
4.5.2. Sample preparation	82
4.5.3. Data acquisition	83
4.6. Small-angle x-ray scattering (SAXS)	83
4.6.1. Setup	83
4.6.2. Sample preparation	84
4.6.3. Data acquisition	84
4.7. Small-angle neutron scattering (SANS)	85
4.7.1. Setup	86
4.7.2. Sample preparation	86
4.7.3. Data acquisition	87
4.8. Reverse Monte-Carlo simulations	87

4.9. Conclusion	88
5. Self-assembly in single phase IONPs as a reference to dumbbells	91
5.1. Introduction	91
5.2. Samples and synthesis	91
5.3. Shape size and crystallinity	93
5.4. Composition and local structure	94
5.5. Magnetic properties	96
5.6. Magnetic field induced self-assembly	98
5.6.1. Energy calculations	98
5.6.2. Assemblies as function of size, concentration and magnetic field	102
5.6.3. Formation of 1D chains	104
5.6.4. Role of shell thickness	109
5.6.5. Magnetic structure	110
5.7. Reverse Monte Carlo (RMC) simulations	112
5.8. Conclusion	115
6. Structural and Magnetic Characterization of Dumbbell Nanoparticles	116
6.1. Dumbbell geometry	116
6.2. Samples and synthesis	117
6.3. Shape, size and crystallinity	118
6.4. Composition and local structure	121
6.5. Magnetic properties	124
6.6. Surface ligand density	129
6.7. Conclusion	132
7. Self-assembly of Dumbbell Nanoparticles	133
7.1. Scattering contrast	133
7.2. Phase separation and macroscopic assemblies	134
7.3. Probing self-assembly : 2D visual analysis	135
7.3.1. 2D SAXS patterns	135
7.3.2. 2D SANS patterns	137
7.4. Types of assemblies and analysis methods	139
7.5. Category O: No assemblies	141
7.5.1. Radial analysis	141

7.6. Category I: 1D chains with disorder	144
7.6.1. Radial analysis	144
7.6.2. Sectoral analysis	145
7.7. Category I: 1D chains	147
7.7.1. Radial analysis	148
7.7.2. Sectoral analysis	148
7.8. Category II: 2D chain assemblies	149
7.8.1. Radial analysis	150
7.8.2. Sectoral analysis	150
7.9. Orientation of Particles	152
7.10. Scattering simulation with BornAgain	156
7.11. Shape induced mechanisms involved in the assembly formation	159
7.11.1. Energy estimates	159
7.11.2. Differences between IONPs and DBNPs	163
7.12. Conclusion	164
8. Conclusion and outlook	166
8.1. Conclusion	166
8.2. Scope for future developments	169
8.3. Outlook	171
A. Structural parameters	174
A.1. Image analysis results	174
A.2. Total scattering refinements	175
A.3. SAXS refinement parameter	177
A.4. SANS fits and parameters	181
A.5. Sector fits	182
B. Magnetic properties	184
C. Energy calculation	186
D. Extended dumbbell analysis	188
List of Abbreviations	193
List of Symbols	194

Bibliography	198
List of Figures	220
Declaration of Authorship	235

1. Introduction

Ribosomes in a cell, swarms of ants, schools of fish, winds forming tornadoes, or the galaxy we live in results from nature's design process, namely, self-assembly. In such phenomena, pre-existing parts come together to form reversible and ordered patterns that are ubiquitous at all scales [1]. Drawing inspiration from nature, nanoparticles (NPs) (size < 100 nm) with controlled shape act as an individual entity for the design and formation of complex structures. Their physical and chemical properties, such as size, composition, surface charges, the coating around NP, geometry, etc., govern their functionality, enabling various applications. These properties allow flexible tuning and possibility to generate rich novel structures beyond the standard face-centered cubic (FCC) or body-centered cubic (BCC) crystals. For instance, magnetic Iron Oxide Nanoparticles (IONPs) containing typically magnetite (Fe_3O_4) NPs are potentially detected and manipulated remotely with magnetic fields resulting in a large number of applications such as for targeted drug delivery, contrast agents for magnetic resonance imaging (MRI), hyperthermia, bioseparation and biosensing [2, 3, 4, 5]. Extensive literature is now available on individual and collective properties of magnetic particles with different shapes, composition and functionalizations [6, 7, 8, 9, 10, 11, 12]. These properties are exploited to realize the formation of 1D, 2D and 3D assemblies in template and dispersions [7, 8, 13, 14]. In parallel, tunable optical properties of metallic NPs such as Au or Ag are well documented due to their interaction with light resulting from surface plasmon resonance [15]. Thus, the metallic NPs are ideal candidates for catalysis, photo-induced hyperthermia, and imaging applications. By the 1990s, methods for synthesizing cubes, rods and discs, commonly comprising metals (for example, gold and silver) and metal oxides (magnetite, maghemite, and hematite), were available.

The interest in nanoparticles has gradually shifted to multi-component nanoparticles in the last two decades. There are growing appeals for developing such hybrid NPs due to the significant benefit of combining magnetic and optical properties in a single system. Owing to the advancements in the synthesis of various shapes (core-

shell, Janus, flower and dumbbell) and sizes, chemical and physical properties are now tested in biomedical applications. In particular, IONPs grown heterogeneously on Au surface results in non-centrosymmetric multi-component NPs with unique morphology called "dumbbell nanoparticles" (DBNPs). The field of hybrid DBNPs only really took off in the early 2000s due to seminal contributions by chemists following a robust chemical seed-mediated growth as opposed to previous physical deposition methods [16, 17]. Since then, a majority of the contributions in the decade aimed to improve the synthesis of such structures and provide mechanisms to control the growth [18, 19]. In parallel, several authors have reported on the structural, magnetic and magnetoplasmonic behavior of such DBNPs. Novel properties were often correlated to interfacial phenomenon arising due to shared interface between Au and IONP [20, 21, 22, 23].

Several researchers have conducted simulations using DBNPs as the basic building blocks and have reported a myriad of potential structures [24, 25, 26]. However, in the limited experiments that reported the formation of assemblies using DBNPs as structural units, self-assembly was mainly achieved through selective surface modification of the DBNPs, creating predefined soft templates or photo-activation of the surface. Assemblies were primarily driven by electrostatic or van der Waal forces and were observed through microscopy/imaging techniques [27, 28, 29, 30]. The magnetic field-induced assemblies using DBNPs without any surface modification have rarely been investigated to the best of our knowledge. Therefore, this thesis primarily aims to address the following:

1. To demonstrate the magnetic field induced self-assembly using diverse and asymmetric DBNPs as building blocks without additional surface modification.
2. To perform comparative studies with the spherical IONP counterparts and identify the relevant parameters using a multi-scale experimental approach.
3. To establish a correlation between the geometry of the individual DBNP and the resulting assembled structure and identify the mechanisms involved in forming assemblies.

1.1. Thesis outline

The thesis is divided into eight chapters. Preliminary advancements in the field of nanoparticles and the overarching goals of this investigation are introduced in

chapter 1. **Chapter 2** sets the theoretical framework with existing theories in nanomagnetism including useful definitions for blocking temperature, superparamagnetism, anisotropy, etc., that is subsequently used in later chapters. The origins of several colloidal forces involved in self-assembly are discussed. The basics of scattering theory are outlined, followed by small-angle and total scattering principles. **Chapter 3** reviews in detail the literature on magnetic dumbbell nanoparticle containing Au - Fe₃O₄ synthesis, reasons for observing novel properties, prior observation of assemblies, and its potential applications. The multiscale experimental methods such as electron microscopy, magnetometry and advanced scattering techniques such as x-ray pair distribution function (xPDF), small-angle x-ray and neutron scattering (SAXS/SANS), along with Reverse Monte-Carlo (RMC) simulations used in the characterization of structural, magnetic and self-assembly behavior are described in **chapter 4**. The richness of parameter space involved in understanding the self-assembly of DBNPs through reference studies on spherical IONPs is demonstrated in **chapter 5**. The synthesis routines to obtain four diverse DBNPs are described in **chapter 6**. The structural and magnetic properties of DBNPs are contrasted and compared with IONPs to establish an ever richer parameter space indicating the complexity of the problem being tackled. This chapter further defines and emphasizes the geometric parameters A_1 and A_2 of the DBNP that plays a crucial role in tuning the self-assembly. **Chapter 7** displays the formation of assemblies through 2D scattering patterns. Several 1D analysis methods are employed to understand, describe and classify assemblies. The formation of assemblies is realized in terms of geometric parameters introduced previously. Ultimately, a comprehensive conclusion summarizes the results of this investigation in **chapter 8**. This chapter also sheds light on the future developments in this project.

2. Theoretical framework

This chapter will describe the framework based on the existing theories in magnetic nanoparticles, nanomagnetism, colloidal forces and scattering theory that reflects the field of inquiry conducted in the thesis. Therefore, this chapter serves as a blueprint from which several hypothesis/terms/equations are borrowed to conduct own investigations in the later chapters.

2.1. Magnetism

In section 2.1 and 2.2, we recall some standard facts in magnetism and nanomagnetism adopted from several books [9, 31, 32, 33, 34]. The subject of magnetism is discussed from a classical and quantum mechanical view point.

2.1.1. Atomic magnetic moment

The elementary object in solid state magnetism is the magnetic moment. Classically, this is viewed as a circulating electric current I , in an oriented elementary loop of area $|d\vec{\mathcal{A}}|$ (see Fig. 2.1 (a)). Then the magnetic moment is written as

$$d\vec{\mu} = Id\vec{\mathcal{A}} \quad (2.1)$$

where the unit is Am^2 . Analogous to electric dipole consisting of two charges separated by a distance, the magnetic dipole can be considered as two magnetic monopoles separated by distance pointed in direction of vector $d\vec{\mathcal{A}}$. The direction of vector is normal to the area of the loop and determined by the right hand cork-screw rule. In atoms, according to the Bohr's model, electrons revolve in circular orbits under the influence of Coulomb potential (Fig. 2.1 (b)). An electron revolving around the nucleus is equivalent to circulating current in a direction opposite to the motion of the negatively charged electron. If the speed of the electron is $|\vec{v}|$, then its period of rotation is $\tau = \frac{2\pi|\vec{r}|}{|\vec{v}|}$ where $|\vec{r}|$ is the radius of the orbit. The equivalent current is

$I = -e/\tau$, where e is the charge of electron (-1.6022×10^{-19} C). The magnetic moment due to this orbital motion is given by $\vec{\mu}_\ell = -\frac{1}{2}e\vec{r} \times \vec{v}$ and is modified as

$$\vec{\mu}_\ell = -\frac{e}{2m_e}\vec{\ell} = \gamma\vec{\ell} \quad (2.2)$$

where angular momentum $\vec{\ell} = m_e\vec{r} \times \vec{v}$, m_e is the mass of electron (9.109×10^{-31} kg) and γ is gyromagnetic ratio. For orbital motion of electron, the minus sign means the $\vec{\mu}$ and $\vec{\ell}$ are in opposite direction. The Bohr's model is a simplified version of quantum mechanical description of an atom. The theory of magnetism is connected

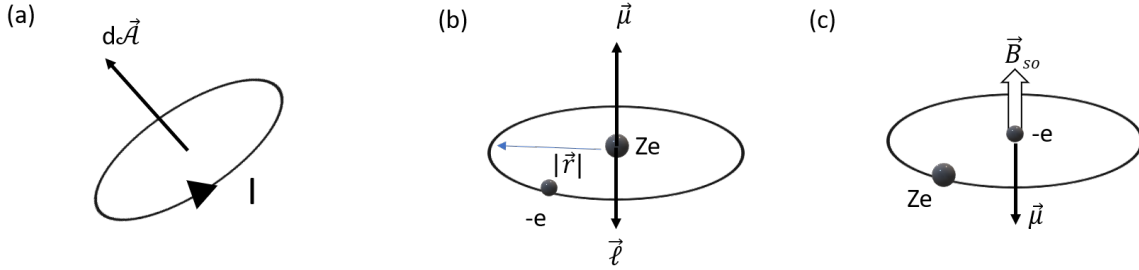


Figure 2.1.: (a) The current carrying loop with moment $\vec{\mu}$ in direction of $d\vec{\mathcal{A}}$. (b) The Bohr's atom where the electron moves in a circular orbit where its $\vec{\ell}$ and $\vec{\mu}$ are in opposite directions and (c) the spin-orbit interaction from the viewpoint of electron.

to the angular momentum of an elementary particle. So quantum theory of magnetism is linked to the quantization of angular momentum. The orbital angular momentum is quantized in units of \hbar in such a way that the component of $\vec{\mu}_\ell$ in some particular direction (chosen as z direction in Cartesian coordinates) is given by

$$\mu_\ell^z = -\frac{e}{2m_e}m_\ell\hbar; \quad m_\ell = 0, \pm 1, \pm 2 \quad (2.3)$$

where m_ℓ is the orbital magnetic quantum number. The unit of electronic magnetism is given by Bohr magneton defined as $\mu_B = \frac{e\hbar}{2m_e}$, where $1 \mu_B = 9.274 \times 10^{-24}$ Am² and the z -component is an integer number of Bohr magneton. The difference in the classical orbit and quantum mechanical stationary state is that the classical motion will cease as a result of radiation loss. The eqn. (2.3) is expressed in terms of g -factor which is the ratio of the magnetic moment (in units of μ_B) to angular momentum (in units of \hbar):

$$|\vec{\mu}_\ell|/\mu_B = g|\vec{\ell}|/\hbar \quad (2.4)$$

in vector notation. Here, the z-component of angular momentum is $m_\ell \hbar$ and thus g-factor is 1 for orbital motion of electron. Electrons possess an intrinsic spin angular momentum \vec{s} with spin quantum number. The associated moment is intrinsic to the electron without any orbital motion. Electron is a point particle with radius $< 10^{-20}$ m which is smaller than the classical radius (2.8×10^{-15} m). Hence, the spin of an electron which is often imagined as spinning top is misleading. The inbuilt angular momentum is a consequence of the relativistic quantum mechanics. Similar to the orbital angular momentum, the associated spin magnetic moment is

$$\vec{\mu}_s = -\frac{e}{m_e} \vec{s} \quad (2.5)$$

where the component of \vec{s} along any axis is $\frac{1}{2}\hbar$ for an electron. The associated component of spin magnetic moment is given by

$$\mu_s^z = -2\frac{e}{2m_e} m_s \hbar; \quad m_s = \pm \frac{1}{2} \quad (2.6)$$

where m_s is the spin quantum number. The spin angular momentum is twice as efficient as orbital angular momentum in creating magnetic moments. The g-factor for intrinsic spin of the electron is 2.002. The electron has two spin states depicted as $|\uparrow\rangle$ and $|\downarrow\rangle$ that are degenerate in zero magnetic field. The energy of an electron in the presence of a magnetic field \vec{B} is

$$E = g\mu_B m_s B \quad (2.7)$$

and this energy that splits electronic levels by an amount $g\mu_B B$ is called Zeeman energy. On an atomic scale, the intrinsic magnetic moments are associated with spin of each electron and contribution of orbital motion around the nucleus. The nucleus itself may possess spin, but the nuclear moments are three orders of magnitude smaller than those associated with electron because the magnetic moments of particle scales as $1/\text{mass}$. The interaction of electron spin and motion gives rise to spin-orbit coupling (SOC). From the electron's point of view, the nucleus revolves with speed $|\vec{v}|$. The motion is equivalent to current loop which creates a magnetic field. The spin-orbit interaction is due to this magnetic field \vec{B}_{so} acting on the intrinsic moment of electron (see Fig. 2.1 (c)). Interaction energy $E_{so} = -\mu_B B_{so}$ can be written as

$$E_{so} \approx -\frac{\mu_o \mu_B^2 Z^4}{4\pi a_o^3} \quad (2.8)$$

where μ_o is magnetic permeability, Z is atomic number and a_o is Bohr radius. The dependence of Z on the spin-orbit interaction indicates a weak perturbation for light elements that becomes more important for heavy elements. Including a relativistic correction the eqn.(2.8) is modified by factor 2. The Hamiltonian for interaction of a single electron SOC is given by

$$\mathcal{H}_{soc} = e_{so}\hat{\ell}\cdot\hat{s} \quad (2.9)$$

where e_{so} is the SOC energy, $\hat{\ell}$ and \hat{s} are the dimensionless operators. In quantum mechanics the physical observables such as angular momentum are represented by differential or matrix operators. The eqns (2.3) and (2.5) in quantum mechanics means that the matrix elements of the operators for $\hat{\mu}$ and $\hat{\ell}$ or \hat{s} are proportional. In general, the total magnetic moment of an electron is the vector sum of the spin and orbital angular magnetic moments and written in operator form is

$$\hat{\mu} = -\frac{\mu_B}{\hbar}(\hat{\ell} + 2\hat{s}) \quad (2.10)$$

The physical quantities that commute can be measured simultaneously. The three components of the angular momentum do not commute, meaning that a precise measurement of z-component will result in indeterminate x and y components. The eigenvalues of \hat{s}_z and \hat{l}_z are $m_s\hbar$ and $m_\ell\hbar$, respectively. The square of the angular momentum commutes with component of angular momentum:

$$[\hat{s}^2, \hat{s}_z] = [\hat{\ell}^2, \hat{\ell}_z] = 0 \quad (2.11)$$

where the eigenvalues of \hat{s}^2 and $\hat{\ell}^2$ are $s(s+1)\hbar^2$ and $\ell(\ell+1)\hbar^2$, respectively.

2.1.2. Magnetic moment due to electrons

There are two limit cases to understand electronic magnetism in solids. One is the localized limit where there is a strong correlation between electron and the ion cores through Coulomb repulsion. Other is the delocalized limit, where electrons confined in a solid weakly interact with the nuclear charge. In the localized limit, the energies of a single electron in a central potential are calculated using hydrogen atom as a model system. The Hamiltonian for a single electron system is given by

$$\mathcal{H}_e = -\frac{\hbar^2}{2m}\nabla^2 - \frac{Ze^2}{4\pi\epsilon_o r} \quad (2.12)$$

where $\hat{p} = -i\hbar\nabla$ and ϵ_o is the permittivity. The Schrödinger equation for energy levels of the atom is $\mathcal{H}\psi_i = \epsilon_i\psi_i$, where ϵ_i and ψ_i are the energy eigenvalues and the corresponding wave functions. The three quantum numbers n, ℓ and m_ℓ are required to define the wavefunction ψ_i which describes the spatial distribution and energy levels of an electron. The fourth quantum number s summarizes the spin angular momentum. A total of four quantum numbers are required to specify completely the state of an electron when bound to an atom. Pauli's exclusion principle clearly states that two fermions (electrons) cannot have the same four quantum numbers within a quantum system simultaneously. Here n is the principle quantum number that takes integer values to defines energy levels and ℓ takes values $0, 1, \dots, (n-1)$ which describes the shape of the orbital. There are $(2\ell+1)$ values for m_ℓ which goes from $0, \pm 1, \dots, \pm\ell$. When more than one electron is present, Coulomb repulsion is added to the eqn. (2.12) to obtain

$$\mathcal{H}_{ee} = - \sum_i \left(\frac{\hbar^2}{2m} \nabla^2 - \frac{Ze^2}{4\pi\epsilon_o|\vec{r}_i|} \right) + \sum_{i<j} \frac{e^2}{4\pi\epsilon_o|\vec{r}_i - \vec{r}_j|} \quad (2.13)$$

where $|\vec{r}_i - \vec{r}_j|$ is the distance between the electrons. When several electrons are present on the same atom, at most two electrons with opposite spins can pair in the same orbital. Usually magnetic ions follow L-S coupling scheme where individual spin and orbital angular momentum add to give resultant quantum numbers:

$$S = \sum_i s_i, M_s = \sum_i m_{s_i}, L = \sum_i \ell_i, M_\ell = \sum_i m_{\ell_i}. \quad (2.14)$$

When the SOC is strong, the ℓ_i and s_i for each electron result in j which is then coupled to total angular momentum. This is the j-j coupling scheme. The Hund's rule prescribes steps to determine the lowest energy state in multielectron atom or ion. Hund's rule are as follows: (i) maximize S for configuration, (ii) maximize L consistent with S and (iii) then couple L and S to form J, $J = L-S$ (if shell is less than half filled) and $J = L+S$ if shell is more than half filled. When it is exactly half, $L = 0$ and $J = S$. The general notation for ground state is $^{2S+1}X_J$. According to this rule, $S = 1, L = 1$ and $J = 0$ for example in carbon $C = 1s^2 2s^2 2p^2$, which results in non-magnetic ground state since $M_J = 0$. The electronic configuration of the magnetic ion Fe^{3+} is $3d^5$ where $S = 5/2, L = 0$ and $J = 5/2$, thus the ground state is $^6S_{5/2}$. SOC is the origin of magnetic effects like magnetocrystalline anisotropy, magnetostriction and anisotropic magnetoresistance. The multi-electron Hamiltonian adapted from the

single electron eqn. (2.9) is

$$\mathcal{H}_{soc} = \frac{\Lambda}{\hbar^2} \hat{L} \cdot \hat{S} \quad (2.15)$$

where $\Lambda = \pm \frac{\lambda}{2S}$ and here $\Lambda > 0$ for first half of $3d$ and $4f$ series and $\Lambda < 0$ for second half of the series. By analogy with eqn. (2.10), the magnetic moment of atom is

$$\hat{\mu} = -\frac{\mu_B}{\hbar} (\hat{L} + 2\hat{S}) \quad (2.16)$$

Writing the eqn. (2.4) in the operator form to calculate the Lande g-factor for multielectron atom or ion using total angular momentum \hat{J} we get

$$g = -\frac{(\hat{\mu} \cdot \hat{J} / \mu_B)}{(\hat{J}^2 / \hbar)} = \frac{\hat{\mu} \cdot \hat{J}}{J(J+1)\mu_B \hbar} \quad (2.17)$$

The numerator of the right hand term is simplified using the eigenvalues as shown below,

$$\begin{aligned} \hat{\mu} \cdot \hat{J} &= -\frac{\mu_B}{\hbar} [(\hat{L} + 2\hat{S}) \cdot (\hat{L} + \hat{S})] \\ &= -\frac{\mu_B}{\hbar} [(\hat{L}^2 + 3\hat{L} \cdot \hat{S} + 2\hat{S}^2)] \\ &= -\frac{\mu_B}{\hbar} [(\hat{L}^2 + 2\hat{S}^2) + \frac{3}{2}(\hat{J}^2 - \hat{L}^2 - \hat{S}^2)] \\ &= -\frac{\mu_B}{\hbar} \left[\frac{3}{2}J(J+1) - \frac{1}{2}L(L+1) + \frac{1}{2}S(S+1) \right] \end{aligned}$$

The Lande g-factor can now be written in the most familiar form

$$g = \frac{3}{2} + \frac{[S(S+1) - L(L+1)]}{2J(J+1)}. \quad (2.18)$$

In the localized limit, the transfer of electrons from one ion site to another is negligible. In the delocalized model, the electronic magnetism occurs due to wave like extended states which forms energy bands. The number of electrons that transfer from one band to another depends on Fermi integral and obey Fermi-Dirac statistics. The delocalized model can be applied to $3d$ and $4d$ metals.

2.1.3. Magnetism in a solid

Further, when atoms are brought together in a solid, the magnetism depends on crystal structure and composition. Electrons in filled shells have paired spin and no net orbital moment. Only unpaired spins usually in the outermost shells contribute to the atomic moments. The hydrogen molecule, where neighbouring atoms each have a single electron, is chosen as the model system. In two neighbouring atoms, Coulomb repulsion in conjunction with Pauli's exclusion principle forbids the two electrons to enter into same quantum state. There is an energy difference between $|\uparrow_i\uparrow_j\rangle$ and $|\uparrow_i\downarrow_j\rangle$ configuration of spins of neighbouring atoms i and j . Since electrons are indistinguishable $|\Psi(1, 2)|^2 = |\Psi(2, 1)|^2$, the only solution for total wavefunction of two electrons must be anti-symmetric

$$\Psi(1, 2) = -\Psi(2, 1). \quad (2.19)$$

The total wavefunction Ψ is the product of spatial $\Phi(\vec{r}_1, \vec{r}_2)$ and spin wavefunction $\chi(\vec{s}_1, \vec{s}_2)$. The simplest model is the hydrogen molecule with two atoms each with 1 electron. The Schrödinger equation is now $\mathcal{H}(\vec{r}_1, \vec{r}_2)\Psi(\vec{r}_1, \vec{r}_2) = \epsilon\Psi(\vec{r}_1, \vec{r}_2)$ neglecting e-e interaction. The two molecular orbits consist of a spatially bonding orbital ϕ_s with electronic charge between the atom and spatially anti-symmetric anti-bonding orbital ϕ_a having a nodal plane and no charge midway given by

$$\phi_s = \frac{1}{\sqrt{2}}(\psi_1 + \psi_2); \phi_a = \frac{1}{\sqrt{2}}(\psi_1 - \psi_2) \quad (2.20)$$

where ψ_1 and ψ_2 are spatial components of individual electron 1 and 2. The $\psi_1(\vec{r}_1)$ and $\psi_1(\vec{r}_2)$ are solutions to Schrödinger equation. The symmetric and anti-symmetric

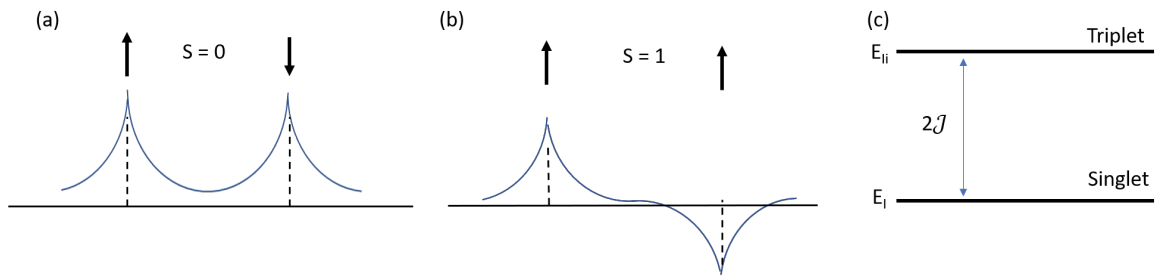


Figure 2.2.: (a) Spatially symmetric and (b) anti-symmetric wave function. (c) Splitting of spin-singlet and triplet states for H_2 molecule.

spin function are spin triplet and spin singlet states:

$$\begin{aligned}
 S &= 1; M_s = 1, 0, -1 \\
 \chi_s &= |\uparrow_1, \uparrow_2\rangle; \frac{1}{\sqrt{2}}(|\uparrow_1, \downarrow_2\rangle + |\downarrow_1, \uparrow_2\rangle); |\downarrow_1, \downarrow_2\rangle \\
 S &= 0; M_s = 0 \\
 \chi_a &= \frac{1}{\sqrt{2}}[|\uparrow_1, \downarrow_2\rangle - |\downarrow_1, \uparrow_2\rangle]
 \end{aligned}$$

According to the eqn. (2.19), the total anti-symmetric wavefunction is the product of the symmetric space and anti-symmetric spin functions or vice-versa:

$$\psi_I = \phi_s(1, 2)\chi_a(1, 2) \quad (2.21)$$

$$\psi_{II} = \phi_a(1, 2)\chi_s(1, 2). \quad (2.22)$$

Energy of two states are

$$\epsilon_{I,II} = \int \phi_{sa}^*(\vec{r}_1, \vec{r}_2)\mathcal{H}(\vec{r}_1, \vec{r}_2)\phi_{sa}(\vec{r}_1, \vec{r}_2)dr_1^3dr_2^3 \quad (2.23)$$

where $\epsilon_I < \epsilon_{II}$ for hydrogen molecule H_2 , meaning the bonding orbitals (spin singlet) lies below anti-bonding orbitals (spin triplet). The energy can be written as

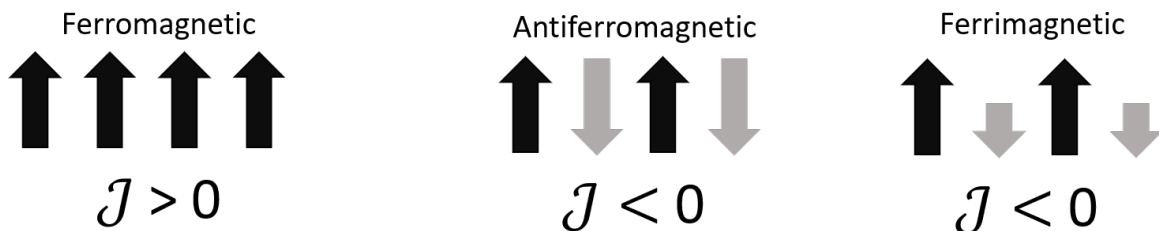
$$\mathcal{H} = -2\mathcal{J}\hat{s}_i \cdot \hat{s}_j \quad (2.24)$$

where the exchange integral $\mathcal{J} = (\epsilon_I - \epsilon_{II})/2$. Heisenberg generalized it to many electron atomic spins \hat{S}_1 and \hat{S}_2 in the well known equation,

$$\mathcal{H} = -2\mathcal{J}\hat{S}_1 \cdot \hat{S}_2 \quad (2.25)$$

where \hat{S}_1, \hat{S}_2 are dimensionless spin operators and \mathcal{J} has the units of energy. When $\mathcal{J} > 0$, the spins are parallel resulting in ferromagnetic (FM) type interaction. For $\mathcal{J} < 0$, anti-parallel arrangement of spins result in anti-ferromagnetic (AF) and ferri-magnetic type (FiM) interaction (see Fig. 2.3). For a lattice, the \mathcal{H} is generalized to sum over all neighbouring pair of atoms on lattice sites i, j :

$$\mathcal{H} = -2 \sum_{i>j} \mathcal{J}_{i,j} \hat{S}_i \cdot \hat{S}_j \quad (2.26)$$

Figure 2.3.: The sign of exchange integral \mathcal{J} resulting in various interactions in a solid

2.1.4. Macroscopic parameters

At this point one can define the macroscopic parameters \vec{M} , χ , \vec{B} and \vec{H} using magnetostatics. Magnetostatics describes the magnetic forces and energies due to distribution of magnetic material through classical physics formalisms. **Magnetization** (\vec{M}) is defined as the sum of the individual moments over the entire sample volume V , given by

$$\vec{M} = \frac{\sum_i \vec{\mu}_i}{V} \quad (2.27)$$

with unit A/m. In magnetostatics the magnetic moment is derived as shown in eqn. (2.1) and \vec{M} of a solid varies smoothly on mesoscopic scale in a continuous medium approximation. **Magnetic field** (\vec{B}) generated due to small current carrying elements is calculated using Biot-Savart's law. The source of \vec{B} -field is current either generated from moving charges, electric current flowing through conductors or magnetic moments. Maxwell's equations states that this \vec{B} -field is divergenceless ($\vec{\nabla} \cdot \vec{B} = 0$). The magnetic field lines form continuous loops and the net flux of \vec{B} across any closed surface is zero (Gauss's theorem). Alternative name for the magnetic field is magnetic flux density or magnetic induction and the unit is Tesla. The \vec{B} -field from a far away source varies as $\sim 1/r^3$. However, for experiments with magnetic field one would require uniform fields in some limited space. Certain structures of current carrying conductors such as inside of infinitely long solenoid, Helmholtz coils or a configuration of permanent magnets (Halbach cylinder) can create such uniform fields. The \vec{H} -field is an auxiliary field that is also known as magnetic field strength or magnetizing force. In a medium with magnetization \vec{M} , fundamental field \vec{B} and internal field \vec{H}_i are related as

$$\vec{B} = \mu_o(\vec{H}_i + \vec{M}) \quad (2.28)$$

where $\mu_o = 4\pi \times 10^{-7} H/m$. In free space $\vec{M} = 0$ then $\vec{B} = \mu_o \vec{H}$. The unit of \vec{H}_i is A/m and the unit of conversion is 1 T \sim 795 kA/m. Demagnetizing field \vec{H}_d depends on the shape of the magnetized material and is given by

$$\vec{H}_{di} = -\mathcal{N}_{ij} \vec{M}_i \quad i, j = x, y, z, \quad (2.29)$$

where \mathcal{N}_{ij} is the demagnetizing tensor. The tensor is generally represented by symmetric 3×3 matrix. The principle components of \mathcal{N} also known as demagnetizing factors in diagonal form is $(\mathcal{N}_{xx}, \mathcal{N}_{yy}, \mathcal{N}_{zz})$. External field acting on a sample is \vec{H} called the applied field. The sample itself does not affect the \vec{H} . The internal field in the sample is given by

$$\vec{H}_i = \vec{H} + \vec{H}_d \quad (2.30)$$

which is the sum of external field and demagnetizing field. The response of linear, isotropic and homogeneous magnetic material in a applied field is characterized by magnetic **susceptibility** given by

$$\vec{M} = \chi' \vec{H} \quad (2.31)$$

where χ' is the external susceptibility. The magnetization related to internal field H_i using eqn. (2.30) by

$$\vec{M} = \chi \vec{H}_i \quad (2.32)$$

where $1/\chi = 1/\chi' - \mathcal{N}$.

2.1.5. Types of magnetic order

The magnetic response of material that do not order in an applied magnetic field is either paramagnetic and diamagnetic. Susceptibility of many paramagnets is given by

$$\chi = \frac{C}{T} \quad (2.33)$$

which is the Curie law (Fig. 2.4 (a)). The susceptibility for some metallic paramagnets, given by Pauli susceptibility ($\chi > 0$) and almost all diamagnets ($\chi < 0$) is independent of temperature (Fig. 2.4 (b)). As discussed in previous section, FM order is a result of the parallel alignment of magnetic moment of individual atoms which results in the spontaneous magnetization M_s . At temperatures above Curie temperature T_C , the FM order collapses and the material becomes paramagnetic

where the atomic moments experience random thermal fluctuations. Above T_C , it follows Curie-Weiss law given by

$$\chi = \frac{C}{T - T_C} \quad (2.34)$$

where C is the Curie constant (Fig. 2.4 (c)). In an AF material, the atomic moments result in $M_s = 0$ due to two equivalent but oppositely oriented sub-lattices ($\vec{M}_A = -\vec{M}_B$). The transition temperature where the moments begin to order is the Néel temperature T_N . If magnetic sub-lattices are oppositely oriented but are inequivalent ($\vec{M}_A \neq -\vec{M}_B$) then there is a net spontaneous magnetization. Such ordering is present in FiM materials.

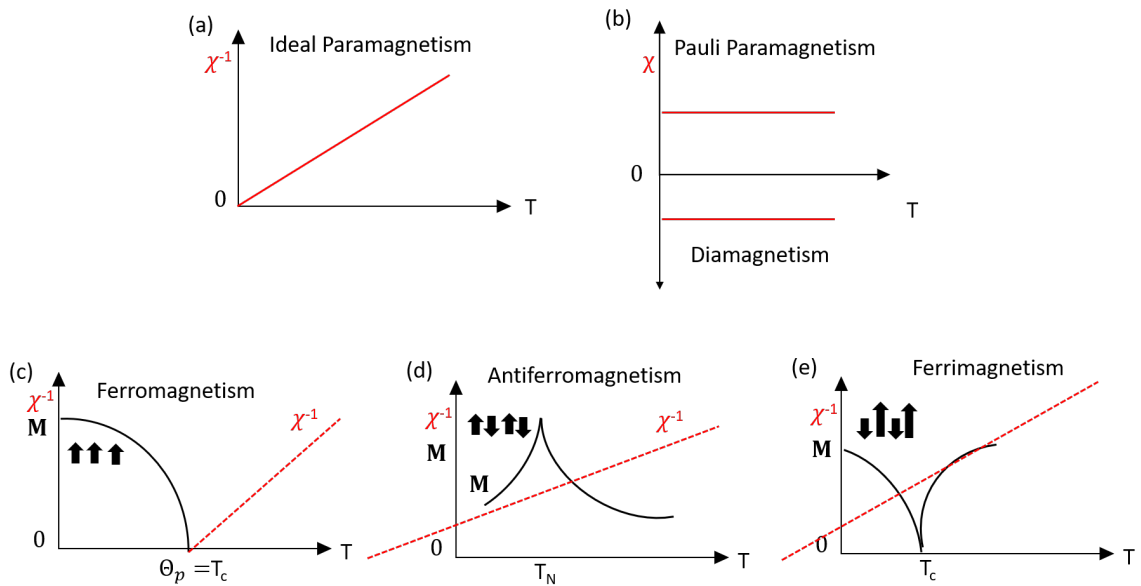


Figure 2.4.: Types of magnetic materials: temperature dependent susceptibility (red) and magnetization (black) curves for (a) an ideal paramagnet, (b) Pauli paramagnet and diamagnets, (c) ferromagnet, (d) antiferromagnet and (e) ferrimagnet ; adapted from [35].

2.1.6. Magnetic anisotropy

Magnetic anisotropy means FM or AF axis of a sample lie along a fixed direction. The tendency of \vec{M} to easily align along a preferred axis would define the easy axis of magnetization. This tendency to align is associated to the total anisotropy energy

which can be written as

$$E_a = K_{eff} V \sin^2 \theta \quad (2.35)$$

where θ is the angle between \vec{M} and anisotropy axis and K_{eff} is the anisotropy constant with units of J/m³. The anisotropy depends on the temperature and tends to 0 at T_C , if there is no applied field. The main sources of anisotropy are related to (a) crystal structure, (b) sample shape and (c) atomic and microscale structure. The terms that contribute to K_{eff} are listed in the table 2.1 [32, 31].

Table 2.1.: Different axial anisotropy constants and mechanisms

Anisotropy	Mechanism	Uniaxial constant
Crystalline	Crystal field	K_1
Shape	Magnetostatic	K_{sh}
Néel	Surface	K_s
Induced	Magnetoelastic, chemical	K_i

2.1.6.1. Magnetocrystalline anisotropy

Magnetization of 3D FM crystals approach saturation at different fields when magnetized in different directions. The origin of such anisotropy is associated with the SOC interaction of orbital containing magnetic electron with potential created at atomic site by rest of crystal. The crystal field tends to stabilize the SOC so that the orbital and the moment is aligned along a particular crystallographic direction. In Fe, the cube edges $\langle 100 \rangle$ are easy directions, while cube diagonals $\langle 111 \rangle$ are hard directions and for Ni, it is the other way round. On the other hand Co has unique hexagonal easy axis $[001]$. Note $\langle \rangle$ denotes set of equivalent directions and $[\]$ a single direction. Expressions for magnetocrystalline anisotropy energy (E_{MCA}) of different crystal symmetries are [31, 32] ;

- **Hexagonal:** $E_{mca} = [K_1 \sin^2 \theta + K_2 \sin^4 \theta + K_3 \sin^6 \theta \cos 6\phi]V$
- **Tetragonal:** $E_{mca} = [K_1 \sin^2 \theta + K_2 \sin^4 \theta + K_3 \sin^4 \theta \sin 2\phi]V$
- **Cubic:** $E_{mca} = [K_1(\alpha_1^2 \alpha_2^2 + \alpha_2^2 \alpha_3^2 + \alpha_3^2 \alpha_1^2) + K_2(\alpha_1^2 \alpha_2^2 \alpha_3^2)]V$

where α_i are directional cosines of magnetization, $\alpha_1 = \sin \theta \cos \phi$, $\alpha_2 = \sin \theta \sin \phi$ and $\alpha_3 = \cos \theta$. The anisotropy of a crystal system with a unique axis of high symmetry is called **uniaxial anisotropy**. In uniaxial crystals $E_{mca} = [K_1 \sin^2 \theta + K_2 \sin^4 \theta]V$,

for large $|K_1|$ the sample has an easy axis when $K_1 > 0$, easy plane perpendicular to symmetry axis when $K_1 < 0$ and conical in case of intermediate values of the constants. For most magnetization models used in nanoparticles, uniaxial anisotropy is considered by ignoring the higher order terms and is equivalent to $K_1 \sin^2\theta$. The type of crystal system is considered for calculating the K_2 .

2.1.6.2. Shape anisotropy

The magnetostatic energy E_m is given by

$$E_m = -\frac{1}{2}\mu_0 \int_V \vec{H}_d \cdot \vec{M} dV \quad (2.36)$$

where demagnetizing field \vec{H}_d is obtained from eqn. (2.29). This magnetostatic energy of the ellipsoid in terms of diagonal demagnetizing factors and components of \vec{M} is given by [32, 31]

$$E_m = \frac{1}{2}\mu_0 V (\mathcal{N}_{xx} M_x^2 + \mathcal{N}_{yy} M_y^2 + \mathcal{N}_{zz} M_z^2) \quad (2.37)$$

where $\mathcal{N}_{xx} + \mathcal{N}_{yy} + \mathcal{N}_{zz} = 1$, it follows that $\mathcal{N}_{\parallel} + 2\mathcal{N}_{\perp} = 1$. The total energy is then given by

$$E_m = \frac{1}{2}\mu_0 V M_s^2 (\mathcal{N}_{\perp} \sin^2\theta + \mathcal{N}_{\parallel} \cos^2\theta) \quad (2.38)$$

where θ is the angle between \vec{M} and rotation symmetry axis of the ellipsoid and M_s is the saturation magnetization. The shape anisotropy energy $E_s h$ related to energy

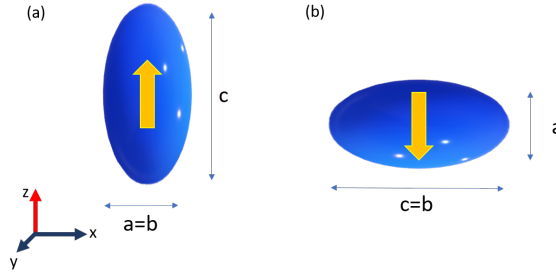


Figure 2.5.: Magnetization along (a) the long axis in a prolate and (b) short axis in oblate shaped ellipsoids with aspect ratio c/a .

difference $\Delta E_m = E_{hard} - E_{easy}$, when the ellipsoid is magnetized along the easy ($\theta = 0^\circ$) and hard directions ($\theta = 90^\circ$), is written as

$$E_{sh} = \frac{1}{2}\mu_0 V M_s^2 (\mathcal{N}_{\perp} - \mathcal{N}_{\parallel}) \quad (2.39)$$

For a prolate ellipsoid where $c > a = b$ with aspect ratio $A = c/a$, the magnetization is aligned along the long axis (see Fig. 2.5 (a)), $\mathcal{N}_\perp = \mathcal{N}_a = \mathcal{N}_b = \frac{1}{2}(1 - \mathcal{N}_c)$ and $\mathcal{N}_\parallel = \mathcal{N}_c$. Here, \mathcal{N}_c is given by [36, 32, 37]

$$\mathcal{N}_c = \frac{1}{A^2 - 1} \left[\frac{A}{2(A^2 - 1)^{1/2}} \times \ln \left(\frac{A + (A^2 - 1)^{1/2}}{A - (A^2 - 1)^{1/2}} \right) - 1 \right] \quad (2.40)$$

For an oblate ellipsoid or disc shaped ellipsoid where $c = b > a$ and magnetization is along the short axis as displayed in Fig. 2.5 (b). The demagnetizing factor along the small axis \mathcal{N}_a is

$$\mathcal{N}_a = \frac{A^2}{A^2 - 1} \left[1 - \frac{1}{(A^2 - 1)^{1/2}} \times \arcsin \left(\frac{(A^2 - 1)^{1/2}}{A} \right) \right] \quad (2.41)$$

where $\mathcal{N}_\perp = \mathcal{N}_c = \mathcal{N}_b = \frac{1}{2}(1 - \mathcal{N}_a)$ and $\mathcal{N}_\parallel = \mathcal{N}_a$. Then, rewriting equation (2.39) in terms of effective demagnetizing factor \mathcal{N}_{eff} , where $\mathcal{N}_\parallel = 1 - \mathcal{N}_{eff}$ and $\mathcal{N}_\perp = \mathcal{N}_{eff}/2$, the shape anisotropy constant is

$$K_{sh} = \frac{1}{4} \mu_o M_s^2 (1 - 3\mathcal{N}_{eff}) \quad (2.42)$$

and this is zero for a sphere when $\mathcal{N}_{eff} = 1/3$. Hence spherical particles as expected have negligible contribution from shape anisotropic energy. Non-ellipsoidal particles are approximately described by effective demagnetizing factor. Shape anisotropy is only effective in samples that are small like nanoparticles and do not break into domains [31].

2.1.6.3. Surface anisotropy

Due to the broken translation symmetry at the surface of small magnetic particles, the total exchange interaction is less for surface atoms than the bulk. Since at the surface, some neighbouring atoms are missing, the total dipole electric field is non zero and is directed normal to the surface. The effective anisotropy for spherical particles usually exhibits the following dependence

$$K_{eff} = K_V + \frac{6K_s}{D} \quad (2.43)$$

where K_V is the anisotropy of macroscopic sample and K_s is surface anisotropy of particles with diameter D . Surface anisotropy can influence the spin configuration of

FM particles as shown in Fig. 2.6. The spin configurations determined numerically by atomic scale Monte-Carlo simulation with simulated anneal are classified into throtled (Fig. 2.6 (b)), hedgehog (Fig. 2.6 (c)) and artichoke (Fig. 2.6 (d)) categories. The common picture from many studies is the presence of a region with spin disorder

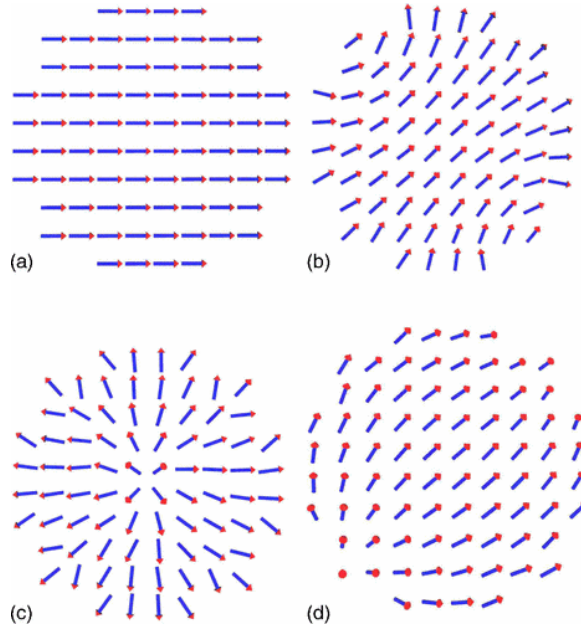


Figure 2.6.: Magnetic spin configurations in FM nanoparticles simulated with (a) no surface anisotropy, (b) and (c) with perpendicular surface anisotropy of increasing strength and (d) in-plane surface anisotropy. Reprinted (abstract/excerpt/figure) with permission from [38] ©(2008) by the American Physical Society.

similar to a spin glass where surface spins are magnetically coupled to the ordered spins in the core of a particle. The particles with FM core and AF shell structure could display the exchange bias phenomenon.

2.1.6.4. Other anisotropic contributions

Elastic energy of magnetic solid contributes to the magnetic anisotropy due to interaction between \vec{M} and strains which is given by

$$E_{me} = [B_1(\alpha_1^2\epsilon_{xx} + \alpha_2^2\epsilon_{yy} + \alpha_3^2\epsilon_{zz}) + B_2(\alpha_1\alpha_2\epsilon_{xy} + \alpha_1\alpha_2\epsilon_{yz} + \alpha_1\alpha_2\epsilon_{xz})]V \quad (2.44)$$

where B -factors are magnetoelastic coupling constants, α_i are the direction cosines and ϵ_i are strain components. Magnetoelastic energy increases anisotropy energy

when subjected to stress. Magnetostriction is due to change in \vec{M} that is related to the variation in dimension of solid. Other causes of induced anisotropy includes deposition, annealing in a magnetic field and chemical treatments.

2.2. Nanomagnetism

2.2.1. Magnetic nanoparticles

A nano-object is a physical object differing in properties from corresponding bulk and have at least one dimension in the nanometer regime. A nanoparticle (NP) is a quasi zero dimensional nano object in which all characteristic linear dimensions are in the nanometer range. Nanorods and nanowires are quasi 1D nano objects. Nanodisks and thin film hetero structures all fall in the 2D category [32]. Magnetic characteristics of atoms containing up to tens of atom are calculated using quantum methods. In macroscopic objects, the number of atoms are very large up to $\sim 10^{23}$, in which case one would additionally use statistics and thermodynamic descriptions. Therefore, the NPs that contain up to $\sim 10^5$ atoms are a bridge between bulk materials and single atoms. Quantum dots are examples of NPs with discrete energy levels. In other cases, NPs are treated using micromagnetic approach. In micromagnetism, magnetic sample is described as a continuous medium of small volume elements with magnetization \vec{M} . The volume element is larger than atomic dimension but smaller than the sample. Each volume element reaches a thermodynamic equilibrium in time much shorter than it takes the whole sample to reach equilibrium. NPs are treated as continuous medium of small size with deviation from bulk by taking into account the finite size effects. The magnetization at every point of the sample is obtained by minimization of the total energy given by

$$E = E_{ex} + E_m + E_a + E_z \quad (2.45)$$

where E_{ex} is the exchange energy (related to \mathcal{J}), E_m is the magnetostatic energy (related to stray fields and shape), E_a is the anisotropy energy (includes MCA, shape anisotropy), and E_z is the Zeeman energy due to applied field.

2.2.2. Single Domain

Magnetic domain structure in a bulk FM is a result of minimizing the magnetostatic energy. Magnetic domains are regions containing magnetic moments aligned in the same direction. Each domain can be represented by a single magnetization vector accounting for all its magnetic moments per volume (Fig. 2.7(a)) They are separated

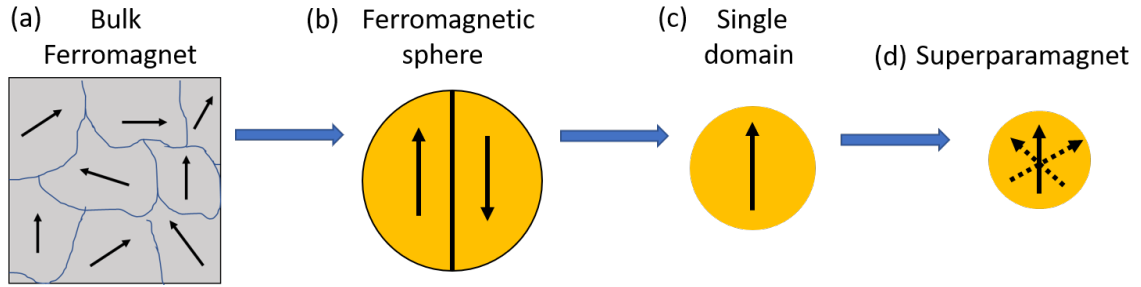


Figure 2.7.: Effect of size on magnetic properties of magnetic material: (a) multidomain bulk FM, (b) ferromagnetic sphere (c) single domain and (d) superparamagnet.

from each other through a domain wall. The domain structure is eliminated by a large enough applied magnetic field to reveal the underlying spontaneous magnetization of a FM. Macroscopic FM has a well defined T_C based on composition above which it is paramagnetic. As the specimen approaches nanosize, the magnetic correlation length diverges at T_C , hence correlated fluctuating moments are influenced by finite size effect of the specimen. Surface effects are due to lack of translational symmetry and reduced coordination number of surface spins. Decreasing size of a specimen will increase the ratio of surface spins to the total number of spins. The surface has different magnetic behaviour with respect to core and the competition between them can define the magnetic properties. Let us start with bulk single spherical sample of FM (or AF) at temperature lower than the ordering temperature T_C (or T_N)(Fig. 2.7 (b)). Each step in size reduction is a thermodynamic process. As the size of specimen decreases and becomes comparable to domain size, the domain configuration is significantly modified. There is a specimen critical size, D_{SD} , below which it is favourable to not have domain boundaries (Fig. 2.7 (c)). The uniformly magnetized core carries a magnetic super moment frozen in magnetocrystalline easy direction. At $D > D_{SD}$, one could magnetize and demagnetize the particle under applied magnetic field by simply moving domain wall with a low energy barrier. When $D < D_{SD}$, only way to change the magnetization of the sample containing spatially fixed single domain is

by overcoming the magnetocrystalline field. The single domain state further depends strongly on the magnetic anisotropy of the specimen. For systems with low anisotropy, as shown in the Fig. 2.8 (a), the configuration inside results in closed rings so the total moment is zero. If crystalline anisotropy is large, as shown in cubic crystals (Fig. 2.8 (b)) most of the moments lie along the easy direction. In strongly uniaxial crystals, single domain particles has uniform magnetization along the unique easy axis (Fig. 2.8 (c)). Therefore, finite size, shape and surface affects the spin configuration

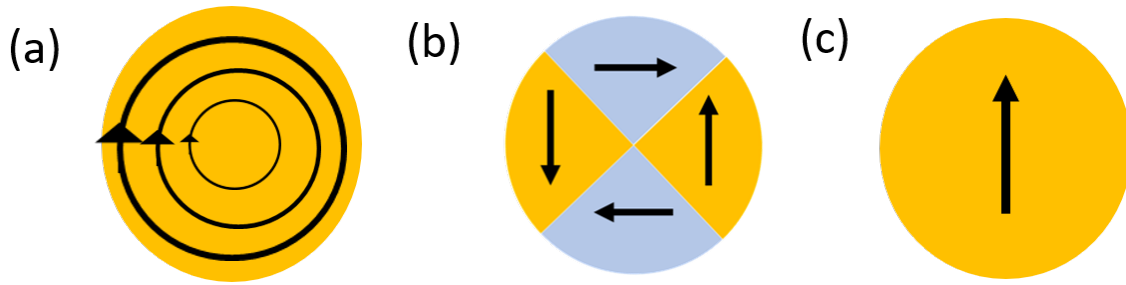


Figure 2.8.: Magnetization in small NP with (a) low anisotropy (b) high anisotropy in cubic crystal and (c) uniaxial system.

of the particle. The thermal energy is comparable to the anisotropy energy for single domain particles at a critical volume. In this condition, the particles behave as superparamagnets, a name derived from behaviour of atomic spins (paramagnets) but here with much larger moments. The magnetization curve of single domain particles with stationary, uniform magnetization is described by Stoner-Wohlfarth (SW) model. In the SW regime, individual atomic moments turn in homogeneous coherent fashion with magnetic field, whereby the magnetization of the whole domain remains parallel to the field. The Néel rotation governs the restructuring of electronic spin states to allow the magnetic moments to reorient irrespective of the orientation of the whole particle (Fig. 2.9 (a)). On the other hand, when the particles are free to rotate like in a fluid, the particles itself may undergo alignment called Brownian rotation (Fig. 2.9 (b)). The theory of Rosensweig is used to decouple the mechanisms based on their relaxation times [39]. The Néel relaxation is

$$\tau_n = \tau_o \exp\left(\frac{K_{eff}V}{k_B T}\right) \quad (2.46)$$

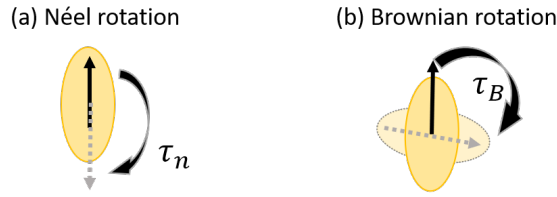


Figure 2.9.: The initial state of the magnetic moment is the ellipsoid with magnetic moment (black arrow) pointing along the long axis. (a) Néel rotation, when the magnetic moment rotates in the ellipsoid and (b) Brownian rotation where the particle itself rotates.

and Brownian relaxation is given by

$$\tau_b = \frac{3\eta V_H}{k_B T} \quad (2.47)$$

where τ_o , V_H and η is the attempt time, hydrodynamic volume and viscosity of the solvent, respectively [40].

2.2.3. Stoner-Wohlfarth (SW) model

In the SW model, FM NP is represented by a single domain ellipsoid. The uniaxial ellipsoid has magnetization \vec{M} that forms an angle θ with easy anisotropy axis (z-axis). The applied field \vec{H} forms an angle ψ with the easy axis (Fig. 2.10) [32, 33]. SW - model consists of simpler micromagnetic approach which neglects exchange term in total energy function (eqn. (2.45)). This treatment is often referred as a macrospin model which assumes coherent reversal of individual atomic magnetic moments so that they behave as a single macroscopic moment. The energy of the ellipsoid is then [32]

$$E = [K_1 \sin^2 \theta - \frac{1}{2} \mu_o M_s^2 (\mathcal{N}_\perp \sin^2 \theta + \mathcal{N}_\parallel \cos^2 \theta) - \mu_o M_s H \cos(\psi - \theta)] V \quad (2.48)$$

$$E = [K_{eff} \sin^2 \theta - \mu_o M_s H \cos(\psi - \theta)] V \quad (2.49)$$

where K_{eff} is the effective anisotropy. The origin of this anisotropy maybe magnetocrystalline (K_1), shape (K_{sh}) and surface (K_s) related. When magnetic field is applied to a FM there is a change in magnetization. The locus of \vec{M} projected along the direction of applied field \vec{H} is plotted as M(H) hysteresis loop. The main characteristics of the hysteresis loop are M_s (saturation magnetization where all moments

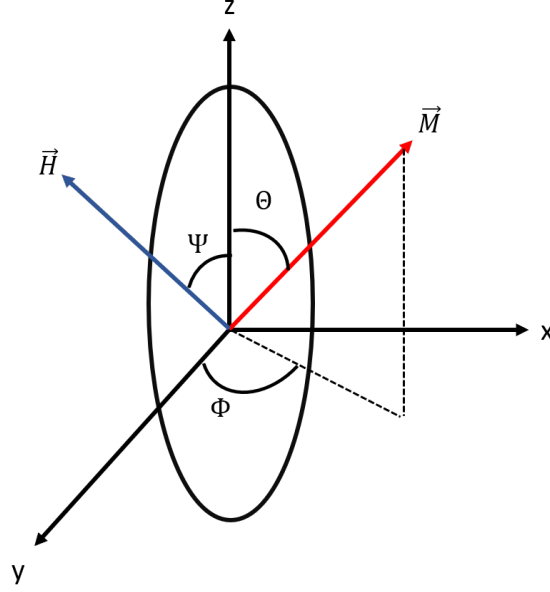


Figure 2.10.: Single domain ellipsoidal particle in a magnetic field \vec{H} with relevant angles between this field, anisotropy z-axis and magnetization \vec{M} .

are aligned in common direction), M_r (remanent magnetization is the leftover magnetization when $H = 0$) and H_c (coercive field at which $M = 0$). The moment will select a direction where total energy given by eqn. (2.49) is minimized. The orientation may occur smoothly (rotation) or suddenly (switching) that will result in discontinuous M at same value of H . We additionally define anisotropy field $H_A = 2K_{eff}/(\mu_o M_s)$ and factor $h = \frac{H}{H_A}$. The energy minimum condition is given by

$$\left(\frac{\partial E}{\partial \theta} \right)_{\theta=\theta^*} = 0 \quad \text{and} \quad \left(\frac{\partial^2 E}{\partial \theta^2} \right)_{\theta=\theta^*} > 0 \quad (2.50)$$

and normalizing the magnetization to saturation we define $\vec{m} = \frac{\vec{M}}{M_s}$ yields

$$[\sin\theta\cos\theta + h\sin(\theta - \psi)]_{\theta=\theta^*} = 0 \quad \text{and} \quad [\cos(2\theta) + h\cos(\theta - \psi)] \geq 0 \quad (2.51)$$

To present the possible solution, we define two components

- (i) longitudinal magnetization, is the projection of \vec{M} along \vec{H} , $m_{\parallel} = \cos(\theta - \psi)$.
 - (ii) transverse magnetization, projection of \vec{M} perpendicular to \vec{H} , $m_{\perp} = \sin(\theta - \psi)$
- The minimum is analytically derived from eqn. (2.51) for $\psi = 0$ and $\psi = \frac{\pi}{2}$;

- (i) At $\psi = 0$, $\theta^* = \cos^{-1}(-h)$ when $h \leq 1$ otherwise $\theta^* = 0, \pi$ yield square hysteresis in

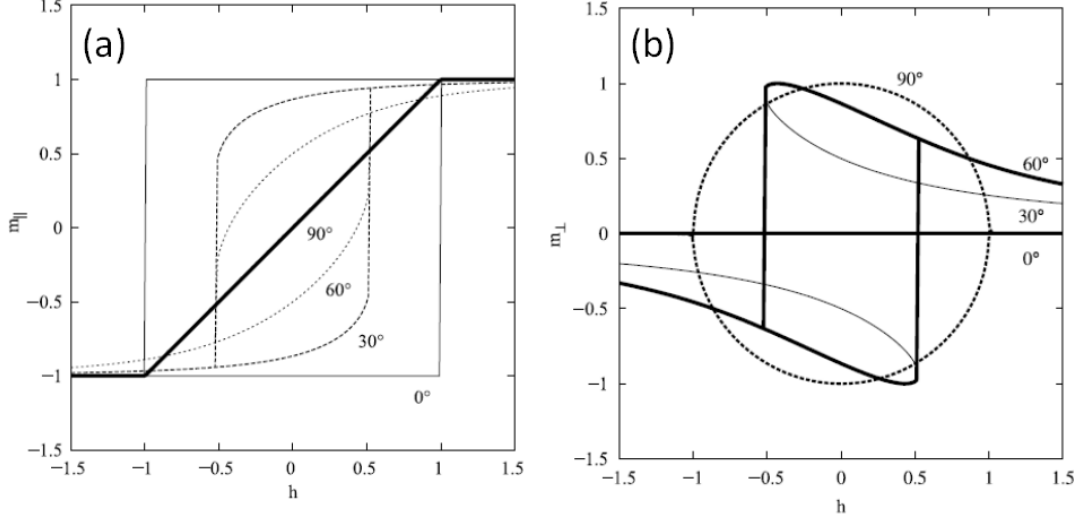


Figure 2.11.: (a) Longitudinal and (b) transverse hysteresis loops for various angles ψ of the field $h = H/H_A$ with the anisotropy axis; reprinted with permission [41].

Fig. 2.11 (a) and a line in m_{\perp} Fig. 2.11 (b).

(ii) At $\psi = \frac{\pi}{2}$, $\theta^* = \sin^{-1}(-h)$ when $h \leq 1$ otherwise $\theta^* = \pi/2$ yield $m_{||} = h$ in Fig. 2.11 (a) and circle for $m_{\perp} = \pm\sqrt{1-h^2}$ in Fig. 2.11 (b)

Model demonstrated how anisotropy energy affects the system hysteresis even without any domain walls. SW-model allows computation of the height of barrier due to anisotropic energy. From the minimization conditions in eqn. (2.50) and (2.51) for $\psi = 0$, there are three solutions given by $\theta = 0$, $\theta = \pi$ and $\theta = \cos^{-1}(H/H_A)$. The third value corresponds to the maximum of the energy barrier. Since $\cos(H/H_A) \leq 1$, this expression gives minimum field that allows inversion of magnetization. The energy barrier is derived as $\Delta E = E_{max} - E(\theta = 0)$ is

$$\Delta E = K_{eff}V \left(1 - \frac{H}{H_A}\right)^2 \quad (2.52)$$

and the barrier height is proportional to $K_{eff}V$ (Fig. 2.12 (a)) and disappears when $H = H_A$ (Fig. 2.12 (b-c)).

2.2.4. Superparamagnetism (SPM)

As given by the SW model, single domain magnetic particle has two energy minima separated by a barrier $E_B = K_{eff}V$. The transition from one minimum to another

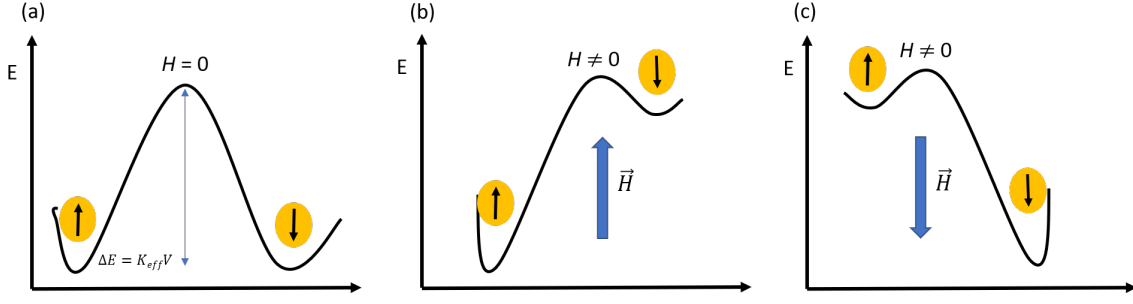


Figure 2.12.: (a) The energy barrier of the single domain ellipsoid at $H = 0$ for a spin flip. Switching of magnetization of a single domain ellipsoid particles across the energy barrier under the action of an external magnetic field H (b) pointing upward and (c) pointing downward; adapted from [41].

is thermally activated, and the probability is high when energy is comparable to or larger than $K_{eff}V$. In an ensemble of magnetized particles at temperature $T \neq 0$, set $H = 0$ at instant $t = 0$, magnetization will evolve with time. Néel proposed that the relaxation of this moment is determined by attempt frequency (τ_o^{-1}) and Boltzmann probability ($\exp(-E_B/k_B T)$) that the particle has the thermal energy necessary to surmount the barrier. The relaxation time from Néel- Arrhenius equation (2.46) can be simplified as

$$\ln(\tau_n) = \ln(\tau_o) + \frac{K_{eff}V}{k_B T}. \quad (2.53)$$

With macroscopic techniques involving direct measurement of \vec{M} , there is an associated measuring time t_m . If the relaxation time τ is shorter than t_m , then the measured magnetization of NP is zero and particles are in **superparamagnetic** (SPM) regime. If the opposite occurs ($\tau > t_m$), particles are in blocked state and non-zero instantaneous magnetization is measured. In most cases, the measuring time is fixed for a measurement, while the sample volume and temperature can be varied to change the energy barrier. Hence, we rearrange eqn. (2.53), to obtain a critical volume

$$V = \frac{k_B T}{K_{eff} \ln\left(\frac{\tau_n}{\tau_o}\right)}. \quad (2.54)$$

The critical volume for a given temperature with $t_m = 100s$ and $\tau_o = 10^{-9}s$ is given by

$$V_{cr}^{SPM} = \frac{25k_B T}{K_{eff}} \quad (2.55)$$

2.2.5. Blocking temperature (T_B)

Conversely to eqn. (2.55), there is a temperature for a given volume where FM behaviour is observed which is given by

$$T_B \approx \frac{K_{eff}V}{25k_B} \quad (2.56)$$

and this temperature T_B is called the **blocking temperature**. The blocking temperature is not uniquely defined and depends on the time scale of measurement, volume and composition of the particle. Thus measurement of T_B will help identify the size of the NP.

2.2.5.1. Langevin function

The temperature dependence of the magnetization on an assembly of particles in SPM regime is described by Langevin function. This is the classical analogue of Brillouin function that describes paramagnetism. Hence, the derivation follows the expression of magnetization for ensemble of paramagnetic atoms with difference being that the angular momentum is not quantized here. The projection of moment along the z-direction is given by

$$\mu^z = \mu \cos\theta \quad (2.57)$$

where θ may take any angle between 0 and π . Taking averages of θ , the expression of magnetic moment projected along z-axis is

$$\langle \mu^z \rangle_T = \mu \mathcal{L}(x) \quad (2.58)$$

where $x = \frac{\mu B}{k_B T}$ and $\mathcal{L}(x)$ is the Langevin function, given by

$$\mathcal{L}(x) = \coth x - \frac{1}{x} \quad (2.59)$$

2.3. Interparticle interactions in colloid

Self-assembly is a process in which components either separated or linked, spontaneously form ordered aggregates. From a living cells containing complex structures to formation of liquid crystal, concepts of self-assembly developed initially for molecular components are both scientifically and technologically important [1]. There are

primarily three size ranges for which self-assembly is important (i) molecular system, (ii) nanoscale system (colloids and nanowires) and (iii) meso to macroscale objects. Rules for self-assembly in each range though similar may not be identical. Chemists have a great control over structures of molecules but little control over the characteristic atoms. By contrast it is possible to choose wide range of interactions: van der Waals, ionic, steric, entropic, magnetic, electrostatic and other forces using components larger than molecules. Non molecules are therefore more flexible when it comes to designing larger structures than molecular system. In this section, we discuss the dominant forces present in colloidal systems which will be the focus of our study in later chapters.

2.3.1. van der Waals (vdW) forces

The van der Waals interactions are ubiquitous attractive forces present between any two physical bodies. In any atom or molecule, random and incessant fluctuation of charges result in an arbitrary electric dipole that induce electric displacement in neighbouring atoms leading to dipole-dipole interactions. In general, these vdW interaction energy between atoms and molecules is given by [42, 43]

$$E_{vdW} = -\frac{C_{vdW}}{r^6} \quad (2.60)$$

where, r is the distance between the atoms or molecules and C_{vdW} is the constant characterizing the interacting species. The constant depends on three distinct interactions namely: [42, 43]

- **Keesom force**, or the orientation force, appears between two permanent dipoles. This is an attractive dipole-dipole interaction over various rotational orientations of dipoles.
- **Debye force** or the induction force, is present between permanent reordering dipole and induced dipole due to polarizability of atoms and molecules. Both Debye and Keesom forces involve at least one permanent dipoles.
- **London dispersion forces** are attractive forces generated by transient dipoles of polarizable bodies.

The simplistic Hamaker integral approximation of these vDW forces in larger systems such as nanoparticles consisting of tens to hundreds of atoms assumes a pairwise

summation of all such molecular interactions. Following this, the integration in case of two spheres show interaction energy falls as r^{-6} when separation distance is much larger than particle size ($s \gg a$). For a large particle, at short separation distance ($s \ll a$), the decay follows as r^{-1} behavior. The vdW energy in case of sphere is [42, 44]

$$E_{vdW} = -\frac{A_{132}}{3} \left[\frac{a^2}{s(s-4a)} + \frac{a^2}{(2s+a)^2} + \frac{1}{2} \ln \frac{s(s-4a)}{(2s+a)^2} \right] \quad (2.61)$$

where A_{132} is the Hamaker constant depends on density and polarizability of interaction for material 1 and 2 interacting over medium 3. Here, A_{102} and A_{1w2} refer to vdW interaction across vacuum and water respectively. For, $s \ll a$ the energy of the sphere can be approximated to $E_{vdW} = -A_{132} \frac{a}{12s}$. For iron oxides, comparing densities of magnetite (Fe_3O_4), maghemite ($\gamma\text{-Fe}_2\text{O}_3$) and hematite ($\alpha\text{-Fe}_2\text{O}_3$) gives $A_{maghemite} < A_{magnetite} < A_{hematite}$ in vacuum. The Hamaker constants for iron oxide (magnetite) in toluene interacting with gold is calculated to be 16×10^{-21} J [45]. In this approximation, many body effect is neglected and further accounted in advanced more precise theories like Dzyaloshinskii-Lifshitz-Pitaevskii (DLP) and discrete coupled dipole method (CDM) [46, 47, 48]. These many body effects are more prevalent in nanoparticles. In discrete coupled method NP is modelled as discrete array of transient dipoles given by dipole moment $p_i = \alpha_i E_i$ where α_i is the frequency dependent polarizability and E_i is the local electric field due to neighbouring dipoles. Set of frequency modes and free energy of the system is obtained by solving set of self-consistent equations for N such dipoles. CDM is computationally more demanding with advantage for calculating vdW for small anisotropic particles. In symmetric particles, the first order approximation remains valid.

2.3.2. Electrostatic (ES) forces

Unlike vdW forces which are primarily attractive, electrostatic forces (ES) can be attractive, repulsive and directional. The magnitude of energy due to vdW forces range from few to $100 k_B T$ in nanoscopic components. While in some cases they can be harnessed to form assemblies, most times this undesired attraction in nanoparticles result in flocculation or precipitation. Repulsive surface forces coexist with vdW forces to stabilize the colloidal dispersion against precipitation [42, 49]. The surface of the particle acquires a charge when immersed in polar fluid through several mechanisms such as disassociation of surface groups or specific absorption. The surface charge is balanced by an excess of counter-ions and depletion region of co-ions in the

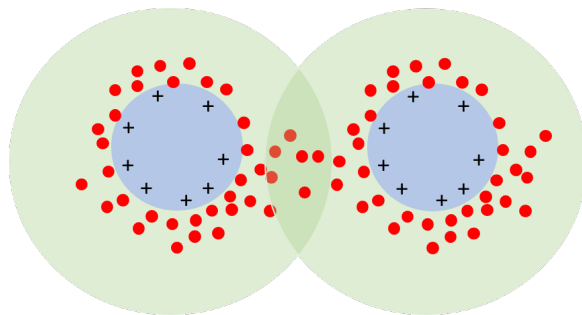


Figure 2.13.: Sketch showing overlap of ionic clouds around positively charged particles (blue spheres). The surface charge is balanced by excess of counterions (red spheres) with depletion of co-ions (green region). This electric double layer is formed when particles are dispersed in a polar solvent.

surrounding volume of the particle. This is called the electric double layer (EDL) as shown in the Fig. 2.13. The interaction length scales of the potential is associated with thickness of the double layer that is given by the Debye length κ^{-1} which decays with distance r . ES interactions depend on the surface charge, dielectric constant of solvent and ionic strength. In a polar solvent, the pair interaction energy depends on ionic concentration and osmotic pressure when EDL overlap rather than Coulombic interaction. The ES for large separation distance ($s > \kappa^{-1}$) is [42, 49, 50]

$$E_{ES} = \frac{64\pi a C_o N_A k_B T \Gamma^2}{\kappa^2} e^{-\kappa s} \quad (2.62)$$

where Γ is the reduced surface potential. The DLVO theory (named after Boris Derjaguin and Lev Landau, Evert Verwey and Theodoor Overbeek) describes colloidal stability of charged particles assuming vdW and ES forces as additive [50, 51]. The DLVO pair interaction energy for two spheres is

$$E_{DLVO}^{ES+vdW} = a \left(\frac{64\pi a C_o N_A k_B T \Gamma^2}{\kappa^2} e^{-\kappa s} - \frac{A}{12s} \right) \quad (2.63)$$

which have two minima separated by a barrier. At ionic concentration, thickness of EDL is small and DLVO is dominated by vdW interaction. The stability of suspensions are strongly affected by the changes in ionic strength, hence for a more robust stabilization nanoscale interactions like steric interactions are needed which are outside the scope of DLVO theory.

2.3.3. Steric force

Steric interactions arise when large molecules adsorbed on the surface of particles prevent direct interparticle contact. Similar to ES repulsions that complement attractive vdW forces through charge stabilization, these forces also prevent uncontrolled aggregation of the particles. Polymers and surfactants with good affinity to both solvent and particle are commonly used for stabilization. Usually in metal oxide, the hydroxyl group tether to surface through hydrogen bonding, ES interaction or acid base interaction. The length scale of interaction corresponds to the thickness of the layer, which relates to molecular weight and conformation of chains. The individual segment of the polymer chain can assume a random coil shape with radius of gyration $R_g = \ell_m \sqrt{\frac{N}{6}}$, where N is the number of monomer segments and ℓ_m is length of each monomer unit [52, 53]. When effective size of polymer is larger than R_g then polymer-solvent interactions are favoured. In poor solvents, where polymer-polymer interactions are favoured, size of the polymer is smaller than R_g . At this point, we can define two regimes [54]: (i) adsorption layer is observed when surface of the particle preferred the polymer and (ii) depletion layer is formed at vicinity of the surface when surface prefers the solvent over polymer. Additionally, high coverage of particle surface increases the thickness of adsorbed layer. The combined effect of solvent conditions and surface coverage results in equilibrium thickness given by

$$t_{eq} = N(\zeta \ell_m^5)^{1/3} \quad (2.64)$$

where ζ is the surface coverage density. There are several ways to bind the polymer to the surface of the particle: (i) surface adsorption and (ii) grafting the polymers on the surface [55]. The steric pair interaction energy is approximately given by exponential decay when $t_{eq}/2 < s < 2t_{eq}$ [52]

$$E_{steric} = \frac{100}{\pi} t_{eq} \zeta^{3/2} k_B T e^{-\pi \left(\frac{s}{t_{eq}} - 1 \right)} \quad (2.65)$$

For nanoparticles coated with long ligand and with curved geometries the steric repulsion energy can also be written as [42]

$$E_{steric} = \frac{2\pi a_1 a_2}{a_1 + a_2} \left(-\ln(u) - \frac{9}{5}(1-u) + \frac{1}{3}(1-u^3) - \frac{1}{30}(1-u^6) \right) \quad (2.66)$$

where $u = \frac{r-a_1-a_2}{2h_o}$, ζ is the surface charge density and $h_o = N \left(\frac{12\zeta \ell_m^5 w}{\pi^2} \right)^{1/3}$.

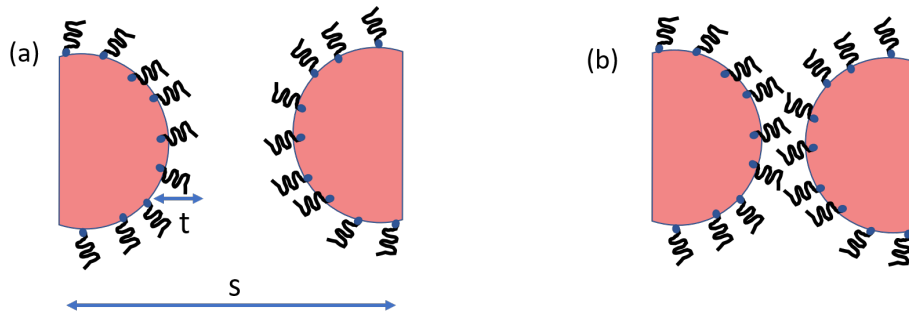


Figure 2.14.: Steric repulsion caused by surfactants or polymers on the surface: (a) when particles have a separation distance larger than twice thickness of surfactant layer $s > 2t$, no repulsion interaction exist and (b) when surfactants are interdigitated $s < 2t$ results in steric repulsion.

2.3.4. Magnetic forces

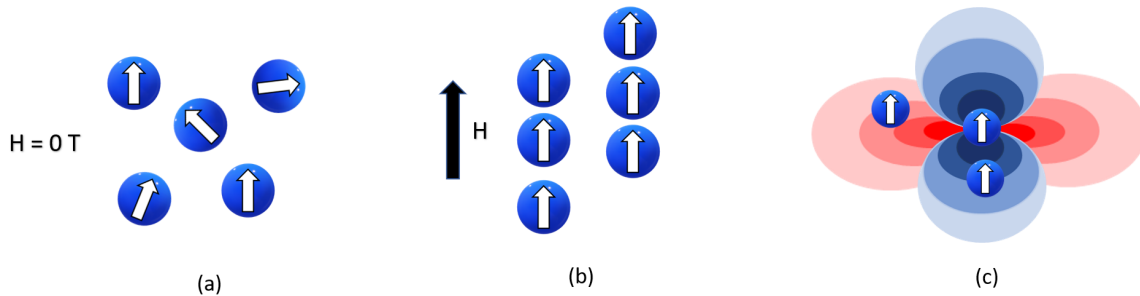


Figure 2.15.: Magnetic dipolar interactions between magnetic nanoparticles: (a) schematic of random orientation of magnetic moments (represented by white arrows) in weakly interacting spherical magnetic nanoparticles when no field is applied and in (b) chain like aggregates are formed when field is applied. (c) The attraction (blue) and repulsive region (red) in between dipoles based on the position of the dipoles; adapted from [42]

As seen in the section 2.2, the magnetic properties are size dependent for MNPs. These properties further affects the interactions that drives the formation of assemblies. At $T > T_B$, MNPs exhibit SPM and weak interactions. At $T < T_B$, the interactions between MNPs are significant. When interactions are strong, the blocking process for individual particles are no longer independent. Dipole-dipole interactions are long range forces of a large magnitude. When there is no direct contact between MNPs, exchange interactions can be neglected. A single spherical magnetic particle

of radius a with magnetization \vec{M} has a magnetic moment (using equation (2.27))

$$\vec{\mu} = \vec{M}V \quad (2.67)$$

where $V = \frac{4}{3}\pi a^3$. The field generated from this moment is given by

$$\vec{B} = \mu_o \vec{H} = \frac{3(\vec{\mu} \cdot \hat{r})\hat{r} - \vec{\mu}}{4\pi r^3} \quad (2.68)$$

where $\hat{r} = \vec{r}/r$ is unit vector. The Zeeman energy of such a dipole particle in the field \vec{B} is

$$E_z = -\mu_o \vec{\mu} \cdot \vec{H} \quad (2.69)$$

such that dipole experiences a force $F = \nabla(\vec{\mu} \cdot \vec{H})$. The dipole-dipole energy between two spheres with magnetic moment μ_1 and μ_2 is [53, 42]

$$E_{dd} = \frac{\mu_o}{4\pi r^3} [\vec{\mu}_1 \vec{\mu}_2 - 3(\vec{\mu}_1 \cdot \hat{r})(\vec{\mu}_2 \cdot \hat{r})]. \quad (2.70)$$

This is the energy required to bring magnetic dipoles $\vec{\mu}_1$ and $\vec{\mu}_2$ from infinity to a separation distance \vec{r} . The schematic of interactions in an applied field are outlined in the Fig. 2.15. This energy can be attractive or repulsive based on the position of vectors. For instance, when the dipoles are aligned in a line, $\vec{\mu}_1 \cdot \vec{\mu}_2 = \mu^2$ and $\vec{\mu}_1 \cdot \hat{r} = \vec{\mu}_2 \cdot \hat{r} = \mu$ results in an attractive energy $E_{dd} = -\frac{\mu_o \mu^2}{2\pi r^3}$. In case of dipoles aligned in a side by side configuration, $\vec{\mu}_1 \cdot \vec{\mu}_2 = \mu^2$ and $\vec{\mu}_1 \cdot \hat{r} = \vec{\mu}_2 \cdot \hat{r} = 0$, the repulsive energy is $E_{dd} = \frac{\mu_o \mu^2}{4\pi r^3}$. Energy scales with the volume of the particles and long range interaction decay as r^{-3} . Multipole expansions maybe required to describe interactions from anisotropic particles.

2.3.5. Gravitational force

Colloidal particle in dispersion can undergo a gravitational drift combined with Brownian forces [56]. Brownian diffusive forces are inherent in the system and result from factors such as viscosity of the fluid. The force of gravity on the system depends on the density of the particle in the dispersion.

2.4. Scattering

Almost all our knowledge in the atomic and nuclear physics have been discovered through scattering experiments. Most prominent examples include Rutherford's discovery of nucleus and discovery of subatomic quarks. A typical scattering experiment consists of a source emitting monochromatic radiation in form of a plane wave with a wave vector \vec{k} [57]. Incident wave interacts with matter either elastically (energy conserved), inelastically (no energy conservation) or absorption occurs. Scattering is a quantum mechanical phenomenon which involves interaction of radiation with matter.

2.4.1. Elastic scattering experiment

In an idealized scattering experiment, scattering of x-ray photon or a neutron by a sample is characterized by change of momentum and energy. The particles with incident wavevector \vec{k} , and energy $\hbar\omega_i$ on interaction with sample results in \vec{k}' and energy $\hbar\omega_f$. The momentum transfer is then expressed as

$$\hbar\vec{k}' - \hbar\vec{k} = \hbar\vec{Q} \quad (2.71)$$

where \vec{Q} is the scattering vector given by $\vec{Q} = \vec{k}' - \vec{k}$. Similarly, energy transfer is

$$E = \hbar\omega \quad \text{where} \quad \omega = \omega_f - \omega_i \quad (2.72)$$

The scattering experiment measures the proportion of incident particles emerging with a given energy and momentum transfer which is encoded in 4-D function $\mathcal{S}(\vec{Q}, \omega)$ [57]. When there is no exchange of energy, this is encoded in the scattering function $\mathcal{S}(\vec{Q}, 0) = \mathcal{S}(\vec{Q})$. Thesis will focus mainly on this special case of elastic scattering where $E = 0$. The elastic scattering experiment in the Fraunhofer approximation is shown in the Fig. 2.16. Here, the size of the sample is assumed much smaller than sample-to-source and sample-to-detector distance. Additionally, the source is monochromatic with wavelength λ [58, 59]. Then the incident wave on sample (\vec{k}) and scattered wave (\vec{k}') incident on the detector are considered as plane waves. In case of x-rays, photons are massless, the dispersion relation is $c = \omega/k$ where c is the speed of light. Then, zero energy transfer condition implies $E = \hbar c|\vec{k}'| - \hbar c|\vec{k}| = 0$. Similarly, for a neutron of mass m_n , the energy transfer is given by the kinetic energy

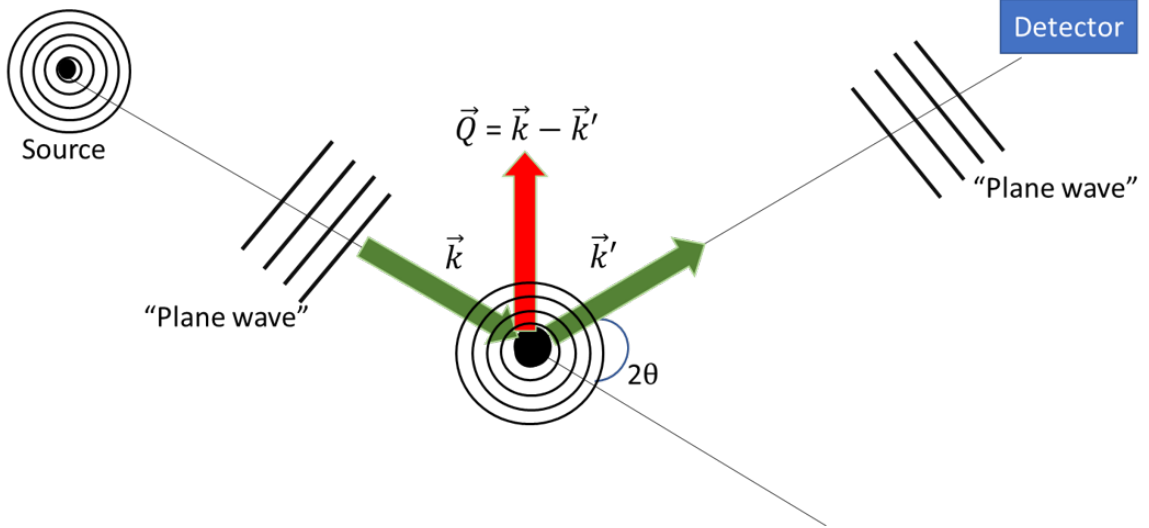


Figure 2.16.: The sketch of the elastic scattering process in the Fraunhofer approximation with a monochromatic source; the sketch is adapted from [58]

$E = \frac{\hbar \vec{k}'^2}{2m_n} - \frac{\hbar \vec{k}^2}{2m_n} = 0$. Then we arrive at the condition for elastic scattering where

$$|\vec{k}| = |\vec{k}'| = \frac{2\pi}{\lambda}. \quad (2.73)$$

From the vector diagram and geometry, $|\vec{Q}|$ can be deduced as

$$|\vec{Q}| = \sqrt{k^2 + k'^2 - 2kk' \cos 2\theta} \rightarrow |\vec{Q}| = \frac{4\pi \sin \theta}{\lambda} \quad (2.74)$$

where 2θ is the angle between \vec{k} and \vec{k}' .

2.4.2. Scattering cross-section

The incoming neutrons/x-rays form a steady stream of particles, the incident flux j_1 is specified as the number of particles per unit time across a unit area normal to the direction of incidence. The rate of arrival of particles (number of particles per unit time) in the direction of (θ, ϕ) into a detector that subtends a small solid angle $d\Omega$ at sample is $Nd\Omega$. The differential cross section is defined as the ratio of the number of particles scattered into direction (θ, ϕ) per unit solid angle, to incident flux [57, 58]

$$\frac{d\sigma}{d\Omega} = \frac{N}{j_1} \quad (2.75)$$

and from the differential the total scattering cross section is obtained by integrating all solid angles

$$\sigma = \int_0^{4\pi} \frac{d\sigma}{d\Omega} d\Omega \quad (2.76)$$

2.4.3. Quantum scattering theory

As shown in the Fraunhofer approximation (Fig. 2.16 (b)), there is a monochromatic source with plane waves impinging on a fixed scattering point, with localized potential $V(\vec{r})$. The aim is to solve the time dependent Schrödinger equation $i\hbar \frac{\partial \Psi(\vec{r}, t)}{\partial t} = \left[-\frac{\hbar^2}{2m} \nabla^2 + V(\vec{r}) \right] \Psi(\vec{r}, t)$ for all incoming particles represented by the wave function $\Psi(\vec{r}, t)$. In the case of pure elastic scattering, the plane waves maybe written as $\Psi(\vec{r}, t) = \psi(\vec{r}) e^{-\frac{iEt}{\hbar}}$. Therefore, we now seek solutions of time independent Schrödinger equation

$$E\psi(\vec{r}) = \left[-\frac{\hbar^2}{2m} \nabla^2 + V(\vec{r}) \right] \psi(\vec{r}). \quad (2.77)$$

Under the action of plane waves on the scattering center, the center becomes a source of spherical standing waves (Huygens principle). The spatial part of the total wavefunction is then the superposition of the plane waves representing beam and spherical waves representing the scattered particles. The asymptotic form of the scattering solution thus becomes

$$\psi(\vec{r}) = e^{i\vec{k} \cdot \vec{r}} + f(\theta, \phi) \frac{e^{ikr}}{r} \quad (2.78)$$

where $f(\theta, \phi)$ is the scattering amplitude. The flow of scattered particles is given by the probability current which is used to compute the outgoing flux and using this in eqn. (2.75), the differential cross-section is then computed as

$$\frac{d\sigma}{d\Omega} = |f(\theta, \phi)|^2. \quad (2.79)$$

2.4.3.1. Lippman-Schwinger equation

In a scattering problem, the Schrödinger equation is solved with a boundary condition that the wavefunction is plane wave at large distance from scattering center. Using $E = \frac{\hbar^2 k^2}{2m}$, the eqn.(2.77) is rewritten as [60, 61]

$$(\nabla^2 + k^2)\psi(\vec{r}) = U(\vec{r})\psi(\vec{r}) \quad (2.80)$$

where $U(\vec{r}) = \frac{2m}{\hbar^2}V(\vec{r})$. The solution then contains

$$\psi(\vec{r}) = \psi_{GS}(\vec{r}) + \psi_{PS}(\vec{r}) \quad (2.81)$$

where $\psi_{GS}(\vec{r})$ is the general solution of the corresponding homogeneous Helmholtz equation $(\nabla^2 + k^2)\psi_{GS}(\vec{r}) = 0$ and $\psi_{PS}(\vec{r})$ is the particular solution of in-homogeneous equation. Such a solution can be found with the Green's function method. The Green function $G_o(\vec{r}, \vec{r}')$ in the solution of $(\nabla^2 + k^2)G_o(\vec{r}, \vec{r}') = \delta(\vec{r}, \vec{r}')$ is given by

$$G_o(\vec{r}, \vec{r}') = \frac{1}{4\pi|\vec{r} - \vec{r}'|} e^{ik|\vec{r} - \vec{r}'|} \quad (2.82)$$

Particular solution is hence,

$$\psi_{PS}(\vec{r}) = \int G_o(\vec{r}, \vec{r}')U(\vec{r}')\psi(\vec{r}')d^3r' \quad (2.83)$$

and finally the eqn. (2.81) is written as

$$\psi(\vec{r}) = \psi_{GS}(\vec{r}) + \frac{1}{4\pi} \frac{2m}{\hbar^2} \int \frac{d^3r'}{|\vec{r} - \vec{r}'|} e^{ik|\vec{r} - \vec{r}'|} V(\vec{r}')\psi(\vec{r}') \quad (2.84)$$

which is the integral form of the Schrödinger equation known as Lippmann-Schwinger equation. The scattering is elastic where $\vec{k}' = k(\vec{r})/r$ and $V(\vec{r}) \rightarrow 0$ at large distances.

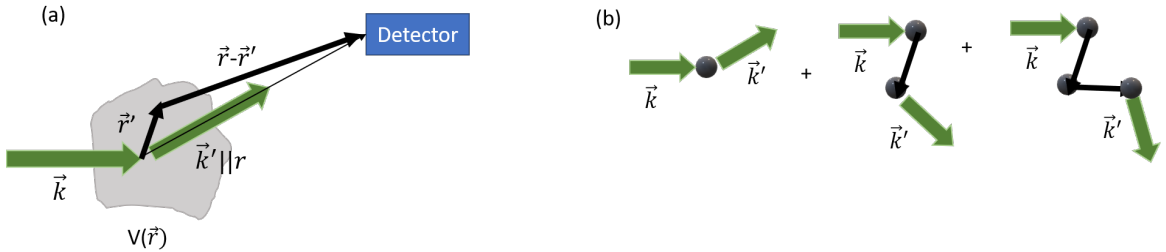


Figure 2.17.: (a) Scattering geometry for calculation of the far field limit at the detector. (b) Diagrammatic form of multiple scattering effects included in the Born approximation.

The integral in eqn. (2.84) gets significant contribution where $|\vec{r}'| \ll |\vec{r}|$ and $V(\vec{r}')$ is different from zero. Under this assumption,

$$|\vec{r} - \vec{r}'| = (r^2 + r'^2 - 2\vec{r} \cdot \vec{r}')^{1/2} = r \left(1 + \left(\frac{r'}{r} \right)^2 - 2 \frac{\vec{r} \cdot \vec{r}'}{r^2} \right)^{1/2} \sim r \left(1 - \frac{2\vec{r} \cdot \vec{r}'}{r^2} \right)^{1/2} \sim r - \frac{\vec{r} \cdot \vec{r}'}{r} \quad (2.85)$$

implies $\frac{1}{|\vec{r}-\vec{r}'|} \sim \frac{1}{r}$ and when used in eqn. (2.84) becomes

$$\psi(\vec{r}) = \psi_{GS}(\vec{r}) + \frac{m}{4\pi\hbar^2} \frac{e^{ikr}}{r} \int e^{-\frac{ik}{r}\vec{r}\cdot\vec{r}'} V(\vec{r}') \psi(\vec{r}') d^3r'. \quad (2.86)$$

As $r \rightarrow \infty$, the second term goes to zero. So the boundary condition of having an incoming plane wave at large distance can be satisfied by choosing the solution of homogeneous Helmholtz equation as $\psi_{GS}(\vec{r}) = e^{i\vec{k}\cdot\vec{r}}$. The solution of eqn.(2.86) is written in form of (2.78) where

$$f(\theta, \phi) = \frac{m}{4\pi\hbar^2} \int e^{-i\vec{k}'\cdot\vec{r}'} V(\vec{r}') \psi(\vec{r}') d^3r' \quad (2.87)$$

2.4.3.2. Born approximation

The Lippmann-Schwinger equation provides the integral form of $f(\theta, \phi)$. In the zeroth order where $V(\vec{r}) = 0$, the scattering function translates to unperturbed plane wave.

$$\psi_0(\vec{r}) = \psi_{GS}(\vec{r}) = e^{i\vec{k}\cdot\vec{r}} \quad (2.88)$$

Considering weak interaction, the total wavefunction $\psi(\vec{r})$ differs slightly from incoming wavefunction $\psi_0(\vec{r})$. So for a first order approximation, we replace $\psi(\vec{r})$ in eqn. (2.84) with $\psi_0(\vec{r})$ to obtain

$$\psi_1(\vec{r}) = \psi_0(\vec{r}) + \frac{1}{4\pi} \frac{2m}{\hbar^2} \int \frac{d^3r'}{|\vec{r}-\vec{r}'|} e^{ik|\vec{r}-\vec{r}'|} V(\vec{r}') \psi_0(\vec{r}') \quad (2.89)$$

which is the first order **Born approximation**. At large distance using eqn. (2.85) we obtain,

$$\psi(\vec{r}) = e^{i\vec{k}\cdot\vec{r}} + \frac{2m}{4\pi\hbar^2} \frac{1}{r} e^{ikr} \int e^{-i\vec{k}'\cdot\vec{r}'} V(\vec{r}') e^{i\vec{k}\cdot\vec{r}'} d^3r' \quad (2.90)$$

with scattering amplitude

$$f(\theta, \phi) = \frac{m}{4\pi\hbar^2} \int e^{i\vec{Q}\cdot\vec{r}'} V(\vec{r}') d^3r' \quad (2.91)$$

where $\hbar\vec{Q} = \hbar(\vec{k} - \vec{k}')$. The scattering amplitude $f(\theta, \phi) = A(\vec{Q})$ is the Fourier transform of the interaction potential. Then we rewrite the first order Born approximation as

$$\psi_1(\vec{r}) = \psi_0(\vec{r}) + \int G_o(\vec{r}, \vec{r}') U(\vec{r}') \psi_0(\vec{r}') d^3r' \quad (2.92)$$

using eqn. (2.83), (2.88) and (2.90). Then second order approximation is written as

$$\psi_2(\vec{r}) = \psi_0(\vec{r}) + \int G_o(\vec{r}, \vec{r}')U(\vec{r}')\psi_1(\vec{r}')d^3r' \quad (2.93)$$

Physically it means that the incoming particle will undergo a sequence of multiple scattering events from the potential as shown in the Fig. 2.17 (b) and total wave-function is represented as

$$\psi(\vec{r}) = \psi_0(\vec{r}) + \psi_1(\vec{r}) + \psi_2(\vec{r}) + \dots \quad (2.94)$$

where the first term is the unperturbed plane wave in a single scattering event followed by higher order scattering terms.

2.4.4. Types of scattering probes: scattering length

The interaction mechanisms in a scattering experiment depends on the charge, spin and energy of the incoming particles. Electrons cannot penetrate deep into the sample

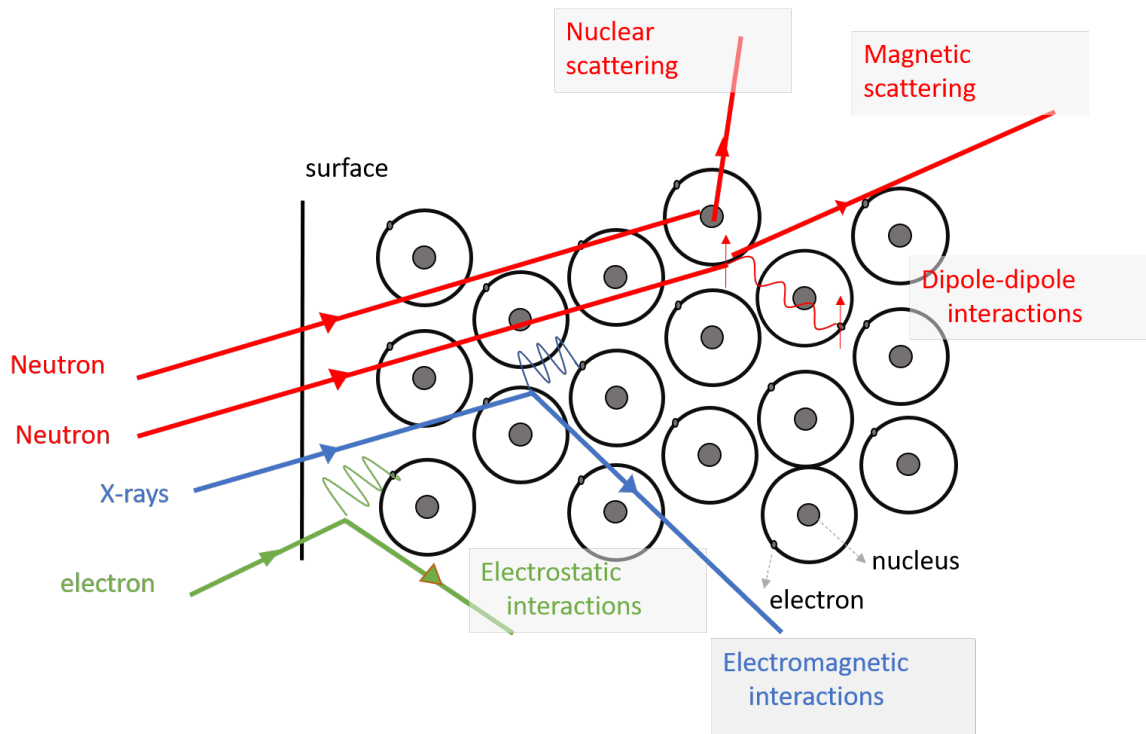


Figure 2.18.: Various interactions mechanisms between atoms and incident radiation; adapted from [62].

due to repulsion from orbital electrons. Therefore electrons are useful surface probes.

X-ray photons have no charge, but as an electromagnetic wave, has oscillating electric and magnetic field which interacts with orbital electrons. X-rays penetrate deeper than electrons. Neutrons are neutral particles and interacts via strong nuclear force that allow penetration deeper into the sample than x-rays and electrons. If atoms are magnetic, the magnetic moment due to unpaired electrons can scatter neutrons through spin dipole-dipole interactions. The interactions due to different scattering probes are schematically represented in Fig. 2.18. From the first Born approximation, the scattering amplitude from eqn (2.91) is

$$A(\vec{Q}) = \frac{m}{4\pi\hbar^2} \int e^{i\vec{Q}\cdot\vec{r}'} V(\vec{r}') d^3r' = \mathcal{F}[V(\vec{r})] \quad (2.95)$$

which is the Fourier transform of the potential $V(\vec{r})$. This amplitude is different for neutrons and x-rays due to differences in their inherent properties.

2.4.4.1. Nuclear scattering length

In case of neutron scattering, the scattering amplitude $A(\vec{Q})$ is equal to $-b$, where the constant b is called the scattering length and has units of length. The scattering length is invariant with wavelength and scattering angle θ . Neutron scattering lengths can be negative or positive, depending on the phase shifts the neutron experiences upon scattering from the nucleus. The scattering length b depends on details of the nuclear structure and can vary strongly from one isotope to the other. It also depends on the combined spin of the nucleus and the neutron, which can take the values $b_+ = I + \frac{1}{2}$ or $b_- = I - \frac{1}{2}$.

2.4.4.2. X-ray scattering length

The characteristic scattering amplitude for x-ray scattering by an atom is different from neutron because of relevant long range electromagnetic interactions with orbital electron. We assume a situation where λ does not correspond to resonant energies for absorption. The scattering length b is real number which diminishes monotonically with increasing θ and decreasing atomic number Z . Strength of scattering depends on number of orbital electrons. In contrast to invariant nuclear scattering length, in x-rays there is a fall off with scattering vector Q and is known as the atomic form factor. Here, $b = Zg(Q)r_e$ where Z is the atomic number, $g(Q)$ is the decay function which varies from 1 to zero as $Q \rightarrow \infty$ and r_e is Thomson scattering length ($r_e = 2.8 \times 10^{-15}m$).

2.4.4.3. Magnetic scattering

Neutrons like electrons possess magnetic dipole moment $\mu_n = -1.193\mu_N$, where $\mu_N (= 5.051 \times 10^{-27} \text{ J/T})$. In addition to nuclear scattering, the neutron is deflected through magnetic interaction between dipole moment and constituents of sample. The main source of magnetism in sample are the unpaired electrons. The magnetic scattering of neutrons is ion specific and has a form factor just like x-rays. However, it does not decrease monotonically with atomic number. The anisotropy in interaction is due to dipole-dipole interactions of neutron spin with magnetic moment (Fig.2.19). Only the component of magnetization M perpendicular to \vec{Q} can be observed in a scattering experiment.

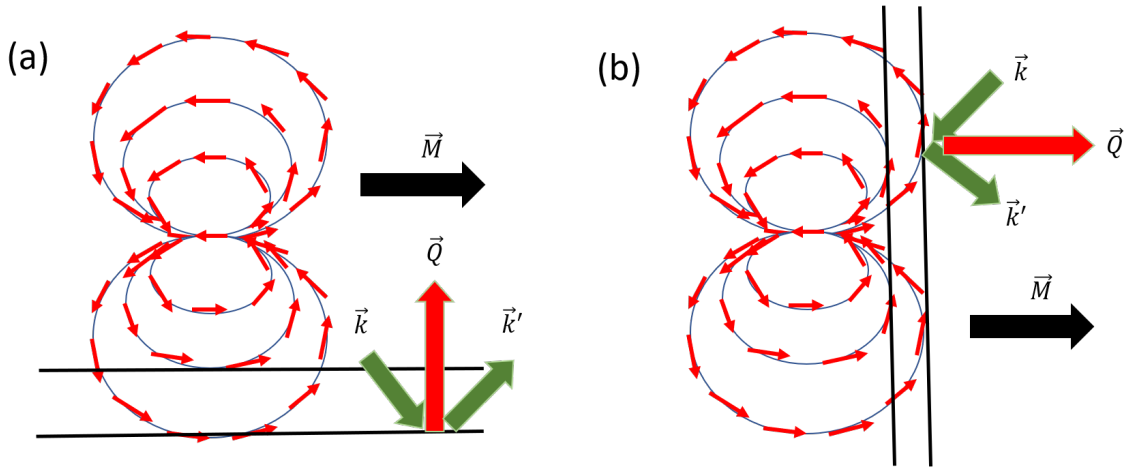


Figure 2.19.: Schematic illustration of dipolar field and the scattering vector \vec{Q} . (a) For $\vec{M} \perp \vec{Q}$, magnetic dipole interaction show constructive interference and (b) $\vec{M} \parallel \vec{Q}$ results in destructive interference; adapted from

2.4.5. Coherent and incoherent nuclear scattering

In a assembly of N nuclei, where i^{th} nucleus at position R_i with scattering length b_i , the incident wave is $\psi_i = e^{i\vec{k}\cdot\vec{R}_i}$. The scattering potential can be written as $V(\vec{r}) = \frac{2\pi\hbar^2}{m_n} \sum_i b_i \delta(\vec{r} - \vec{R}_i)$. The scattering amplitude is

$$A(\vec{Q}) = \sum_i b_i e^{i\vec{Q}\cdot\vec{R}_i} \quad (2.96)$$

which is the Fourier transform of the potential. Different isotopes with random nuclear spin orientations are distributed randomly over all sites of sample. Hence the

differential cross-section is calculated as

$$\frac{d\sigma}{d\Omega} = |A(\vec{Q})|^2 = \left\langle \sum_i b_i e^{i\vec{Q}\cdot\vec{R}_i} \cdot \sum_j b_j^* e^{-i\vec{Q}\cdot\vec{R}_j} \right\rangle. \quad (2.97)$$

which is the average taken over the random distribution of scattering lengths. The expectation value of the product of scattering lengths on different sites have two case

$$\langle b_i b_j \rangle = \begin{cases} \langle b \rangle \langle b \rangle = \langle b \rangle^2, & i \neq j \\ \langle b^2 \rangle = \langle b \rangle^2 + \langle (b - \langle b \rangle)^2 \rangle, & i = j \end{cases}$$

In the case 1, for different site the scattering length are uncorrelated. For a case $i = j$, there is an additional term arising from correlation associated with the mean quadratic deviation from the average. There eqn. (2.97) becomes

$$\frac{d\sigma}{d\Omega} = \langle b \rangle^2 \left| \sum_i e^{i\vec{Q}\cdot\vec{R}_i} \right|^2 + N \langle (b - \langle b \rangle)^2 \rangle \quad (2.98)$$

where the first term is the coherent scattering which contains the phase factors and result from coherent superposition of the scattering from scatterers. The second term is the incoherent scattering differential cross section which is proportional to N , the number of atoms. The term corresponds to scattering from single atoms which superimpose incoherently.

2.5. Small-angle scattering (SAS)

In the elastic scattering regime, small-angle scattering (SAS) experiments are conducted at small scattering angles ($\theta \leq 10^\circ$). This will enable study of structure and interaction in systems of the order of 10-1000 Å.

2.5.1. SAS fundamentals

The simplest SAS setup consists of a source of x-rays or neutrons, a set of optical elements that defines the beam energy, the beam geometry, collimation and 2D position detector as shown in the Fig. 2.20. The sample is placed in the incident beam and scattering profile is recorded on the 2D detector. The measured intensity for a sample of volume V is

$$I = \frac{1}{V} \frac{d\sigma}{d\Omega} = \frac{d\Sigma}{d\Omega} \quad (2.99)$$

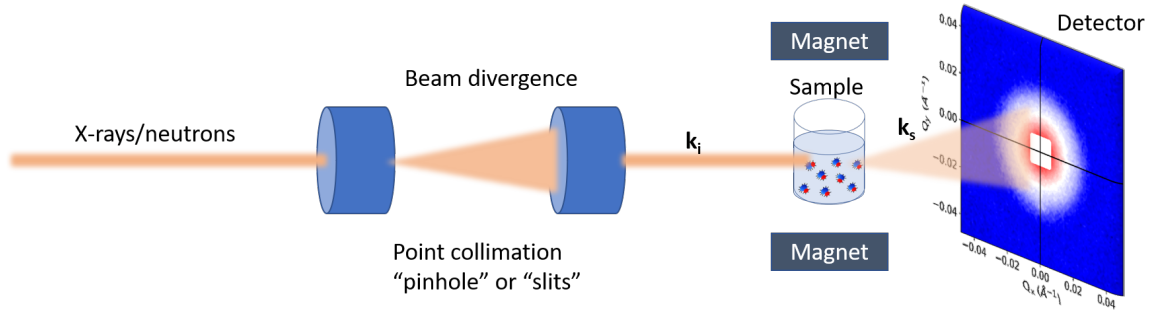


Figure 2.20.: Transmission geometry set-up for small-angle scattering (SAS).

where $\frac{d\Sigma}{d\Omega}$ is the macroscopic cross-section and has units of cm^{-1} . The scattered intensity is directly related to the structure of the sample. The local interaction as discussed previously depends on kind of beam and is characterized by the scattering length b_i . The density of scattering lengths can be written as $\rho(\vec{r}) = \sum \rho_i(\vec{r})b_i$ where $\rho_i(\vec{r})$ is the local density of scatters. SAS experiments probe structure of particles on length scales of tens to hundreds of atoms and we cannot distinguish exact position of atom within the sample. The **scattering length density (SLD)** is defined as

$$\rho(\vec{r}) = \frac{\sum_i b_i}{V}, \quad (2.100)$$

which is the sum of all scattering length b_i within a volume element V . Then we can write eqn. (2.96) in general form as

$$A(\vec{Q}) = \int_V \rho(\vec{r}) e^{i\vec{Q}\cdot\vec{r}} d^3r \quad (2.101)$$

for a sample volume V . In a real experiment, the Fourier transform of potential is not directly accessible. The measured intensity corresponds to the squared amplitude in which case the phase information is lost. The macroscopic cross-section is given by;

$$\frac{d\Sigma}{d\Omega} = \frac{1}{V} \left| \int_V \rho(\vec{r}) e^{i\vec{Q}\cdot\vec{r}} d^3r \right|^2 \quad (2.102)$$

2.5.2. Form and structure factors

Consider a particle of in-homogeneous density $\rho(\vec{r})$. For a given orientation, the scattering amplitude of a particle is [63]

$$a(\vec{Q}) = \int_{V_p} \rho(\vec{r}) e^{i\vec{Q}\cdot\vec{r}} d^3r = F(\vec{Q}) \quad (2.103)$$

and yields intensity,

$$I_p(\vec{Q}) = a(\vec{Q})a^*(\vec{Q}) = |F(\vec{Q})|^2 = V_p^2 P(\vec{Q}). \quad (2.104)$$

Here, the $P(\vec{Q})$ is called the particle **form-factor** given by

$$P(\vec{Q}) = \frac{1}{V_p^2} \iint_{V_p} \rho(\vec{u})\rho(\vec{v}) e^{i\vec{Q}\cdot(\vec{u}-\vec{v})} d^3u d^3v. \quad (2.105)$$

This accounts for the spatial extent of the scatterer. Another way to represent the form-factor is through the correlation function $\Gamma(\vec{r})$ which is the convolution of the real space SLD with itself where $\Gamma(\vec{r}) = \frac{1}{V_p} \int_{V_p} \rho(\vec{r}')\rho(\vec{r}'+\vec{r})d^3r' = \frac{1}{V_p} P_{Pat}(\vec{r})$ where, $P_{Pat}(\vec{r})$ is Patterson function of particle. Therefore, it follows

$$P(\vec{Q}) = \frac{1}{V_p} \int_{V_p} \Gamma(\vec{r}) e^{i\vec{Q}\cdot\vec{r}} d^3r. \quad (2.106)$$

The integral is taken over relative separations between two points in the particles. Averaging over all orientations, the $\Gamma(\vec{r}) = \langle \Gamma(\vec{r}) \rangle_\Omega$. Similarly, $P(Q) = \langle P(\vec{Q}) \rangle_\Omega$ and can be written as

$$P(Q) = \frac{1}{V_p} \int_{V_p} \left(\frac{1}{4\pi} \int_\Omega \Gamma(\vec{r}) d\Omega \right) e^{i\vec{Q}\cdot\vec{r}} d^3r \quad (2.107)$$

consequently, the Fourier transform reduces to one dimensional scalar integral given by

$$P(Q) = \frac{1}{V_p} \int_0^D 4\pi r^2 \Gamma(r) \frac{\sin(Qr)}{Qr} dr \quad (2.108)$$

where D is the maximum point-point distance in the particle. The intensity per unit volume of a suspension containing N identical particles is

$$I(\vec{Q}) = \frac{N}{V} V_p^2 P(\vec{Q}) \quad (2.109)$$

where V is volume of total system. Study of form-factors are important in colloidal systems where objects can be anisotropic or composite and in general, are studied in dilute suspensions. For disoriented anisotropic objects, the form-factor can be first calculated in one of the two ways: (i) calculate the modulus of Fourier transform of the SLD function using eqn.(2.105) or (ii) perform Fourier transform on the correlation function using eqn.(2.106) and then average it over the different available orientations. When N particles scatter independently, eqn. (2.109) can be applied. In the case of identical correlated particles, for a given set positions, the total intensity is $I(\vec{Q}) = \frac{A(\vec{Q})A^*(\vec{Q})}{V}$. When particles are undergoing Brownian diffusion, the intensity is changing for each configuration and is measured as average in time ;

$$I(\vec{Q}) = \left\langle \frac{A(\vec{Q})A^*(\vec{Q})}{V} \right\rangle = \frac{1}{V} \left\langle \left[\int \rho(\vec{r}) e^{i\vec{Q} \cdot \vec{r}} d^3r \right] \left[\int \rho(\vec{r}') e^{-i\vec{Q} \cdot \vec{r}'} d^3r' \right] \right\rangle \quad (2.110)$$

where $\langle \rangle$ is average over all available positions and orientations of the particles. If the centre position of particle is \vec{r}_i , then $\vec{r} = \vec{r}_i + \vec{u}$ and intensity develops into

$$I(\vec{Q}) = \frac{1}{V} \left\langle \left[\sum_{i=1}^N e^{i\vec{Q} \cdot \vec{r}_i} \int \rho(\vec{u}) e^{i\vec{Q} \cdot \vec{u}} d^3u \right] \left[\sum_{j=1}^N e^{-i\vec{Q} \cdot \vec{r}_j} \int \rho(\vec{v}) e^{-i\vec{Q} \cdot \vec{v}} d^3v \right] \right\rangle. \quad (2.111)$$

The intensity is the average of the product:

$$I(\vec{Q}) = \frac{N}{V} \left\langle \left[\iint \rho(\vec{u}) \rho(\vec{v}) e^{i\vec{Q} \cdot (\vec{u} - \vec{v})} d^3u d^3v \right] \left[\frac{1}{N} \sum_{i=1}^N \sum_{j=1}^N e^{i\vec{Q} \cdot (\vec{r}_i - \vec{r}_j)} \right] \right\rangle. \quad (2.112)$$

In the special case of spherical particles with identical interaction, the average of the product is the product of average. The first part of the term in eqn. (2.112) is the form factor $V_p^2 P(\vec{Q})$ as defined previously. The second term is

$$S(\vec{Q}) = 1 + \frac{1}{N} \left\langle \sum_{i=1}^N \sum_{j \neq i}^N e^{i\vec{Q} \cdot (\vec{r}_i - \vec{r}_j)} \right\rangle \quad (2.113)$$

where $S(\vec{Q})$ is the **structure factor**. Then the intensity can be written in the common expression given by

$$I(\vec{Q}) = \frac{N}{V} V_p P(\vec{Q}) S(\vec{Q}) \quad (2.114)$$

where this factorization into particle form-factor and structure factor is useful because they can be calculated separately in experiments. The form-factor is obtained

from the particle morphology. On the other hand structure factor is associated with interactions between particles which involves theoretical calculations using statistical models. For an isotropic distribution of scattering elements averaged over all orientations the vector can be dropped, the macroscopic cross-section $\frac{d\Sigma}{d\Omega}(Q) = I(Q)$ is now simply written as a function of Q , and plotted in fig. 2.21 (a). Here, the intensity is plotted considering no interactions and due to only orientationally averaged form-factor $P(Q)$. In Fig. 2.21 (b), the $I(Q)$ (red curve), is proportional to product of $P(Q)$ (red curve) and isotropic azimuthally average structure factor $S(Q)$ (blue curve). An alternative strategy to obtain the structure factor is to first obtain the form-factor for dilute system independently and then to divide this form-factor from the experimental intensity to obtain the structure factor.

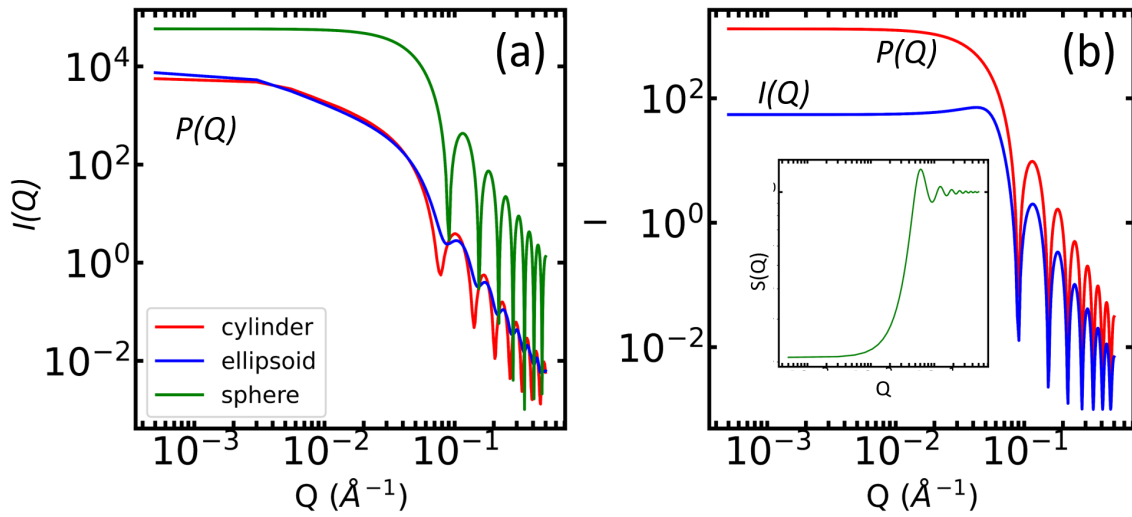


Figure 2.21.: (a) The intensity associated with particle form-factor $P(Q)$ for various shapes averaged over all orientations. (b) The scattering intensity (in blue) includes product of particle form-factor of sphere (red) and structure factor associated with hard sphere potential (green).

2.5.3. Behaviour at low Q : Guinier regime

In a dilute system or in dispersions where structure factor can be neglected, the scattering in the limit $|\vec{Q}| \rightarrow 0$ can be analyzed using eqn. (2.108);

$$P(Q) = \frac{1}{V_p} \int_0^D 4\pi \Gamma_P(r) \frac{r}{Q} \left[Qr - \frac{(Qr)^3}{6} + \dots \right] \quad (2.115)$$

This equation can be related to radius of gyration R_g where $R_g^2 = \frac{1}{2} \frac{\int_{V_p} r^2 \Gamma_P r dr}{\int_{V_p} \Gamma_P dr}$, then

$$P(Q) = \frac{1}{V_p} \int_0^D 4\pi r^2 \Gamma_P(r) \left[1 - \frac{(QR_g)^2}{3} + \dots \right] \quad (2.116)$$

Guinier approximation is valid in regime where $QR_g < 1$. The radius of gyration is effectively the size of the scattering "particle". Since it is shape independent, the particle could be chains, micelles, nanoparticles, proteins. This Guinier region can be affected by instrumental smearing or inter-particle interactions. Scattering particle is smaller than the probed Guinier region (see Fig. 2.22 (a) and (b)).

2.5.4. Behaviour at high Q: Porod regime

The analytical description of form-factor of other shapes is not always easy and cannot be usually stated in closed form. When $Q \ll R^{-1}$, based on scattered intensity of the spheres decays as Q^{-4} , while for thin disc and long rods as Q^{-2} and Q^{-1} , respectively. The Q^{-4} is behaviour for most objects due to orientation. Porod's law estimates the inhomogeneities through slope measurement at high Q. In general the equation can be approximated to

$$P(\vec{Q}) = \frac{A}{Q^P} + B \quad (2.117)$$

where P is the Porod constant and value of this constant describes the surface and dimension of the scattering object (Fig. 2.22 (c)). For instance $P = 4$ represents a smooth surface), 3 a rough surface, $5/3$ a swollen ring or $P = 2$ in a chains or 2D structures.

2.5.5. Guinier-Porod model

Considering the asymptotic regimes in scattering (low Q and high Q regimes), model independent functions can be defined. A Guinier-Porod formalism was developed to fit for non spherical objects as described in detail in prior reports [65]. In order to generalize the Guinier - Porod model to account for non-spherical scattering objects, the following functional form is used:

$$I(Q) = \begin{cases} \frac{G}{Q^s} e^{\left(\frac{-Q^2 R_g^2}{3-s}\right)}, & \text{for } Q \leq Q_1 \\ \frac{D}{Q^d}, & \text{for } Q \geq Q_1 \end{cases}$$

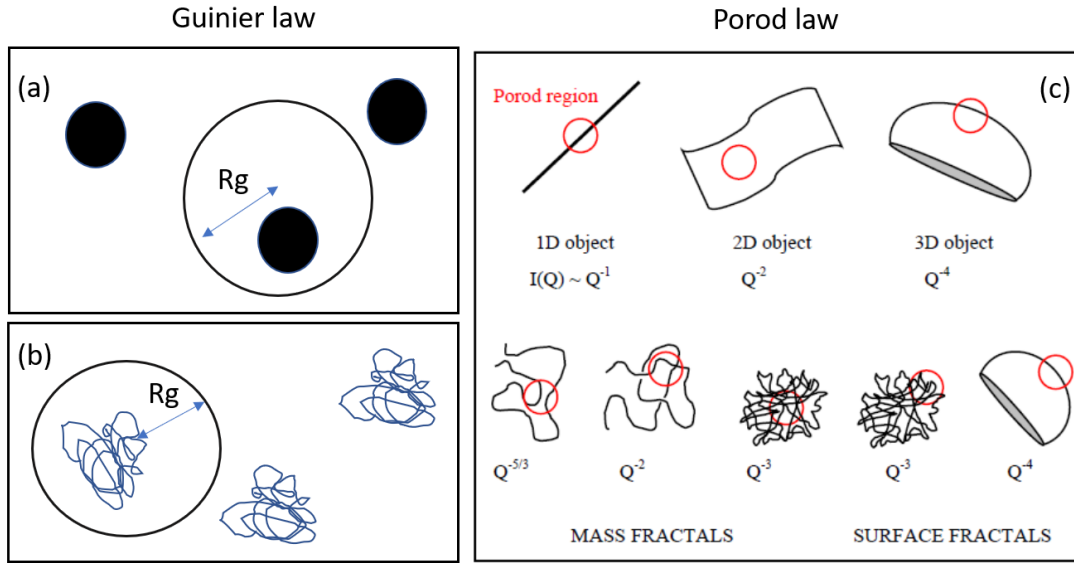


Figure 2.22.: (a) and (b) represents the R_g for particles of different types of particle (adapted from [64]) (c) Porod constants for different objects; taken from [64])

where G and D are Guinier and Porod scale factors, respectively. Here, the requirement for the Guinier, Porod terms and their slopes must be continuous at value Q_1 . The s parameter can be used to define non-spherical objects. For 3d globular object, $s = 0$, $s = 1$ for rods and $s = 2$ for lamellae.

2.5.6. Contrast variation using neutrons

The neutron coherent scattering length for hydrogen ^1H is -0.38×10^{-14} m and for its isotope deuterium ^2H is 0.66×10^{-14} m. This variation in b can be exploited in the so called contrast variation experiment. The basic principle is the substitution of nuclei with its isotope, which does not introduce any significant change in properties of material but strong variation in scattering length. Here, we mainly discuss neutron scattering experiments. Consider N identical objects located at position vectors \vec{r}_j oriented at $\vec{\Theta}_j$ where $j = 1, 2, \dots, N$ as shown in Fig. 2.23 (a). These identical particles are randomly distributed in a matrix of SLD η_o which can be a solvent or medium where objects are embedded. Then the scattering length density $\rho(\vec{r})$

$$\rho(\vec{r}) = \eta_o + \sum_{j=1}^N \hat{\eta}_p(\vec{r} - \vec{r}_j, \vec{\Theta}_j) \quad (2.118)$$

where η_o is the SLD of the solvent and here

$$\hat{\eta}_p(\vec{r}, \vec{\Theta}_j) = \begin{cases} \eta_p(\vec{r}, \vec{\Theta}_j) - \eta_o, & \vec{r} \text{ inside the particle} \\ 0, & \vec{r} \text{ inside the solvent} \end{cases}$$

Fourier transform of the invariant function is δ -function and shifted function are related through phase factors. Applying this and the SLD in eqn. (2.102) we get,

$$\frac{d\Sigma}{d\Omega} \propto \left| (2\pi)^3 \delta(\vec{Q}) + \sum_{j=1}^N e^{i\vec{Q} \cdot \vec{r}_j} \int_{V_{\vec{\Theta}_j}} \hat{\eta}_p(\vec{r}, \vec{\Theta}_j) e^{i\vec{Q} \cdot \vec{r}} d^3r \right|^2 \quad (2.119)$$

where $V_{\vec{\Theta}_j}$ is the volume of the particle that is centred at the origin with orientation $\vec{\Theta}_j$. We also know from eqn. (2.98), the presence of coherent and incoherent neutron scattering. The summation in eqn. (2.119) is expanded and the coherent terms for uncorrelated positions \vec{r}_i and \vec{r}_j , is

$$\frac{d\Sigma}{d\Omega} \propto \sum_{j=1}^N \left| \int_{V_{\vec{\Theta}_j}} \hat{\eta}_p(\vec{r}, \vec{\Theta}_j) e^{i\vec{Q} \cdot \vec{r}} d^3r \right|^2, \quad (2.120)$$

where the sharp signal at $\vec{Q} = 0$ has been neglected. This is the intense unscattered beam which would damage the sensitive detector and this is the reason for placing a beamstop at the centre of the detector for SAS measurements. Consider spherical symmetric particles with constant SLD η_{core} , with radius R then,

$$\hat{\eta}_p(\vec{r}, \vec{\Theta}_j) = \begin{cases} \eta_{core}, & |\vec{r}| < R \\ 0, & \text{otherwise} \end{cases}$$

and in a sphere the orientational average is redundant, thus $\hat{\eta}_p(\vec{r}, \vec{\Theta}_j) = \hat{\eta}_p(r)$. Similar to eqn. (2.108), the Fourier transformation corresponds to 1d integral which is $\frac{d\Sigma}{d\Omega} \propto N(4\pi)^2 \left| \int_0^R r^2 \hat{\eta}_p(r) \frac{\sin(Qr)}{(Qr)} dr \right|^2$. Then,

$$\frac{d\Sigma}{d\Omega} \propto N \left(\frac{4\pi(\eta_{core} - \eta_o)}{Q} \right)^2 \left| \int_0^R r \sin(Qr) dr \right|^2 \quad (2.121)$$

where the integral $\int_0^R r \sin(Qr) dr = \frac{\sin(QR) - (QR)\cos(QR)}{Q^2} = R^2 j_1(QR)$ is related to spherical Bessel function j_1 . Consider a multi-component spherical system with

$$\hat{\eta}_p(\vec{r}, \vec{\Theta}_j) = \begin{cases} \eta_{core}, & \text{for } |\vec{r}| < R_1 \\ \eta_{shell}, & \text{for } R_1 \leq |\vec{r}| < R_2 \end{cases}$$

Using eqn. (2.121), for a core-shell the macroscopic cross-section is

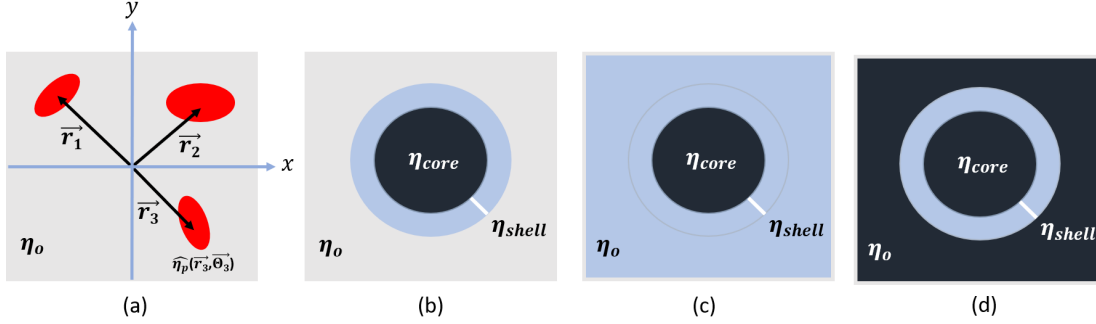


Figure 2.23.: (a) Schematic illustration of eqn. (2.118) where grey is the matrix in which anisotropic particles are embedded. (b) The concept of contrast variation in core-shell particles in natural contrast, (c) shell contrast; $\eta_o = \eta_{shell}$ and (d) core contrast; where $\eta_o = \eta_{core}$; adapted from ref [57]

$$\frac{d\Sigma}{d\Omega} \propto N \left(\frac{4\pi}{Q} \right)^2 [(\eta_{core} - \eta_o) R_1^2 j_1(QR) + (\eta_{shell} - \eta_o) [R_1^2 j_1(QR_2) - R_1^2 j_1(QR_1)]] \quad (2.122)$$

and in a natural contrast is schematically shown in Fig. 2.23 (b). The analysis will be simpler when separate measurements are made such that solvent in which particles are suspended are adjusted for scattering length by adjusting percentages of hydrogen and deuterium such that $\eta_{shell} = \eta_o$ (Fig. 2.23 (c)) and $\eta_{core} = \eta_o$ (Fig. 2.23 (d)).

2.5.7. Polarized neutrons: SANSPOL

Neutron has an inherent spin defined just like for an electron, with spin $S = 1/2$ and angular momentum. Magnetic moment of neutron is $|\vec{\mu}_n| = g_n S \mu_N \approx \mp 1.913 \mu_N$, where nuclear magneton $\mu_N = 5.05 \times 10^{-27}$ J/T. Polarization of neutron beam is the normalized average over particle ensemble of neutron spins $\vec{P} = 2\langle \vec{S} \rangle$. In a magnetic

field \vec{H} , neutrons split in spin up and spin down states. The beam polarization is

$$-1 < P = \frac{n_{\uparrow} - n_{\downarrow}}{n_{\uparrow} + n_{\downarrow}} < 1 \quad (2.123)$$

where n_{\uparrow} and n_{\downarrow} are neutron up and down states respectively. Consider the scattering nuclei where $I \neq 0$ and the interaction is spin dependent. The two possible spin states from coupling the neutron spin and spin of the nucleus are $J_+ = I + \frac{1}{2}$ and $J_- = I - \frac{1}{2}$. These states are associated with scattering lengths b_+ and b_- . Now the three contributions to nuclear scattering $|N_{\vec{Q}}^2|$ include

1. **coherent scattering** as discussed in section 2.4.5, due to the interaction of neutron with nuclei of the sample through strong forces,
2. **isotope-incoherent scattering** resulting from variation in scattering lengths due to isotopes (section 2.4.5),
3. **spin-incoherent scattering** due to interaction of neutron spin with the random distribution of spins,

where the $N_{\vec{Q}} = \sum_i^N e^{i\vec{Q}\cdot\vec{r}_i}$. Non spin-flip scattering (NSF) is when polarization state remains unaffected and the spin-flip scattering (SF) is when the polarization of neutron beam is reversed due to interaction. The sum of the coherent and isotopic incoherent nuclear scattering result in NSF scattering and this can be separated from spin-incoherent scattering which results in SF scattering. About two thirds of spin incoherent scattering is SF. In polarization analysis there are four relevant scattering cross-section corresponding to two NSF and two SF scattering cross-sections denoted by $\frac{d\Sigma^{++}}{d\Omega}$, $\frac{d\Sigma^{--}}{d\Omega}$, $\frac{d\Sigma^{+-}}{d\Omega}$ and $\frac{d\Sigma^{-+}}{d\Omega}$. As seen in section 2.4.1, magnetic scattering is a result of anisotropic dipolar interaction with spin of neutron and dipolar field in sample. Here, only magnetic component $\vec{M}_{\vec{Q}}^{\perp}$ perpendicular to scattering vector \vec{Q} is detected. The magnetic scattering will be SF scattering when the polarization of the beam is parallel to the scattering vector ($\vec{P} \parallel \vec{Q}$). SANS experiments performed with incident polarized beam and no analysis of polarization at detector are called SANSPOL experiments. The unpolarized SANS and SANSPOL setup is illustrated in the Fig. 2.24. The difference is the presence of polarizer and flipper in the SANSPOL setup. The beam is polarized using (i) total reflection of one orientation of neutron from magnetic multilayers (Fe/Si supermirrors), (ii) Bragg reflection from monochromator results in constructive interference for one spin state and (iii) using polarized He-3 filters where parallel spins pass the filter while the anti-parallel spins are absorbed

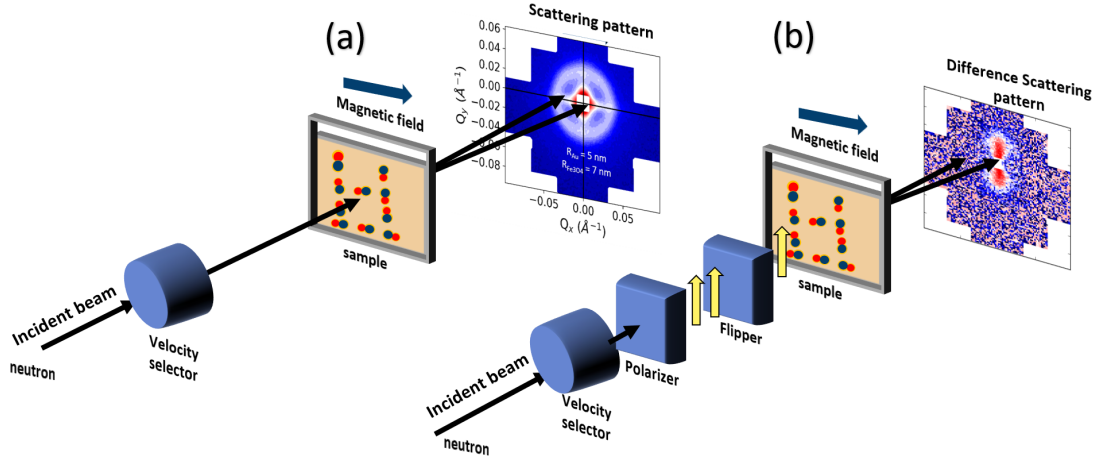


Figure 2.24.: (a) Schematic of the SANS experimental setup including velocity selector for selection of wavelength and (b) SANSPOLEX setup includes velocity selectors along with a polarizer to polarize the neutron beam and flipper to reverse the polarization on the neutron beam.

[58]. SANSPOLEX provides half polarized scattering cross-sections $\frac{d\Sigma^+}{d\Omega}$ and $\frac{d\Sigma^-}{d\Omega}$ which combine NSF and SF :

$$\text{'spin-up': } \frac{d\Sigma^+}{d\Omega} = \frac{d\Sigma^{++}}{d\Omega} + \frac{d\Sigma^{+-}}{d\Omega} \quad (2.124)$$

$$\text{'spin-down': } \frac{d\Sigma^-}{d\Omega} = \frac{d\Sigma^{--}}{d\Omega} + \frac{d\Sigma^{-+}}{d\Omega} \quad (2.125)$$

In case unpolarized SANS, the cross section is then

$$\frac{1}{2} \left(\frac{d\Sigma^+}{d\Omega} + \frac{d\Sigma^-}{d\Omega} \right) = \frac{d\Sigma}{d\Omega} \Big|_{\text{unpolarized}} \quad (2.126)$$

The nuclear SLD is defined using eqn. (2.100), as $\eta_N = \sum_i c_i b_i / V_i$, where b is the nuclear scattering length, c is concentration of the particle and V is the volume. The magnetic SLD is defined due to interaction between the neutron spin with assembly of magnetic moment gives rise to magnetic SLD defined by

$$\eta_M = 0.27 \times 10^{-12} (\text{cm}) \frac{\sum_i c_i \vec{M}_i^\perp}{V_i} \quad (2.127)$$

where only projection of magnetic moment \vec{M}_i^\perp onto a plane perpendicular to scattering vector \vec{Q} . In a classical SANS experiment, the beam is unpolarized and spins are

randomly distributed. Consider, the simplest case of spheres in dilution limit, where the scattering cross-section is reduced to one-dimensional integral as in eqn. (2.121) and when linked to eqn.(2.121) can be written as

$$\frac{d\Sigma}{d\Omega} \propto |F_N|^2, \quad F_N(Q) = \Delta\eta V_p f(QR) \quad (2.128)$$

The scattering intensity is sum of squared amplitudes from individual magnetic and nuclear contrasts [66, 67]. The nuclear SLD $\Delta\eta$ is the contrast difference between SLD of particle and matrix. Similarly $\Delta\eta_m$ and form-factor $F_M^\perp(\vec{Q})$ are vectors which depend on the orientation of the moment with respect to \vec{Q} . For a magnetic sample in an applied magnetic field \vec{H} , the unpolarized scattering cross-section in general form is given by,

$$\frac{d\Sigma}{d\Omega} = A(Q) + B(Q)\sin^2\alpha \quad (2.129)$$

where $A(Q)$ and $B(Q)$ are related to isotropic and anisotropic terms, respectively and α is the angle between \vec{H} and \vec{Q} . In a saturated state, all the magnetic moments are aligned along \vec{H} , then $A(Q) = F_N^2$ is purely nuclear and $B(Q) = F_M^2$ is the squared difference of saturation between particle and matrix. Here the intensity measured perpendicular to the magnetic field, $I(\vec{Q} \perp \vec{H})$ gives the sum of nuclear and magnetic contribution $A(Q) + B(Q)$. In $I(\vec{Q} \parallel \vec{H})$, yields nuclear contribution $A(Q)$. The eqn.(2.128) is validated by analyzing the 2D scattering intensity $I(\alpha)$ along different azimuthal angles. Usually in unpolarized SANS, this is difficult to detect due to weak magnetic contrast compared to nuclear one. In SANS POL, the scattering cross-sections are obtained [66]

$$I^+(Q) = F_N^2 + [F_M^2 + 2Pf^\pm F_N F_M] \sin^2\alpha \quad (2.130)$$

$$I^-(Q) = F_N^2 + [F_M^2 - 2PF_N F_M] \sin^2\alpha \quad (2.131)$$

where P is degree of polarization, f^\pm is efficiency of spin-flipper.

$$\frac{(I^+(Q) + I^-(Q))}{2} = A(Q) + B^\pm(Q)\sin^2\alpha \quad (2.132)$$

where,

$$B^\pm(Q) = F_M^2 - 2P(1 - 2f^\pm)F_M F_N. \quad (2.133)$$

The difference in the intensities,

$$I^-(Q) - I^+(Q) = B_{int} \sin^2 \alpha \quad (2.134)$$

and here $B_{int} = 4P f^\pm F_N F_M$. In SANSPOLE, the evaluation of scattering cross section in the "spin up" and "spin down" states and their difference will reveal the nuclear and magnetic form-factors along with nuclear-magnetic cross term. These equations are valid only in dilute solution of MNPs where structure factor may be neglected.

2.5.8. Experimental aspects: data treatment

In a SAS experiment, isotropic scattering intensity, $I(x, y)$, is recorded on position sensitive 2D detector intensity where x, y are detector coordinates (Fig. 2.25 (a)). Standard treatment of isotropic data where intensity is not dependent on azimuthal direction in detector involves several corrections and steps. First, the beam centre coordinates are determined using standard calibrant. For the given the experimental conditions, the average value of $|\vec{Q}|$ is [63]

$$Q = \frac{4\pi}{\lambda} \sin \left(\frac{1}{2} \tan^{-1} \left(\frac{|\vec{r}|}{L} \right) \right) \quad (2.135)$$

where λ is wavelength, L is the sample-to-detector distance and \vec{r} is position on the detector given by coordinate (x, y) . The intensity $I(Q)$ obtained through radial integration is now 1D intensity plotted as a function of Q (Fig. 2.25 (b)). The intensity is corrected for sample thickness, absorption and backgrounds from sample container and solvents. The data is normalized to incident flux, geometrical factors, detectors cell efficiency and put on absolute scale (cm^{-1}) using the scattering cross-sections with standard reference samples. In scattering experiment, the measured intensity from sample and container is I_{S+EC}^m and empty container is I_{EC}^m . Background in scattering can be due to room background and electronic noise. In SANS this background given by dark current I_{DC} is measured by replacing sample with cadmium, which is very good neutron absorbent. The transmission of the sample is $T_S = \frac{T_{S+EC}}{T_{EC}}$. The total scattering of sample inside the container is

$$I_{S+EC}^m = T_S T_{EC} I_S + T_S T_{EC} I_{EC} + I_{DC} \quad (2.136)$$

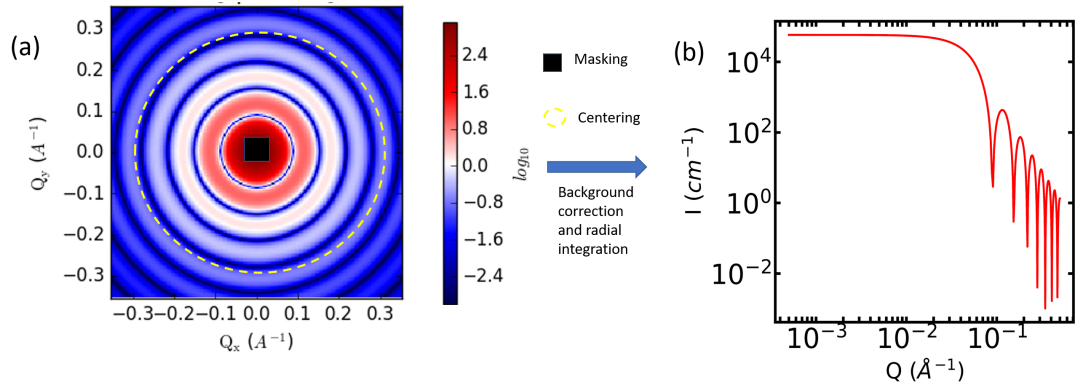


Figure 2.25.: (a) 2D scattering pattern obtained for particles in a matrix are corrected and integrated radially (in general) to obtain (b) $I(Q)$.

and for the empty container

$$I_{S+EC}^m = T_{EC} I_{EC} + I_{DC} \quad (2.137)$$

We can write $I_{EC} = \frac{1}{T_{EC}}(I_{EC}^m - I_{DC})$ and inserting this in eqn.(2.136) results in scattering intensity from particles on solvent [63]

$$I_S = \frac{I_{S+EC}^m - I_{DC}}{T_{S+EC}} - \frac{I_{EC}^m - I_{DC}}{T_{EC}} \quad (2.138)$$

Background solvent scattering following similar protocol is subtracted to obtain net scattering of particles. The scattering intensities $I(Q)$ is subjected to smearing because of uncertainty in \vec{Q} which is called the **instrumental resolution**. The uncertainties arise from the (i) instruments having finite wavelength distribution $\frac{\Delta\lambda}{\lambda}$ of incident beam, (ii) finite divergence of incident beam and depends on collimation distance, (iii) aperture defining the beam and (iv) spatial resolution of detector. All particles identical in size and shape are known as monodisperse particles. If there is a variation or polydispersity, but no correlation in location and orientation. The polydispersity affects the resultant differential cross-section as seen in the measured intensity $I(Q)$ plot in Fig. 2.26.

2.6. Wide angle scattering

Elastic coherent scattering on highly crystalline or ordered phases of matter gives rise to diffraction peaks. In contrast to SAS, diffraction is done at much higher scattering

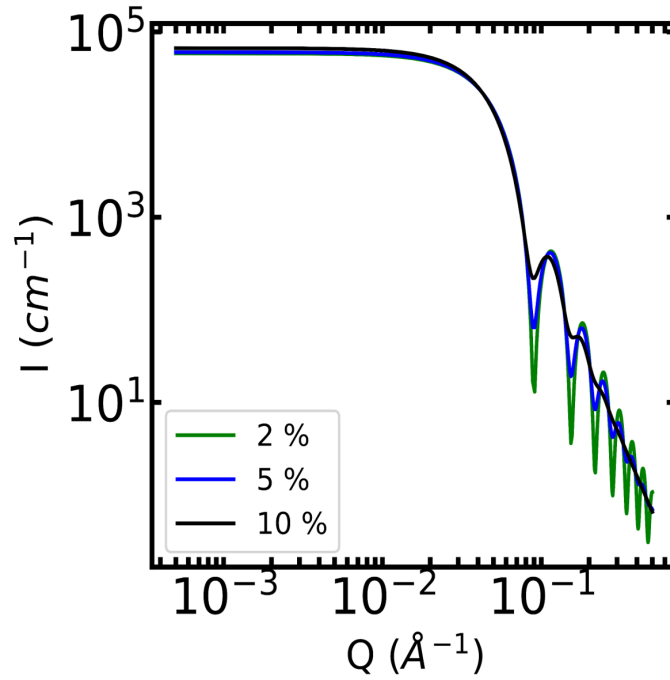


Figure 2.26.: Radially averaged SAS intensity $I(Q)$ smeared due to polydispersity (2%, 5% and 10%) in NPs.

angles and is often referred to as wide angle scattering. This section will discuss the origin of Bragg peaks in crystalline samples and the construction of Ewald sphere to visualize the reciprocal lattice. Experimental aspects and challenges to probe crystalline nanostructures will be addressed through diffraction experiments with pair distribution function (PDF). The books and papers from which various concepts and equations are borrowed for this section are listed in [57, 68, 69, 70, 71].

2.6.1. Fundamentals: Bragg's Law

Mathematically, the SLD at a given position in the crystalline sample can be written as

$$\eta(\vec{r}) = \eta(\vec{r} + n_1\vec{a}_1 + n_2\vec{a}_2 + n_3\vec{a}_3) \quad (2.139)$$

for any set of integers n_1 , n_2 and n_3 due to its periodicity. The magnitude of the vectors \vec{a}_i , for $i \in (1, 2, 3)$, defines the length of the basic unit cell. The differential scattering cross-section linked to the SLD function from basics of elastic scattering discussed previously is written as,

$$\frac{d\sigma}{d\Omega} = \left| \int_V \eta(\vec{r}) e^{i\vec{Q}\cdot\vec{r}} d^3r \right|^2 \quad (2.140)$$

where V is the volume of the illuminated sample. Then from eqn.(2.139), the integral can be equated as

$$\int_V \eta(\vec{r}) e^{i\vec{Q}\cdot\vec{r}} d^3r = L_R(\vec{Q}) \int_{V_{cell}} \eta(\vec{r}) e^{i\vec{Q}\cdot\vec{r}} d^3r \quad (2.141)$$

where V_{cell} is volume of the unit cell and here

$$L_R(\vec{Q}) = \sum_{n_1, n_2, n_3} \exp[i\vec{Q}\cdot(n_1\vec{a}_1 + n_2\vec{a}_2 + n_3\vec{a}_3)]. \quad (2.142)$$

Summation of exponential cancels out unless they are added coherently. Thus,

$$\vec{Q}\cdot(n_1\vec{a}_1 + n_2\vec{a}_2 + n_3\vec{a}_3) = \phi_o + 2\pi n \quad (2.143)$$

where ϕ_o is the constant and n is an integer. The eqn.(2.143) is achieved when

$$\vec{Q} = h\vec{A}_1 + k\vec{A}_2 + l\vec{A}_3 \quad (2.144)$$

where h, k and l are integers and $\vec{A}_1 = \frac{2\pi\vec{a}_2 \times \vec{a}_3}{\vec{a}_1 \cdot (\vec{a}_2 \times \vec{a}_3)}$, $\vec{A}_2 = \frac{2\pi\vec{a}_3 \times \vec{a}_1}{\vec{a}_1 \cdot (\vec{a}_2 \times \vec{a}_3)}$, $\vec{A}_3 = \frac{2\pi\vec{a}_1 \times \vec{a}_2}{\vec{a}_1 \cdot (\vec{a}_2 \times \vec{a}_3)}$. Here the vectors obey $\vec{a}_i \cdot \vec{A}_j = 2\pi\delta_{ij}$, $\forall i, j \in (1, 2, 3)$. So that in eqn.(2.143), $\phi_o = 0$ and $n_1h + n_2k + n_3l = n$. At isolated non-zero points, the

$$L_R(\vec{Q}) = \sum_{h, k, l} \delta[\vec{Q} - (h\vec{A}_1 + k\vec{A}_2 + l\vec{A}_3)] \quad (2.145)$$

defines the reciprocal lattice with lattice vectors \vec{A}_i . Although the Fourier transform of SLD in eqn.(2.141) is for all \vec{Q} , the discrete nature of $L_R(\vec{Q})$ with which it is multiplied results in non-zero specific values of Q known as Bragg peaks.

2.6.2. Atomic planes and Ewald sphere

The link between discrete nature of scattering and atomic structure is based on reciprocity of Fourier transform in real and inverse Q space. The atomic plane spacing of a crystal given by d in real space appears with periodicity $\frac{2\pi}{d}$ in Q -space. For a unit vector \hat{n} normal to this crystal plane, a position \vec{r} in the crystal is given by $\vec{r} \cdot \hat{n} = Nd + \Delta$, where Δ is the offset and $N = 0, \pm 1, \pm 2 \dots$ (see Fig. 2.27(a)). The spacing gives rise to peaks in Q -space where $\vec{Q} = \frac{2\pi}{d} N \hat{n}$ [57]. Equating the magnitude of \vec{Q}

with eqn. (2.74),

$$|\vec{Q}| = \frac{4\pi \sin\theta}{\lambda} = \frac{2\pi N}{d} \quad (2.146)$$

results in the well known formulation of Bragg's law

$$N\lambda = 2d\sin\theta. \quad (2.147)$$

Hence, Bragg peak indexed by h,k,l correspond to planes with normal \hat{n} given by $\hat{n} = \frac{\lambda}{4\pi \sin\theta_{h,k,l}}(h\vec{A}_1 + k\vec{A}_2 + l\vec{A}_3)$ where the scalar prefactor ensures unit length.

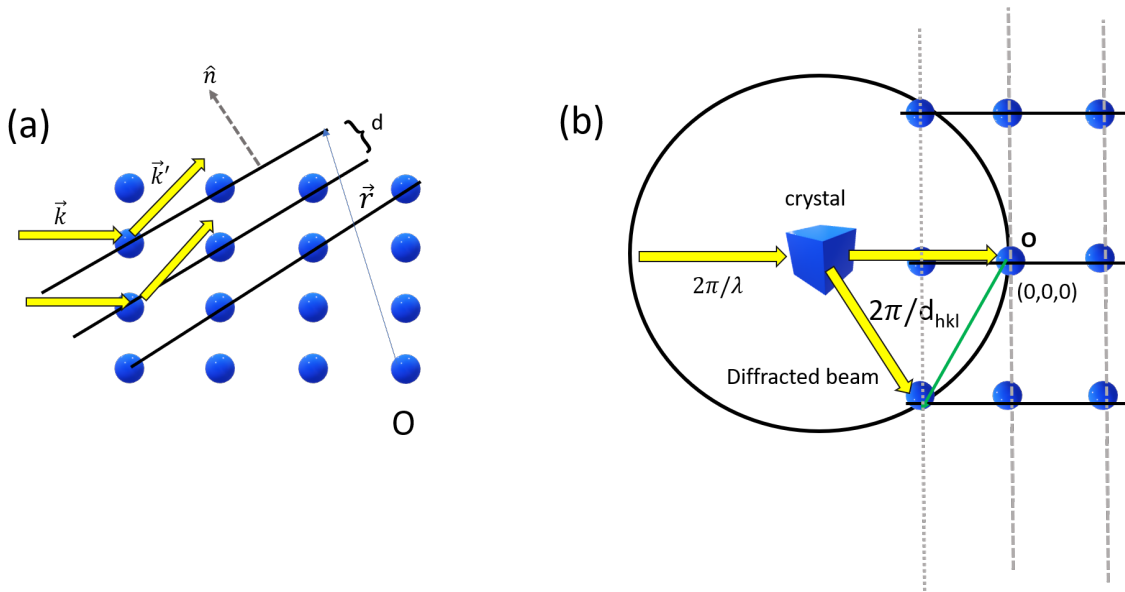


Figure 2.27.: (a) Atomic planes with a vector normal \hat{n} and interplanar spacing d . (b) Ewald sphere with crystal at origin of the sphere and radius $2\pi/\lambda$. The beam of x-rays/neutrons strikes the crystal and are diffracted along directions passing through the atoms. The origin of the reciprocal lattice is indicated by O .

Ewald sphere is a geometrical construction to visualize these Bragg planes (Fig. 2.27 (b)). Consider a sphere of radius $\frac{2\pi}{\lambda}$ (in crystallography often the choice is $1/\lambda$) with crystal placed at the centre of the sphere. The origin of reciprocal space is point of exit of direct beam on the sphere labelled as O . When the set of the planes satisfy the Bragg condition, the diffracted vector lies on the surface of Ewald sphere. Combining eqn. (2.141) and (2.145), we can define a structure factor $\mathcal{F}_{h,k,l}$ for crystal structure. Note that this structure factor is different from the structure factor $S(\vec{Q})$ defined for SAS previously. Here, this function describes amplitude and phase of wave

diffraction from crystal lattice planes h, k, l by n atoms in unit cell.

$$\mathcal{F}_{h,k,l} = V \int_{x,y,z=0}^1 \eta(x, y, z) e^{i2\pi(hx+ky+lz)} dx dy dz \quad (2.148)$$

2.6.3. Powder diffraction: Bragg peaks

Compared to single crystals, powders consist of a large ensemble of randomly oriented crystallites. Thus, the resulting differential scattering cross-section is spherically symmetric where $(\frac{d\sigma}{d\Omega}) \propto \mathcal{S}_{el}(\vec{Q}) = \mathcal{S}_{el}(Q)$. The diffraction pattern is independent of the azimuthal angle and $|\vec{Q}|$ depends on the wavelength λ and scattering angle θ . This leads to circular rings of uniform intensity on detectors during diffraction experiment. Then for a fixed λ , the peaks in the radially averaged intensity function $I(Q)$ occurs at d-spacing which satisfies Bragg's law. Then the terms from eqn. (2.144) and (2.146)

$$\frac{4\pi \sin\theta}{\lambda} = |h\vec{A}_1 + k\vec{A}_2 + l\vec{A}_3| \quad (2.149)$$

must be satisfied by more than one set of Miller indices. The area under Bragg peak $I \propto \sum_{h,k,l} |\mathcal{F}_{h,k,l}|^2$, which essentially corresponds to sum of structure factor intensities at several reflections where h, k, l obeys eqn. (2.149). The atoms are assumed to be fixed but in reality the thermal motion affects the scattering intensity. The intensity due to increased thermal atomic displacements is given by

$$\mathcal{S}_{el}(Q) = [\mathcal{S}_{el}(Q)]_{T=0} \times e^{-\frac{\alpha_T Q^2}{2}} \quad (2.150)$$

where, the right term indicates the exponential fall in scattering intensity with Q^2 and is called Debye-Waller factor. The shape and spread of Bragg peaks result from combination of instrument factors such as angular resolution, collimation distances, source-sample-detector distance and intrinsic properties of crystals. The finite size of crystal gives rise to Bragg peaks of width

$$\beta_{h,k,l} = \frac{\mathcal{K}\lambda}{L_{hkl} \cos\theta} \quad (2.151)$$

where $\mathcal{K} = 0.94$ for spheres with cubic unit cell and depends on the shape of crystallite with thickness L_{hkl} given in the direction perpendicular to N planes.

2.6.4. Total scattering experiments: Bragg and diffuse peaks

The challenge to perform crystallography for nanoparticles is illustrated in the Fig. 2.28. Figure 2.28 (a) represents conventional x-ray diffraction of crystalline sample with sharp peaks and Fig. 2.28 (b) represents the diffuse and broad peaks obtained for a nanocrystalline sample. There are two evident challenges to retrieve nanostruc-

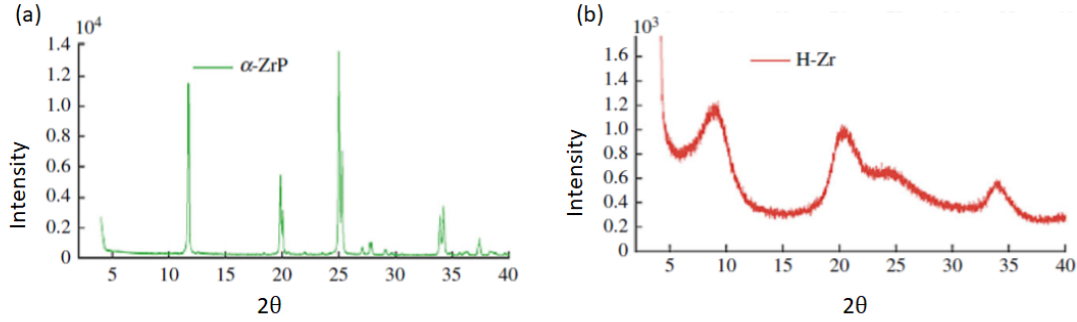


Figure 2.28.: Conventional x-ray diffraction of (a) crystalline and (b) nanocrystalline sample indicating broad and diffuse peaks; taken from [69]

ture from the diffraction [70, 69]: (i) The short range information is embedded in the diffuse scattering which is hard to detect in typical diffraction experiment and (ii) nanocrystalline samples display broad and weak Bragg peaks which are difficult to analyze. Debye scattering equation is an alternative method to describe diffraction pattern on a collection of randomly oriented crystallites without relying on the crystalline periodicity. For a collection of identical grains, the scattering intensity is

$$I_{coh}(Q) = \sum_{m,n} f_m(Q) f_n^*(Q) \frac{\sin(Qr)}{Qr} \quad (2.152)$$

which sums over all scattering centres with corresponding scattering power $f_i(Q)$. In x-rays, the scattering power is the atomic form-factor and for neutrons it is given by coherent scattering cross-section. The total scattering technique is used to resolve structures with low coherence volume by analyzing both Bragg and diffuse scattering simultaneously. The mathematical formulation of this starts with the definition of pair distribution function $g(r)$ which is defined as

$$g(r) = \frac{1}{4\pi\rho_o r^2 N} \sum_i \sum_{j \neq i} \delta(r - r_{ij}) \quad (2.153)$$

where ρ_o is the average number density of atoms, N is the total number of atoms, r_{ij} is the distance between atom i and j . Here, $\delta(r - r_{ij})$ is Dirac delta function which is 1 when $r = r_{ij}$. In practice, reduced pair distribution function $G(r)$, where

$$G(r) = 4\pi r \rho_o [g(r) - 1] \quad (2.154)$$

is used for computational convenience. $G(r)$ can be calculated from total scattering function $\mathcal{S}(Q)$ through Fourier transform

$$G(r) = \frac{2}{\pi} \int_0^{\infty} Q[\mathcal{S}(Q) - 1] \sin(Qr) dQ. \quad (2.155)$$

Experimentally it is not possible to access the 0 and ∞ and the limits range from Q_{min} to Q_{max} . High quality PDFs are produced as long as the value of Q_{max} is sufficiently high. Accurate data analysis can be conducted on PDFs produced with $Q_{max} > 20 \text{ \AA}^{-1}$ is often reduced below the experimental maximum to eliminate the noisy data. The value of Q_{max} is Fourier transform that will also determine the real space resolution of the PDF. Accessing finite values of Q_{max} results in termination ripples at low r . The normal scattering intensity $\mathcal{S}(Q)$ is obtained by measuring $I_{coh}(Q)$ and related to

$$\mathcal{S}(Q) = 1 + \frac{I_{coh}(Q) - \sum c_i |f^i(Q)|^2}{|\sum c_i f^i(Q)|^2} \quad (2.156)$$

where c_i is atomic concentration of the i^{th} element and $f^i(Q)$ atomic x-ray scattering factor or neutron scattering length and $I_{coh}(Q)$ is the coherent intensity defined previously. Thus, the $g(r)$ related to collected intensity can be used to model the structures in real space.

2.6.5. Experimental aspects: data treatment

Synchrotron x-ray and spallation neutron sources due to its large flux can give access to high Q_{max} values, enabling collection of high quality data for PDF analysis. For instance, laboratory x-ray diffraction with Mo source gives a Q range upto $Q_{max} \simeq 14 \text{ \AA}^{-1}$. The total x-ray scattering experiments carried out at x-ray synchrotron can reach $Q_{max} \simeq 25\text{-}30 \text{ \AA}^{-1}$. The thesis mainly focuses on total scattering experiments with x-rays and hence will discuss the data treatment for x-ray pair distribution function (xPDF) analysis. For xPDF, the detector is very close to sample to access high Q

values (Fig. 2.29 (a)). A commercial Ni or CeO₂ powder sample is used to both calibrate sample-to-detector distance and determine the instrument resolution parameter Q_{damp} . The 2D detector intensities of the sample are centered and integrated after calibration (Fig. 2.29 (b-c)) to obtain measured intensity as function of Q (Fig. 2.29 (d)). Since these experiments rely on preserving Bragg and diffuse scattering peaks, separate background measurements (sample container) are to be made. The coherent intensity $I_{coh}(Q)$ can be obtained from experimentally measured total intensity $I(Q)$ when corrected for incoherent intensity, background noise and detector efficiency. The intensity is then used in eqn. (2.156) to obtain total scattering function $\mathcal{S}(Q)$ plotted in fig 2.29 (e). The oscillations in this function are more pronounced and converges to 1 at large values of Q . This means that during experiments high counting statistics are required to measure intensity at high Q region. A reduced scattering function $\mathcal{F}(Q)$ is defined as

$$\mathcal{F}(Q) = Q[(\mathcal{S}(Q) - 1)]. \quad (2.157)$$

oscillates at 0 for large values of Q (Fig. 2.29 (f)). Reduced scattering function is replaced in eqn. (2.155) to obtain a real space function $G(r)$ plotted in Fig. 2.29 (g). XPDFs obtained are real space functions that are more intuitive to analyze. As shown in Fig. 2.30 (a-b), the peak position indicates distance between atomic pairs. The area under the peak reveals the abundance of such atomic pairs weighted by scattering factors. The full width half maxima of the the peak then corresponds to the atomic vibration and structural disorder within the sample. The maximum distance up to which oscillations persist in the PDF correspond to observed coherent domain. To calculate PDF for a known structure, an atom is placed at the origin and a delta function appears at the interatomic position for every atom the circle of radius r intersects (Fig. 2.30 (c)). Thermal motion causes these delta functions to broaden into a Gaussians type functions. The PDF is a sum of these independent Gaussian functions. Following such modelling process $G(r)$ can be fit using structural models as shown in Fig. 2.30(d) to determine the local and intermediate range structure of nanoparticles.

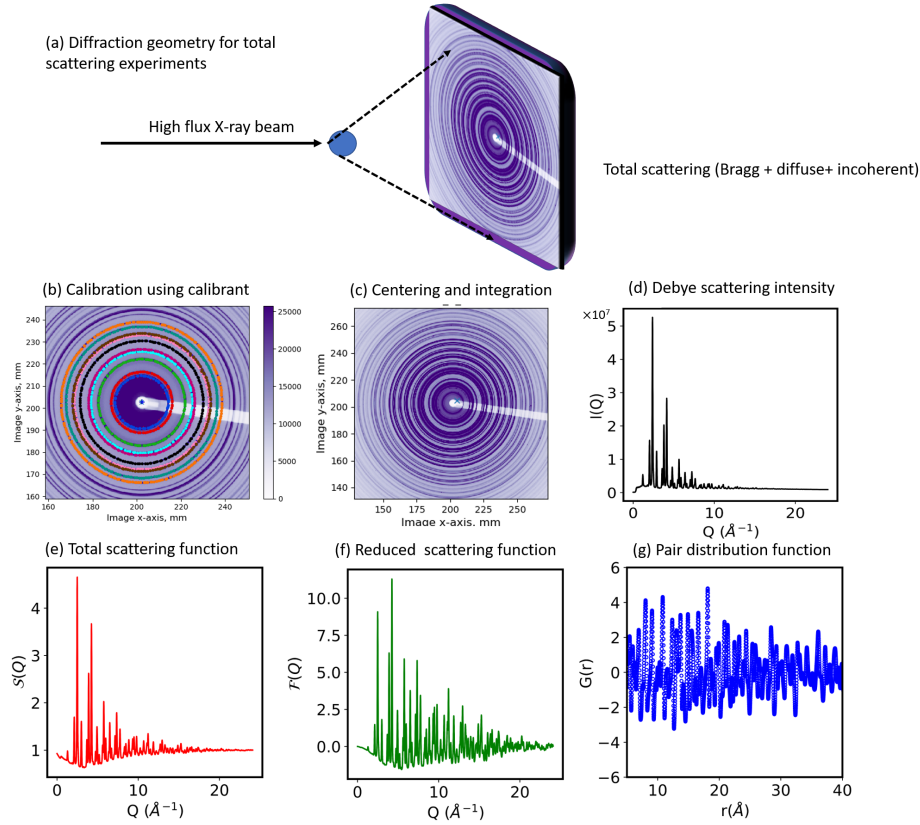


Figure 2.29.: (a) Total scattering experiment geometry with x-rays. Data treatment steps followed to obtain pair distribution function: (b) Calibration of the sample-to-detector distance by fitting the powder rings of the calibrant (CeO_2 for x-rays). Here the colored rings are the fit to the powder rings. (c) 2D data in usual scattering experiments are centred using values in (b) and integrated to obtain (d) Debye scattering intensities $I(Q)$. Normalized and corrected $I(Q)$ is further analyzed to obtain (e) total scattering function $\mathcal{S}(Q)$ (using eqn. (2.156)), (f) reduced scattering function $\mathcal{F}(Q)$ as a function of Q (using eqn. (2.157)). (g) Finally a real spaced pair distribution function $G(r)$ is obtained by Fourier transform of the $\mathcal{F}(Q)$.

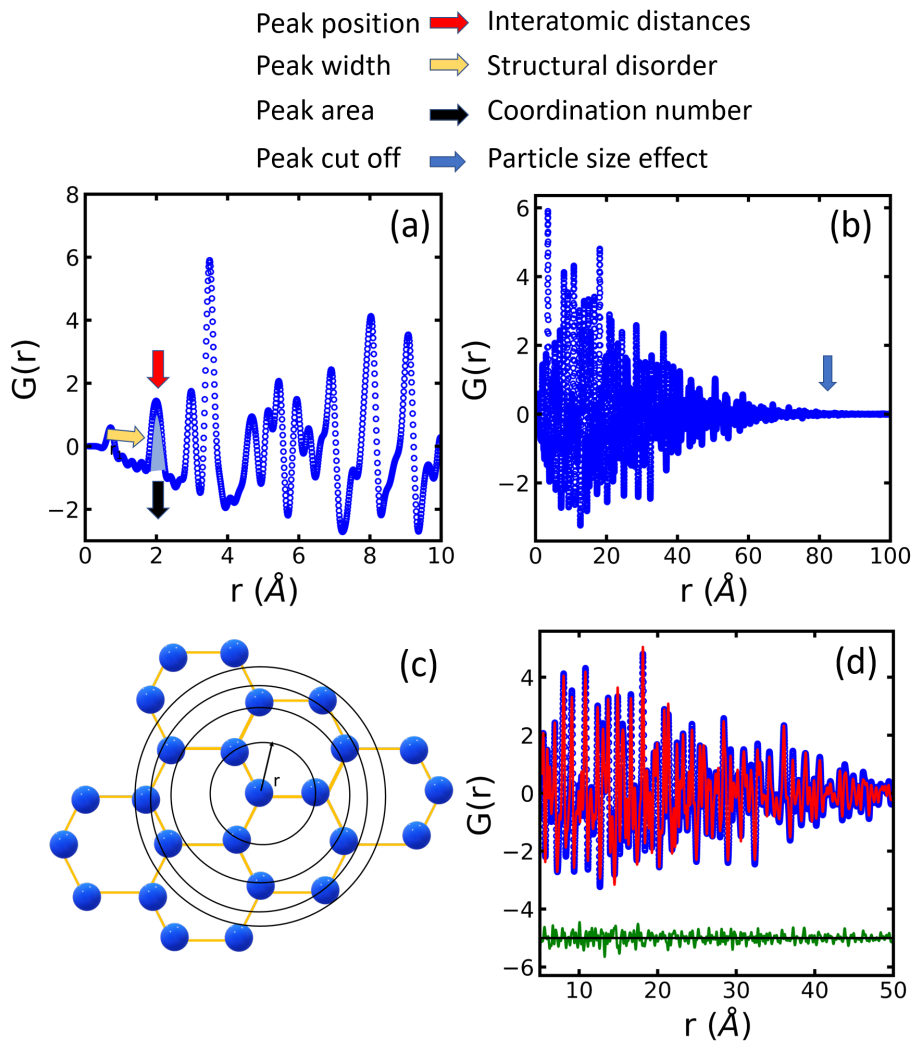


Figure 2.30.: Analysis of $G(r)$ functions: (a) Peak position, area under peak and width (FWHM) of the peaks in the PDF corresponds to various structural aspects of the nanostructure. (b) The crystallite size is denoted by the peak cut-off in the PDF. (c) Schematic process for modelling the PDF considers the atom at the origin and (d) Fit of $G(r)$ data with experimental data in blue open circles and calculated pattern is the red curve based on the modelling described in (c) and difference between calculated and experimental data is the green difference curve.

3. Review of magnetic dumbbells nanoparticles

This chapter discusses and reviews the literature on hybrid magnetic dumbbell-shaped nanoparticles. Dumbbell nanoparticles (DBNPs), sometimes called "snowman particles," is a generic name for two different/similar particles in close contact with a unique morphology. Therefore, this name has been used extensively for soft, hard, organic, and inorganic particles. This chapter focuses mainly on DBNPs containing metal and metal oxide nanoparticles, in particular, Au-Fe₃O₄. Along with a brief introduction to Au and iron oxide's individual physical and magnetic properties, the chronological order of events that led to their current synthesis trends, including the discovery of novel properties, are discussed. Different assemblies formed by DBNPs are reviewed with mention of potential applications. Finally, the gaps in the literature relevant to the thesis are revisited.

3.1. Single phase nanoparticles

3.1.1. Gold nanoparticles

Technologically, Au NPs have been used for optical properties like staining glass since ancient times. Systematic investigations on gold colloids began in mid nineteenth century and their breakthrough use for biological applications were discovered only in the last two decades with advent of nanotechnology. The toolbox now allow controlled synthesis and characterising methods that did not exist before [72]. The most prominent detection techniques are based on the interaction of light with Au NPs. Au NPs absorb and scatter visible light. Upon absorption, the light energy excites the free electrons in the Au particles of 4-40 nm to a collective oscillation to exhibit the localized surface plasmon resonance (SPR) at wavelength of 510-530 nm [73, 74]. The excited electron gas relaxes thermally by transferring the energy to the Au lat-

tice, leading to heated Au NPs. Gold particles larger than around 20 nm can be directly imaged with optical microscopy in phase or differential interference contrast mode. Efficient absorption and scattering of light at specific wavelength based on shape and size of Au NPs can be used for labelling with different colours. The Au NPs can be imaged using photothermal, photoacoustic and fluorescence microscopy. The molecules adsorbed on the surface of Au is introduced into cells where molecules can be detached [75]. Au NPs' ability to absorb copious amounts of X-ray radiation can be used to enhance cancer radiation therapy or increase imaging contrast in diagnostic computed tomography (CT scans) [76]. The Au NPs can shield the unstable drugs or poorly soluble imaging contrast agents and facilitate their efficient delivery to inaccessible regions of body. Unique properties of Au are still beginning to be fully realized in range of medical diagnostic and therapeutic applications [77, 78, 79].

3.1.2. Iron-oxide nanoparticles

Iron oxides have extensive applications in magnetic recording medium, catalysts, pigments, optical devices and electromagnetic devices [80]. They exist in rich variety of structures and oxidation states. By definition, superparamagnetic iron oxide nanoparticles (IONPs) are classified based on the size of the particle. Due to their high saturation magnetization, high magnetic susceptibility and low toxicity, IONPs have found several applications in biomedicine. For example as efficient contrast agents that are used to enhance the relaxation difference between healthy and pathological tissues in magnetic resonance imaging (MRI) [81, 82]. IONPs can be used as drug delivery systems for cancer therapy and killing tumour cells in magnetic hyperthermia [83, 84]. Naturally occurring IONPs in form of chains can be found in magnetostatic bacteria that enable geomagnetic navigation in aquatic habitats [85]. Chemists have now successfully synthesized and characterized IONPs of different morphologies including spheres, rods, cubes and flowers [86, 87]. The resulting properties are highly dependent on synthetic route, shape and size. Thus, there has been much development to produce high quality iron oxide systems [88, 89, 90, 91]. Among several crystalline modifications the magnetic phases include rhombohedral hematite (α -Fe₂O₃), cubic maghemite (γ -Fe₂O₃), cubic magnetite (Fe₃O₄), cubic wüstite (FeO) and less common ϵ -Fe₂O₃. In the α -structure, all Fe³⁺ have an octohedral coordination whereas γ -Fe₂O₃ has the cation deficient AB₂O₄ spinel. The metal atoms A and B occurs in tetrahedral and octahedral environment, respectively. Hematite is AF at temperature below 950 K while above Morin point (260 K) it exhibits weak FM. Bulk maghemite

is FiM below 620 °C. Among all, magnetite phase posses interesting properties because of the presence of iron cations in two valence states Fe^{2+} and Fe^{3+} in inverse spinel structure. The cubic spinel is FiM at temperature below 858 K. Cubic wüstite is AF with $T_C = 185$ K in bulk state. Magnetite has a larger bulk $M_s = 92\text{--}100$ emu/g than maghemite $M_s = 60\text{--}80$ emu/g and a lower Curie temperature due to antiparallel interactions between the electron spins of tetrahedral-coordinated Fe^{3+} and octahedral-coordinated $\text{Fe}^{3+}/\text{Fe}^{2+}$ in magnetite. Self-assembly into 1D, 2D and 3D structures with controlled shapes, alignment and spacing have been successfully achieved in IONPs [92, 93, 94, 95].

3.2. Types of dumbbell

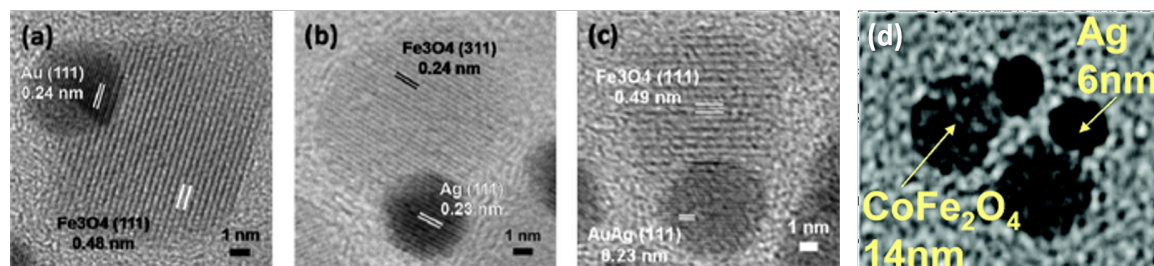


Figure 3.1.: (a) Au- Fe_3O_4 (b) Ag- Fe_3O_4 (c) AuAg- Fe_3O_4 and (d) Ag- CoFe_2O_3 DBNPs. (a-c) Reprinted (adapted) with permission from [96] ©2010 American Chemical Society and (d) reprinted (adapted) with permission from [97] ©2005 American Chemical Society.

Multi-functional DBNPs that combine and intertwine materials from transition metal oxides (Fe_3O_4) to metals (Au, Ag, Pt) are expected to display novel properties as a result of this attachment. A number of authors have synthesized Au- Fe_3O_4 , Ag- Fe_3O_4 , AuAg- Fe_3O_4 , and Ag- CoFe_2O_4 DBNPs, as shown in the microscopy images in the Fig. 3.1 (a-d). Gu. et. al prepared Ag- CoFe_2O_4 DBNPs for instance by mixing AgNO_3 in aqueous phase with Fe_3O_4 dispersed in organic solution [98]. Ultrasonic emulsification triggered self-assembly at the liquid-liquid interface to produce such DBNPs. The sequential growth of DBNPs by thermal decomposition of one component on the other was first successfully established by Yu. et al. in 2005 [16].

3.3. Review of current synthesis methods

The difference in synthesis compared to core-shell particles lies in the heterogeneous nucleation combined with a lattice mismatch of two components (Fig. 3.2). In DB-NPs, a significant lattice mismatch favors the growth of one component on the crystal plane of the other [99]. The seed to precursor ratio also plays a critical role. The increased concentration of Au seeds means more surfaces are available, leading to the precursor atoms nucleating on the other surface resulting in a core-shell structure. Electron transfer at the interface of the two components affects the morphology of the dumbbell. The surface of the component can be active sites for the other component to nucleate by controlling the solvent polarity [16, 100].

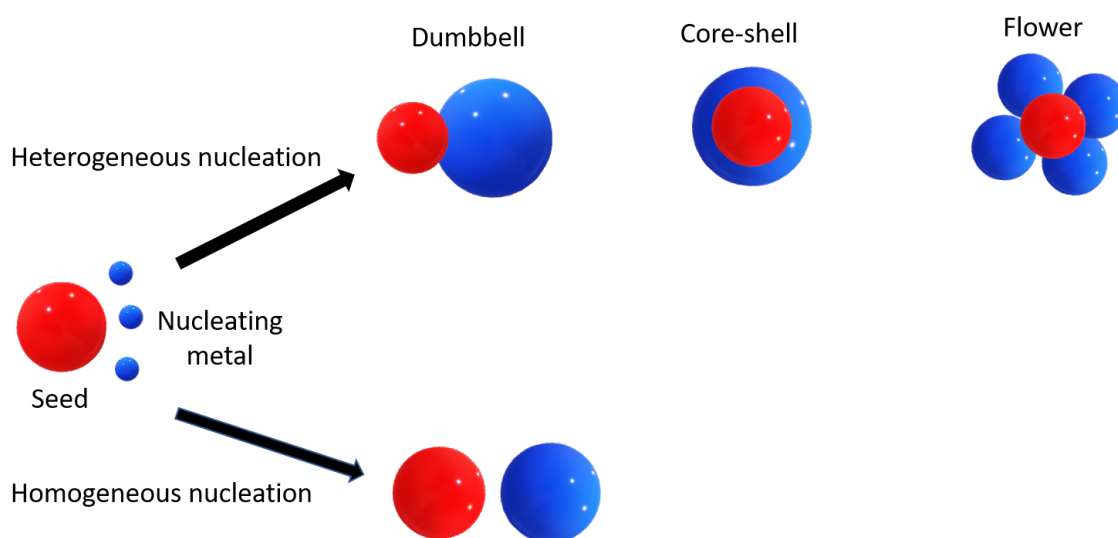


Figure 3.2.: Sketch representing the heterogeneous nucleation and homogeneous nucleation of one component (blue) on the preformed seed of other (red). Homogeneous nucleation results in composite system containing two disjoint particles. Heterogeneous nucleation results in dumbbell, core-shell and flower nanoparticle; Figure adapted from [18].

The primary challenge for the synthesis of DBNPs was obtaining precise control over their size and morphology. The earlier bifunctional systems were prepared by physical deposition of thin Au film on spherical particles, adsorption techniques or electroplating [101, 102]. One of the earliest successful synthesis of DBNPs with no prior treatment of the surface were reported in 2005 by Yu, H. et al. using solution-phase synthesis [16]. They achieved this remarkable result through thermal decomposition of iron pentacarbonyl $\text{Fe}(\text{CO})_5$ on the surface Au nanocrystals followed by

oxidation in air. The described protocols can produce Au-Fe₃O₄ with size-tunable components up to 20 nm that can easily convert to Au-Fe₂O₃ and Au-Fe DBNPs. Au nanoparticles were pre-formed or synthesized by in situ injections of HAuCl₄ solution into the reaction mixture. Au and Fe(CO)₅ are mixed in the presence of oleic acid and oleylamine to provide the coating around DBNPs to avoid irreversible aggregation in a 1-octadecene solvent. This mixture is heated to reflux ($\approx 300^\circ$ C) to produce the DBNPs. Several groups have optimized these protocols for precise size control of DBNPs size in the next decade. DBNPs are synthesized similar to the seed-mediated growth in core-shell NPs. However, the nucleation and growth are anisotropically centered on one specific crystal plane around the seeding NPs. The control of seed to precursor ratio achieves this heterogeneous nucleation; here, the Au NPs are the seeds while Fe(CO)₅ is the precursor. Several parameters such as seed to precursor ratio, reaction time and temperature, and solvents were systematically investigated for precise size control [18, 19]. The controlled growth of only one Fe₃O₄ on the seed under current conditions is attributed to the possible electron transfer between Au and Fe. In the growth process Fe(CO)₅ decomposes into Fe and nucleates on Au NP. Once the Fe nucleus is formed on Au, free electrons from Fe tend to flow across Au, as a result the interface becomes electron rich [17]. When exposed to air, Fe is oxidized to Fe₃O₄, thus electrons from Au must compensate for charge induced by polarized plane at interface thus making other facets of Au unsuitable for multinucleation. The type of surface ligand is critical in the growth condition. The compatibility requires the ligands to bond not so strongly to particle surface. For instance, thiol can hinder epitaxial growth of metal oxide on noble metal NPs producing a composite showing individual properties of each component.

3.4. Emergence of novel properties

Au NPs have a characteristic surface plasmon resonance at wavelength of 520 nm, which may broaden and shift depending on size and concentration. During growth process, electrons flow from Fe to Au. However, small variations in electron transfer at interface may lead to drastic change in properties as seen in wavelength shift to 538 nm for Au in Au-Fe₃O₄. The red shift occurs in these DBNPs due to electron deficiency in Au caused by the interface [16, 103]. The interface is also responsible for enhanced magnetic moment observed in Fe₃O₄ due to presence of Au [104]. Spin polarization of non magnetic metals in contact with ferromagnet was extensively

studied experimental and theoretically since the 70s' for bulk [105, 106, 107]. They found that the spin polarization can penetrate in a length scale of 1-2 nm in non-magnetic metal in contact. In another example, the hysteresis measured in two types of DBNPs Au-Fe₃O₄ with length scales 3- 14 nm and 3-6 nm were compared to single spherical Fe₃O₄ of similar sizes [16]. The 14 nm magnetite attached to DBNP show similar hysteresis loop as the spherical counterpart due to negligible Au content. However, there is a slow increase in moment with field in 6 nm magnetite of the DBNP. The slope is also attributed to the spin canting of the small magnetite which is aggravated by Au [20]. Exchange bias corresponds to a shift of the hysteresis loop of a ferromagnet along the magnetic field axis due to interfacial exchange coupling with an adjacent antiferromagnetic layer. Exchange bias effect is therefore not expected in single phase Fe₃O₄ nanoparticles. Hence observation of this exchange bias effect in magnetite of the DBNP is a novel behaviour. This effect is attributed to electron transfer at the interface from Au NP to ferrimagnetic Fe₃O₄ reducing the interface to antiferromagnetic FeO [22]. Since the structure is limited to nanometer scale, any variations in the electron transfer between the two species may result in the drastic effect in property change in either NPs leading to novel properties [108]. DBNPs are shown to exhibit enhancement in contrast with potential as improved contrast agent for magnetic resonance imaging (MRI) to improved catalysis [21].

3.5. Previous observation of assemblies

Several reports exist on self-assembly of multi-functional yet spherically symmetric particles like Janus particles and soft organic materials [109, 110, 111, 112, 113, 114]. DBNPs in the micron size regime are shown to assemble in to well defined clusters or chains [115]. Dumbbell shaped microgels have been used as model systems to show phase transitions as a function of volume fraction and aspect ratios [116]. Monte Carlo simulations on DBNPs where one surface is attractive and other is repulsive indicate formation of various structures ranging from spherical micelles to bilayers based on the center to center separation, size ratio and volume fraction of the colloids [24]. Recently, several reports have demonstrated experimentally the formation of assemblies into vesicles and spheres through selective functionalization where surface of IONPs are made repulsive through electrostatic interactions while Au lobe is made attractive via hydrophobic interactions [27, 29, 117]. Such experiments often probe self-assembly using microscopy techniques like electron microscopy and high-

angle annular dark-field scanning transmission electron microscopy (HAADF-STEM). Contrasting the magnetic dumbbells, non magnetic dumbbells were shown to form chains when dispersed in ferrofluid containing magnetic sphere. These spheres were controlled by a combination of magnetic and electric fields [118]. Pre-designed block copolymer led to DBNPs arranging in arrays [119]. Atomic force microscopy imaging of DNA coupled with DBNPs are shown to align in the magnetic field. DNA is easily coupled with Au surface via the Au-S chemistry and Fe_3O_4 is used to manipulate in magnetic field to identify different bending modes of the DNA [120]. In the most recent report, Niehues. et. al in 2021 demonstrated that through selective functionalization of the surface with a photo responsive material, light could be used to assemble the DBNPs through host guest interactions [30]. An overview of such assembly patterns formed are summarized in the Fig. 3.3.

3.6. Applications

The advantages of DBNPs that are exploited in several applications include (i) the presence of two distinct surfaces that allow dual functionalization, (ii) the unique morphology provides a rotational degree of freedom, and (iii) multifunctionality is encoded in the system.

1. **Dual probe biomedical imaging:** The multifunctionality of the system, for instance optically active Au attached to magnetic iron oxide is suitable for simultaneous optical and magnetic detection, hence its potential as a dual probe for biomedical imaging [16, 121, 122, 123]. The caffeic acid functionalized Au- Fe_3O_4 and Pt- Fe_3O_4 heterodimers were excellent agents to enhance the effect of x-ray radiation on 2D-3D tumour cells while protecting the healthy breast cells [124]. Both Au and iron oxide are non-toxic and bio-compatible for in-vivo drug applications [125, 126]. Unique morphology of the DBNPs offers two active surfaces that make it multi-functional and suitable for target specific imaging and delivery systems [98, 127].
2. **Catalysis:** Such structures are also excellent candidates for catalysis. The enhanced catalysis in these particles is associated to modified electronic structure in both oxide and metal interfaces. This modification leads to electron transfer from oxide to metal resulting in oxygen vacancies that become active sites [128, 103]. Wang et al. reported a 20-fold increase in mass activity toward oxygen

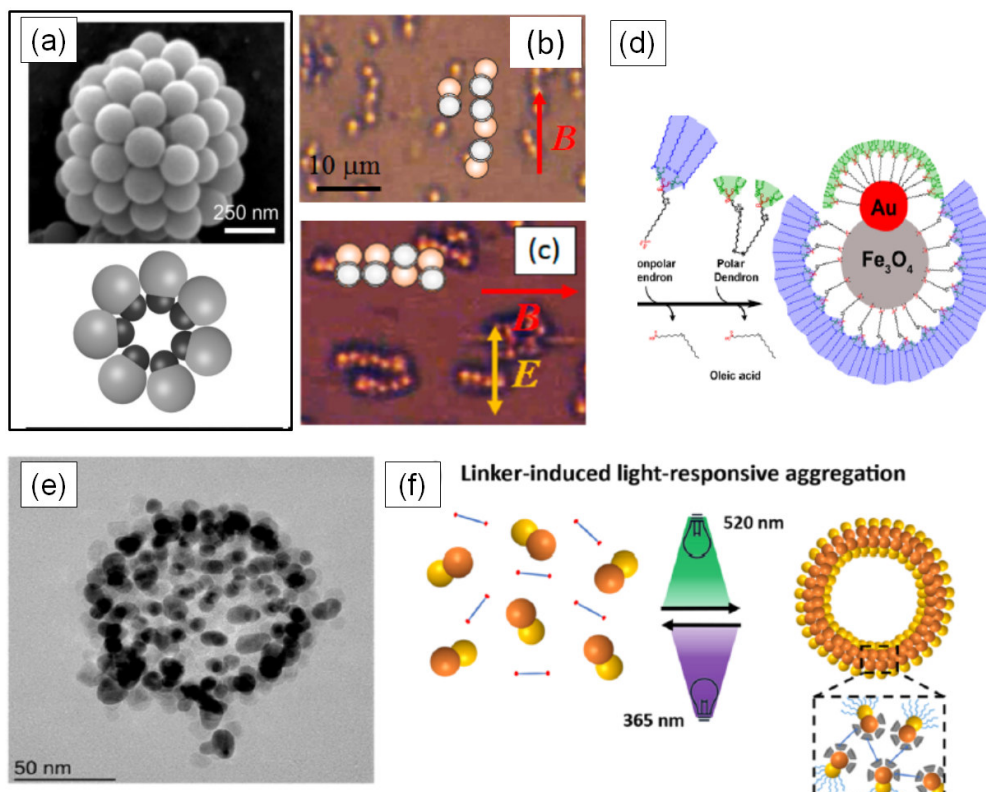


Figure 3.3.: (a) Micrometer sized dumbbells containing organic compounds forming vesicles, reprinted (adapted) with permission from [109] ©2018 American Chemical Society. (b) and (c) Non magnetic DBNPs in ferrofluid dispersion forming chains with simultaneous application of magnetic and electric field, reprinted (adapted) with permission from [118], ©2015 American Chemical Society. (d) Scheme of surface functionalization of Au- Fe_3O_4 with hydrophilic and hydrophobic ligand to induce assembly, reprinted (adapted) with permission from [29] ©2017 American Chemical Society. (e) Vesicle formation as result of the surface functionalization of Au- Fe_3O_4 DBNPs, reprinted with permission from [27] ©2018 American Chemical Society. (f) The photo activated self-assembly in Au- Fe_3O_4 surface functionalized DBNPs, reprinted with permission from [30] ©2021 American Chemical Society.

reduction reaction for Pt-Fe₃O₄ DBNPs compared with the single component Pt NPs [17]. Au-Fe₃O₄ are found to be more active than individual Au or Fe₃O₄ in the catalysis reduction of H₂O₂ [129].

3. **Sensors:** DBNPs such as PtPd-Fe₃O₄ are one of the most sensitive probe to quantitatively detect H₂O₂ in biological environment [124]. An electrochemical immunosensor has been developed using novel kind of label based on DBNPs such as Au-Fe₃O₄ for the detection of cancer biomarkers [129]. Ultrasensitive colorimetry for Salmonella typhimurium detection was achieved with such DBNPs [130].

3.7. Conclusion

In many cases, theoretical and experimental studies on DBNPs have predicted and confirmed ordered patterns. Often these assemblies are tuned through surface modification of the DBNPs and controlled through electrostatic interactions. However, external magnetic fields are preferred stimuli for most relevant biomedical applications. Therefore, tuning and controlling assemblies via magnetic field is essential for an in-vivo environment. So far, the assemblies have been mainly observed through microscopy techniques. Scattering experiments offer an advantage in investigating self-assembly in an environment close to real applications to explore parameter space. To the best of our knowledge, there have been no prior reports on assemblies using scattering methods on DBNPs. Multi-scale approach, including microscopy and scattering techniques, will offer new insight into the self-assembly phenomenon.

4. Experiments: Instruments, Methods and Simulations

Self-assembly of magnetic nanoparticles (MNPs) in dispersion depends on various parameters, including size, shape, composition, magnetic properties, magnetic structure, and thickness of coating around a nanoparticle. These multi-scale parameters of MNPs are extracted in this thesis for dumbbell nanoparticles (DBNPs) and reference iron oxide nanoparticles (IONPs) using several experimental methods. The methods outlined in this chapter include imaging, total scattering and small-angle scattering experiments, magnetometry, thermogravimetric and elemental analysis.

4.1. Samples

The samples investigated in this thesis include four different DBNPs (labeled: A12F10, A9F11, A10F14 and A13F14) that primarily consist of a gold NP seed attached to an IONP. Particles are stabilized by coating the surface with oleic acid and oleylamine. Before detailed studies on DBNPs, six reference IONPs surface stabilized with oleic acid are investigated individually (F05, F10, F20, F21, F24 and F27). Detailed synthesis protocols and sizes of IONPs and DBNPs are outlined in chapters 5 and 6, respectively. These IONPs and DBNPs are initially dispersed in homogeneous toluene. However, different sample handling protocols were established for the methods described below.

4.2. Electron Microscope (EM)

Two different EMs employed to inspect the shape, size and structure of the IONPs and DBNPs are (i) transmission electron microscope (TEM) and (ii) scanning electron microscope (SEM). The electron-matter interactions involved while imaging the specimen with electrons are outlined in Fig. 4.1.

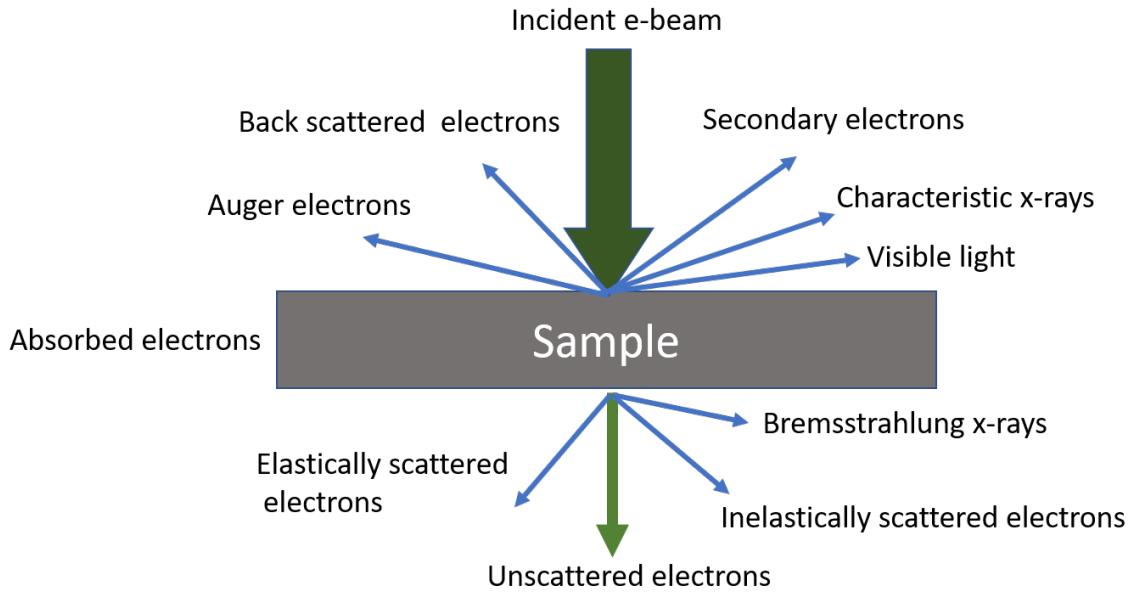


Figure 4.1.: Different electron interactions in an electron microscope; inspired from several sources [131, 132].

The primary electron beam incident on the sample and interactions of electrons with atoms can be broadly classified into three categories [133, 134]:

- Backscattered electrons (BSE) are elastically scattered electrons deflected at an angle greater than 90° from the direction of the primary beam due to electrostatic interaction with positively charged atoms. The energy of the electrons is close to the primary beam.
- Elastically scattered electrons are similar to BSE, except that electrons are deflected at an angle less than 90° from the direction of the primary beam. Due to elastic scattering, the energy of the scattered electrons is close to the primary beam.
- Inelastically scattered electrons are electrons that lose energy through interactions with the electron cloud of the sample. Several processes can give rise to signals due to inner-shell ionization, Bremsstrahlung or braking radiation, secondary electrons, phonons, plasmons, and cathodoluminescence. The atom's loosely bound electrons can be ejected at low energies to yield secondary electrons. Due to energy transfer and excitation of the inner electronic shell, the unstable atom causes the outer-shell electrons to fill the hole, which leads to a release of characteristic x-rays or Auger electrons. Bremsstrahlung radiation are

uncharacteristic x-rays generated when the atomic nucleus decelerates charged particles.

The main components of the EM are (a) electron gun, (b) electromagnetic lens, (c) vacuum system, (d) camera/detector and (e) processing system. The electron gun generates electrons through thermionic emission (Tungsten, LaB₆) or field emission. EMs are maintained at a high vacuum level to avoid any collision, which affects the image's resolution. The voltage difference causes the acceleration of the electrons in the system. The wavelength of the electrons is dependent on their momentum and is varied through a range of accelerating voltages. Higher accelerating voltages produce high-energy electrons with smaller wavelengths. The electrons are accelerated through the electromagnetic lens to produce a focused beam of electrons to image the specimen and gain information about its structure. The electromagnetic lens consists of copper winding through which current passes to generate a magnetic field that will determine the lens's focal length. An EM designed to use 200-300 keV electrons offers the advantage of high resolution. They have a very high magnification range, typically 10-500,000 times for SEM and 2000-1 million times for TEM. Thus, EM enables characterization at many different length scales, from micro- to nanoscale.

4.2.1. TEM

4.2.1.1. Working principle

The working principle and the components of TEM are schematized in Fig. 4.2. The first lens system bundles the electrons to determine the beam's brightness and guide it to the sample. In TEM, mainly the transmitted elastically scattered electrons are used for imaging. Therefore, the specimens must be thin (~ 70 nm) and are usually mounted on top of a carbon-coated grid for the electrons to penetrate the sample and form a primary image at the objective lens. As a result, this gives information about the sample's inner crystal structure, morphology, and stress state. The magnetic field strength at the objective lens is used to focus the image. The final magnification is determined by the projective lens, which projects the final image on the fluorescent screen or CCD camera. The circular path of the electrons leads to rotation of the image, which is corrected with corrector coils.

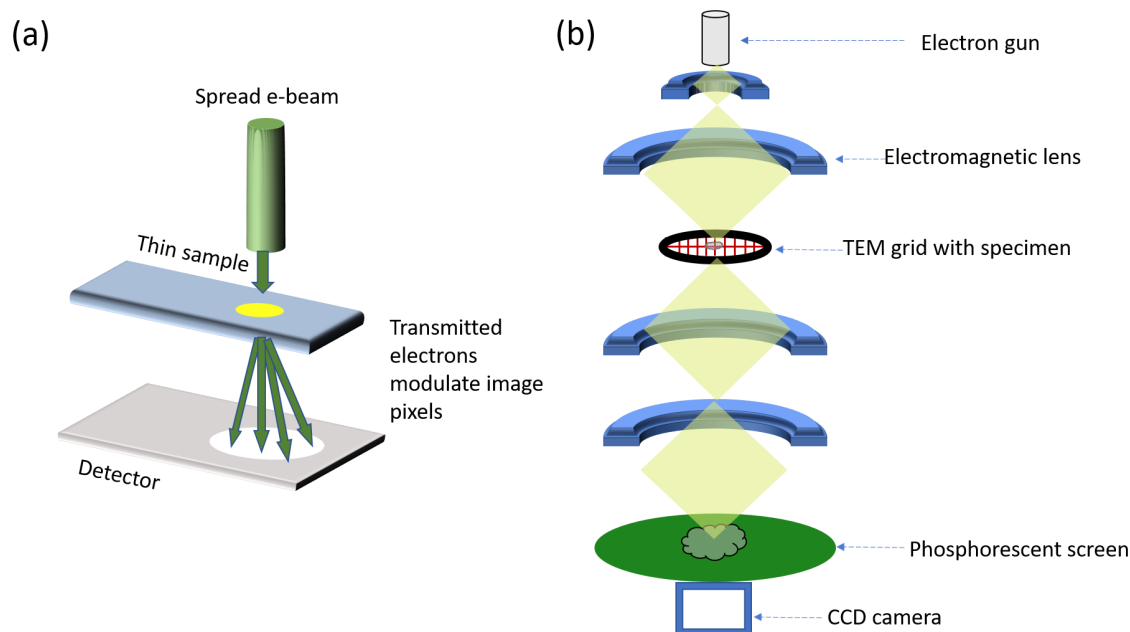


Figure 4.2.: (a) The working principle of TEM involves imaging thin samples in transmission mode. (b) Principal components of the TEM setup; adapted from [131, 132].

4.2.1.2. Sample preparation

The measurements were carried out in Ernst Ruska centre at Forschungszentrum Jülich GmbH with Philips CM20 and FEI Technacai using an accelerating voltage of 200 kV. The samples were prepared by evaporating a drop of about 25 μl of solution of IONPs and DBNPs on a carbon coated copper grid. The TEM images from IONPs were obtained by Dr. Sascha Ehlert (Forschungszentrum Jülich) and some images of DBNPs by Dr. Elvira Fanatechi (University of Pisa).

4.2.2. SEM

4.2.2.1. Working principle

The working principle and components of SEM are displayed in Fig. 4.3. The SEM image is created by detecting the reflected or knocked-off electrons. This image provides information about the sample surface and composition. The difference from TEM is that now specimens can be thicker since it does not have to be permeable to electrons.

4.2.2.2. Sample preparations

The SEM studies were limited to F27 IONPs that formed assemblies in a magnetic field. Two deposition modes were employed to prepare (a) drop-cast and (b) spin-coated samples. The SEM studies were carried out at the PGI-7 institute, Forschungszentrum Jülich GmbH on Hitachi SU8000 with an accelerating voltage of 20 kV. In drop-casted samples, about 25 μl of F27 IONPs were dropped on a silicon substrate and were allowed to dry out at ambient conditions for three days. The spin-coated sample was prepared by dropping 25 μl IONPs on the substrate placed in a spin coater set to a rotation speed of 30 rps for one minute.

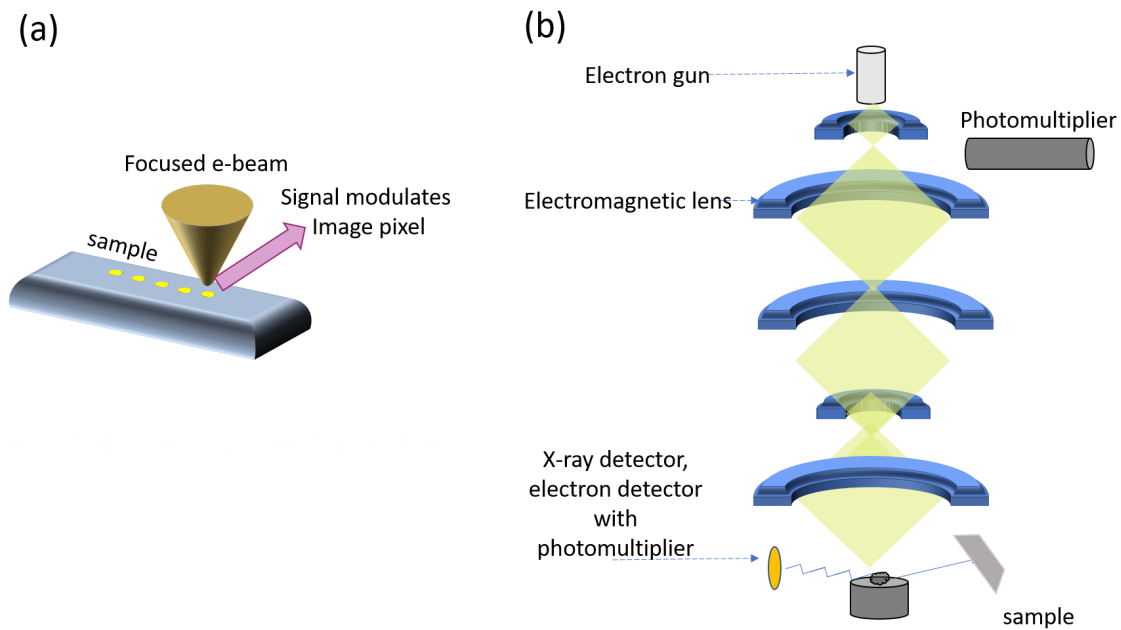


Figure 4.3.: (a) The working principle of a SEM involves imaging samples in scanning mode and can be thicker than TEM samples. (b) Principal components of the SEM setup; adapted from [131, 132].

4.3. Magnetometer

4.3.1. Working principle and setup

Magnetization and susceptibility measurements can categorize different magnetic materials. Magnetometers are magnetic sensors that detect the induced magnetic moment of the sample. The vibrating sample magnetometer (VSM) is one of the most

common modes for extracting information about magnetic moment. In the scheme shown in Fig. 4.4 (a), the sample is introduced in a constant uniform magnetic field which induces a magnetization in the sample. As the sample is vibrated, the external field experiences perturbations. A set of pickup coils arranged around the sample can be used to measure the electromotive force (emf) generated due to a change in magnetic flux. The time-dependent induced voltage induced in the pickup coil by changing magnetic flux is $V_{coil} = \frac{d\phi}{dt} = \left(\frac{d\phi}{dz}\right)\left(\frac{dz}{dt}\right)$. The emf depends on the amplitude and frequency of vibration, external field, and sample magnetization for a particular geometry. Magnetometry measurements on IONPs and DBNPs were carried out on the PPMS-DynaCool system from Quantum design at JCNS-2, Forschungszentrum Jülich (Fig. 4.4 (b)). The DynaCool is the new generation of physical property measurement systems requiring no liquid cryogenes. A wide range of measurements, including electrical and magnetic transport, may be performed. However, for measurements included in the thesis, the DynaCool system was mainly used in VSM mode (Fig. 4.4 (c)) to extract magnetic moment. This option requires a puck-based coil set with integrated temperature sensors and a high-resolution linear transport motor. The magnetic moment of the sample can be acquired at fast acquisition rates of 1 second average per data point with a sensitivity of 10^{-6} emu. The lock-in measurement technique isolates the sample signal from external noise. Through calibration measurement of palladium sample, a residual field of ~ 20 Oe was determined for this system.

4.3.2. Sample preparation

Samples of required concentration were prepared by melting weighted paraffin wax at 50 °C. The IONPs and DBNPs in the original dispersion state were measured, extracted using pipettes and added to this melted wax. The mixture is allowed to cool and the wax-like ball is loaded in plastic capsules (Fig. 4.5 (a)). The prepared capsules are then sealed by melting the capsule edges and wrapped in Teflon to prevent any contamination of the magnetometer system. Prior to alignment measurements, the samples are adjusted by loading in the brass sample holder as shown in Fig. 4.5 (b).

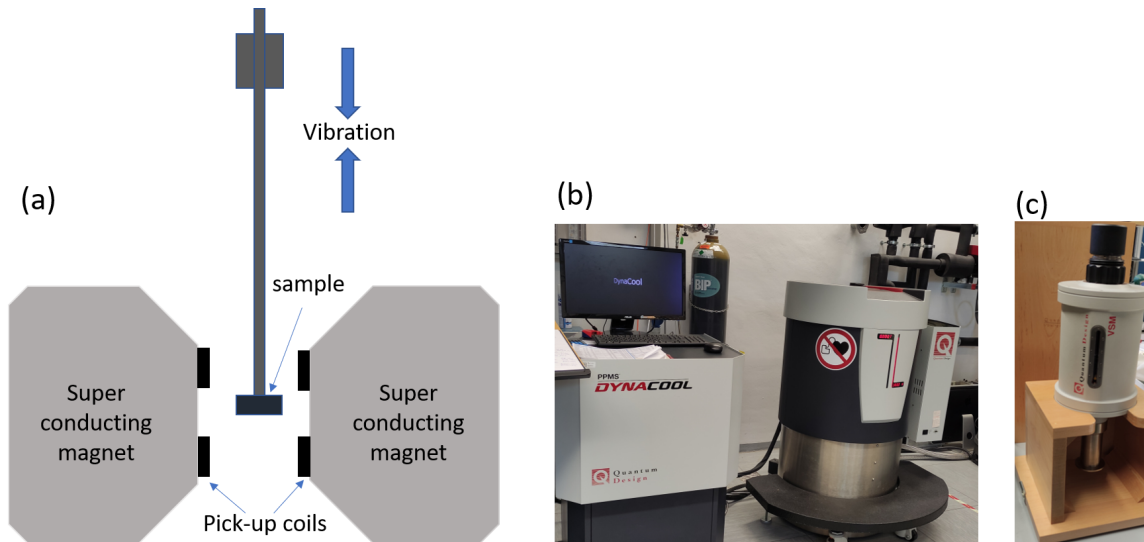


Figure 4.4.: (a) Schematic of the magnetometer in VSM mode. (b) The PPMS-DynaCool system and (c) VSM module from Quantum Design at Forschungszentrum Jülich GmbH.

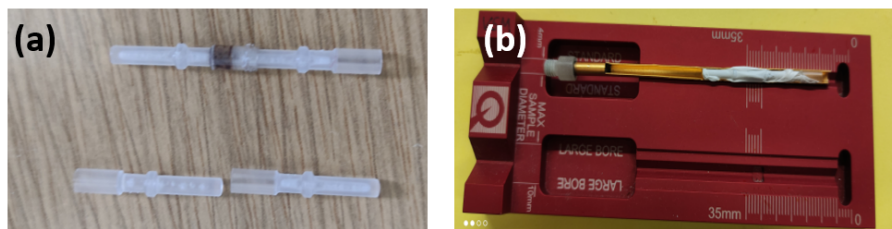


Figure 4.5.: (a) VSM capsule loaded with sample. (b) The teflon covered capsule loaded on the brass sample holder and aligned for VSM measurement.

4.3.3. Data acquisition

For data presented in the thesis, DC magnetization measurements were carried out at temperatures from 5-300 K. A standard zero-field cooled (ZFC) measurement involves first cooling the sample in zero field from 300 K to 5 K. The sample is measured in the VSM mode as the sample is warmed from 5 K to 300 K in 100 Oe magnetic field. Maintaining this field, field cooled (FC) curve is measured as the sample is cooled from 300 K to 5 K. The collected ZFC-FC measurements are used to obtain temperature-dependent magnetization curves which is further analyzed to determine the blocking temperatures T_B . For field-dependent magnetization measurements, a strong field of 1 T is applied to the sample at 300 K and cooled to a target temperature of 5 K. At 5 K and 300 K, the magnetic moment is measured in VSM mode on applying a field from 5T to -5 T and back to 5 T. The magnitude of exchange bias field is

calculated as $|H_{EB}| = |H_{c1} + H_{c2}|/2$, where H_{c1} and H_{c2} are the positive and negative coercive fields, respectively. The diamagnetic contribution was subtracted from field-dependent magnetization measurements by calculating the magnetization slope at the large fields.

4.3.4. Elemental analysis

Inductively coupled plasma - optically emission spectroscopy (ICP-OES) was performed to obtain the mass of Au and IONP in DBNP samples. ICP-OES can identify atomic composition of material. These measurements were carried out ZEA-3, Forschungszentrum Jülich GmbH. The solution containing the sample is prepared and aerolized using a nebulizer and pumped into the plasma chamber. A high energy plasma contains Argon ions generated by high power RF signal that ionizes the gas to form electrons and other charged species. Interaction of plasma with aerolized sample results in degradation of individual elements each of which has a characteristic optical signal that can be detected spectroscopically. The capsules measured with magnetometer was opened and leached out with 3 ml HCl, 3 ml HNO₃ and 1 ml H₂O₂ at 80°C on hot plate for 72 hrs. Each digestion solution was made upto 50 ml. Three replicable solution of each digestion was prepared and analyzed.

4.4. Thermogravimetric Analysis (TGA)

The thermogravimetry analysis (TGA) was performed at in-house NETZSCH TG 209 F1 Libra (Fig. 4.6 (a)). The sample was loaded into aluminum crucible (Fig. 4.6 (b)). The mass of a substance is monitored as a function of temperature or time as the sample specimens are subjected to a controlled temperature program in a nitrogen atmosphere.

4.5. Total scattering experiments-xPDF

4.5.1. Setup

Synchrotron radiation is the radiation emitted by a relativistic charged particle under the action of a magnetic field. A series of particle accelerators accelerate electrons generated by the electron gun before being injected into the large storage ring. As the electron passes through each bending magnet, it loses energy as light, which is

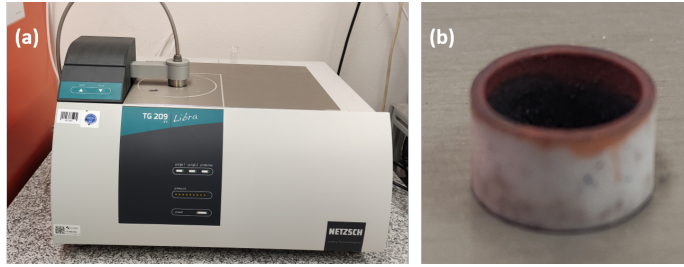


Figure 4.6.: (a) The NETZCH TG 209 F1 Libra at Forschungszentrum Jülich GmbH in which (b) the aluminium crucible loaded with sample is placed in nitrogen atmosphere to obtain TGA curves.

channeled out of the storage ring into the beamline stations. A typical synchrotron consists of a storage ring through which electrons circulate, passing through several bending magnets and undulators.

The synchrotron x-ray pair distribution function (xPDF) measurements were conducted at several beamlines:

- MS-x04SA beamline at Swiss Light Source, Paul Scherrer Institute (PSI) in Switzerland operates in the energy range 5 - 40 keV, with flux at 12 keV around 2×10^{13} photons/s [135]. The experiments used a wavelength $\lambda = 0.432$ Å. The intensities were collected by a rapid MYTHEN II point detector with a maximum resolution of 3.7 milli degree in 2θ , covering a range of 120° in 2θ as shown in Fig. 4.7 (a-b).
- P02.1 beamline at Petra III facility at DESY in Hamburg, Germany operates in the range up to 60 keV, with a flux of 4×10^{10} photons/s [136]. The operating wavelength is $\lambda = 0.232$ Å. The intensities were collected using a 2D Dectris Pilatus detector which provided powder averaged rings as shown in Fig. 4.7 (c-d).
- The experiments at 11-ID-B beamline, Advanced Photon Source (APS) in Argonne National Laboratory, USA operates in the range 58.6 keV-86.7 keV, with a flux of 2.3×10^{12} photons/s at 58.6 keV. The experiments were conducted using wavelength $\lambda = 0.2115$ Å. The intensities were collected using a 2D detector. This research used resources of the Advanced Photon Source, a U.S. Department of Energy (DOE) Office of Science User Facility, operated for the DOE Office of Science by Argonne National Laboratory under (GUP-69551).

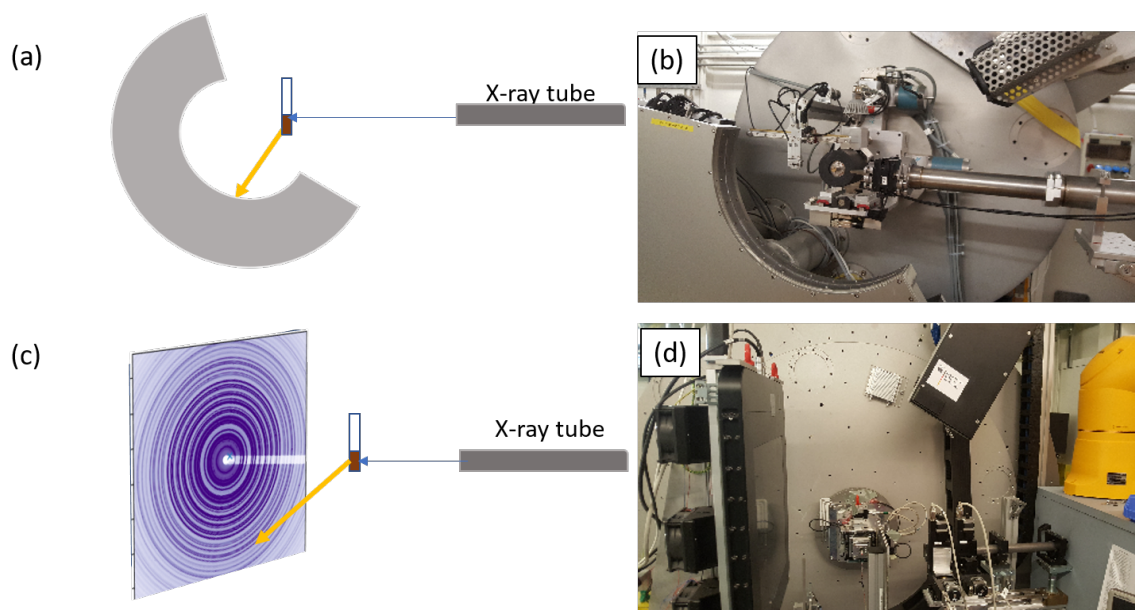


Figure 4.7.: xPDF setup: (a) schematic and (b) actual Mythen-II point detector at PSI, SLS. (c) Schematic and (d) actual 2D detector at DESY, Hamburg.

4.5.2. Sample preparation

IONP dispersions were dried at ambient conditions and filled in quartz capillaries for SLS measurements (see Fig. 4.8 (a)). For DESY measurements, IONP samples were dried and filled in Kapton capillaries and sealed with glue/clay (see Fig. 4.8 (b)). The DBNPs were filled in Kapton capillaries directly as dispersions for measurements at APS. The bulk samples of various iron oxides and gold powder obtained from Sigma Aldrich were measured as a reference.

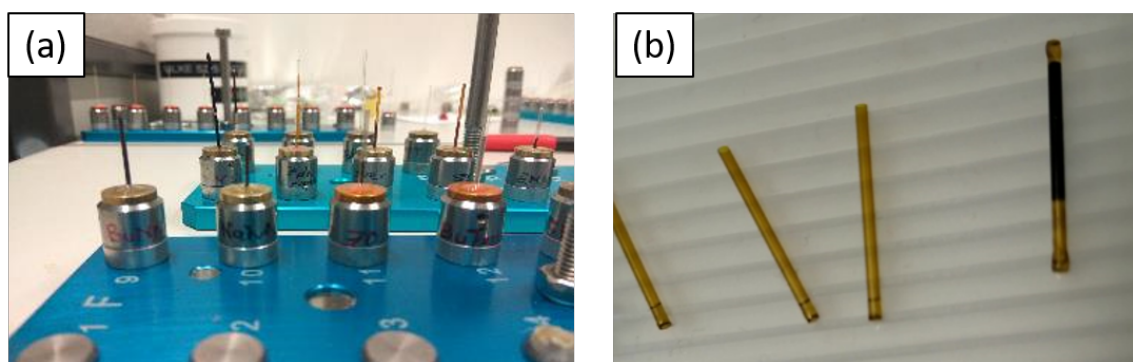


Figure 4.8.: (a) The quartz capillaries used at SLS and (b) kapton capillaries used at APS and DESY.

4.5.3. Data acquisition

The 2D data is treated using principles and equations mentioned in sections 2.6.4 and 2.6.5. In the case of 2D detectors, *GSAS-II* is used to obtain measured intensity as a function of Q . The background includes measurements of the empty capillary, solvent and dark current. The standard Ni bulk, LaB₆ and CeO₂ were measured to estimate the beam centers of 2D diffraction patterns and resolution of the instrument (Q_{damp} and Q_{broad}). The measurements were carried out at room temperature in ambient conditions. The scattering structure factor $\mathcal{S}(Q)$, reduced scattering $\mathcal{F}(Q)$ and PDF $G(r)$ with the corrections for background scattering, x-ray transmission and Compton scattering are obtained from the same diffraction data using *PDFgetX3* [137]. The obtained PDF was fit using *PDFgui* [138].

4.6. Small-angle x-ray scattering (SAXS)

4.6.1. Setup

Small-angle x-ray scattering (SAXS) was performed at the high brilliance laboratory instrument the Gallium Anode Low Angle X-ray Instrument (GALAXI), which is operated by JCNS, Forschungszentrum Jülich GmbH [139]. The sketch of the components and photograph of the instrument are as shown in the Fig. 4.9. The x-ray source uses liquid metaljet of GaInSn alloy as anode. The electrons of 200 W power hits the metal jet and x-rays are produced. The parabolic optics are used to obtain parallel, monochromatic beam with Ga K_α radiation of wavelength 1.34Å. At the sample position flux of 1×10^9 photons/mm² · s is received. The sample position, with two rotational and two translational degrees of freedom can be adjusted. There is a second holder, 140 mm in front, containing all samples for calibrating the beam. The x-ray path is completely evacuated and 2D position sensitive Pilatus 1M detector with 169 x 179 mm² active area collects the scattered intensity. The samples were studied in two distances, the large sample-to-detector distance LSDD (3535 mm) and short sample-to-detector distance SSDD (835 mm) in order to cover Q -range of 0.004-0.3 Å⁻¹.

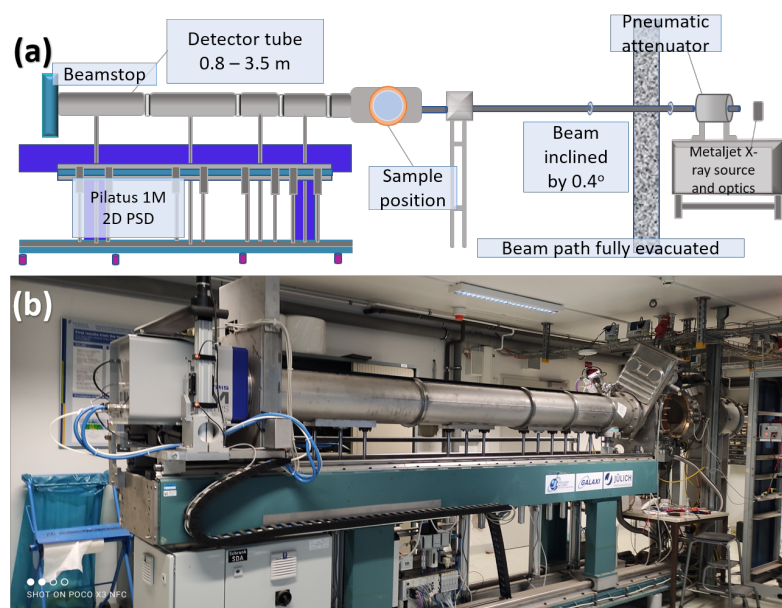


Figure 4.9.: (a) Schematic of GALAXI setup with its components, here the x-ray source is on the far right separated by the wall to the other components including optics to align the beam, evacuated detector tube and 2D position detector on the left. (b) Photograph of the GALAXI setup at JCNS, Forschungszentrum Jülich GmbH.

4.6.2. Sample preparation

The IONPs and DBNPs dispersed in toluene were filled in borosilicate capillaries of 2 mm in diameter with a wall thickness of 0.05 mm. These capillaries were sealed shut by oxygen flame. To ensure no leakage, the ends of capillaries were double sealed with hot glue. For measurements in magnetic field, capillaries of length 4-5 cm with above specifications were used.

4.6.3. Data acquisition

Permanent magnets were used to produce a magnetic field of 0.9 T to induce self-assembly. The field is generated horizontal to the capillary and perpendicular to incoming beam. A 4-5 cm capillary is inserted vertically into the holder as shown in Fig. 4.10 (a). However, to measure samples without field, the magnet holder was replaced with a holder shown in Fig. 4.10 (b). Here several NP dispersions in capillaries in horizontal position are measured. The 2D data was collected at 5 different vertical positions of the detector to obtain a merged image. The calibrants silver behenate (AgBH) and fluorinated ethylene propylene (FEP) were measured to

obtain the beam center of the direct beam and to calibrate the intensity in absolute units (cm^{-1}), respectively. Empty capillary and the toluene samples are measured to obtain the thickness and buffer subtraction. The transmitted sample intensity is given by

$$I_S = I_{S+EC} - T_S I_{EC} \quad (4.1)$$

where, I_{S+EC} and I_{EC} is measured intensity of nanoparticle dispersion in a capillary and empty capillary, respectively. T_S is the sample transmission ratio. *FIT2D* along with python routine are employed to center, mask, reduce and integrate the 2D SAXS pattern. The radially averaged intensities are further fit to models available on *SasView* software package [140].

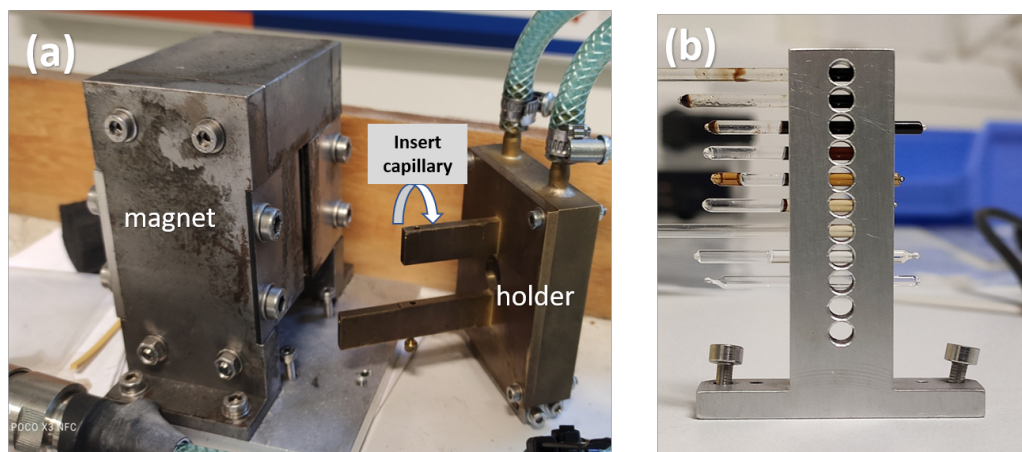


Figure 4.10.: (a) The magnetic field setup includes magnet of 0.9 T on (left) and the holder on (right) to insert capillary of about 4 cm vertically. (b) The sample holder setup to load capillaries for zero field measurements.

4.7. Small-angle neutron scattering (SANS)

Neutrons are produced in fission reactors or spallation sources. In fission reactors, the chain reaction is triggered when slow neutron is captured by uranium. In spallation sources, high energy protons are accelerated to neutron rich targets. Further, the spallation sources offers a precise time structure on the neutron beam due to the well defined relationship between incoming proton and exiting neutrons.

4.7.1. Setup

KWS-1 is the SANS beamline instrument operated by the Heinz Maier-Leibnitz Zentrum (MLZ) in Garching, Germany [141]. Figure 4.11 (a) presents the main components of the SANS setup at KWS-1, which includes a neutron chopper to select the required wavelength (5 \AA), followed by a long collimation chamber with movable neutron guides to adjust sample-to-detector distances, a sample table for conventional SANS and a non-magnetic hexapod to carry heavy magnetic field setups. It consists of a large 2D position-sensitive detector with an average pixel size of $0.35 \times 0.35 \text{ mm}$. The exit point of the neutron beam just after it strikes the sample is photographed in Fig. 4.11 (b). The instrument is optimised for high resolution measurements with wavelength spread $\frac{\Delta\lambda}{\lambda} = 10 \%$ for the neutron velocity sector. The maximum neutron flux hitting the sample is $1 \times 10^8 \text{ neutrons/cm}^2\cdot\text{s}$. The covered Q range extends from 0.007 \AA^{-1} to 0.5 \AA^{-1} that accounts for size in the range between 10 \AA - 9000 \AA . In the SANSPOLE setup, an additional Fe/Si supermirror and RF spin flipper are installed before the collimation line. All measurements are carried out in ambient conditions.

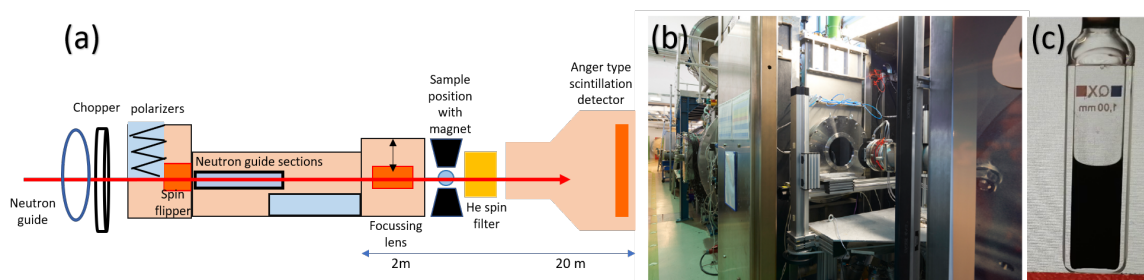


Figure 4.11.: (a) Schematic of the SANS setup at (b) KWS-1 at MLZ, Garching, adapted from [141] and (c) Hellma cells in which dispersions are filled.

4.7.2. Sample preparation

- **IONPs:** Among the six IONPs, F20 and F27 were prepared in several concentrations ranging from 2 - 9 mg/ml. The F27 IONPs are dispersed in 100 %, 78 %, 56 % and 0 % deuterated toluene for contrast variation studies. Additional contrast variation experiments were performed remotely at Spallation Neutron Source (SNS)-Oakridge. Here, F20 and F27 IONPs were measured in two different contrasts (100% d-and 0% h-toluene).
- **DBNPs:** All four DBNPs were measured in original concentration. The original

concentration of the four DBNPs were fairly equal, $\sim 5 - 8$ mg/ml for Au and $\sim 7 - 10$ mg/l for Fe in 100 % h-toluene. Contrast variation experiment was carried out on A10F14 DBNP in one contrast (78 % d-toluene).

4.7.3. Data acquisition

All MNPs were filled in 1 mm wide quartz Hellma cells. The measurements were carried out at room temperature with a wavelength of 5 Å. The dark current, empty cell and only solvent were measured for background corrections. Plexiglas (PMMA polymer) was measured to account for the detector sensitivity.

- **Beamtime with IONPs:** A vertical magnetic field in the range 0-2.2 T was applied to Hellma cells containing IONPs, perpendicular to the neutron beam. The unpolarized SANS data were collected at three sample-to-detector distances; 14 m, 8 m and 2 m. The scattering intensities were collected for 1 hour at every field point. The field is varied from 0 to 2.2 T and back to 0 T to verify the reversible formation of assemblies. For SANS POL measurements, the data was collected for 1 hour at various field points.
- **Beamtime with DBNPs:** A horizontal magnetic field in the range 0-3 T was applied to Hellma cells containing DBNPs, perpendicular to the neutron beam. The unpolarized SANS data were collected at two detector distances; 8 m and 20 m. The scattering intensities were collected at each magnetic field point for 600 seconds. In one case, the field is varied from 0 to 3 T and back to 0 T to verify the reversible formation of assemblies. In the second case, the time dependence is observed by fixing the field for 1 hour and collecting data every 600 seconds. SANS POL data is collected at saturating 1 and 3 T magnetic fields for 1200 seconds at each polarization state.

4.8. Reverse Monte-Carlo simulations

Reverse Monte Carlo (RMC) modeling is a widely used method to solve inverse structure-related problems in condensed matter physics. Here, we describe numerical modeling using RMC to simulate the 2D SANS patterns as shown in Fig. 4.12 (a). A typical simulation starts with assuming a random initial configuration of particles in a box under periodic boundary conditions where particle wall interactions are included. The size of the box L , is obtained from the minimum value of Q given by

$L = \frac{2\pi}{Q_{min}}$. The total number of particles N in RMC are fixed based on the particle concentration and Q_{min} (Fig. 4.12 (b)). In the case IONPs, the box is assumed to contain core-shell spherical particles with fixed values of diameter and polydispersity obtained from other experiments. Simulated intensity is calculated as

$$I_{sim}(\vec{Q}) = \left| \sum_{j=1}^N F_{core-shell} \exp(-i\vec{Q} \cdot \vec{r}_j) \right|^2 \quad (4.2)$$

where \vec{Q} is the scattering vector and $F_{core-shell}$ is form-factor of the core-shell particles (as seen in chapter 2, eqn. (2.122)). Individual Monte Carlo steps are performed by randomly choosing a particle and moving it in a box. Each step entails one of the three randomly chosen actions given by A, B and C in Fig. 4.12 (b);

1. **Linear:** the particle moves in a straight line with a step size that is twice the diameter.
2. **Jump:** The particles makes a jump in a close contact to another randomly chosen particle.
3. **Orbit:** The particle makes orbits around a neighbouring particle

In all three cases, the action with particle overlap is avoided. A classic Metropolis algorithm is used to decide the acceptance of each step [142]. The acceptance depends on the reduced value of χ^2 , which is the difference between simulated and experimental intensity, at every step. The full code currently available on <https://github.com/lestercbarnsley/SasRMC>

4.9. Conclusion

Direct imaging techniques (TEM and SEM) provide information about the shape and morphology of the NPs. The composition is determined through structural analysis of xPDF data. Temperature and field-dependent magnetization studies reveal the macroscopic magnetic properties. In this work, SAXS and SANS are used in zero and applied magnetic fields to obtain NPs' structural and collective behavior in dispersions. The length scales in these experiments combine the range from nanometers to micrometers suited to observe a large variety of self-assembling systems. Parameters including size, composition, morphology, surfactant coating around nanoparticles and

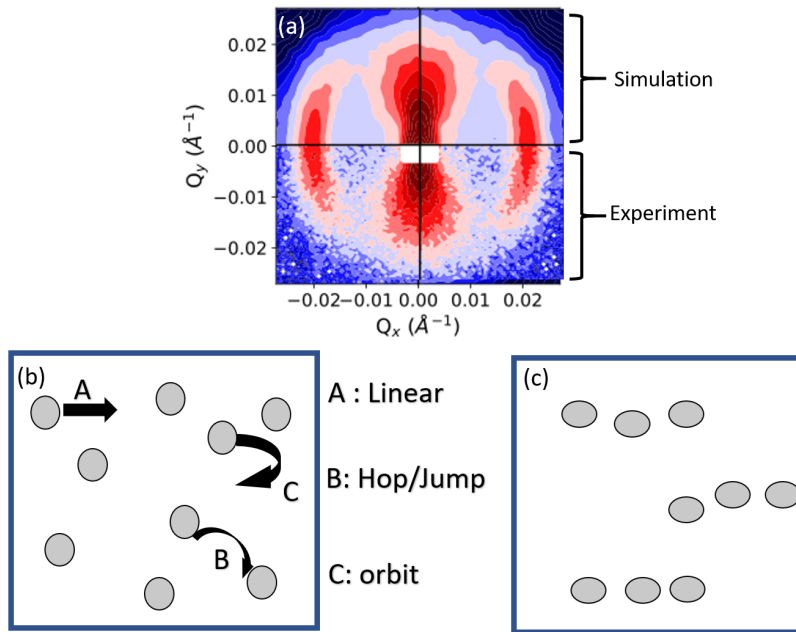


Figure 4.12.: (a) 2D SANS simulated patterns (top) and experimental (bottom) patterns. (b) The initial configuration of the box with particles and random motions described as A, B and C. (c) Particles after fitting experimental 2D pattern.

magnetic properties are obtained by a combination of techniques summarized in Fig. 4.13.

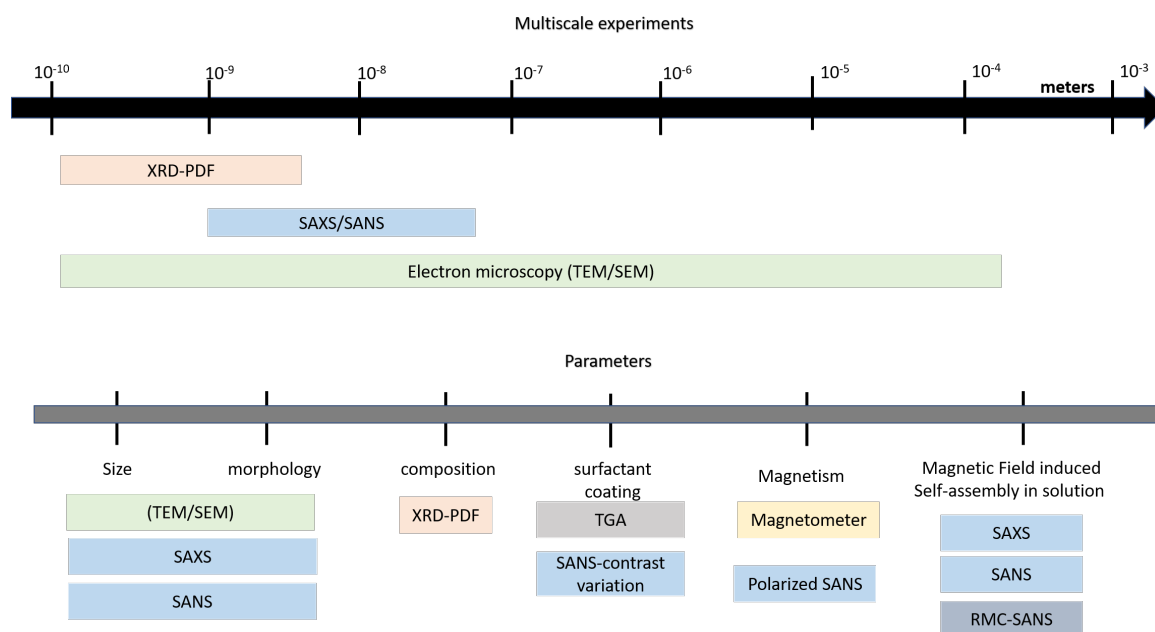


Figure 4.13.: Summary of the multiscale experiments and range of parameters probed with experiments.

5. Self-assembly in single phase IONPs as a reference to dumbbells

5.1. Introduction

To investigate self-assembly mechanism in complex multi-component dumbbell nanoparticles (DBNPs) where Au is attached to iron oxide nanoparticles (IONPs), we first conduct reference studies on isolated IONPs. The self-assembly of IONPs is driven by the balance of attractive (dipolar, magnetic and van der Waals) and repulsive (electrostatic and steric) forces [143]. These forces further depend on several factors such as the size, particle geometry, concentration, composition, thickness of the organic molecules attached to the surface of IONPs, temperature and the applied magnetic field. In the presence of a magnetic field, the spherical core-shell IONPs were previously shown to self-assemble into a 1D, 2D or 3D structures [144, 145, 7]. In this chapter, we investigate parameters in IONPs which may also influence the formation of assemblies in DBNPs. The major part of the following results described in the chapter are published [14].

5.2. Samples and synthesis

The summary of the IONPs obtained from different laboratories, both commercially and specifically synthesized, are presented in Table. 5.1. The commercially synthesized IONPs labelled F05 and F10 dispersed in hydrogenous toluene were purchased from Nanomaterials and Nanofabrication laboratories (NN labs), F21 and F24 were obtained from OceanNanotech laboratories. Spherical IONPs labelled F20 and F27 were specifically synthesized through user program proposal at Center for Integrated Nano Technology (CINT), Los Alamos National Laboratory (LANL) and Sandia National Laboratories. The extended LaMer mechanism used to synthesize these particles yielded a large quantity of highly-crystalline nanoparticles with a narrow size

distribution [146]. The method first includes synthesis of iron (III) oleate precursor which is obtained through vigorous stirring of the mixture containing 3.3 g (9.3 mmol) of $\text{Fe}(\text{acc})_3$ and 15 ml (47.3 mmol) of oleic acid in nitrogen atmosphere at 320 °C in a molten metal bath. Intermediate iron (II) oleate is formed at 290 °C but thirty minutes after this temperature is attained, the reaction was removed from heat bath and quenched. The precursor thus formed is used without further purification. A syringe loaded with as synthesized iron (III) oleate precursor diluted in octadecene solution is dripped at rate of 3 ml/h into the reaction flask containing the stirred mixture of 2.5 g of docosane and 2.5 ml oleic acid at 350 °C. The nucleation event was observed with an instantaneous change in the color of the reaction solution from dark brown to black. Aliquots were withdrawn from the reaction as close as possible to the nucleation event, and at periodic intervals thereafter. Particle sizes are controlled by varying reaction duration and volume of added precursor. This modified approach results in reproducible synthesis with precise control for larger sizes of IONPs. The reference samples, Fe(II, II) oxide nanoparticles bulk powder and F50 nanoparticles with a wide size distribution (50-100 nm) were obtained from Sigma Aldrich.

Table 5.1.: Summary of commercial and synthesized IONPs with their corresponding sample IDs, diameters D and polydispersity (%) obtained from TEM analysis.

Source	Sample ID	Diameter (nm)	Polydispersity (%)
NN-labs	F05	5.2 ± 0.6	12
NN-labs	F10	9.5 ± 0.9	9
Los Almos	F20	20.1 ± 1.9	9
Oceannanotech	F21	21.1 ± 1.5	7
Oceannanotech	F24	24.3 ± 2.2	9
Los Almos	F27	26.2 ± 2.1	8

The advanced LaMer mechanism used to synthesize F20 and F27 resulted in a large quantity of IONPs. This makes it suitable for both neutron scattering experiments and potential industrial applications. The specifically synthesized particles are dark brown and jelly-like in appearance with original concentration of 45 mg/ml. The IONPs were scooped and dispersed in toluene for scattering experiments in appropriate concentration. The commercially synthesized IONPs nanoparticles were obtained in already dispersed state and appear as dark brown in original concentration of 25 mg/ml.

5.3. Shape size and crystallinity

The shape, size and crystallinity of IONPs are visualized using TEM and in high resolution TEM (Fig. 5.2 (a-f) and insets).

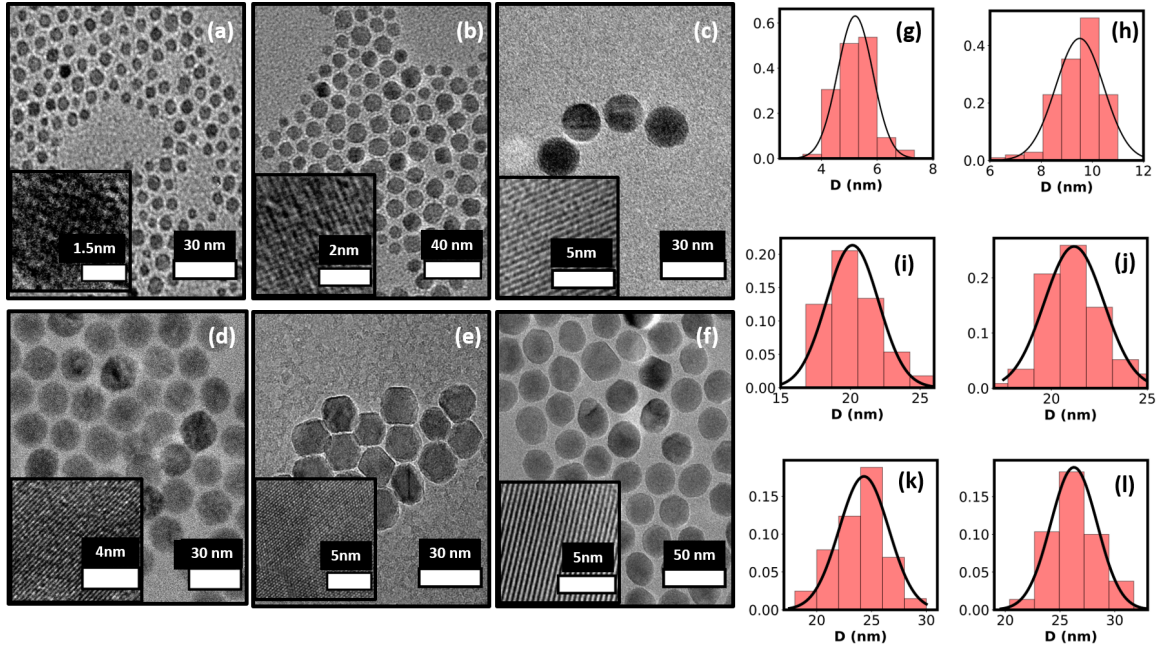


Figure 5.1.: TEM and normal size distribution of (a and g) F05, (b and h) F10, (c and i) F20, (d and j) F21, (e and k) F24 and (f and l) F27 IONPs. The high resolution TEM micrographs in the bottom inset.

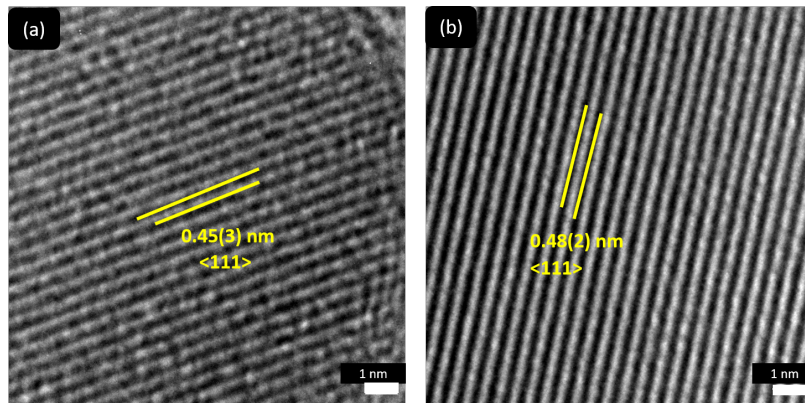


Figure 5.2.: High resolution TEM micrographs of (a) F20 and (b) F27 IONPs. The crystalline lattice spacing corresponds to $\langle 111 \rangle$ crystal plane.

The diameters of IONPs from TEM are determined using *ImageJ* software. The normal size distributions reveal the polydispersity of the samples (Fig. 5.2 (g-l)).

These distributions are a number weighted average as opposed to the volume weighted averages in scattering techniques. The crystalline planes are visible in the case of F20 and F27 proving that IONPs with LaMer technique are fairly monodisperse of high crystalline quality. The crystalline lattice spacing of F20 and F27 is 0.45(3) nm and 0.48(2) nm, respectively which corresponds to $\langle 111 \rangle$ plane. The Table. 5.1 summarizes the diameters and polydispersities of the IONPs obtained from TEM.

5.4. Composition and local structure

Synchrotron x-ray PDF measurements were conducted on selected IONPs in order to probe the composition and local crystal structure. To compare lattice constants, total scattering experiments were also carried out on the reference samples including 50 nm nano (F50) and bulk iron (II and III) oxide powders from Sigma Aldrich. Several phases of iron oxides may coexist in IONPs which is well documented in the literature [147, 148, 149, 150, 151, 152]. The possible phases are antiferromagnetic FeO (wüstite), ferrimagnetic Fe_3O_4 (magnetite), antiferromagnetic $\alpha\text{-Fe}_2\text{O}_3$ (hematite) and ferrimagnetic $\gamma\text{-Fe}_2\text{O}_3$ (maghemite). Refinements of the structure models at 300 K against PDF data sets were done in the range of 1 to 40 Å using the program *PDFgui*. The instrument resolution Q_{damp} and Q_{broad} was obtained by refinement of the standard calibrant data and fixed to refined value of 0.033 and 0.007, respectively, for other data sets. The quality of the fits are shown in Fig. 5.3. The best fit of the experimental data for F20 and F27 samples was obtained by the model including two phases: maghemite (*P4332* ISCD-79196) and magnetite (*Fd-3m* ISCD-65339). The best model for F20 and F27 includes a mixed composition of magnetite and maghemite. The atomic displacement parameter (ADPs) were constrained according to atom type and chemical environment; for example ADPs for Fe-atoms in tetrahedral site in magnetite were constrained to refine as one parameter, and Fe atoms at octahedral site as another. The scale factor, lattice constants, ADPs and linear atomic correlation factor δ_1 were refined for each phase in the range of 1–40 Å. Detailed information about all refined parameters in Appendix A.2. The lattice constants of two phases in the MNPs are reduced compared to their bulk counterparts. Such finite-size effect has been previously reported for metallic NPs [153]. During refinements of PDF data for F20 and F27 particles, the coordinates of all atoms were fixed to the bulk values. There are indications of local disorder and anti-phase boundaries due to deviation from model at $r < 12$ Å as seen in F20.

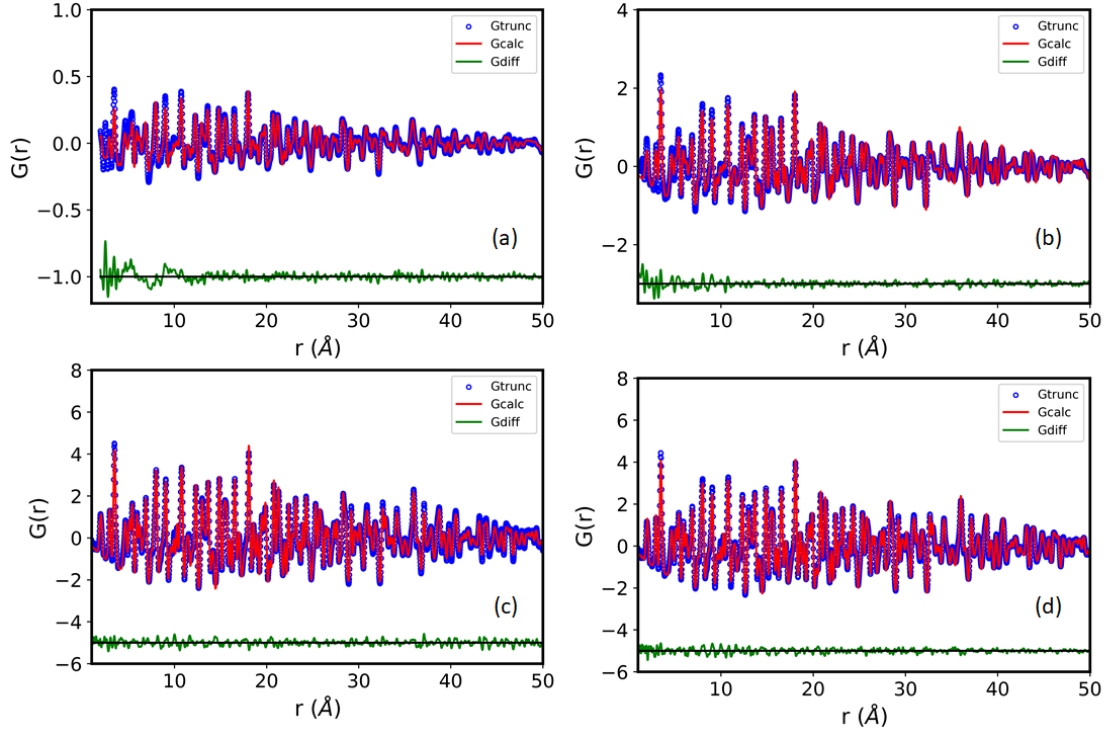


Figure 5.3.: The best refinements of PDF data for (a) F20 (b) F27 (c) F50 MNPs and (d) magnetite powdered bulk, with experimental data in open circles, calculated pattern in red and difference curve in green.

Table 5.2.: Summary of the xPDF refinement fits of F20, F27, F50 and Bulk reference sample. The fits yield lattice constants scale, a , δ_1 , atomic displacement factors U_{iso} , mass percentage of the phases.

Samples	F20		F27		F50	Bulk iron-oxide
Phase	γ -Fe ₂ O ₃ ^(a)	Fe ₃ O ₄ ^(b)	γ -Fe ₂ O ₃	Fe ₃ O ₄	Fe ₃ O ₄	Fe ₃ O ₄
crystal structure	P4332	Fd-3m	P4332	Fd-3m	Fd-3m	Fd-3m
a [Å]	8.37(6)	8.34(3)	8.355(7)	8.349(6)	8.372(1)	8.379(1)
mass (%)	30	70	34	66	100	100
R_w	0.216		0.169		0.135	0.117

$Q_{damp} = 0.032 \text{ \AA}^{-1}$, $Q_{broad} = 0.008 \text{ \AA}^{-1}$, $Q_{max} = 23 \text{ \AA}^{-1}$ for F20 and F27 and $Q_{max} = 28 \text{ \AA}^{-1}$ for references, ^(a) fit using cif file ICSD-79196, ^(b) fit using structural file obtained from standard database ICSD-65339. Details about the fit parameters available in Appendix A.2.

Both the IONPs contain magnetite and maghemite with reduced lattice constant to bulk magnetite and nanopowders of large size.

5.5. Magnetic properties

The zero field (ZFC) and field cooling (FC) magnetization data of the IONPs subjected to an applied magnetic field of 0.01 T are plotted as a function of temperature in Fig. 5.4. The blocking temperature, T_B , depends on the size, concentrations, composition and size distribution and can be obtained from ZFC-FC curves. In non-interacting samples, the average T_B corresponds to the peak temperature in ZFC curve. In monodisperse identical NPs, the T_B is related to energy barrier. However, in real systems there is an energy barrier distribution due to presence of polydisperse particles. Even with identical particles, random orientation of the easy axis can result in energy barrier distribution. Thus, the polydispersity in F10 IONPs, results in the shift of peak temperature from the splitting point of ZFC-FC curves. As expected, the peak of the ZFC curve shifts to higher temperatures with increasing size of the IONPs. The ZFC and FC curves coincide at highest measured temperature (300 K) for F05, F10, F20 and F21, unlike F24 and F27 where they continue to remain split. Since magnetometer can reliably measure T_B only up to room temperature, one can estimate that $T_B > 300$ K for F24 and F27. The appearance of peak temperature can be understood as follows. Particles are first cooled in zero field to low temperatures below peak temperature where moment is zero. When a small field is applied, the particles with T_B lower or equivalent reaches a thermal equilibrium. With increasing temperature, the net moment increases as more particles reach equilibrium and are unblocked. Since all moments are unblocked at the peak temperature any increase will result in lowered net moment. The FC curves are obtained by cooling the sample in a small applied field. In this case NPs are subject to an effective field which is the sum of the applied field and interaction field. By introducing such mean field approximations to SPM models, the FC curves show a reduction in net magnetic moment with temperature [154]. Indeed such interactions may exist in F20, F21, F24 and F27 where we observed a lowered or fairly constant FC curve with temperature compared to F05 and F10. We further note the similarity in ZFC-FC curves of particles obtained from the same source indicating that the synthesis and presence of complex magnetic phase may play a critical role to describe various shapes of the ZFC-FC curve. Previous reports have confirmed antiferromagnetic phases for ZFC-FC curves that resembles F21 and F24 [155]. The XPDF results confirms magnetite and maghemite in F20 and F27 with no indication of wüstite phase. This phase may exist in F21 and F24 and is yet to be determined. The concentration of the IONPs in

all measurements are around ~ 5 mg/ml. The metal-insulator transition usually found

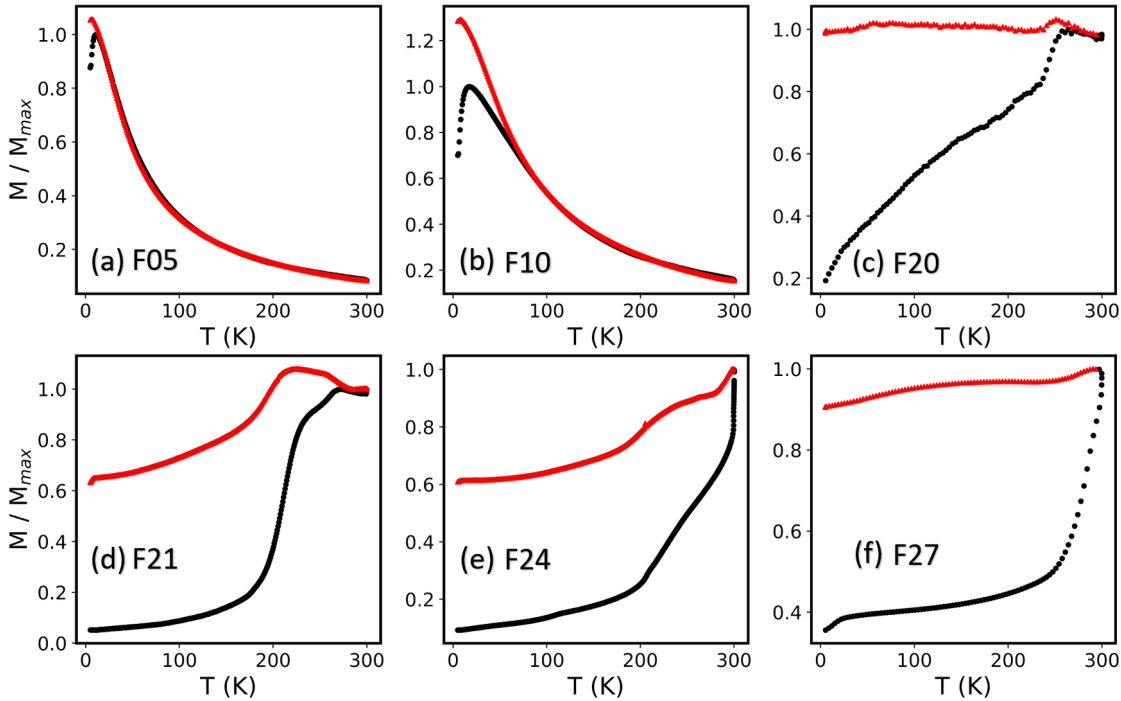


Figure 5.4.: ZFC (●) and FC (▲) magnetization in an applied field of 0.01 T as a function of temperature for (a) F05 (b) F10 (c) F20 (d) F21 (e) F24 (f) F27 IONPs.

in strongly correlated magnetite Fe_3O_4 is characterized by the first order structural Verwey transition temperature that occurs at around 124 K. However, it is worth noting that despite the presence of magnetite phase in the analyzed IONPs, as quantified from the xPDF, there are no evident signs of Verwey transition in our IONPs. This transition exists in F50 nanopowders as a cusp around 110 K which is clearly visible in the ZFC magnetization (Fig. 5.5 (a)). Thus, it is conclusive that Verwey transition is suppressed in our samples for IONPs with diameters smaller than 50 nm. Occurrence of Verwey transition still remains an open question in nano regime due to the difficulty in the size dependent stoichiometric control. According to existing literature there are still conflicts in the critical size below which Verwey transition is suppressed [156, 157, 158, 159]. The T_B is calculated using eqn(2.56) and plotted as a function of diameter in Fig. 5.5 (b). Here, the solid blue and red lines is the calculated T_B , assuming bulk anisotropy constants for magnetite ($K_{\text{magnetite}} = 1.3 \times 10^4 \text{ J/m}^3$) and maghemite ($K_{\text{maghemite}} = 8000 \text{ J/m}^3$), respectively. The calculated T_B is lower compared to the experimentally measured temperature for respective sizes

in all cases. There are several reasons for this discrepancy. The effective anisotropy constant in IONPs can be higher compared to the bulk values, as it was observed for Co NPs [160]. However, no existing literature was found that discussed large values of anisotropic constants for magnetite or maghemite in spherical IONPs. In the SW model, the T_B in eqn.(2.56) is calculated assuming no inter-particle interaction for particles in superparamagnetic regime. An appropriate explanation for the increase in T_B can then be accounted to the presence of magnetic dipole-dipole interactions. In F27, even with dilution the T_B remains greater than 300 K. The energy of magnetic dipole-dipole interactions (E_{int}) increases the energy barrier $\Delta E = K_{eff}V + E_{int}$ and consequently the T_B [161, 162]. The magnetization is measured as a function of magnetic field at temperature $T = 5$ K and $T = 300$ K as shown in Fig. 5.6 (a) and (b), respectively. The measured saturation field is around the bulk value of 0.2 T for all samples, except for F24 at 0.5 T. The FC-DC magnetization curves measured with an applied field of 1 T revealed a finite coercive field that is evident for all samples at 5 K (Fig. 5.6 (a) inset). This value is the largest for F21. In contrast at 300 K, the coercive field becomes negligible (Fig. 5.6 (b) inset) for all samples but a finite value for F27 and F50. It appears that the temperature-dependent magnetization measurements demonstrate that the particles remain blocked at 300 K for F24, F27 and F50. The coercive fields (H_{c1}) and exchange bias fields (H_{EB}) determined from the DC magnetization curves are summarized in Table 5.3. This is plotted as a function of diameter in Fig. 5.6 (c) and 5.6 (d) at 5 K and 300 K. The exchange bias field (H_{EB}) measured at 5 K is the largest for F21 and origin in this sample is unclear. Possible explanation suggests presence of AF wüstite and ferrimagnetic magnetite phase.

5.6. Magnetic field induced self-assembly

5.6.1. Energy calculations

The influence of dipole-dipole interactions leading to changes in blocking temperatures is well documented in literature [163]. To quantify the phenomenon, the dipolar coupling strength (γ) and Bjerrum length, (λ_B) are introduced given by,

$$\gamma = \frac{\mu_0\mu^2}{2\pi k_B T D^3}; \quad (5.1)$$

$$\lambda_B = \gamma^{1/3} \quad (5.2)$$

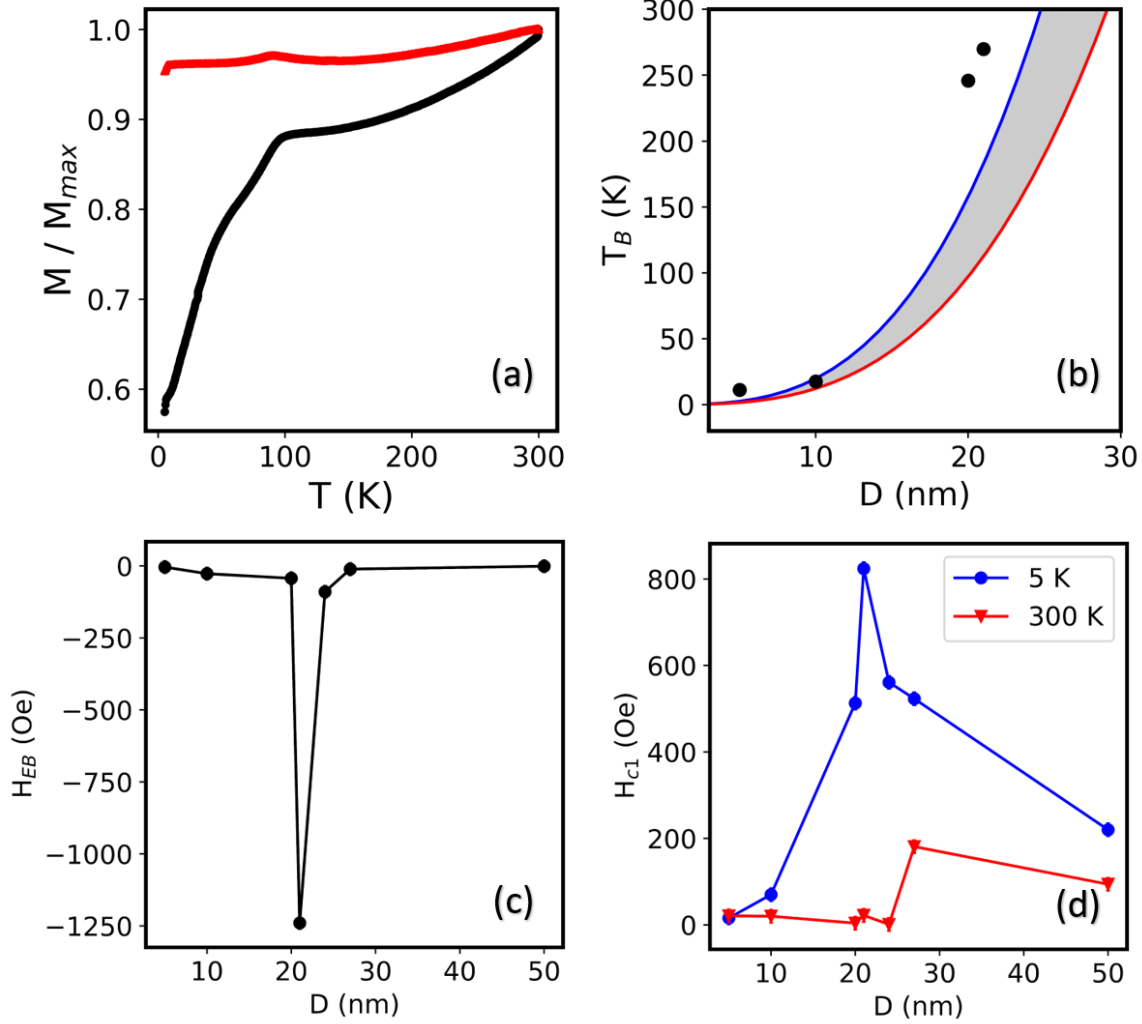


Figure 5.5.: (a) ZFC (\bullet) and FC (\blacktriangle) magnetization at 100 Oe as a function of temperature for F50. (b) The experimental T_B (\bullet) plotted as a function of particle diameter. The blue (magnetite) and red (maghemite) solid lines are calculated T_B using K . (c) H_{EB} plotted as function of diameter at 5 K and (d) H_{c1} as a function of particle diameter at 5 K (\bullet) and 300 K (\blacktriangledown). Solid lines are guides for the eye.

where, μ_0 is the vacuum permeability, μ is dipole moment calculated for bulk magnetite, k_B is the Boltzmann constant, T is temperature and D is the diameter of the IONP. Experiment results suggests that the $\gamma > 1$ for all IONPs except F05 as shown in Fig. 5.7 (a). The Fig. 5.7 (b) plots λ_B which is the length scale up to which dipolar interactions are dominant compared to thermal energies. Based on Langevin mean-field approximations, the chain formation in dilute dispersions is predicted to occur depending on the aggregation parameter N^* [164, 165]. This parameter is calculated

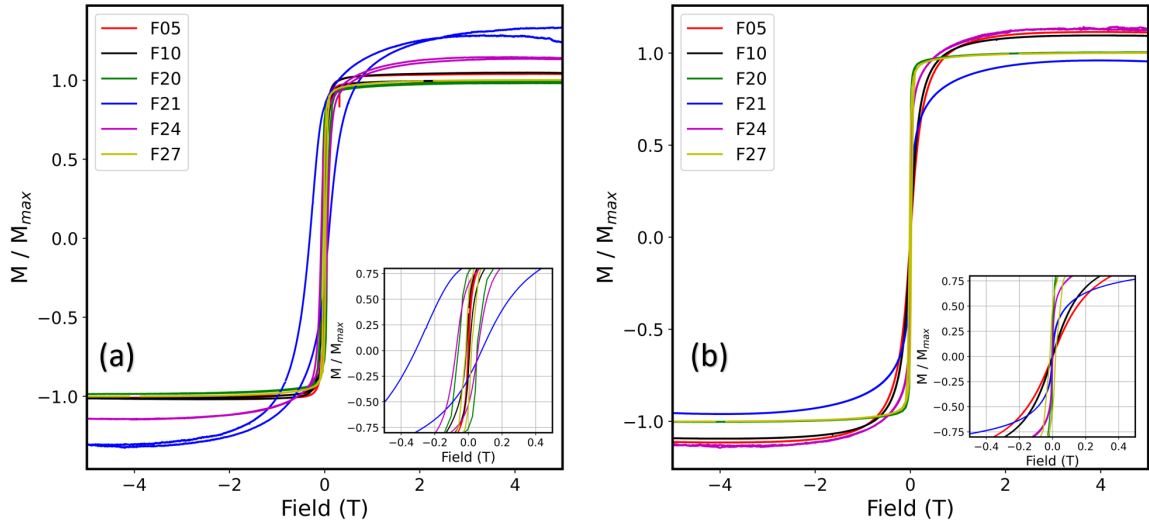


Figure 5.6.: DC magnetization as a function of applied magnetic field at (a) 5 K (b) 300 K. Inset shows the same (a) and (b) but expanded to show lower fields.

Table 5.3.: Summary of sample IDs, calculated blocking temperatures (T_B) for maghemite/magnetite and experimental values, exchange bias field (H_{EB}) at 5 K and coercive (H_{c1}) fields at 300 K. Other details can be found in the appendix.

Sample ID	Calculated T_B ^(a) (K)	Calculated T_B ^(b) (K)	Measured T_B (K)	H_{EB} (± 28 Oe)	H_{c1} ^(c) (± 20 Oe)
F05	2	3	10	4	21
F10	10	85	18	27	20
F20	99	160	250	43	4
F21	116	188	270	1156	22
F24	174	283	300	90	1
F27	218	355	>300	11	181
F50	1517	2465	>300	1	94

^(a) The blocking temperatures are calculated using eqn. (2.56) and using $K_{eff} = K_{maghemite} = 8000$ J/m³. ^(b) The blocking temperatures are calculated using eqn. (2.56) and $K_{eff} = K_{magnetite} = 1.3 \times 10^4$ J/m³, ^(c) residual field of 20 Oe present in the PPMS-DynaCool system.

from equation $N^* = \sqrt{\phi_0 e^{\gamma-1}}$, where ϕ_0 is the volume fraction of the IONPs. There are three possible scenarios to predict chain formation based on N^* even if $\gamma > 1$;

- $N^* < 1$: No formation of chains
- $N^* \sim 1$: Formation of equilibrium chains
- $N^* \gg 1$: Formation of non equilibrium chains that grow exponentially

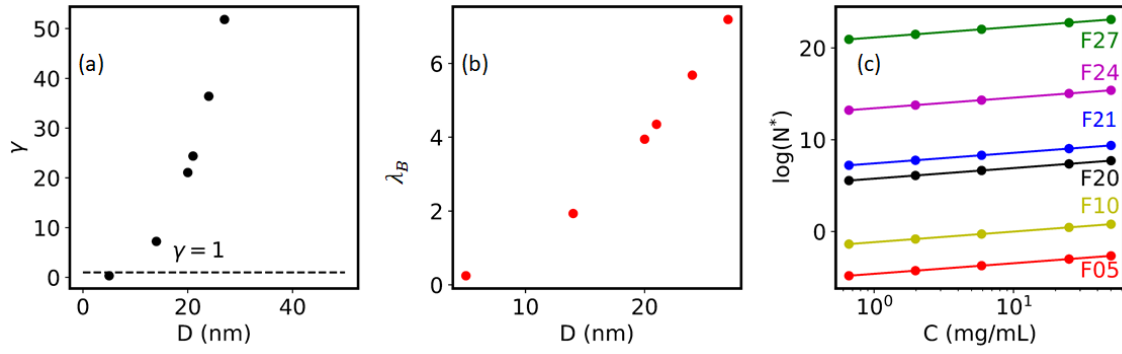


Figure 5.7.: (a) The dipolar coupling strength and (b) Bjerrum length plotted as a function of diameter. The aggregation parameter N^* plotted as a function of concentration for (c) F05, F10, F20, F21, F24 and F27 samples. Solid lines are guides for the eye.

As mentioned, in field directed assemblies the chain formation occur before 2D/3D assemblies [7, 94]. Since $\gamma < 1$ in F05 and $N^* < 1$ in F10, there should be no chain formation in these IONPs according to calculations. Moreover, IONPs of other sizes in the given concentrations are predicted to self-assemble into chains. The typical energies such as dipole-dipole, van der Waal, Zeeman and steric repulsion energies normalized to thermal energies are plotted as a function of distance between IONPs (Fig. 5.8) and formulas used can be found in the appendix C. Clearly, the energies involved in the formation of IONPs assemblies are dominated by magnetic field induced dipole-dipole interactions in field and dipole-dipole interactions at 0 T for distances larger than 1 nm. However, below 1 nm steric repulsion may dominate.

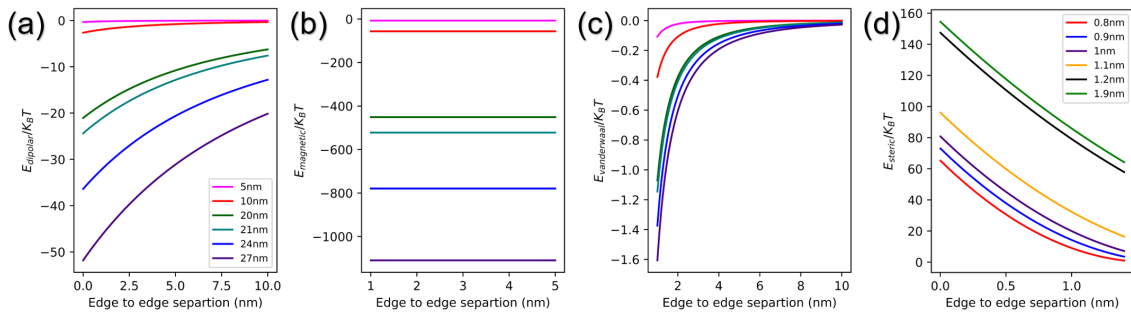


Figure 5.8.: (a) Dipole-dipole energies (b) van der Waal's (c) Zeeman energies calculated for F05, F10, F20, F21, F24 and F27 IONPs, and (d) steric energies calculated for F27 IONP with varying shell thickness ranging from (0.8 nm to 1.9 nm). All energies are plotted as a function of edge to edge separation between IONPs in assemblies.

5.6.2. Assemblies as function of size, concentration and magnetic field

SAXS and SANS techniques are employed to observe and investigate the type of assemblies formed in the IONPs. First, the SAXS scattering patterns are analyzed to determine the effect of size, concentration and field on the formation of assemblies. The 2D SAXS patterns at 0 T for different sizes in a fixed concentration of 25 mg/ml are visually isotropic, indicating no assemblies are formed in 0 T. On application of 0.9 T magnetic field, the 2D scattering pattern still remain isotropic for F05, F10, F20 and F21 as shown in Fig. 5.9 (a-d). In contrast, stripe patterns perpendicular to field direction appeared in F24 (Fig. 5.9 (e)) and F27 (Fig. 5.9 (f)). The 2D pattern at 0 T is reduced to radially averaged 1D intensities as shown in Fig 5.10 (a-b). The 1D data is fit to spherical form-factor in all cases except for F27 (fit parameters in Appendix A.3). In F27 IONP, there is a change in slope at low Q region with a small peak at $Q = 0.018 \text{ \AA}^{-1}$. The linear pearl model is used to describe F27 scattering curve which indicates the presence of small chains even at 0 T. The model describes the form factor for N spheres of radius R linearly joined by straight strings with negligible thickness. The edge separation parameter $d_{ETE} = d_{CTC} - D$, where d_{CTC} is the center-to-center distance between the particles and D is the diameter of IONP [166]. This anisotropy at $H = 0.9 \text{ T}$ is further pronounced in the 1D radial averages as shown in Fig. 5.10. There appears to be a size effect indicating assembly formation in IONP with diameters, $D > 21 \text{ nm}$, at fixed concentration and magnetic field. This is in sharp contrast to the prediction based on Langevin calculations of N^* . Since N^* also depends on concentration, IONPs were investigated in concentrations ranging from 1.9 mg/ml - 25 mg/ml. The SAXS data of self-assembling F24 and F27, at 0.9 T in different concentrations obtained by consequently diluting IONPs with toluene are as shown in Fig. 5.11 (a-b), respectively. For F24 IONPs the intensity of the peak is significantly reduced at concentrations below 1.98 mg/ml. On the contrary, the peak is clearly visible for F27 at similar concentration. The anisotropy in the 2D scattering pattern of F27 (Fig. 5.11 (b) top inset) diluted by a factor of 30 from its original concentration revealed the presence of structures which disappears in F24 for a similar dilution (Fig. 5.11 (a) top inset). This is further emphasized in the structure factor $\mathcal{S}(Q)$ obtained at various concentrations by dividing the experimental data by the form-factor intensity of a single nanoparticle form factor as shown in bottom insets of Fig 5.11. Here, decrease in $\mathcal{S}(Q)$ with concentration is more drastic for F24 compared

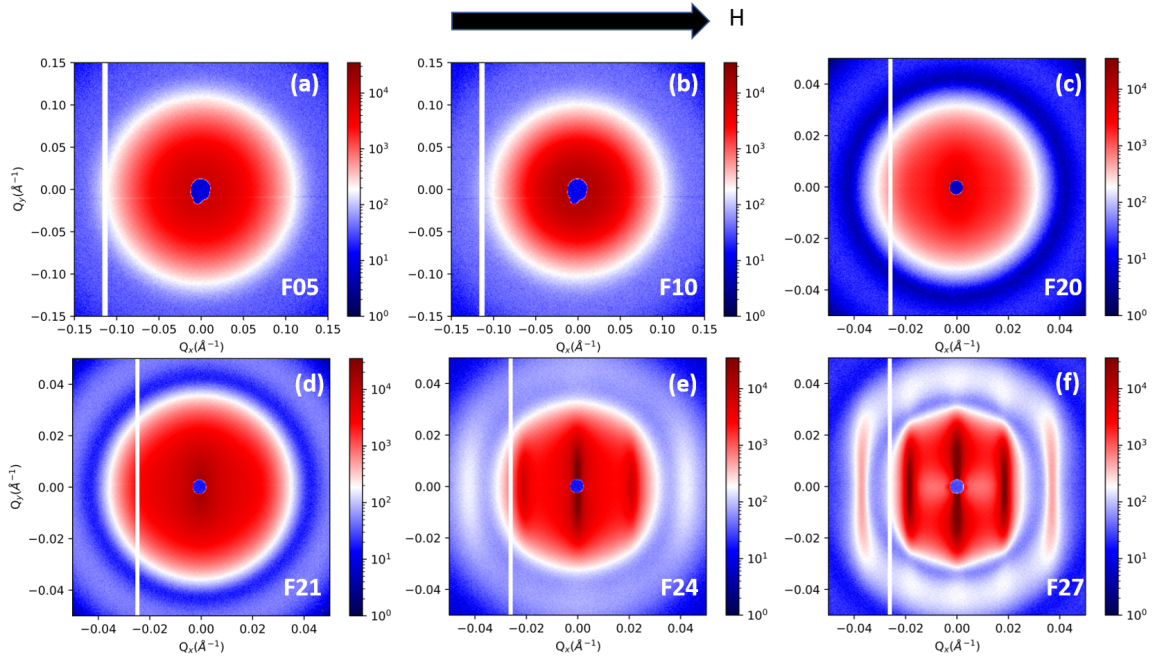


Figure 5.9.: 2D SAXS patterns at applied magnetic field, $H = 0.9$ T and in concentration of 25 mg/ml for (a) F05, (b) F10, (c) F20, (d) F21, (e) F24 and (f) F27 IONPs. The intensities are in log scale. The black vertical line in the pattern is the gap between two detectors which is masked during reduction of the data.

to F27 IONPs. The edge to edge separation ℓ extracted from linear pearl model fits plotted as a function of concentration in Fig. 5.11 (c), further highlighted this difference. The value of ℓ increases at lower concentration for F24, while remaining relatively constant for F27. Additionally, the ℓ in F27 IONPs is larger with magnetic field as compared to data at 0 T which is perhaps a counter-intuitive observation that will be treated in detail in the next section. The most critical aspect of concentration studies is another contradiction in the prediction that $N^* > 1$ implies chain formations, since chains are absent in F24 for concentrations below 1.9 mg/ml. Further, there are no signs of assembly formation in F20 even at highest concentration. This pertains to a critical question, what curtails formation of assemblies in these IONPs despite the predictions;

1. The calculations overestimate the magnetic moment by assuming bulk values of magnetite since NPs are known to have reduced magnetic moment due to internal magnetic structure. Polarized SANS can help determine the magnetic form-factor as will be shown in the next section. Such reductions could not

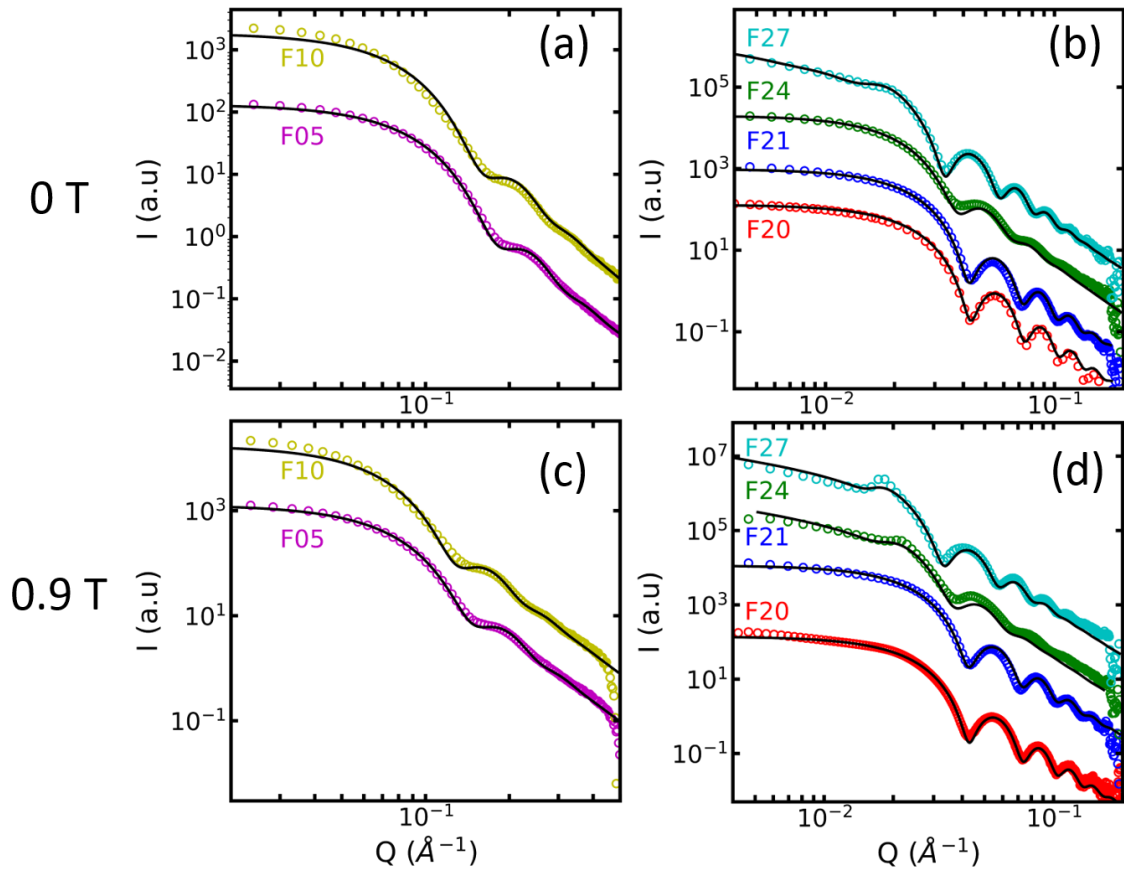


Figure 5.10.: The radially averaged SAXS data at (a),(b) 0T and (c)(d) 0.9 T for F05,F10, F20, F21, F24 and F27. The IONPs are fixed to concentration 25(2) mg/ml. The intensities are therefore scaled for easy visualizations. The open circle in respective colours are experimental data and solid black lines are fits to form-factor models as described.

be accounted for from those measurements to indicate lowered moment which inhibits the assemblies

2. Presence of repulsive forces originating from organic content coated around the NPs in the dispersion.

5.6.3. Formation of 1D chains

Surprisingly, increasing the interparticle interactions in F20 by increasing the concentration did not yield ordered assemblies. Two contrasting cases are discussed as follows: (i) F20 IONPs, where no chains were observed at high concentration and/or high field and (ii) F27 IONPs, where chains exist in low concentration and zero field.

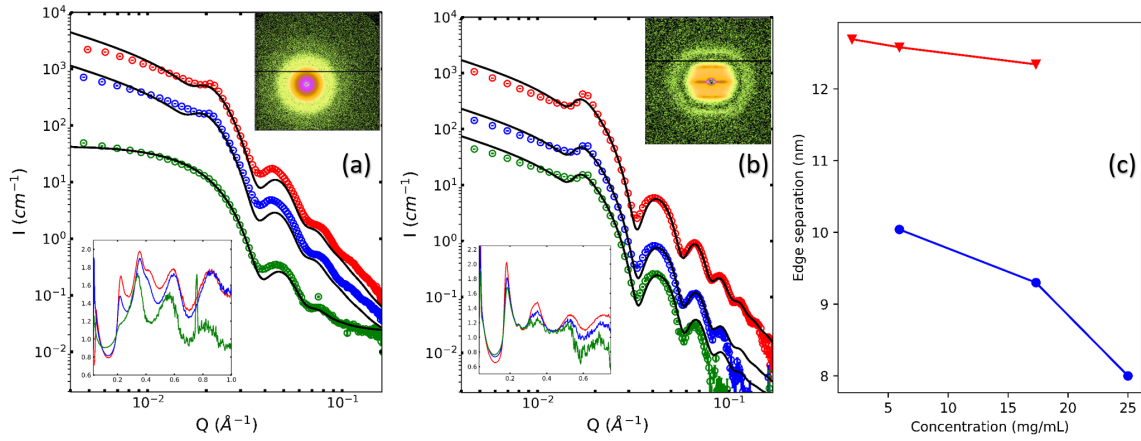


Figure 5.11.: The radially averaged SAXS data measured in applied field of 0.9 T for (a) F24 (b) F27 samples in a concentration of 22(2) mg/mL(\circ), 5.9(1) mg/mL(\circ), 1.9(9) mg/mL(\circ) with the experimental data as open symbols and linear pearl model fit as solid black lines. The bottom insets show the structure factors and the top inset shows the 2D pattern at 0.66 mg/mL. (c) The edge separation parameter l as a function of concentration for F27 (\blacktriangledown) and F24 (\bullet) samples. Solid lines are guides for the eye.

Table 5.4.: Summary sample IDs, diameters, and size distributions obtained from TEM, SAXS and SANS measurements of IONP. (*Discrepancy in F10 between SAXS and TEM is due to the fact the both 9 nm and 5 nm particles are present in F10 IONPs, also seen as shift in peak temperature from ZFC-FC splitting)

Sample Id	D_{TEM} (nm)	ΔD (%)	D_{SAXS} (nm)	ΔD (%)	D_{SANS} (nm)	ΔD (%)
F05	5.2	12	4.7	14		
F10	9.5	9	5.3	14		
F20	20.1	9	20.7	6	20.0	6
F21	21.1	7	21.0	7		
F24	24.3	9	23.0	11		
F27	26.2	8	26.4	8	26.6	8

Unique properties of neutron scattering are exploited in order to explore the internal magnetic structure and magnetic interactions in our samples. SANS of F20 revealed a similar isotropic pattern as SAXS even in varying applied magnetic field. The 2D SANS patterns of F27 samples under applied magnetic fields are as shown in Fig. 5.12 (a-f). The 2D SANS pattern of F27 at a low field (0.004 T) resembles bent stripes that evolve into straight stripes at 2.2 T. Additionally, these field induced patterns

can be reverted back to the original state when brought back to 0 T. These chains are confirmed with the 1D radial averaged intensities fit to linear pearl model. However, radial averaged intensities do not provide a complete analysis due to anisotropy in the 2D pattern. IONPs that align vertically along the applied field will contribute to the horizontal stripes in the inverse Fourier Q space. The separation between the stripes in Q space corresponds to the distance between IONPs in real space. To determine the correlation distances and chain lengths associated with these assemblies, 2D SANS pattern is integrated over azimuth sector width of 15° . The axis of the sector is centred at $\alpha = 0^\circ$, where α is the angle between Q and the external field direction.

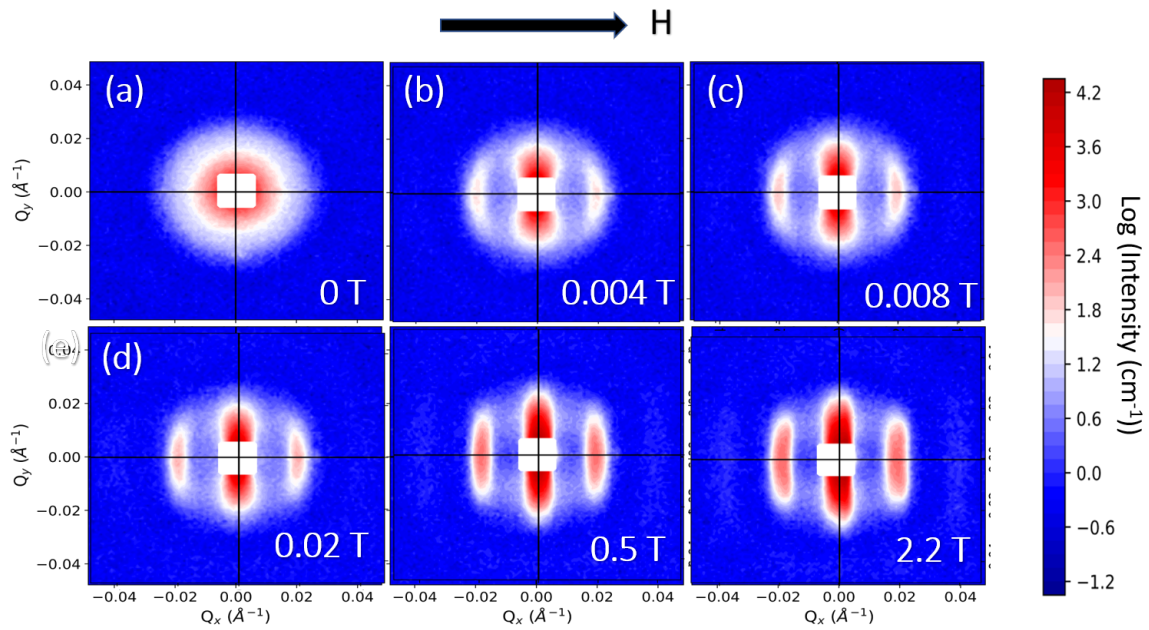


Figure 5.12.: 2D SANS patterns of F27 MNPs in solution in applied magnetic field of (a) 0 T, (b) 0.004 T, (c) 0.008 T, (d) 0.02 T, (e) 0.5 T and (f) 2.2 T. The magnetic field was applied perpendicular to the incident neutron beam as indicated by the black arrow. The colour scale is in units of scattering cross section (cm^{-1}) and represented in the log-scale.

The resulting correlation peak for integrated intensity of the sector parallel to H is modelled with a Gaussian function described below

$$I = (\text{scale}) * \exp\left[-\frac{1}{2} \frac{(Q - Q_{pp})^2}{W^2}\right] \quad (5.3)$$

to obtain the peak position (Q_{pp}) and width (W) as shown in Fig. 5.13. The peak

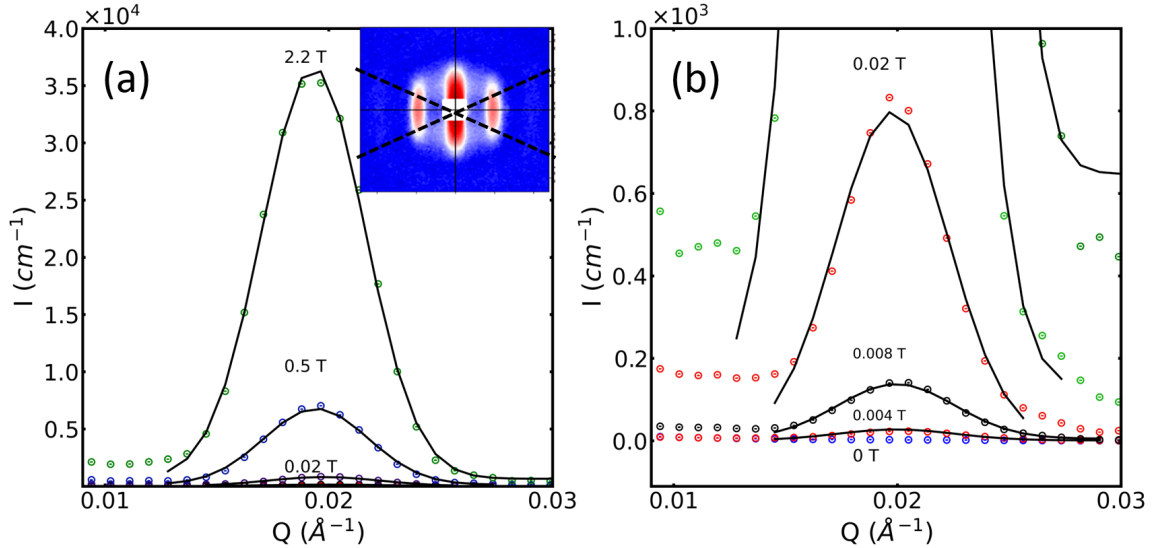


Figure 5.13.: (a) 1D sector integrated intensities of F27 IONPs along the sector centered at $\alpha = 0^\circ$, where α is the angle between \vec{H} and \vec{Q} for fields ranging from 0 - 2.2 T, inset: The sector of width 15° , in 2D SANS pattern. (b) The peaks from (a) are zoomed in for further visualization. The solid lines are the fits to Gaussian functions.

position corresponds to the projection of center-to-center distance of the IONPs on the field axis ($\ell_{\parallel} = \frac{2\pi}{Q_{pp}}$) [66]. The width of the peak describes the correlation length given by $\zeta = \frac{2\pi}{W}$, where W is the width of the correlation peak, related to the chain length. The dependence of both parameters on field magnitude is depicted in Fig. 5.14 (a-b). The schematic, (Fig. 5.14 (c)), describes the variation of ℓ_{\parallel} from low to high magnetic fields. The projected distances ℓ_{\parallel} increase as the chains align and straighten at high fields. The distance eventually saturates at $H \geq 0.5$ T, because the straight chains are in the most energetically favorable configuration. Figure 5.14 (d) depicts the increase in chain length with magnetic field. The effective correlation length obtained at 2.2 T is ~ 270 nm and contains about 8-9 individual IONPs. Despite the intense attraction, there is no continuous growth of chains as predicted by the Langevin simulations. A similar equilibrium state was previously observed for Co MNPs with chain lengths of ~ 65 nm [167]. Chain-formation induced in a dispersion is also observed on the substrate at ambient conditions. The SEM images of drop-cast F27 IONPs display randomly distributed entangled chains over the entire sampling region as shown in Fig.5.15 (a). In contrast, the spin-coated sample shows ordered alignment of the long chains along a given direction (Fig.5.15 (b)) extending over to μm -range. These results imply that F27 MNPs form long chains which can be aligned

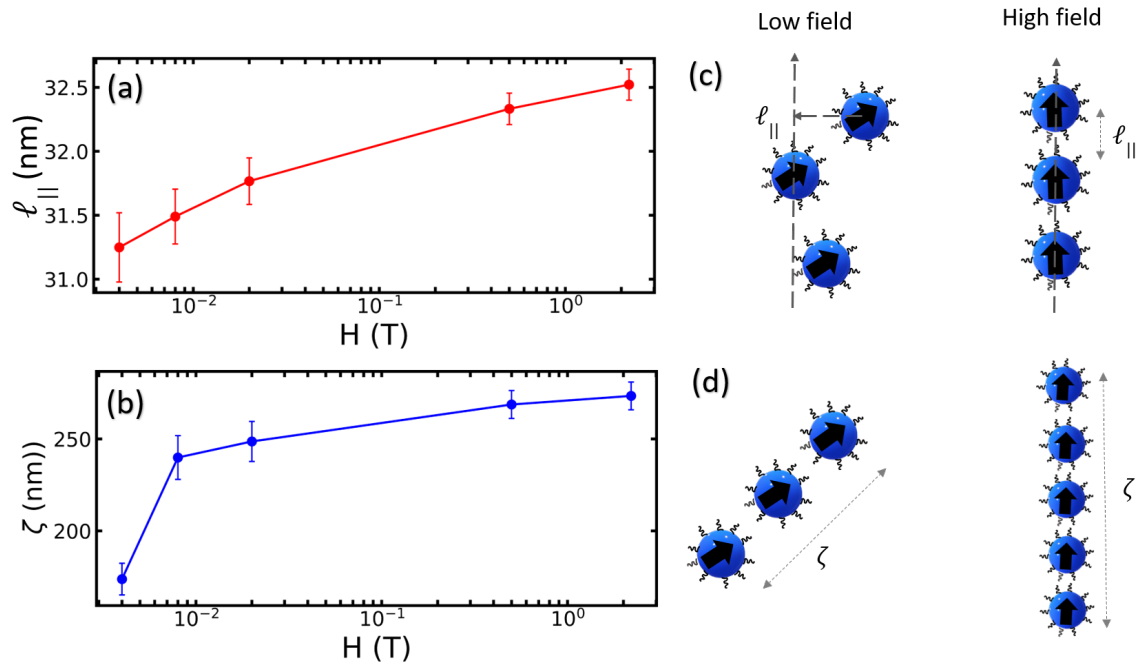


Figure 5.14.: (a) The projected distance between nanoparticles ℓ_{\parallel} and (b) the correlation length ζ plotted as a function of the magnetic field. Schematic representation of the change in (c) ℓ_{\parallel} and (d) ζ in IONPs as they respond to low field (left) and strong field (right).

with a combination of the centrifugal forces and surface tension. It is in agreement with previous observations of zero-field chains with cryoTEM [168].

Indeed, the chain lengths in solution of F27 IONPs are much shorter than those ob-

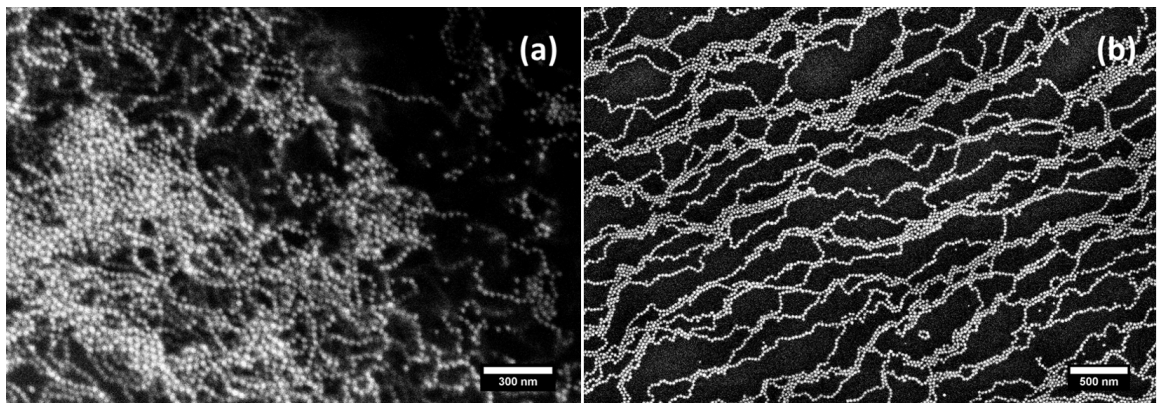


Figure 5.15.: SEM image of F27 IONPs when (a) drop-casted (b) spin-coated.

served for the same particles deposited on a substrate due to disorder forces such as Brownian motion. The flexibility of chains in dispersion are controlled by tuning the

applied magnetic field. At higher applied fields, the strong interaction of the dipoles with magnetic field along with dipole-dipole interactions between IONPs disentangle the dipolar chains into straight chains. [169].

5.6.4. Role of shell thickness

IONPs in dispersion are coated with a surfactant containing oleic acid (OA) to prevent irreversible aggregation of NPs due to van der Waals interactions. OA consists of a hydrophilic head group (-COOH) and a hydrophobic tail (-C₁₇H₃₂) connected by a double bond. The tail is bent due to the double bond and in a full stretched configuration its length is about 2.1 nm [11]. Contrast variation, was employed to unambiguously determine the ligand shell thickness and assess its properties during self-assembly. The initial experiments performed at KWS-1 reported in [14]. The initial experiments at KWS-1 resulted in refined shell thickness $t_{shell} = 1.0(1)$ nm and 1.3(4) nm in h and d-toluene, respectively for F20. These experiments were repeated for two contrasts at SNS-Oakridge for F20 and F27 (100 % h-toluene and d-toluene). The 1D SANS data of F20 IONP dispersions prepared in h- toluene is fit to a core-shell model with fixed radius value obtained from SAXS data and refined shell thickness of 3.2(1) nm as shown in Fig. 5.16 (a). The discrepancies in value of t_{shell} for h-toluene is due to the poor contrast of the shell component with the solvent. In the prepared d-toluene due to improved contrast the shell can be distinguished. However, the form-factor is completely smeared in d-toluene which is an indication of excess OA present in the shell. The surface coverage governs the strength of steric repulsion. A shell thickness of 1.8(4) nm was obtained on refinements of 100 % d-toluene contrast (core contrast) for core-shell form-factor. Dispersions were prepared in four contrasts for F27 IONPs as shown in Fig. 5.16 (b). Using the diameter and polydispersity of the core obtained from TEM and SAXS studies as constraints, the thickness of the shell $t_{shell} = 1.7(4)$ nm was determined by initially refining it for 100 % d-toluene scattering data. To improve the reliability of the fit for the other contrasts, this value was fixed and SLDs of the solvents were refined for other contrasts as shown in Fig. 5.16 (c). Both values are smaller than the nominal length of fully stretched out OA. TGA performed on all IONPs (Fig. 5.16 (d)) are used to quantify the organic material present without assuming a core-shell model. In fact all sizes exhibit a variation in the TGA curve indicating distinct nature of distribution of surfactant coating and ligand content. There are significant weight losses observed at the boiling point of

free OA (95-115 °C) in all commercial samples compared to F20 and F27, indicating a negligible amount of free OA in both samples. The significant weight loss occurred at around 380-430 °C due to complete combustion of organic material for F20 and F27. The loss percent is significantly larger in F20 (~ 80%) compared to other sizes indicating a larger percentage of OA. The other losses at higher temperatures is due to phase transition of the IONPs. The lack of prominent scattering features in the F20 d-tol contrast and large amount of organic content detected from TGA curve points to the explanation that free micelles are possibly attached to the shell of the IONPs. The free OA in forms of micelles attached to the shell will have much higher boiling point. Micelles existing in between IONPs can cause steric repulsion which presumably explains the lack of formation of assemblies in F20 despite strong dipolar interactions.

5.6.5. Magnetic structure

The SANS POL scattering patterns of F20 sample are displayed in Fig. 5.17. Figure 5.17 (a) and (b) show the patterns associated with different spin configurations of the neutron, I^- and I^+ , respectively. The sum signal (Fig. 5.17 (c)) and difference signal (Fig. 5.17 (d)) correspond to the scattering obtained with unpolarized SANS and nuclear-magnetic cross term, respectively. The difference signal follows $\sin^2 \alpha$ dependence from α , as is evident from the fit of the data to eqn. 2.132 at various Q values (Fig. 5.17 (e)). The magnetic and nuclear form factors were obtained using methods described previously in [66] and the best fits are shown in Fig. 5.17 (f). In the case of nuclear form factor, SLD of the core ($\eta_{nuclear-c} = 6.93 \times 10^{-6} \text{ \AA}^{-2}$) and SLD of the solvent ($\eta_{sol} = 0.94 \times 10^{-6} \text{ \AA}^{-2}$) were fixed while the diameter was refined. Similar strategy was employed to refine the magnetic form factor where the magnetic SLD of the core ($\eta_{magnetic-c} = 1.46 \times 10^{-6} \text{ \AA}^{-2}$) was fixed [170]. The results of refinements for nuclear and magnetic form factors revealed that magnetic and nuclear diameters of F20 IONPs are equal to 19.7(7) nm. Therefore a conclusion is derived that the F20 MNPs have a uniformly magnetized core, with no indications of surface canted spins that reduce the overall magnetization of the IONPs. It is in agreement with SEM and TEM studies, as well as with PDF results showing highly-crystalline order in synthesized IONPs. Additionally, the explanation of lowered magnetic volume is unlikely in these IONPs. Not surprisingly, the SANS POL experiments on self-assembling F27 IONPs revealed additional anisotropy arising from interactions between the particles

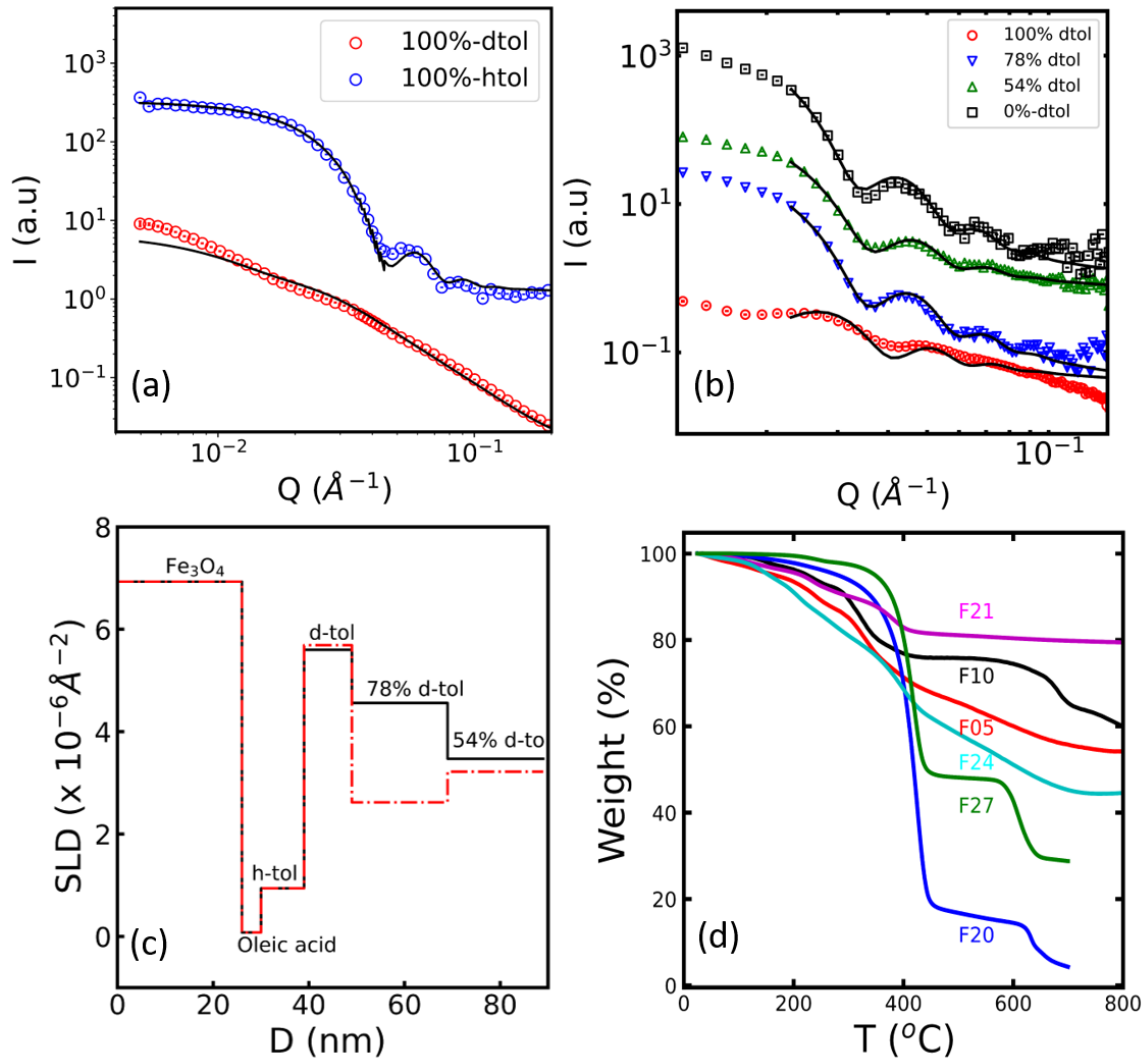


Figure 5.16.: (a) SANS of F20 at two different contrasts, in (100 %) h-tol (blue) and (100 %) d-tol (red) measured at SNS. The black lines are fit to core-shell model (b) SANS of F27 prepared in four different contrasts (100 %, 78%, 54 % and 0% d-tol) measured at KWS-1, here the solid lines are fit to core-shell model. (c) Calculated SLD (black) and refined SLD (red dots and dashed line) as function of diameter. (d) Weight loss plotted as a function of temperature obtained via TGA for F05, F10, F20, F21, F24 and F27.

(Fig. 5.18 (a) and (b)). Anisotropic magnetic structures with a local magnetization direction M and a preferred axis lead to a significantly complex dependence of the scattering cross-section due the interplay of this axis with Q and applied magnetic field [171]. The difference pattern as shown in the Fig. 5.18 (d) can not be factorized

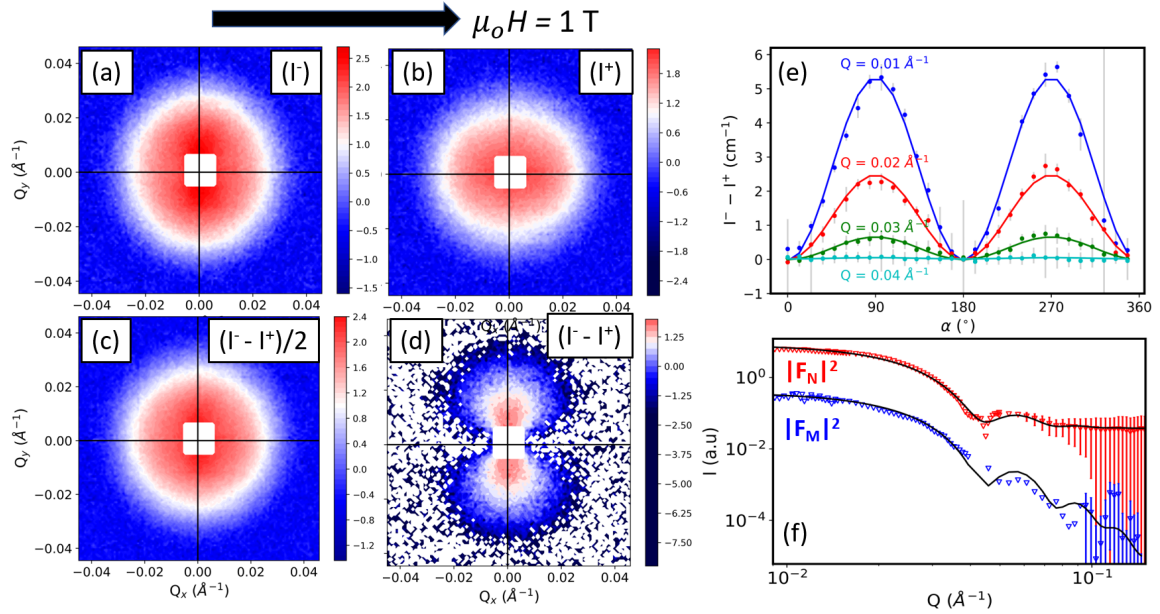


Figure 5.17.: 2D SANSPOLE scattering patterns of F20 at 1 T (a) I^- (b) I^+ (c) $(I^- + I^+)/2$ and (d) $I^- - I^+$, (e) Intensity of (d) plotted as a function of α where solid lines are the fit to $\sin^2 \alpha$ for different values of Q . (f) Q -dependence of the nuclear and magnetic form factors, where solid lines are fit to spherical form factor.

in to nuclear and magnetic form-factors as simply as in F20. SANSPOLE pattern is divided into different sectors with centers at $\alpha = 0^\circ, 30^\circ, 60^\circ$ and 90° and intensity is integrated along these sectors of width 15° as shown in Fig. 5.18 (e)-(h), following analysis adopting in literature [66, 172]. At $\alpha = 0^\circ$, the correlation peak for both I^+ and I^- coincide, indicating a purely nuclear origin of the scattered intensity. This correlation peak vanishes at $\alpha = 60^\circ$ and $\alpha = 90^\circ$ indicating absence of any 2D or 3D assemblies. The difference in the intensities between I^+ and I^- are evident for these two sector and clearly indicates the presence of magnetic scattering.

5.7. Reverse Monte Carlo (RMC) simulations

The chain formation of IONPs in dispersion is confirmed through several independent experimental methods. Radially averaged SAXS/SANS intensities were modeled using linear pearl models. Parameters of the chains were obtained using sectoral analysis of 2D SANS, including distances between IONPs in a chain and chain lengths. However, the 2D scattering patterns in their entirety are rarely analyzed in the literature

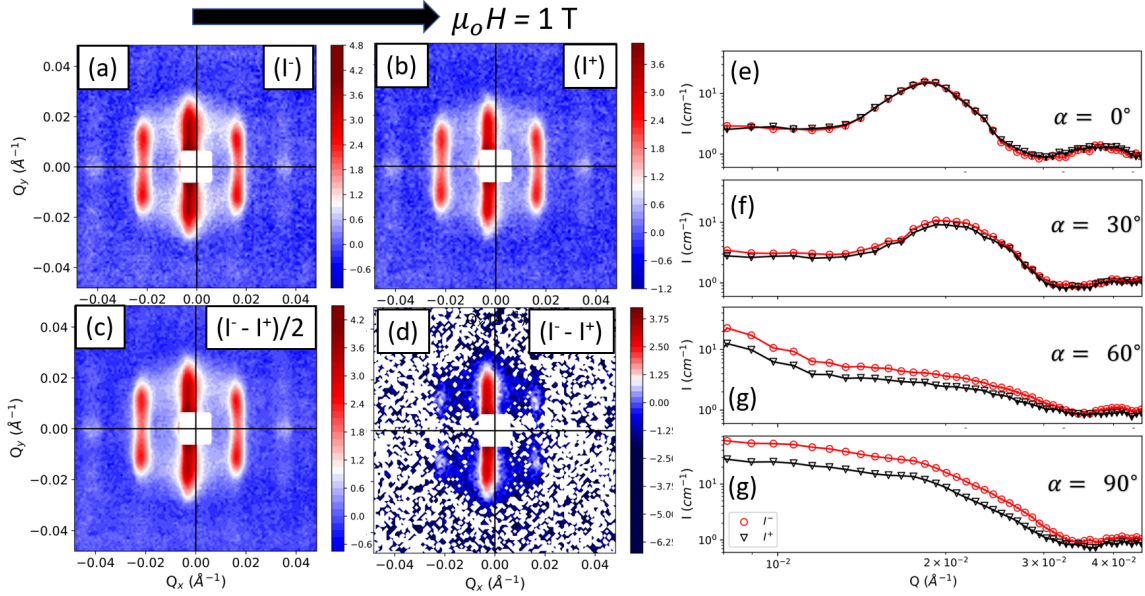


Figure 5.18.: 2D SANSPOLE scattering patterns of F27 at 1 T (a) I^- (b) I^+ (c) $(I^- + I^+)/2$ and (d) $I^- - I^+$, the colour scale is in units of scattering cross section (cm^{-1}) and represented in logscale. (e) Integrated intensity of I^- (\circ) and I^+ (∇) of sectors 15° in width, with sector centers at $\alpha = 0^\circ$ (f) 30° (g) 60° (h) 90° . Solid lines are guides for the eye.

without complex energy descriptions of the system. We have developed the RMC method to analyze the 2D SANS patterns. The advantages are multifold:

- The method helps avoid a complex energy calculation
- Radially/sector averaged intensities do not account for the complete anisotropy in the 2D pattern without loss of structural information.
- The chains observed with microscopy techniques are typically observed by spatially confining them on the substrate. RMC provides a tool to gain the real-space visualization of chain formations in dispersions as intended in applications.

We employed RMC simulations to analyze 2D SANS data of F27 in 50% d-toluene at a 14 m detector distance. We have access to low Q at this distance, which contains high-resolution information about the structure factor. The core and shell parameters obtained from SAXS and SANS were used to define the box's particles. The number of particles in the box matched the actual concentration. The total number of steps is computed by multiplying the particles with Monte Carlo steps, i.e., for 300 particles and 100 random RMC movements would imply 30000 steps. The 2D experimental

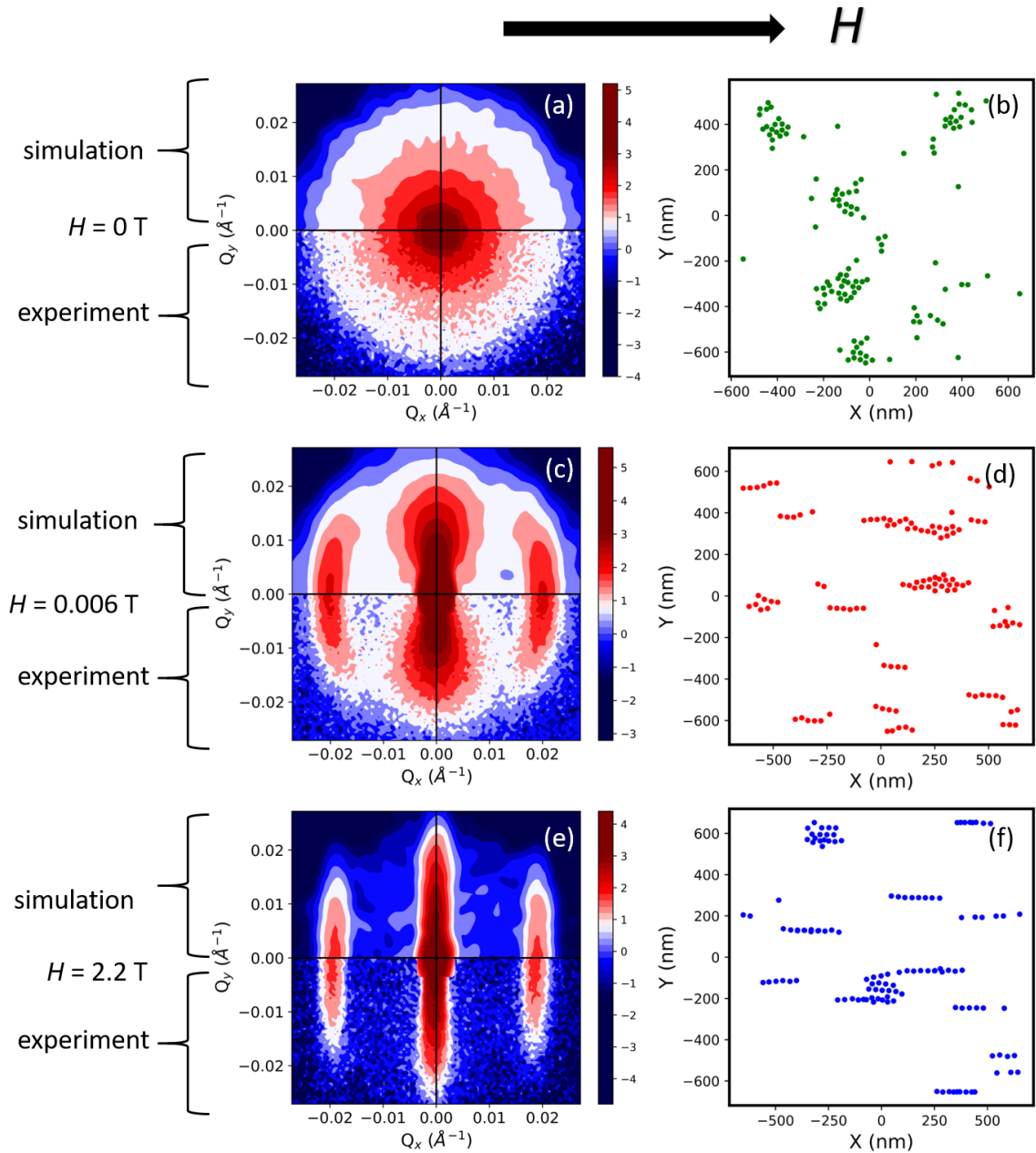


Figure 5.19.: Simulated and experimental halves of the 2D SANS patterns and real space distribution of IONPs in space at (a-b) 0 T (c-d) 0.006 T (e-f) 2.2 T.

(bottom half) and simulated pattern (top half) along with real space visualization at zero field are shown in Fig. 5.19 (a-b). As exhibited in the Fig. 5.19 (c-d) for IONPs at $\mu_o H = 0.006$ T, there are linear chains bent along the field axis. At $\mu_o H = 2.2$ T, the field-dipole interactions result in straight stiff chains as displayed in Fig. 5.19

(e-f). The direction of the effective dipolar field experienced by a single IONP is determined by random orientation and arrangements of its neighbors. On application of a magnetic field, the direction of the dipole moment of a single IONP competes with the effective dipolar field from the clusters forcing more particles to align with the field and extend into ordered chains. The actual distances between IONPs are determined through particle analysis of RMC real-space assemblies using imaging software *ImageJ*. We confirm from SANS and simulations that IONPs self-assemble into finite chain structures

5.8. Conclusion

In conclusion, various parameters that influence self-assembly in IONPs for a size range between 5-27 nm are identified. The attractive dipolar interactions mainly responsible for the 1D chain formation in IONPs depend on size, crystalline quality, composition, concentration (1.9 - 25 mg/ml), magnetic structure, and magnitude of the applied magnetic field. Such interactions between particles result in an increased value of blocking temperature (T_B). On the other hand, steric repulsion depends on the thickness of the ligand coated on NPs. In some cases, we have shown that the presence of excessive ligands may inhibit such chain formation. A range of experiments, including TEM, SEM, xPDF, magnetometry, TGA and SAS techniques, were performed to study these parameters. Several methodologies were adopted to analyze SAXS and SANS pattern formation for these assemblies, including (i) fitting shape-dependent functions to radially integrated 1D curves to obtain individual parameters of the IONPs, (ii) peak analysis of sectorally integrated intensities along the field to obtain interparticle distance and chain lengths, and (iii) direct visualization of real space assemblies in dispersion via SANS-RMC simulations. Individual IONPs can be manipulated to form 1D chains than can be bent and straightened with a magnetic field. Since these IONPs are the magnetic component of the Au-Fe₃O₄ dumbbells, similar interactions are expected in DBNPs. Along with the parameters of IONPs, the morphology of DBNPs will be a critical parameter in defining the non-trivial correlation lengths in assemblies formed by DBNPs.

6. Structural and Magnetic Characterization of Dumbbell Nanoparticles

This chapter describes the physical properties of dumbbell nanoparticles (DBNPs) containing Au noble metal linked to IONP. The seed-mediated approach used to synthesize DBNPs is a robust strategy for obtaining samples of varying sizes. Several structural and magnetic parameters of DBNPs, such as length scales of Au and IONP, crystallinity, interplanar spacing, phase composition, blocking temperatures and magnetic moment, are determined. These properties play a significant role in the functionality of the DBNPs and extend our knowledge of systems more complex than IONPs. This chapter compares the physical properties of DBNPs with spherical IONPs from chapter 5.

6.1. Dumbbell geometry

The dumbbell is a non-centrosymmetric structure and has several relevant geometric length scales. The particle geometry deviating from perfectly spherical shapes, is of significance in colloidal assembly because it influences the particle “recognition”, determines the particle packing, and ultimately dictates the formation of assemblies. Therefore, to understand the relationship between the shape of the building block and their assemblies, several length scales are defined (see Fig. 6.1). A DBNP of length L_D consists of Au seed of diameter L_A on which iron oxide is grown with diameter D_F and length L_F along the symmetry direction such that $L_D = L_A + L_F$. The coating, of thickness t , contains a mixture of oleic acid and oleylamine ligands. These DBNPs are labeled such that the number following A and F represents the length of Au and iron oxide, respectively. For instance, A13F14 consists of a Au seed with $L_A = 13$ nm on which the IONP of $L_F = 14$ nm is grown.

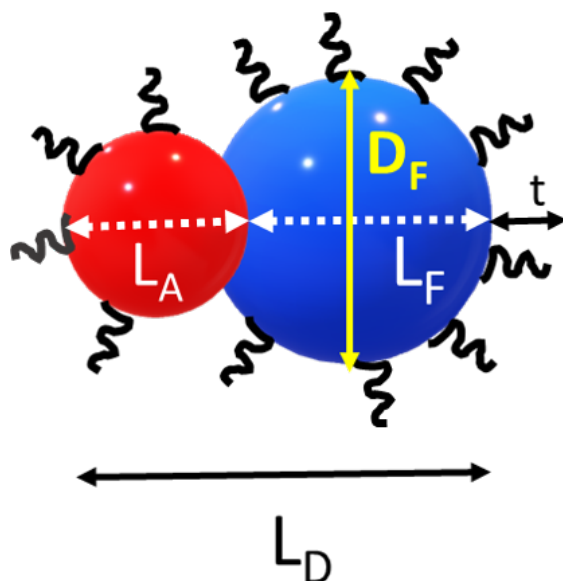


Figure 6.1.: The morphology of DBNP and its length scales. The red sphere represents the Au seed of diameter L_A . The blue non-spherical structure represents the IONP with diameter D_F that is grown on Au. The length of IONP along symmetry axis is L_F such that length of DBNP, $L_D = L_A + L_F$. The surface is coated with ligands of thickness t .

6.2. Samples and synthesis

DBNPs are not available commercially, and meticulous synthesis of these samples was required. Collaborators from the University of Pisa, Prof. Dr. Francesco Pinieder and Dr. Elvira Fanatechi, prepared several different sizes of DBNPs that are described in this thesis. The aim was to synthesize DBNPs with a narrow size distribution and a total size comparable to IONPs used in the previous chapter. The DBNPs are synthesized using the seed mediated approach which involves growth of iron on the spherical preformed seeds of Au [18]. The steps involved in the seed-mediated approach are outlined in Fig. 6.2. The nucleation event of Fe occurs due to thermal decomposition of the $\text{Fe}(\text{CO})_5$ precursor on the Au surface. $\text{Fe}(\text{CO})_5$ is injected into a hot mixture (120 °C) of preformed Au seeds, oleic acid, oleylamine and 1-octadecene. The mixture is stabilized at 315 °C for 50 min, before being allowed to cool down and exposed to air. The above described conditions were maintained in the preparation of A10F12 and A13F14 DBNPs. In the case of A9F11, the only difference is the addition of 1,2-dichloroethane into hot mixture containing Au seeds before injection of iron pentacarbonyl ($\text{Fe}(\text{CO})_5$). Seed mediated growth involving one pot synthesis

with conditions as described in [19] was followed for A10F14 DBNPs. In this method, the Au seeds are also prepared in-situ before the growth of IONPs. A freshly prepared gold solution of HAuCl_4 is injected into hot mixture containing 1-octadecene, oleic acid, oleylamine. Subsequently, $\text{Fe}(\text{CO})_5$ is injected at 150 °C. The temperature was increased and maintained at 200 °C for 90 minutes. The temperature was further stabilized at 300 °C for 60 minutes till it was allowed to cool. The Cl^- ions, either as ingredients in the reaction pot as HCl or 1,2-dichloroethane counter the ions of Au salt, that enable growth at low reaction temperatures and larger domain of iron oxide in the dumbbell [18, 19]. The $[\text{Fe}]/[\text{Au}]$ molar ratio, together with ligands, solvents, heating rate, and reaction time, control the effective morphology and size. Through mild changes in the synthesis, four diverse DBNPs are prepared. All suspensions of DBNPs were re-dispersed in toluene for further experiments. Each of the DBNPs mentioned along with materials, parameters and synthesis methods are summarized in Table 6.1.

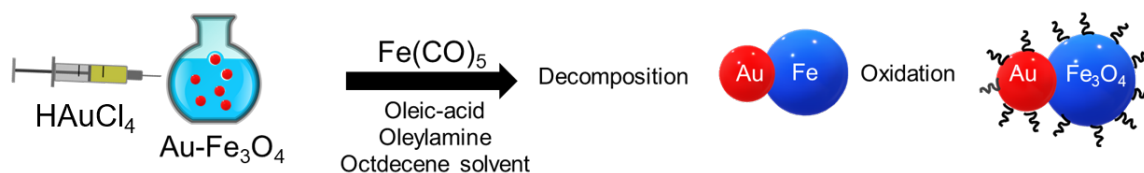


Figure 6.2.: Steps involved in seed mediated growth of $\text{Au-Fe}_3\text{O}_4$. The primary steps include: formation of Au seeds, decomposition of iron pentacarbonyl on the surface of Au and oxidation of grown Fe.

6.3. Shape, size and crystallinity

The TEM images of the DBNPs are as shown in Fig. 6.3. In these images produced by bright-field TEM, the difference in the brightness contrast is associated with variation in mass density or crystallinity. Thus, the Au components appear darker compared to iron oxide because this region is enriched with heavy atoms of gold. Through parallel illumination, TEM images are essentially 2D projection of 3D objects. In such anisotropic particles, particles lying flat on the substrate and standing up have a different projections on the image plane. One way to separate various projections is to tilt the sample and collect several images over various tilt angles. Such precise tilting experiments were not performed here. Nevertheless, due to the multi-component nature and the fact IONPs are grown on spherical Au, the particle size distribution

Table 6.1.: Summary of the DBNP synthesis protocols including amount of materials, parameters and method

Sample Id	Material	Parameters	Method
A12F10	Au(35 mg) + Fe(CO) ₅ (0.38 mmol) + Oleylamine(0.92 mmol) + Oleic acid (0.92 mmol) + 1-octadecene(20 ml)	[Fe]/[Au] = 2 [ligand]/[Fe] = 5 concn of Au ~ 8 mg/ml concn of Fe ~ 7.4 mg/ml	Seed-mediated cooled and exposed to air [18]
A9F11	Au(35 mg) + Fe(CO) ₅ (0.38 mmol) + Oleylamine(0.92 mmol) + Oleic acid (0.92 mmol) + 1-octadecene(20 ml) + 1,2-dichloroethane (0.79 mmol)	[Fe]/[Au] = 2 [ligand]/[Fe] = 5 concn of Au ~ 5.7 mg/ml concn of Fe ~ 7.9 mg/ml	Seed-mediated cooled and exposed to air [18]
A10F14	HAuCl ₄ (35 mg) + Fe(CO) ₅ (0.38 mmol) + Oleylamine(3 mmol) + Oleic acid (1 mmol) + 1-octadecene(20 ml)	[Fe]/[Au] = 2 [ligand]/[Fe] = 5 concn of Au ~ 4 mg/ml concn of Fe ~ 9.8 mg/ml	Seed-mediated one-pot synthesis [19]
A13F14	Au(35 mg) + Fe(CO) ₅ (0.38 mmol) + Oleylamine(0.92 mmol) + Oleic acid (0.92 mmol) + 1-octadecene(20 ml)	[Fe]/[Au] = 2 [ligand]/[Fe] = 5 concn of Au ~ 8 mg/ml concn of Fe ~ 7.4 mg/ml	Seed-mediated cooled and exposed to air [18]

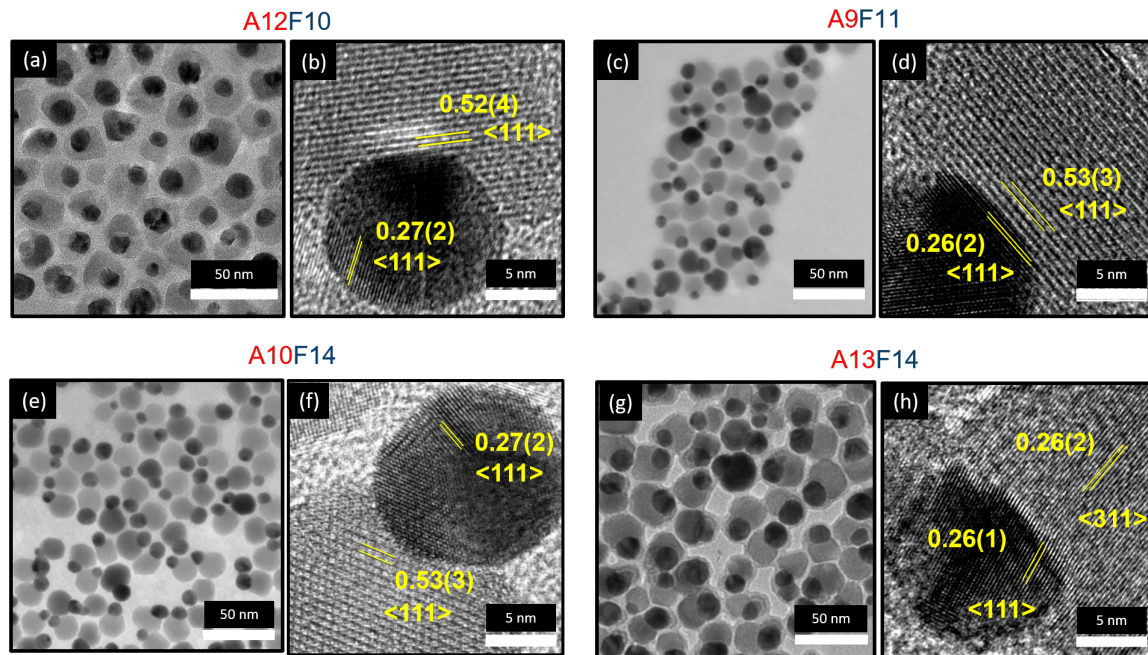


Figure 6.3.: TEM (left) and high resolution (right) TEM micrographs of (a-b) A12F10 (c-d) A9F11 (e-f) A10F14 and (g-h) A13F14. The crystal plane spacing is shown with yellow lines in each case.

analysis is first performed assuming individual spheres of Au to get reliable diameter of gold L_A . Since the IONPs grown on Au cause DBNPs to have different projections

along the image plane, the length along the growth axis L_F and the largest diameter of the IONP D_F obtained perpendicular to the former, are measured separately. Further, the whole length of DBNP L_D is also measured and the standard deviation of L_D , obtained from particles size analysis, now accounts for the various projections in the sample and intrinsic size variations. The major contributing factor to uncertainties in L_A is the intrinsic polydispersity in the spherical Au. The uncertainties in determination L_F and D_F together account for polydispersity of IONP. The geometric lengths L_A , L_F , L_D , D_F and corresponding polydispersities obtained from TEM, are compiled in Table 6.2. Through particle size analysis, we have shown that $L_D \sim L_A + L_F$. The lattice spacing of each component of the DBNP is visible in the high resolution TEM images (see Fig. 6.3).

Table 6.2.: Summary of DBNP length scales L_A , L_F , D_F , total length of dumbbell L_D , polydispersity (ΔL_D) and the aspect ratios ($A_1 = \frac{L_D}{L_A}$ and $A_2 = \frac{D_F}{L_F}$) obtained from TEM for DBNPs.

Sample ID	L_A (nm)	L_F (nm)	D_F (nm)	L_D (nm)	ΔL_D (%)	A_1	A_2
A12F10	12.9 ± 2.2	10.9 ± 1.8	22.9 ± 2.4	22.1 ± 3.5	15	1.7 ± 0.4	2.1 ± 0.4
A9F11	9.7 ± 2.0	11.6 ± 1.4	16.3 ± 1.7	19.8 ± 2.5	12	2.0 ± 0.4	1.4 ± 0.2
A10F14	10.4 ± 1.2	14.1 ± 1.6	18.0 ± 1.8	23.8 ± 2.1	9	2.3 ± 0.3	1.3 ± 0.2
A13F14	13.9 ± 1.9	14.2 ± 1.7	22.3 ± 2.5	26.7 ± 3.3	12	1.9 ± 0.4	1.6 ± 0.3

The resulting hybrid nanoparticles exhibits a dumbbell-like morphology, and such different length scales are rarely mentioned in the previous literature [96, 16]. Reports suggest that Au enlargement potentially causes detachment from the iron oxide NPs due to increased mechanical stress. However, despite the large size of metal NP, the particles are still attached. The polydispersities in DBNPs are large compared to the reference IONPs. The lengths of DBNP (L_D) are larger than those reported in existing literature [16, 18, 22] while the diameter of the IONPs (D_F) in the DBNP is equivalent to the previously described single IONPs. Distinct assemblies are observed in TEM and simulated previously through fine tuning another parameter that is the aspect ratio A of the dumbbell [27, 109, 173]. In general, the aspect ratio by definition is the ratio of the largest length to shortest length. Similar definitions exist for 1D nanostructures such as nanowires and ellipsoids made of same material. To account for the multi-component nature of the DBNPs, two aspect ratios A_1 and A_2 are considered. The aspect ratio A_1 is defined as $\frac{L_D}{L_A}$, which is the ratio of the length scale

along the long axis L_D to the short axis length given by L_A . The aspect ratio A_2 is defined to consider the loss of sphericity of the IONP due to its growth on Au and is defined as $\frac{D_F}{L_F}$.

The high-resolution TEM shows the alignment of iron oxide crystal plane along the planes of Au particle. The lattice parameter of Au and Fe_3O_4 are 4.08 Å and 8.39 Å, respectively, from previously reported bulk values. The large lattice mismatch between these components lead to the atoms of iron oxide nucleating on $\langle 111 \rangle$ crystal plane. that are and in Au and iron oxide, respectively. The inter planar spacing of IONP $d = 5.3(2)$ Å is almost double that of Au $d = 2.6(2)$ Å indicating $\langle 111 \rangle$ orientation in IONP for all cases but A13F14. Here the planes spacing of IONP correspond to 2.7(1) Å, the $\langle 311 \rangle$ lattice plane (Fig. 6.3 (d)). This indicates that IONP with crystal plane $\langle 311 \rangle$ is grown on $\langle 111 \rangle$ plane of Au. It is worth noting that, however precise, TEM provides statistically limited information on particles due to limited area analysis.

6.4. Composition and local structure

The composition of the DBNPs are determined by the x-ray pair distribution function (xPDF) measurements. Fig. 6.4 (a) and (b) show xPDF data and modeling of the reference IONP and Au bulk samples. The best fit was obtained using cubic phases of Au (space group Fm-3m, Inorganic Crystal Structure Database(ICSD) collection code 52249) and magnetite Fe_3O_4 (Fd-3m, ICSD code 65339). The reference IONP consists of 50 nm iron oxide (II and III) oxide nanopowder from Sigma Aldrich. The best agreement with experiment data of IONPs was obtained by using structural model of 100% magnetite phase to yield a lattice constant of 8.3901(7) Å. Powdered bulk gold data refinement fit with 100% Au gave a lattice constant of 4.0792(3) Å. In the case of DBNP, the xPDF data is dominated by scattering from the Au component of the sample due to its higher contrast for x-rays. For A12F10, a reasonable fit is obtained for a phase composition of 22% Au and 78% magnetite as shown in the Fig. 6.4 (c). As shown in the fit in Fig. 6.4 (d) in A13F14 the mass fraction of Au seems larger (61%) and compared to IONP (39%). This is presumably because A13F14 are sedimenting particles and the large amount of residual Au particles maybe found in the supernatant phase. In this modelling approach, one cannot determine the interface between Au and IONP, since it assumes a mixed phase of Au and iron oxide. The quality of fits in A13F14 needs to be improved to confirm the lattice constant

expansion of IONP. The lattice constants of A12F10 and A13F14 are listed in Table 6.3, along with those for Au and Fe_3O_4 reference samples.

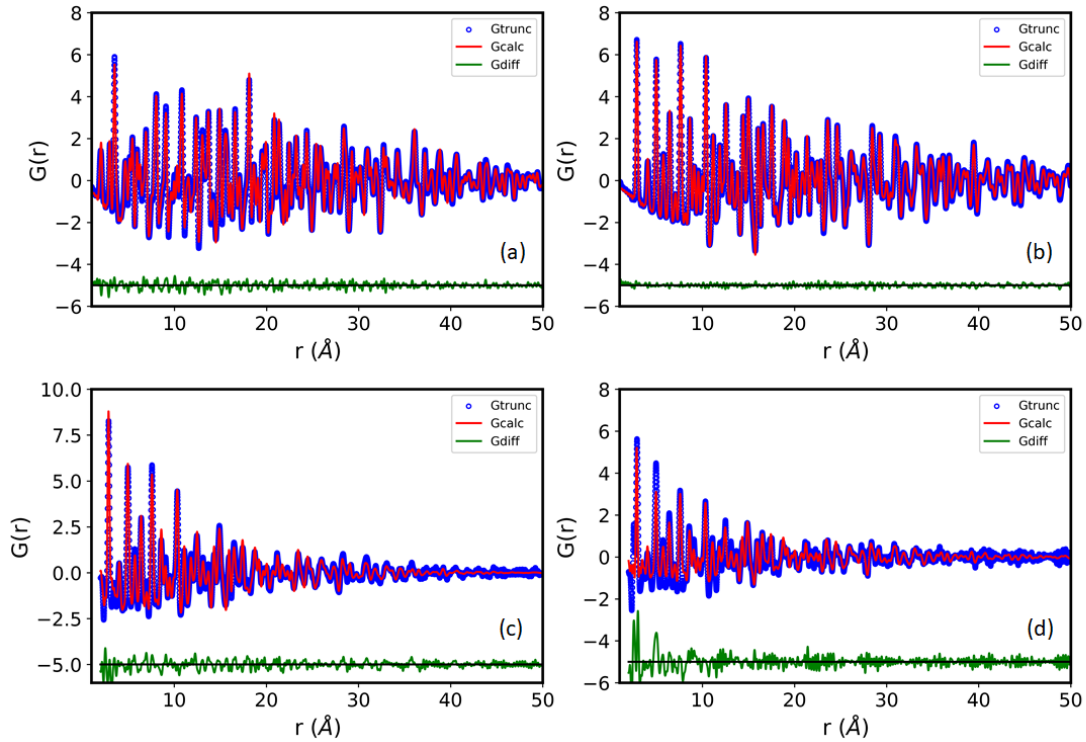


Figure 6.4.: The best refinements of xPDF data for (a) bulk iron oxide Fe_3O_4 , (b) bulk Au, (c) A12F10 and (d) A13F14 with experimental data in open blue circles, calculated pattern in red curve and difference curve in green.

Table 6.3.: Summary of the xPDF refinement fits bulk reference iron oxide, powdered Au compared to A12F10, A13F14 DBNPs. The fits yield lattice constants a , $\delta 1$, atomic displacement factors U_i so, masses of magnetite and Au. Here, $Q_{damp} = 0.0377 \text{ \AA}^{-1}$, $Q_{broad} = 0.007 \text{ \AA}^{-1}$, $Q_{max} = 24 \text{ \AA}^{-1}$ The detailed refinement parameters can be found in the appendix A.2.

Samples	Bulk iron-oxide	Au powder	A12F10		A13F14	
Phase	Fe_3O_4	Au	Au	Fe_3O_4	Au	Fe_3O_4
crystal structure	Fd-3m	Fm-3m	Fm-3m	Fd-3m	Fm-3m	Fd-3m
a [\AA]	8.3901(7)	4.0792(3)	4.0499(7)	8.42(3)	4.054(1)	8.40(8)
mass (%)	100	100	22	78	61	39
R_w	0.126	0.065	0.218		0.42	

$Q_{damp} = 0.0377 \text{ \AA}^{-1}$, $Q_{broad} = 0.007 \text{ \AA}^{-1}$, $Q_{max} = 24 \text{ \AA}^{-1}$. Au structural fit using cif file ICSD-52249, iron oxide fit using structural file obtained from standard database ICSD-65339.

Details about the fit parameters available in Appendix A.2.

The lattice constants of the Au in the DBNPs are significantly lower than the bulk value. Conversely, the lattice constants of Fe_3O_4 in DBNPs are found to be larger as compared to bulk values. Reliable refinement of atomic displacement parameter of oxygen in oxides is challenging given the poor contrast of x-rays with light elements. A simple Scherrer formalism is limited and complicated by the multi-component overlapping peaks in the diffraction pattern. Possible reduction in lattice constants of the Au can be associated with the finite size effects in DBNPs [22]. The $G(r)$ function converges to zero at higher r , due to the finite-size of our particles as shown in the Fig. 6.5 (a) for all particles. Due to the sedimentation nature of A9F11 and A10F14

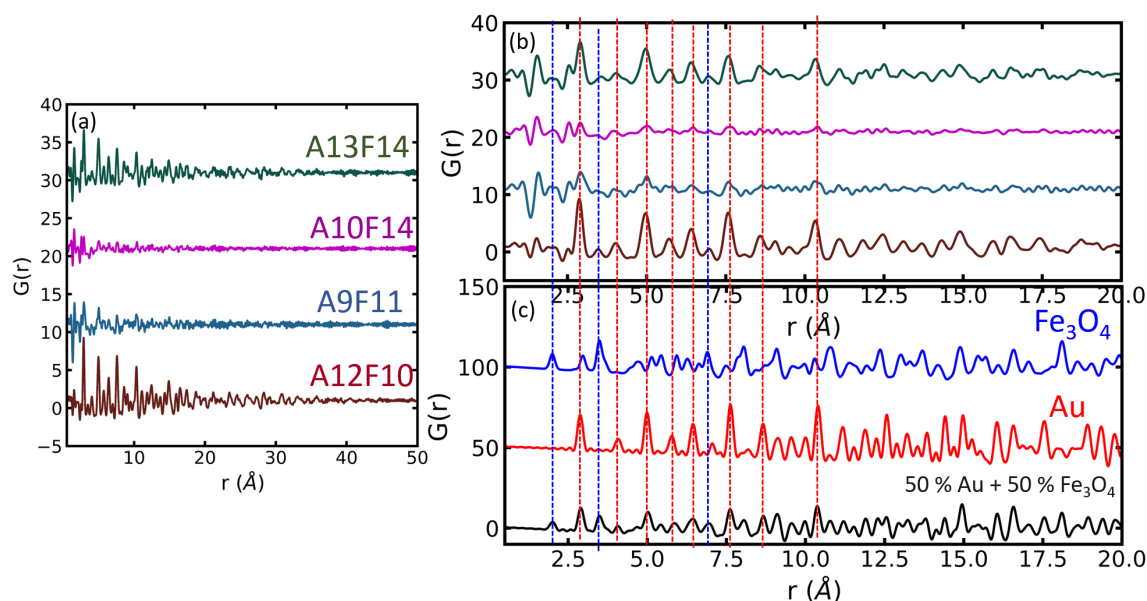


Figure 6.5.: $G(r)$ function plotted for DBNPs in the range of (a) 1 - 50 \AA and (b) 1 - 20 \AA . (c) The simulated $G(r)$ plotted for bulk gold (red), magnetite (blue) and 50 % mix fraction of gold and magnetite (black). The red and blue dashed lines extending through (b) and (c) represent the corresponding Au-Au and Fe-Fe peaks found in simulated and experimental data.

DBNPs, the signal to background ratio is low for obtaining a good fit. The modelling involves no specific consideration of the sample interface or shape of the particles and simply assumes a mixed phase model. In Fig. 6.5 (a), the finite size effect from the xPDFs for all DBNPs terminate indicates crystalline NPs of ~ 5 nm. At $r < 2$ \AA (Fig. 6.5 (b)), systematic peaks not associated to the phase of any expected component are present in all four DBNPs. These peaks can be the residuals from Fourier transforms applied to scattering intensities and can be identified by fine tuning Q_{max} . However,

no such indications exist at the moment. It must be noted that in the xPDF measurement, the DBNPs are measured along with all the residual particles in the solvent. The C-C bonds from organic material and disorder within the DBNP can also contribute to such the peaks. Further, to make a qualitative assessment of the composition in these DBNPs, the xPDF curves are compared peak by peak to the simulated $G(r)$ function for reference and mix phases in the range of 1 - 20 Å for all sizes in Fig. 6.5 (b-c). Thereby, one can conclude that the DBNPs mainly contains mixed phase of Au and magnetite. Due to large scattering intensity of Au, the different magnetic phases cannot be uniquely identified.

6.5. Magnetic properties

The Fe_3O_4 and Au nanoparticles are often explored as individual systems, the iron oxide for magnetic properties and Au for optical/electrical properties. Combining them together in a single system is fundamentally interesting to understand variations in the magnetic properties of IONPs when in a bifunctional system. Structural Verwey transition is commonly observed at temperature close to 120 K due to presence of magnetite in IONP. As discussed in chapter 5, debate exists in the community regarding the observation of this transition in ZFC-FC curves. The reference IONPs used in Chapter 5 indicate no sign of Verwey transition for NPs below 50 nm. On the other hand, there are reports presenting Verwey transition in ultrasmall shape controlled NPs [158]. The ZFC-FC measurements at an applied field of 100 Oe of the DBNPs are as shown in the Fig. 6.6 (a-d).

The ZFC-FC curves present a typical behaviour of an interacting system with no visible Verwey transition. Nevertheless, xPDF has confirmed the presence of magnetite despite the absence of visible Verwey transition in both spherical IONPs and DBNPs. As defined in the previous section, the aspect ratio A_2 that connects the two length scales D_F and L_F of the grown IONPs accounts for its non-spherical nature. Using these length scales and fixed anisotropy constant of magnetite ($K_{eff} = 1.3 \times 10^4 \text{ J/m}^3$), the lower of the energy barrier is calculated as follows $\Delta E_{min} = \frac{4\pi}{3} K_{eff} \left(\frac{L_F}{2}\right)^3$. Likewise the upper limit is $\Delta E_{max} = \frac{4\pi}{3} K_{eff} \left(\frac{D_F}{2}\right)^3$. Using eqn. (2.56), minimum and maximum values of T_B are obtained for the respective DBNPs and plotted with respect to A_2 in fig. 6.7 (a). The shaded region between the calculated minimum and maximum value of T_B depicts the possible range of expected blocking temperatures for the grown IONPs of different aspect ratios. As expected when $A_2 \rightarrow 1$, the

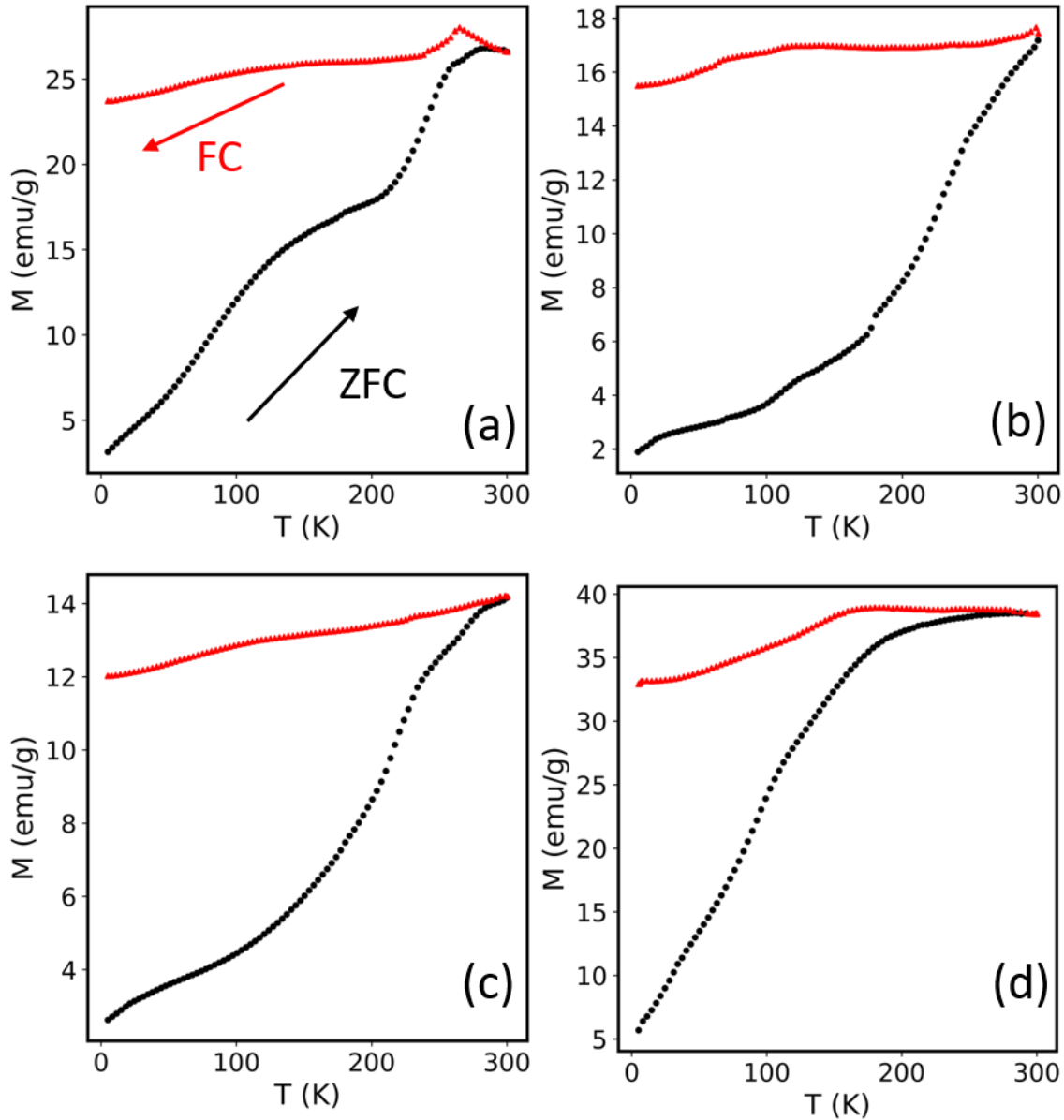


Figure 6.6.: ZFC (black) and FC (red) magnetization as function of temperature in an applied field of 100 Oe for (a) A12F10 (b) A9F11 (c) A10F14 (d) A13F14.

reduction in shaded area corresponds to the fact that the temperatures coincide to a single value of T_B if IONPs are purely spherical. For all DBNPs, from Fig. 6.6 the observed $T_B > 250$ K and lies outside the shaded calculated region. Dilutions of DBNPs only show slightly variation in T_B . Comparing the observed T_B of IONPs in DBNPs with single-phase IONPs from chapter 5, additional shifts in T_B cannot be merely accounted as a consequence of dipolar interactions. For instance, the $T_B \sim$

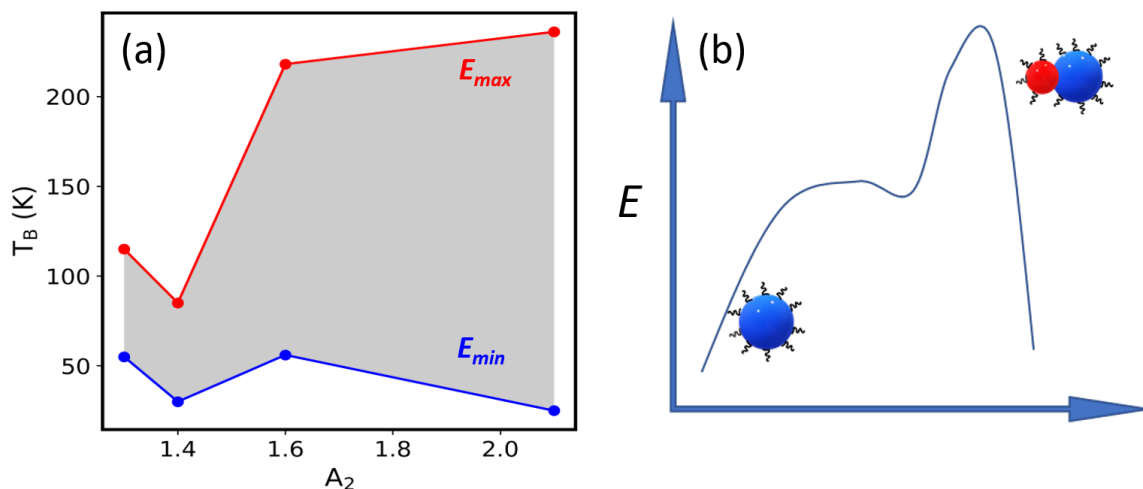


Figure 6.7.: (a) Calculated T_B corresponding to energy barrier E_{min} (blue) and E_{max} (red), plotted as a function of IONPs' aspect ratio (A_2). (b) Schematic representing the energy barrier increase as a result of the anisotropy in the DBNPs.

18 K for F10 IONP and close to 300 K for A12F10 DBNP of similar short axis length. As noted in previous reports on powdered Fe_3O_4 sample, the strong dipolar interaction only induces a shift in the value for T_B by a few degrees [174]. The key factor responsible for the shift in DBNPs is the enhanced anisotropy, which can increase the energy barrier and consequently the T_B . In DBNPs, the IONPs are grown along $\langle 111 \rangle$ crystal plane of Au NP as observed in TEM. The interface between Au and IONP are possibly subjected to stress due to their growth. Further, these IONPs are not spherical as single-phase IONPs. The loss of sphericity is captured in the definition of aspect ratio A_2 , hence there is a suggested contribution of shape, stress and magnetocrystalline anisotropy to the effective magnetic anisotropy [175]. The shift due to enhance anisotropy has been explored in prior studies on Ag- Fe_3O_4 DBNPs [176]. Recent reports on AC frequency dependent blocking temperatures on such DBNPs also exhibit similar characteristics. The AC susceptibility was fit to two separate models; non-interacting Néel-Arrhenius and weakly interacting Vogel Fulcher model to determine the discrepancy. However, a weak accuracy in the description of a suitable model is a clear indication of the complexity of the problem at hand [177]. The shift in T_B up to room temperature can be then accounted by the enhanced magnetic anisotropy. We concur that the ZFC curve in a DBNP clearly exhibits two contributions. At low temperatures, the magnetization emerges due to the anisotropy of individual IONPs, and at high temperature it is added to the anisotropy of the

DBNPs as a whole leading to a very large energy barrier distribution, with blocking temperatures higher than room temperature [176] (Fig. 6.7 (b)). Field dependent magnetization $M(H)$ curves recorded at temperatures 5 K and 300 K after being field cooled at 1 T, are displayed in Fig. 6.8. In all the cases, there are no obvious signs of exchange bias field as reported before in literature [22, 21]. However, we observed high linear contribution in $M(H)$ curves associated with the diamagnetic moment. The diamagnetic content has been subtracted through following steps: (a) fitting the linear curve for the magnetization data where field, $H > 3$ T and (b) subtracting the linear diamagnetic contribution using the following slope. These curves do not follow the usual Langevin model at room temperature present in SPM systems. Saturation magnetization M_s (emu/g) is the magnetic moment per gram of iron oxide and which is calculated assuming that iron holds 70 % of the nanoparticle weight. This is achieved by dividing the maximum value of magnetization M_{max} given in emu by mass of Fe obtained from separate ICP-OES measurement and multiplying with 0.7 factor [178]. The amount of Fe and Au present in the sample are separately obtained through ICP-OES measurement (see Appendix for more details). The field cooled curves corrected and normalized to iron oxide mass in the DBNP system reveal a steady increase in M_s that scale with volume associated with L_F . The reduction in saturation magnetization at 300 K compared to 5 K is expected because magnetic moments can no longer freely align with thermal energy. At low temperatures such as 5 K, the loops show the presence of two contributions (i) linear magnetic susceptibility at high field and (ii) ferromagnetic component at low field. The blocking temperatures, exchange bias fields, coercive field and corresponding saturation magnetization of the DBNPs are detailed in Table 6.4.

The bulk saturation magnetization value of Fe_3O_4 is about 91 emu/g [179]. In all the DBNPs, this is much reduced but A13F14 the saturation magnetization is ~ 108 emu/g. Saturation magnetization can be reduced in NPs due to several reasons such as finite size effects, surface spin canting due to lower coordination number, surface strain, magnetically depleted layers and antiphase boundaries [180, 181, 182, 183]. Au coated IONPs show further reduction in the magnetic moment [184, 185]. The surface moments are disordered further due to interaction with Au electrons leading to reduced saturation moment. Despite the overwhelming reports on reduced magnetization, in parallel there are several studies on magnetism enhanced in non magnetic oxides, borides and graphite [186, 187, 188, 189]. The associated origin in these materials have been attributed to orbital magnetism occurring in nanosize

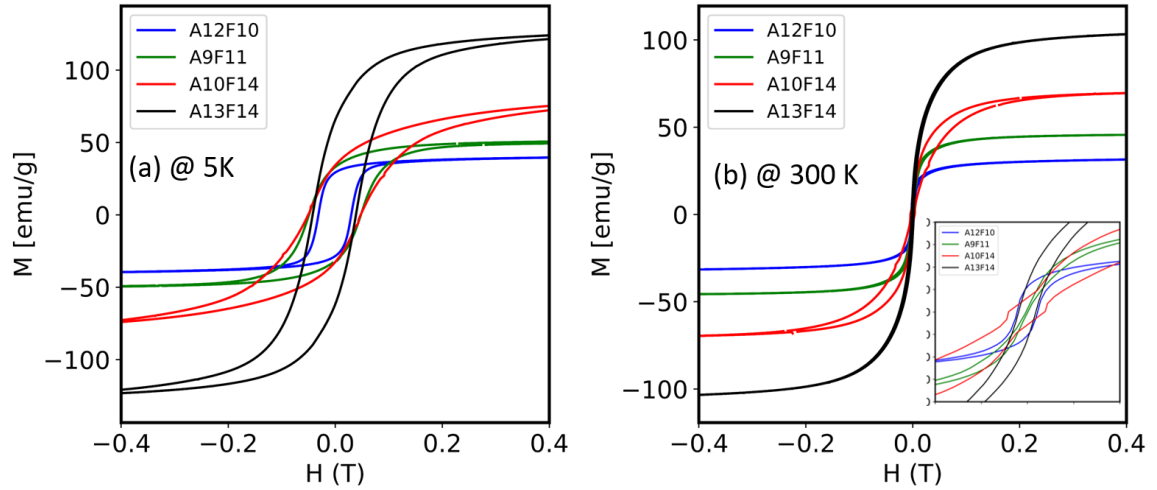


Figure 6.8.: Field-cooled DC magnetization $M(H)$ curves as a function of magnetic field at (a) 5 K and (b) 300 K with 1 T cooling field, inset; $M(H)$ is zoomed in at low fields to indicate the waist shaped curved for A9F11 (green) and A10F14 (red)

Table 6.4.: Summary of the calculated and measured T_B of DBNPs compared with IONPs using ZFC-FC curves. Exchange bias field H_{EB} and coercive field H_{C1} at 300 K from $M(H)$ hysteresis loops. The saturation magnetization M_s at 300 K.

Sample ID	T_B (min) (K)	T_B (min) (K)	Measured DBNPs T_B (K)	Measured IONP T_B ^(a) (K)	H_{EB} (± 28 Oe)	H_{C1} ^(b) (± 20 Oe)	M_s @ 300 K ^(c) (emu/g)
A12F10	25	236	290	10 (F05)	7	21	33.9 ± 0.4
A9F11	30	85	>300	18 (F10)	15	0	46.7 ± 2.0
A10F14	55	115	>300	250 (F20)	15	36	73.9 ± 1.5
A13F14	56	218	>290	270 (F21)	17	18	108.6 ± 2.9
				300 (F24)			
				>300 (F27)			

^(a) observed blocking temperatures of IONPs from chapter 5, ^(b) The errors correspond to the residual fields present in the PPMS-dynacool system, ^(c) saturation magnetization is obtained as follows M_s (emu/g) $\rightarrow \frac{M_{max}}{\text{mass of [Fe]}} \times 0.7$ where mass of [Fe] is obtained from ICP-OES results in appendix.

defects. Polymer stabilized metallic Au and Pd were found to be magnetic [190]. Further, thiol capped single phase Au NPs are reported to have an apparent FM due to localized 5d holes that arise from the bond between Au and thiol surfactant [191]. Further studies on bare Au and Pd particle also show 4d FM [192, 193, 194]. The presence of magnetism is not limited to just thiol capped but also Au NPs capped in a mixture of oleic acid and oleylamine surfactant similar to our system [195]. It has also been observed that coating IONP containing magnetite with Al multilayer system has shown enhancements in magnetism. Often enhancement in magnetization

are associated with an interfacial effect [196]. Enhancement in the magnetic moment is also observed in gold coated IONP core-shell structures [197, 104]. One contesting theory is the induced moment in Au due to proximity in a magnetic material. Banerjee et al., have shown that there is a chemical gradient at the interface responsible for trapping the conduction electron of Au [104]. These electrons contribute to the orbital magnetic moment. The magnetic character of IONPs is in particular also affected by the oxygen content in the system. Numerous studies on thin film systems exist which elucidate the change in exchange coupling in Fe as function of oxygen. A complete review of all the physics related to iron oxidation in general is well beyond the scope of this work. These studies are however limited in nanoparticle system, one because of the poor sensitivity to light element in experiments such as x-ray total scattering experiments. Hence, separate experiments have to be carried out to quantify oxygen diffusion and their role in potentially enhancing the magnetic moment. Another interesting feature not observed in previous case is the waist shaped hysteresis loop. At 300 K, the $M(H)$ hysteresis loop width narrows as magnetization goes to zero in A9F11 and A10F14. These waist-shaped curves are visible in the zoomed inset in Fig. 6.8 (b). The origin of these curves in other system presents as a consequence of mixed magnetic phase containing soft and hard magnetic subsystems. A recent study by Lopes. et. al observed a similar waist shaped hysteresis loops in Ag-Fe₃O₄ dumbbells [176]. Magnetization enhancement in the DBNPs can be extremely useful while designing MNPs suitable for hyperthermia applications.

6.6. Surface ligand density

The surface coating is yet another parameter to consider for self-assembly. TGA is an excellent tool to characterize the surface bound ligands as seen in the Chapter 5. It was shown how the large quantity of surfactant on the shell of certain IONPs inhibited the formation of assemblies. The DBNPs are coated with surfactant such as oleic acid (OA) and oleylamine (OLA) in the 1:1 ratio. An approximate value of the grafting density for a spherical IONP coated with oleic acid can be obtained through weight loss percentages from the TGA given by,

$$\sigma(\text{ligands}/\text{nm}^2) = \frac{\frac{\text{wt}\%_{\text{shell}}}{\text{wt}\%_{\text{core}}} \rho_{\text{core}} \frac{4}{3} \pi \left(\frac{D_{\text{core}}}{2}\right)^3 N_A}{MW_{\text{OA}} \cdot 4\pi \left(\frac{D_{\text{core}}}{2}\right)^2} \quad (6.1)$$

where wt%shell is weight loss obtained from TGA equivalent to the relative mass of the organic shell and the residual mass of NP is given by wt% core; $\rho_{core} = 5.17$ g/cm³ denotes the density of IONP core; $MW_{OA} = 282,47$ g/mol is the molecular weight of OA; D_{core} is the diameter of the core obtained through TEM, SAXS and N_A is the Avagadro number. The Fig. 6.9 depicts the TGA curves for DBNPs. For a DBNP geometry, to calculate the surface ligand density, Eqn. (6.1) is modified. The equation can be modified assuming OLA capped Au and OA is coated around IONP.

$$\sigma(\text{ligands}/\text{nm}^2) = \frac{\frac{\text{wt}\%_{\text{shell}}}{\text{wt}\%_{\text{core}}} \frac{4}{3}\pi \left[\rho_F \left(\frac{D_F}{2}\right)^3 + \rho_A \left(\frac{L_A}{2}\right)^3 \right] N_A}{4\pi \left[MW_{OLA} \cdot \left(\frac{L_A}{2}\right)^2 + MW_{OA} \cdot \left(\frac{D_F}{2}\right)^2 \right]} \quad (6.2)$$

where $\rho_F = 5.17$ g/cm³ denotes the the density of IONP, $\rho_A = 19.3$ g/cm³ is the density of Au, $MW_{OLA} = 267$ g/mol is the molecular weight of OLA, D_F is the diameter of the IONP and L_A is the diameter of the Au NP obtained through TEM analysis. The observed weight loss before 200 °C is attributed to unbound surface ligands. The boiling point of the bound OA and OLA ia about ~ 460 - 500 °C. At this temperature point the major mass loss is observed for all samples, though the amount of ligand varies in all samples. Larger mass losses indicate presence of higher ligand density. These mass losses and calculated ligand density are presented in the Table 6.5.

Table 6.5.: Summary of the ligand density σ calculated for DBNPs and IONPs using the respective geometric length scales.

Sample ID	wt%shell ^(a) (%)	σ ^(b) (ligands/nm ²)	Sample ID	wt%shell ^(c) (%)	σ ^(d) (ligands/nm ²)
F05	47	~ 8.6	A12F10	58	~ 61
F10	24	~ 6	A9F11	86	~ 192
F20	83	~ 189	A10F14	74	~ 102
F21	10	~ 4	A13F14	75.9	~ 134
F24	46	~ 39			
F27	51	~ 54			

^(a) Weight loss percent obtained from TGA curves for IONPs from chapter 5 , ^(b) calculated using eqn. (6.1), ^(c) weight loss percent obtained from TGA curves of DBNPs, ^(d) calculated using eqn. (6.2).

In the case of IONPs, these calculation concur with the findings presented in Chapter 5 where ligand density is the highest for F20 which in turn inhibits formation of assemblies. However in DBNPs, the geometric aspect again plays a role. These ligand densities are calculated assuming two spheres. Based on preliminary assumptions,

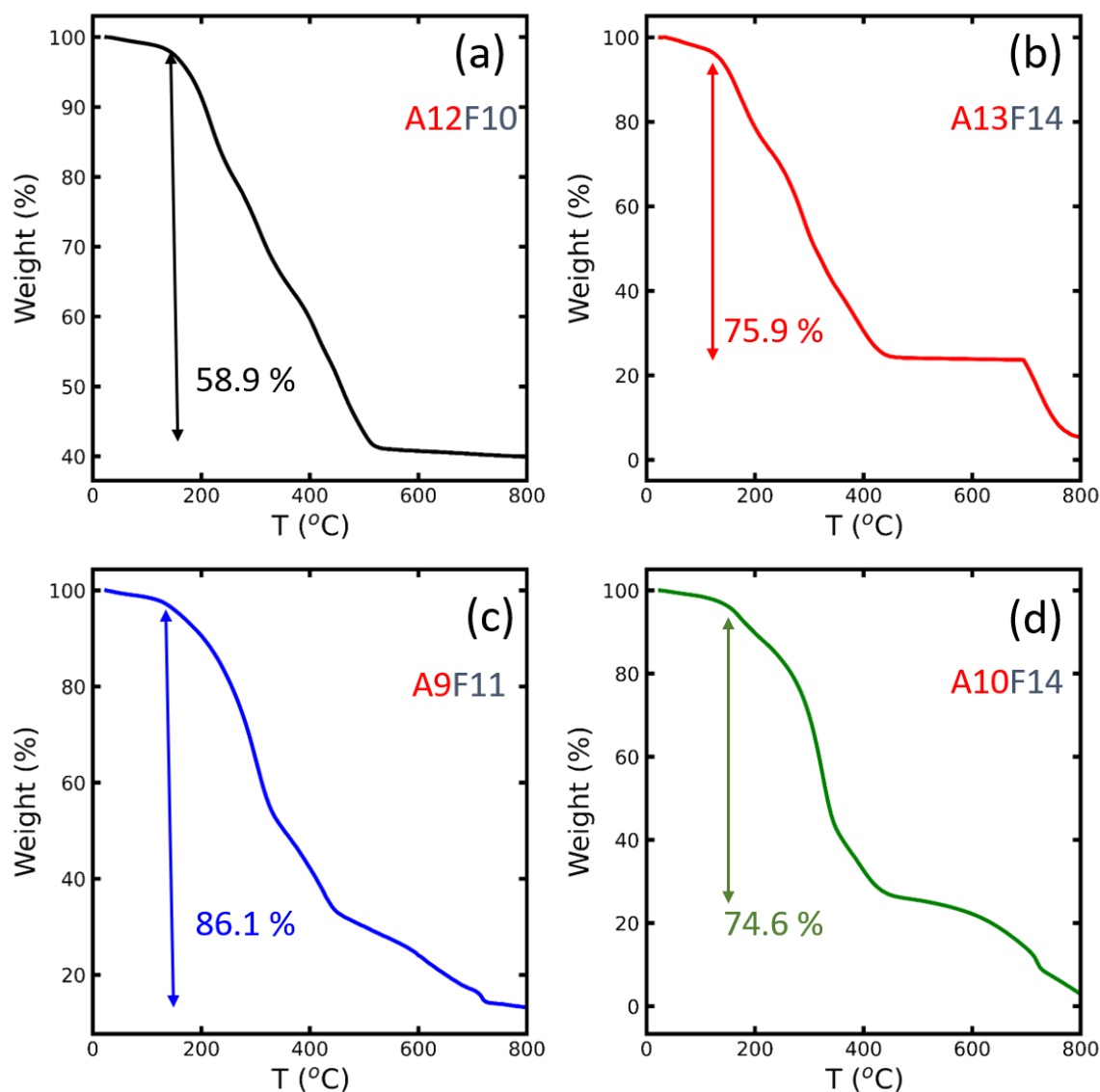


Figure 6.9.: TGA curve representing the mass loss as a function of temperature for (a) A12F10, (b) A13F14 (c) A9F11 and (d) A10F14

A12F10 has the lowest ligand density, while A9F11 and A13F14 has the highest. The aspect ratio is closely connected to these estimations. These densities are much larger than IONPs as expected due to larger surface area. The long carbon chains attached to the DBNP surfaces are responsible for the stability of the colloids. The steric interactions between them effectively control the minimum distance between the DBNPs. Further, interactions can also exist between the surface of NP and the ligand in the form electrostatic repulsion, van der Waals or hydrogen bond. The OLA consists of an amine head group ($-\text{NH}_2$) which can only bind to single motif as opposed to OA

(-COOH) which can bind 3 times more to the surface. The charge stabilized on these surfactants is also shown to play a role in driving assemblies in Au-Fe₃O₄ systems [27]. Liu et al. have shown how tuning the hydrophobic and van der Waals interactions through hydrophobic OLA capped Au and hydrophilic Fe₃O₄ was critical for forming various assemblies. Alternatively, the thickness of the coating around NPs could also play a vital role in hindering the formation of assemblies as seen in Chapter 5 for F20 IONPs. Moreover, dual functionalization of the DBNP surface due to large surface area and its further application in tuning interactions will play a key role in its use as diagnostic and drug carrier system for biomedical applications.

6.7. Conclusion

This chapter investigates DBNPs consisting of IONPs grown on Au seeds by a seed-mediated approach. The epitaxial relationship between Au and the IONPs particles are evidenced by either the small mismatch between IONPs $\langle 311 \rangle$ and Au $\langle 111 \rangle$ [$< 5\%$] or the interfringe distance of IONP $\langle 111 \rangle$ being 2 times that of Au $\langle 111 \rangle$. The multicomponent and non-spherical nature of the DBNPs is characterized by the definition of A_1 and A_2 . Improved dumbbell morphology is expected as the aspect ratio $A_1 \rightarrow 2$. Further, the loss of sphericity in IONP of the DBNP corresponds to a high value of A_2 . In individual spherical IONPs, the dominant dipolar interactions are shown to shift the measured T_B . However, along with dipolar interactions, the most remarkable result in DBNPs is the shift in measured T_B associated with anisotropy. The loss of sphericity combined with constrained growth of IONPs on $\langle 111 \rangle$ crystal plane of Au can enhance magnetic anisotropy. Contribution to anisotropy emerges from the associated shape, stress, magnetocrystalline and other induced effects in IONP of the DBNPs. Due to finite size effects, Au NPs in DBNPs are shown to undergo structural contraction of the lattice constant compared to bulk. The enhanced magnetization in DBNPs compared to bulk magnetite may be a consequence of interfacial effects, magnetism in Au, or the effect of oxygen-induced magnetic behavior. Stabilizing ligands prevents irreversible agglomeration; however, there is no indication of excessive ligands in DBNPs. Our recommendations to predict the assemblies are linked to geometric aspect ratios. Parameters, techniques and these geometric parameters developed will be employed to analyze the assemblies formed by DBNPs.

7. Self-assembly of Dumbbell Nanoparticles

This chapter describes the self-assembly of DBNPs using scattering methods and simulations. As discussed previously, DBNPs have different structural and magnetic properties compared to their spherical counterparts. Though the literature on preparing such non-spherical particles has grown over the decade, reports on assemblies into 1D, 2D and 3D structures are still infrequent. Often in limited cases, the self-assembly of DBNPs is achieved in the liquid phase using linkers or templates [119, 120]. In this chapter, the DBNPs are shown to assemble readily and reversibly into structures in an applied magnetic field, and this phenomenon is identified through anisotropy in the 2D SAXS and SANS scattering patterns. Based on the anisotropy and the assembly formed, we classify the DBNPs into three separate categories. The scattering patterns are analyzed using shape-dependent and independent models to reveal interparticle correlations and particle arrangements. Novel scattering patterns observed are qualitatively analyzed using simulations. Particle aspect ratio and magnetic field strength are identified to play a crucial role in the stability and formation of self-assembled structures.

7.1. Scattering contrast

Au-Fe₃O₄ DBNPs coated with oleic acid and oleylamine surfactants in a dispersion of toluene forms a system with different scattering contrast for x-rays and neutrons (see Fig. 7.1). For x-rays, scattering intensity is dominated by the Au particles that have nearly three times the scattering length density (SLD) than that of Fe₃O₄ (Fig. 7.1 (a)). Conversely, neutron SLD of Fe₃O₄ is larger when compared to Au (see Fig. 7.1 (b)). Thus, simultaneous refinement of small-angle x-ray and neutron scattering data can be used to increase accuracy in the determination of structural parameters of the multi-component DBNPs.

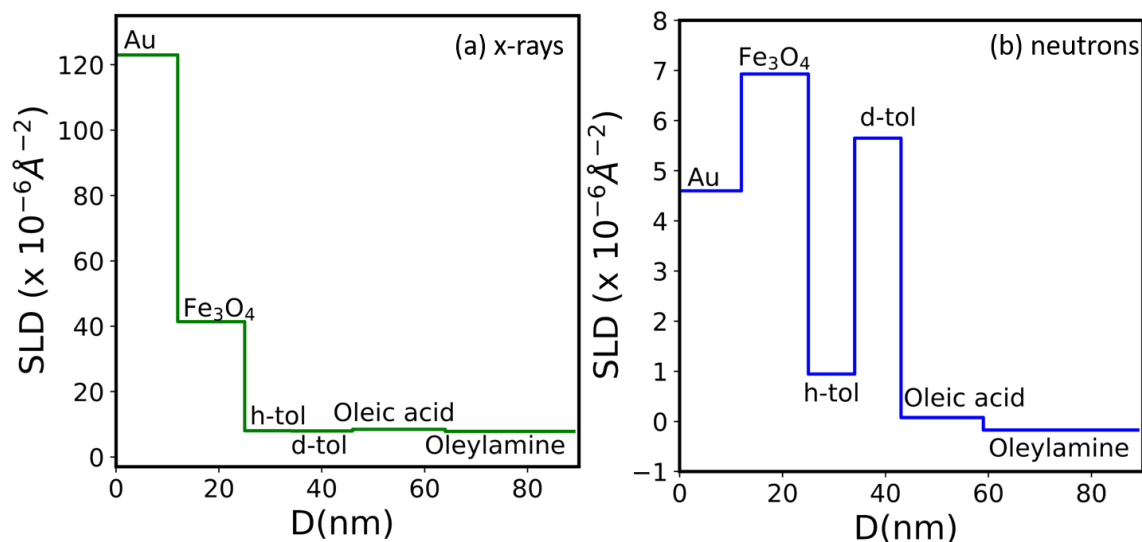


Figure 7.1.: Scattering length density of various components in a surfactant coated Au-Fe₃O₄ DBNP system suspended in h-toluene with (a) x-rays and (b) neutrons.

7.2. Phase separation and macroscopic assemblies

Among the four DBNPs (A12F10, A9F11, A10F14, A13F14) presented in the previous chapter, A9F11 and A10F14 DBNPs sediment almost immediately due to large heavy gold particles as shown in Fig. 7.2. Shaking the cells re-disperses the DBNPs (Fig. 7.2 (a)). However, the Brownian diffusive force combined with gravitational force separates the DBNPs from the supernatant phase, which lies above (Fig. 7.2 (b)). In the presence of an inhomogeneous magnetic field from a handheld magnet, the DBNPs behave like macroscopic iron filings (see Fig. 7.2 (c)). The nanosized DBNPs form long needle-like macroscopic structures affected. The nanoscale configuration of these DBNPs is probed using SAXS and SANS in an applied magnetic field. The field gradient values are not directly measured in both cases and may vary in different setups. The SAXS patterns for DBNPs are collected only at 0.9 T field point using a set of permanent magnets at GALAXI (see chapter 4 for instrument details). For SANS, a range of fields up to 3 T can be applied horizontally to the sample using the current setup of the magnetic field at KWS-1. For SANS measurement on IONPs (from chapter 5), the field setup at KWS-1 was different and had a vertical electromagnet producing fields up to 2.2 T. The system of DBNPs in a dispersion can be described as a combination of the supernatant and particle phase.

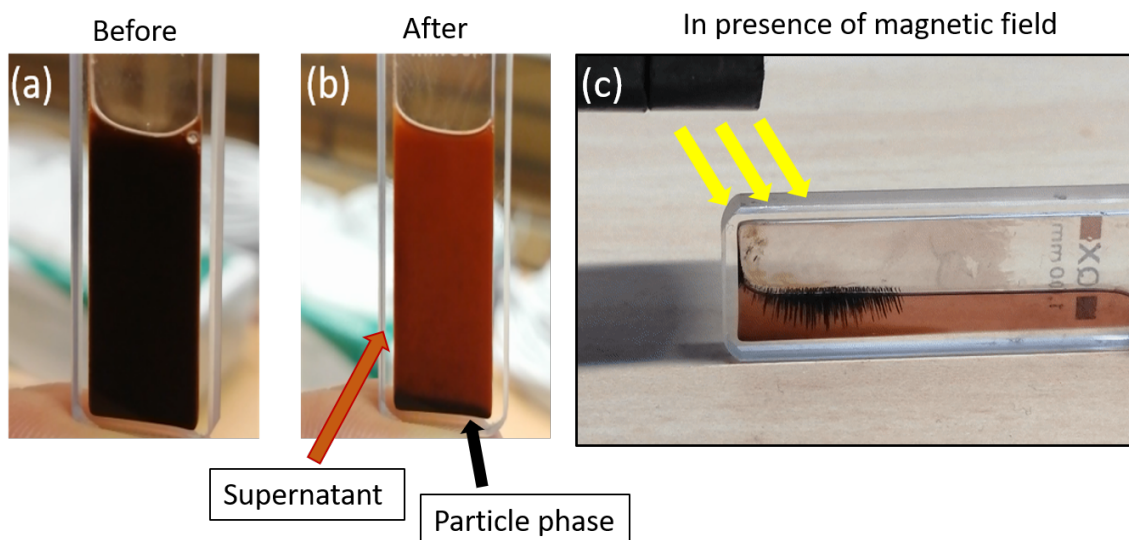


Figure 7.2.: Sedimentation of DBNPs: Hellma cells filled with A10F14 DBNPs in toluene dispersion (a) before and (b) after sedimentation, the supernatant is the solution phase containing residual particles above the dark sedimented particles collected at bottom of the cell. (c) The same DBNPs in the presence of 200 Oe hand held in inhomogeneous field, here the DBNPs clearly separate out of dispersion to form macroscopic structures.

7.3. Probing self-assembly : 2D visual analysis

7.3.1. 2D SAXS patterns

DBNP dispersions were filled in ~ 2 mm wide borosilicate capillaries with a wall thickness of 0.05 mm and ~ 4 -5 mm in length for SAXS measurements at room temperature. Dilution methods to study individual particle behavior or concentration effects on assembly are not straightforward in these DBNPs compared to IONPS. In IONPS, due to the stability of the dispersion, extraction with pipettes for further dilution was trivial and the concentration of each dispersion could be accurately determined. However, in DBNPs, the extraction of liquid and particle-phase to accurately obtain the diluted concentration remains a challenge due to gravity and particle separation. Hence in this thesis, all DBNP samples were measured in the initial overall concentration of ~ 7 -8 mg/ml obtained during synthesis without further dilution. The beam of size $\sim 0.7 \times 0.7$ mm² can gauge different positions of the in-homogeneous sample. For zero-field measurements, the filled capillaries are placed horizontally, as shown in Fig. 7.3 (a), and due to sedimentation of DBNPs, the particle phase lies near the edge of the holder

and most of the measured signal is due to the supernatant phase. The capillaries in the field setup are placed vertically and exposed to a horizontal 0.9 T magnetic field. Due to phase separation combined with its response to the applied magnetic field, the particle phase rises towards strong field gradients displacing the supernatant phase. The x-ray beam is focused at two different vertical positions on the capillary to probe this phase (see Fig. 7.3 (b)) and the detector images collected at these positions of the capillaries are as shown in Fig. 7.3 (c). Visually the anisotropy in the 2D SAXS pattern at a fixed field remains the same with varying intensities along different positions of the capillary as long as the gauged volume lies in particle phase. Due to the complete absence of DBNPs, the 2D SAXS pattern is isotropic with low scattering intensity from residual particles and solvent at a position along the capillary in the supernatant phase. The 2D SAXS patterns collected along different positions and the

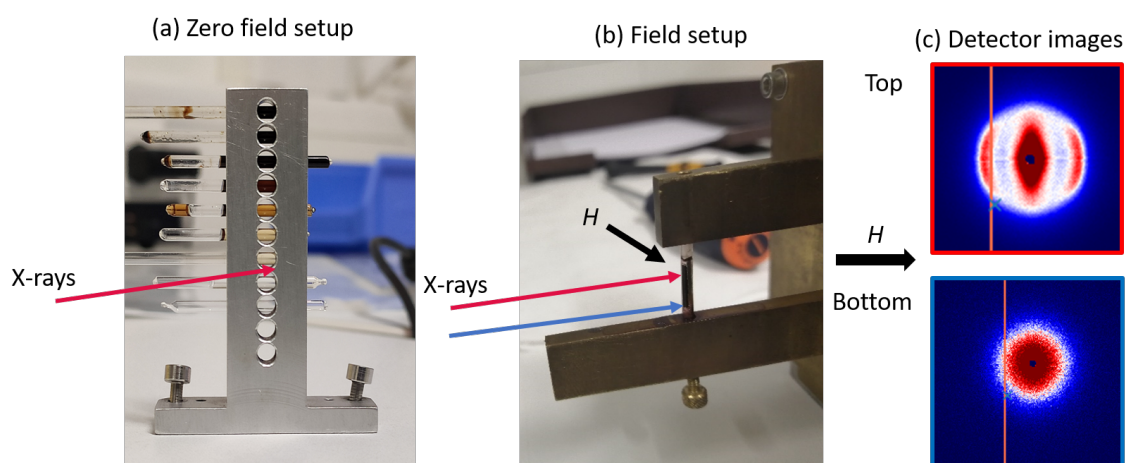


Figure 7.3.: (a) The capillaries are held horizontally for zero field and (b) vertically for magnetic field SAXS measurements on DBNPs at GALAXI. In (b) due to phase separation and magnetic field response, the x-ray beam is focused at two different positions on the capillary represented by blue and red arrow. The direction of applied field \vec{H} is given by the black arrow. (c) The SAXS patterns of A9F11 DBNP collected from top (red outline) and bottom (blue outline) of the capillary. Note the capillaries in the figure are just representative and do not contain the actual DBNPs samples.

scattering patterns with maximum intensity at 0.9 T and 0 T, for the four different DBNPs, are displayed in Fig. 7.4. The SAXS patterns of the stable and well dispersed A12F10 DBNPs, remain isotropic at all positions along the capillary and the circular pattern at 0 T. However, at 0.9 T the pattern is elongated at the centre (Fig.

7.4 (a-b)). This is an indication that DBNPs orient in the magnetic field resulting in an elongation although no assemblies are formed in these DBNPs. However for remaining DBNPs, due to phase separation and horizontal configuration of the zero field setup, the SAXS pattern has lowered intensity at 0 T. The 2D SAXS patterns reveals anisotropy at 0.9 T. The 2D SAXS patterns of A13F14 and A9F11 have stripe patterns with a diffuse ring in the former case. The stripe pattern for A9F11 DBNPs is similar to the one observed for IONPs in chapter 5 that indicates the formation of chains (Fig. 7.4 (c)). The cross pattern of A10F14 is unique because it is unlike any scattering pattern observed previously for NP systems. Visual interpretation already depicts rich variety of assemblies formed in three of the four DBNP samples.

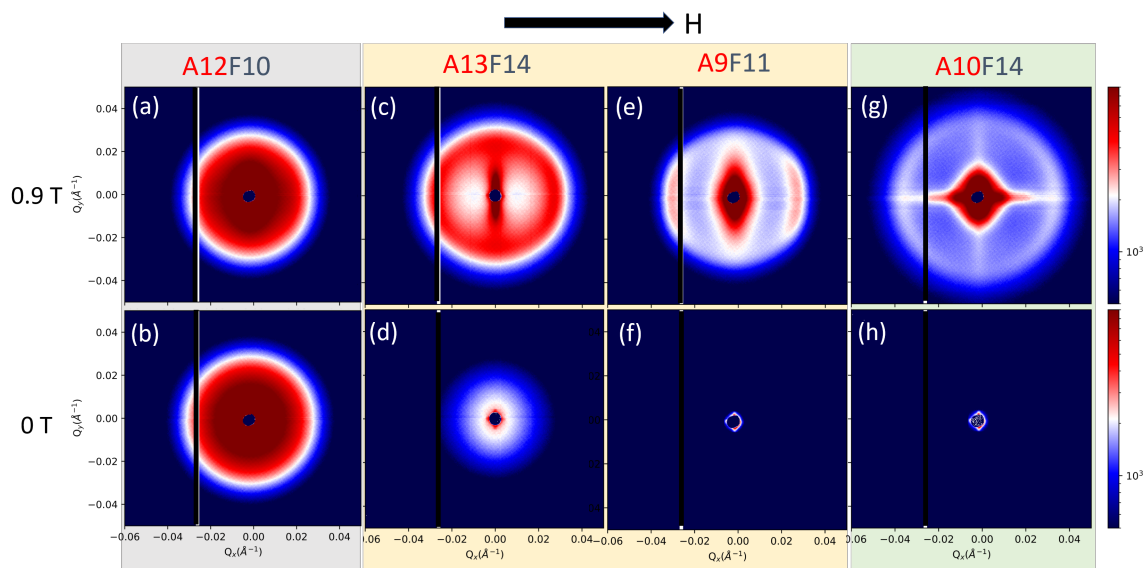


Figure 7.4.: The 2D SAXS patterns of (a-b) A12F10 (c-d) A13F14 (e-f) A9F11 and (g-h) A10F14 DBNPs collected at $H = 0.9$ T (top panel) and 0 T (bottom panel). The black area represents the insensitive part of the detector. The DBNPs with similar 2D SAXS pattern are classified into same category.

7.3.2. 2D SANS patterns

Dispersions prepared for SANS measurements are filled in 110 type Hellma cells which are ~ 10 mm wide and ~ 1 mm thick. The sample preparation is described in chapter 4. The beam size of the neutron beam on a sample is 6×8 mm² (width x height). Different parts of the sample cell cannot be focused using neutron beam in SANS done with SAXS experiments. Here, the neutron beam is incident at the center

of Hellma cells. For well-stabilized dispersions, the behavior of NPs in the gauged volume is representative of the entire volume of the dispersion. However, in DBNPs, the gauged volume concentration varies due to the formation of supernatant and particle-phase combined with a macroscopic response to the field. The 2D SANS patterns collected for four DBNPs in fields ranging from 0-3 T are displayed in Fig. 7.5.

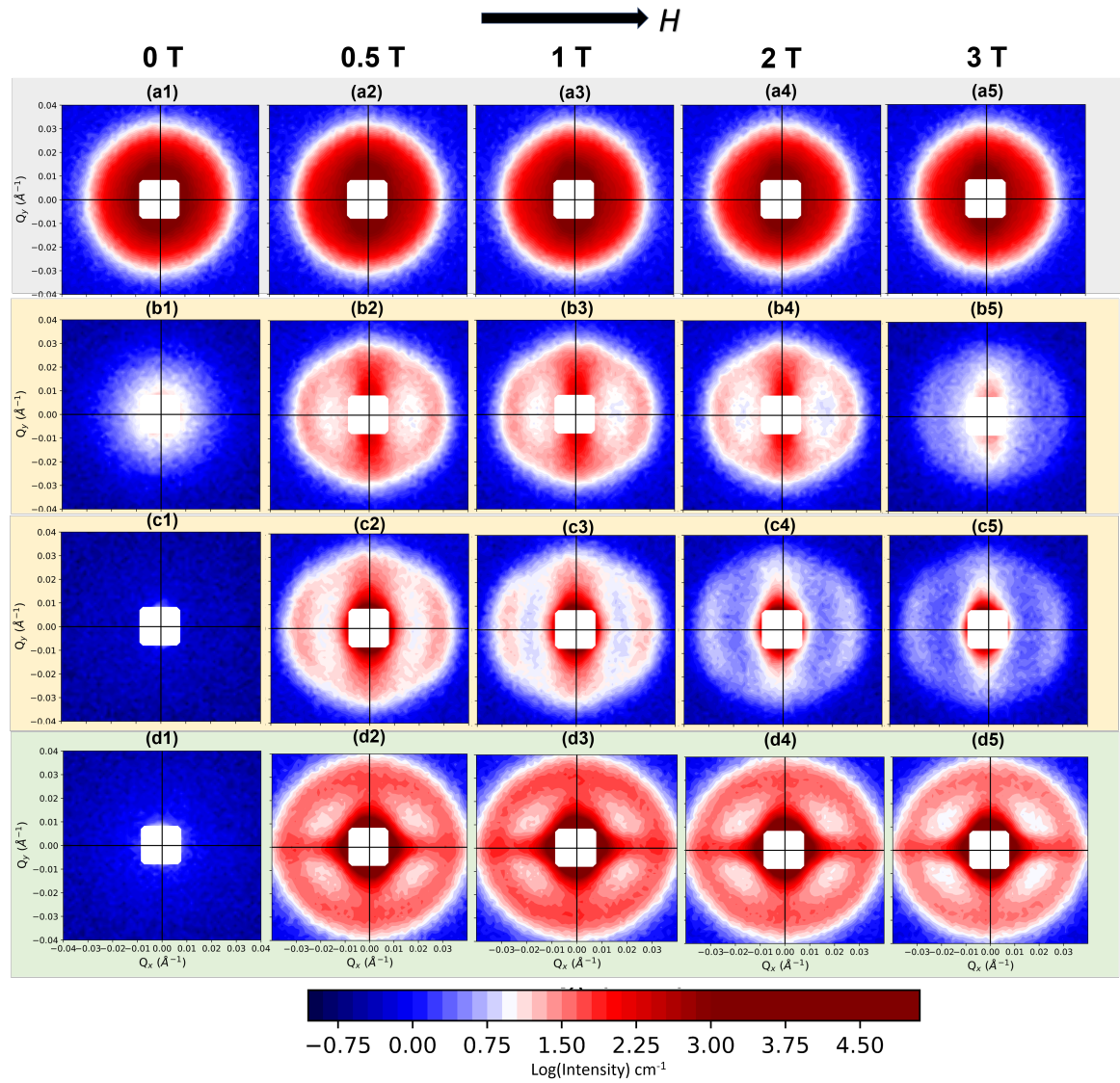


Figure 7.5.: 2D SANS patterns of (a1-a5) A12F10, (b1-b5) A13F14, (c1-c5) A9F11, and (d1-d5) A10F14 DBNPs in the field ranging from 0 T to 3.3 T. The horizontal panels from left to right displays the 2D pattern collected at 0, 0.5, 1, 2 and 3 T for respective sizes.

The anisotropy in the 2D patterns for their respective sizes at 1 T concurs with SAXS at a similar field. Additionally, even at the highest applied field of 3 T, there are no visible changes in the pattern of A12F10, indicating the non-assembling and homogeneous phase of DBNPs. On the other hand, the remaining three DBNPs show anisotropy in the 2D SANS pattern. There is a visible drop in intensity at low and high fields in these cases and the reasons are illustrated in Fig. 7.6. The particles are still sedimented at the bottom of the cells in low fields. The maximum scattering intensity is recorded for intermediate fields since the gauged volume contains DBNPs lifted due to the magnetic field gradient. The intensity further drops at high fields due to a strong attraction of particle phase to the magnets' pole. The patterns remain stable and the intensity is invariant at a fixed field for 1 hr of data acquisition, regardless of how the field was applied.

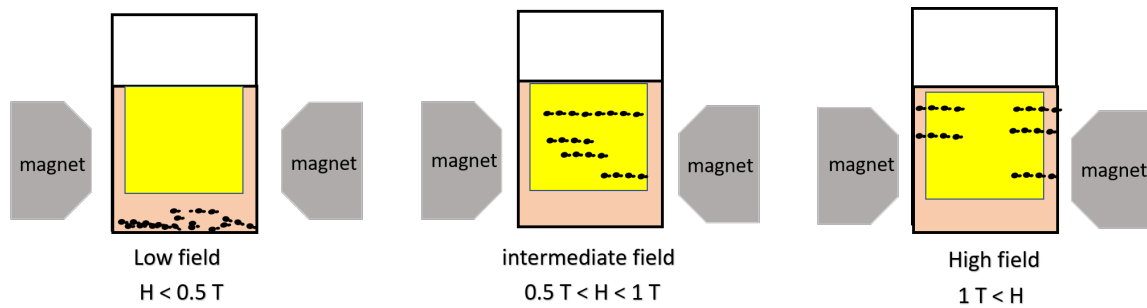


Figure 7.6.: The loss of intensity in the 2D SANS patterns at low and high fields is due to the inhomogeneous sample and the limited size of the neutron beam (shown by the yellow region). (a) At low fields, magnetic forces compete with phase separation and sedimentation forces. (b) In the intermediate field region, magnetic forces lift the particle phase to displace the supernatant. (c) Strong fields further tear apart the assemblies to pull the DBNPs to the edge of the cells resulting in lowered intensities.

7.4. Types of assemblies and analysis methods

Through visual analysis, it is evident that different types of assemblies are formed in A13F14, A9F11 and A10F14 while A12F10 indicates no such formation. Based on the scattering patterns, we classify the DBNPs in to three main categories;

1. **Category-O:** In A12F10, the 2D SAXS and SANS pattern have elongation at the centre and remain isotropic at high Q in all fields. These DBNPs orient and do not indicate any assembly.

2. **Category-I:** The stripe pattern is present in both A9F11 and A13F14. However, there is an additional diffuse ring in A13F14. From chapter 5 on IONPs, such 2D patterns are signature of 1D chains assemblies.
3. **Category-II:** The cross pattern of A10F14 is unique and with indication of assemblies in two directions resulting in 2D chains.

The two most common approaches to analyze such scattering patterns are (i) radial analysis and (ii) sectoral analysis.

The DBNPs are much more complex and the form factor of a multicomponent realistic dumbbell model is currently not available on SAXS/SANS data analysis softwares. The analytical form-factor derivation of DBNP described in the outlook will provide a means to analyze these DBNPs systematically. Nonetheless, before building a more sophisticated model, an alternative analysis of the particle morphology begins with inspection of asymptotic behaviour using shape independent Guinier-Porod models. Further, applying scattering contrast assumptions we can fit spherical models on the radially integrated 1D SAXS and SANS data. To avoid any loss of information through radial averaging, the 2D SAXS and SANS intensities are integrated in a sector of width 20° centered on an axis parallel ($\alpha = 0^\circ$) and perpendicular ($\alpha = 90^\circ$) to the applied magnetic field. Here, α is the angle between scattering vector \vec{Q} and applied field \vec{H} . The peak obtained from the integrated intensities are fit to Gaussian model to obtain the peak positions and peak width. The peaks position (Q_{pp}) corresponds to the distance between particles (ℓ) and peak width (w) to correlation length ζ in real space. These parameters are in general defined as

$$\ell = \frac{2\pi}{Q_{pp}} \quad (7.1)$$

$$\zeta = \frac{2\pi}{w} \quad (7.2)$$

where $\ell = \ell_{\parallel}, \zeta = \zeta_{\parallel}$ are interparticle distances for the sector parallel to the field. Correspondingly, $\ell = \ell_{\perp}, \zeta = \zeta_{\perp}$ are correlation lengths for sector perpendicular to the applied magnetic field. Albeit corresponding parameters have been determined in assemblies formed by IONPs in Chapter 5, there are some crucial differences for DBNPs as listed below ;

- The center-to-center distance is no longer trivial as for spherical IONPs.
- The multicomponent and unique morphology can be accounted through two

aspect ratios A_1 and A_2 defined in chapter 6. Here, A_1 can be associated with the shape factor of the whole DBNP while A_2 to the shape of the magnetic IONP.

- The phase of IONPs remains homogeneous and the dispersion remains stable in the entire time frame of the experiment. However, instantaneous phase separation and formation of macroscopic assemblies in DBNPs can result in non-trivial analysis.

7.5. Category O: No assemblies

In this section, The results from the 1D analysis of the SAXS (see Fig. 7.4 (a-b)) and SANS scattering patterns (see Fig. 7.5 (a1-a5)) of A12F10 DBNPs are discussed. These patterns belongs to a category of DBNPs where no assemblies were inferred from direct visualisation.

7.5.1. Radial analysis

A simplified analysis on radially integrated 1D SAXS at 0 T and 0.9 T of A12F10 DBNP follows fitting the entire data range with the Guinier-Porod model as shown in Fig. 7.7 (a) (see chapter 2, section 2.3 for details about the model). Since DBNP

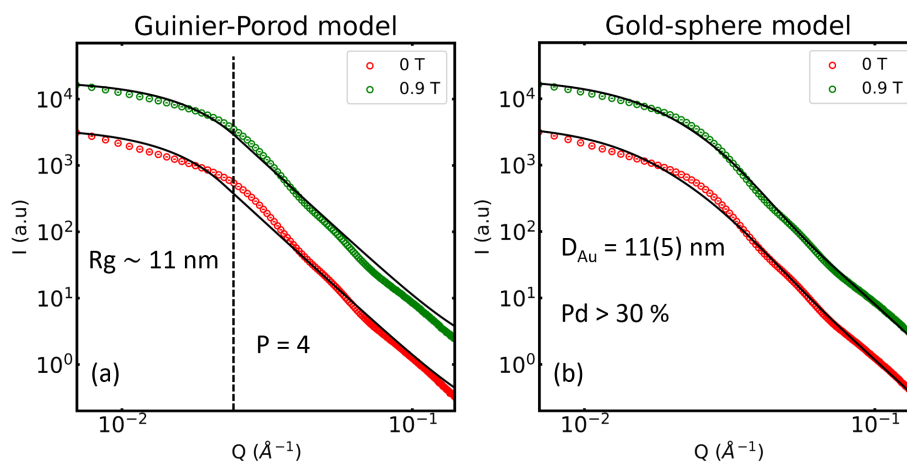


Figure 7.7.: SAXS fits of A12F10 ; radially integrated SAXS intensities of A12F10 at 0 T (red) and 0.9 T (green) fit to (a) Guinier-Porod model to fit asymptotic limits and (b) a gold sphere model. The intensities are scaled for visualization.

is a 3D object, the dimension variable s is set to 0 and the slope at high Q follows the behaviour with Porod exponent $P = 4$. The radius of gyration obtained from the fits corresponds to $R_g \sim 11$ nm for 0T. Further, since the x-ray SLD of Au is almost three times than that for IONPs (see Fig. 7.1 (a)), a simplistic model containing non-interacting Au spheres is employed to fit the data (Fig. 7.7 (b)). The SLD of Au ($\eta_{core} = 1.23 \times 10^{-4} \text{\AA}^{-2}$) and h-tol ($\eta_{solvent} = 8.03 \times 10^{-6} \text{\AA}^{-2}$) is fixed for this model, while the diameter of Au and the size distribution parameters are refined. The mean diameter $D_{core} = 11$ nm with very large size distribution describes the data. From the scattering data, it is also impossible to determine simultaneously the shape and size distribution of a polydisperse system. Hence for this model, the large polydispersity is an indication of the deviation from its spherical shape. Albeit the large size distribution, the mean value of the diameter is in fair agreement with the diameter of gold (L_D) obtained from TEM for such a simplistic model fit.

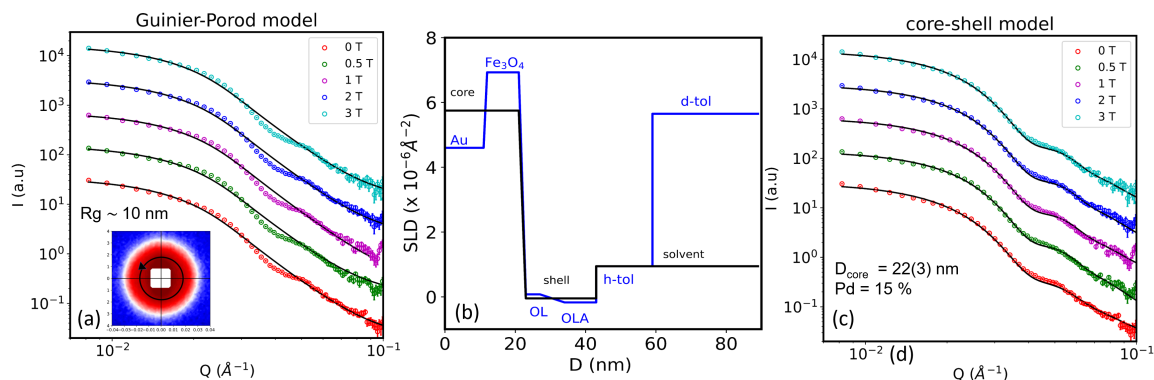


Figure 7.8.: (a) Radially integrated SANS intensities of A12F10 DBNP in fields ranging from 0-3 T, where the solid black lines are fits to Guinier-Porod model, bottom inset: The isotropic 2D SANS pattern of A12F10 DBNP at 1 T. The intensities integrated along the black ring represents the intensity at a single Q value. The integrated intensities are plotted as function of Q for radial analysis. (b) The blue solid line is the neutron SLD of the original DBNP system and the black solid line is the calculated SLD of the composite core-shell model used to describe A12F10. (c) SANS 1D data of A12F10 at various fields fit to a composite core-shell model described in (b).

Following the similar analysis for SANS data at various fields, the radially integrated intensities are fit to Guinier-Porod model by setting $s = 0$ and $P = 4$ (Fig. 7.8 (a)). The obtained radius of gyration $R_g \sim 10$ nm is in fair agreement with value obtained from x-rays. This value is about half the length of the entire DBNP estimated from

TEM ($\sim \frac{L_D}{2}$). As discussed in chapter 2, intensities integrated along different orientations assuming homogeneous particles result in spherical and core-shell form-factor descriptions that are simpler to calculate and easier to reconstruct from scattering data. In section 2.5.6, the equation (2.118), clearly demonstrates how the overall scattering length density $\rho(\vec{r})$ of the system depends on the SLD of the solvent (η_o) and the SLD of the particle ($\hat{\eta}_p(\vec{r}, \vec{\Theta})$) summed over the entire particle ensemble. Here, η_o is a constant value that is dependent on the embedded environment of the particle. On the other hand, particle SLD $\hat{\eta}_p(\vec{r}, \vec{\Theta})$ depends on the internal homogeneity and the particle orientation ($\vec{\Theta}$). Therefore, it becomes impossible to get an unique reconstruction of an arbitrary inhomogeneous 3D structure without additional *a priori* information. Since the radially integrated intensities cannot differentiate scattering along various orientations, we assume a composite core-shell spherical model to fit the 1D scattering data. Here the SLD of the Au-IONP composite core is calculated as

$$\eta_{core} = \frac{V_A}{V_D} \eta_{Au} + \frac{V_F}{V_D} \eta_F \quad (7.3)$$

where V_A and V_F is the volume of Au and IONP, component in the DBNP respectively with total volume $V_D = V_A + V_F$. Additionally, $\eta_{Au} = 4.6 \times 10^{-6} \text{ \AA}^{-2}$ and $\eta_F = 6.63 \times 10^{-6} \text{ \AA}^{-2}$ is the calculated neutron SLD of Au and IONP(magnetite), respectively. Using the geometric length scales defined in the Fig. 6.1 and determined from TEM in the previous chapter, we calculate

$$V_A = \frac{4}{3} \pi \left(\frac{L_A}{2} \right)^3 \quad (\text{gold-sphere}) \quad \text{and} \quad V_F = \frac{4}{3} \pi \left(\frac{L_F}{2} \right)^2 \frac{D_F}{2} \quad (\text{IONP ellipsoid}). \quad (7.4)$$

The value of $\eta_{core} = 5.75 \times 10^{-6} \text{ \AA}^{-2}$ for A12F10 DBNPs. Further, the composite shell SLD consisting of (1:1) mix of OA and OLA is calculated as follows:

$$\eta_{shell} = 0.5\eta_{OA} + 0.5\eta_{OLA} \quad (7.5)$$

where, $\eta_{OA} = 0.077 \times 10^{-6} \text{ \AA}^{-2}$ and $\eta_{OLA} = -0.172 \times 10^{-6} \text{ \AA}^{-2}$ are the neutron SLDs of OA and OLA, respectively. Using the above mentioned practical considerations, the SLD model is constructed as shown in Fig. 7.5 (b) and employed to generate fits to field dependent data in Fig. 7.5 (c). The average diameter of this composite core, obtained from the fits, is $D_{core} = 22 \pm 3 \text{ nm}$, with shell thickness $t_{shell} = 3.3 \pm 0.5 \text{ nm}$. The uncertainties in the fit values are determined from size distribution or the polydispersity index which is about 15 % for this model. The thickness of the shell

may be overestimated due to poor contrast between shell and solvent of the system. However, the polydispersity is in agreement with the size distribution obtained from TEM. As summarized in Fig 7.9, it is instructive to compare the length scales of DBNPs from various experiments to resolve its structure. The length of DBNP, $L_D = 22$ nm with 15% size distribution, is in reasonable agreement from TEM, SAXS and SANS experiments.

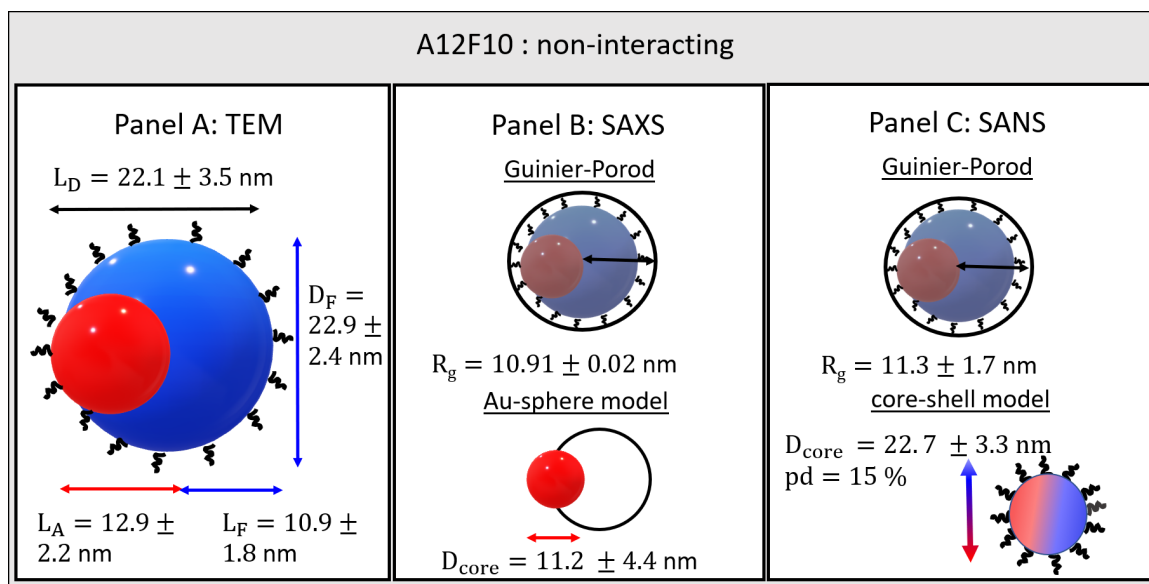


Figure 7.9.: Summary of various geometric parameters of A12F10 DBNP determined from (Panel A) TEM image analysis, (Panel B) SAXS and (Panel C) SANS analysis.

7.6. Category I: 1D chains with disorder

Among the three assembling DBNPs, the stripe and diffused ring pattern observed in SAXS (Fig. 7.4 (g-h)) and SANS (Fig. 7.5 (d1-d5)) of A13F14 are discussed in this section.

7.6.1. Radial analysis

Radial integrated SAXS and details of the modelling functions can be obtained from the appendix. For radially integrated SANS at various fields, equations (7.3), (7.4) and (7.5) are employed to calculate core and shell SLD for A13F14 DBNPs to yield $\eta_{core} = 5.88 \times 10^{-6} \text{ \AA}^{-2}$ and $\eta_{shell} = -0.0475 \times 10^{-6} \text{ \AA}^{-2}$, respectively. The results of the

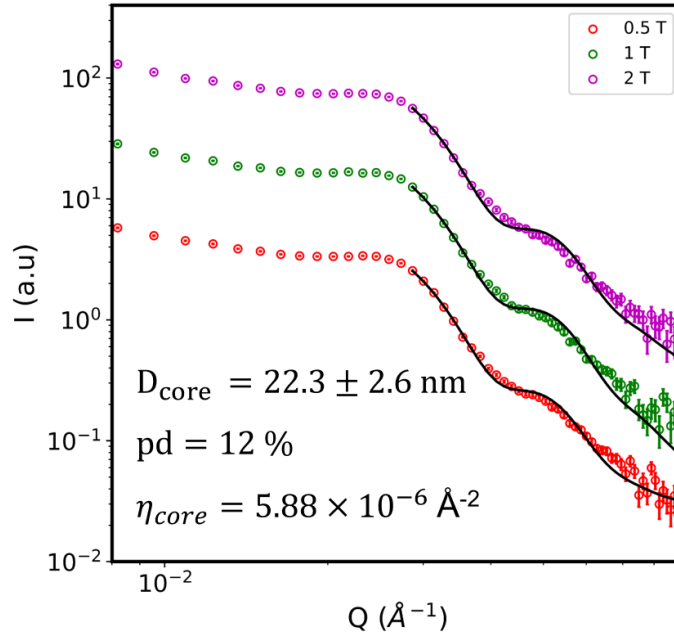


Figure 7.10.: SANS 1D data of A13F14 at 0.5, 1 and 2 T fit to composite core-shell model constrained to high Q . Black solid lines are fits to data. The result of the fits are given in the appendix.

composite core-shell model are as shown in Fig. 7.10. The refined diameter of the composite core is $D_{\text{core}} = 22.3 \pm 2.6$ nm with 12 % size distribution and shell thickness $t_{\text{shell}} = 7.0 \pm 0.8$ nm. The errors in the fit value are calculated from the polydispersity in the core. The shell thickness maybe overestimated due to poor contrast conditions with solvent.

7.6.2. Sectoral analysis

The sectorally integrated intensities, as presented in Fig. 7.11 (a) and (b) for SAXS and SANS data, are fit to Lorentzian and Gaussian functions, respectively. The correlation distances (ℓ_{\parallel}) and lengths (ζ) are determined, and plotted as a function of applied magnetic field (see Fig. 7.11 (c-d)). Due to its phase separation and macroscopic response to field, it is difficult to separate the absolute intensities from supernatant and particle phase. The chain lengths may vary as result of the strong field gradient and the inability to gauge the entire sample. Nevertheless, at intermediate fields ($0.5 \text{ T} < H < 1 \text{ T}$) the average correlation length remain fairly constant for SANS data and is equivalent to the value determined from SAXS peak at 0.9 T. The uncertainties plotted as error bars, are determined from the residuals of the fitting

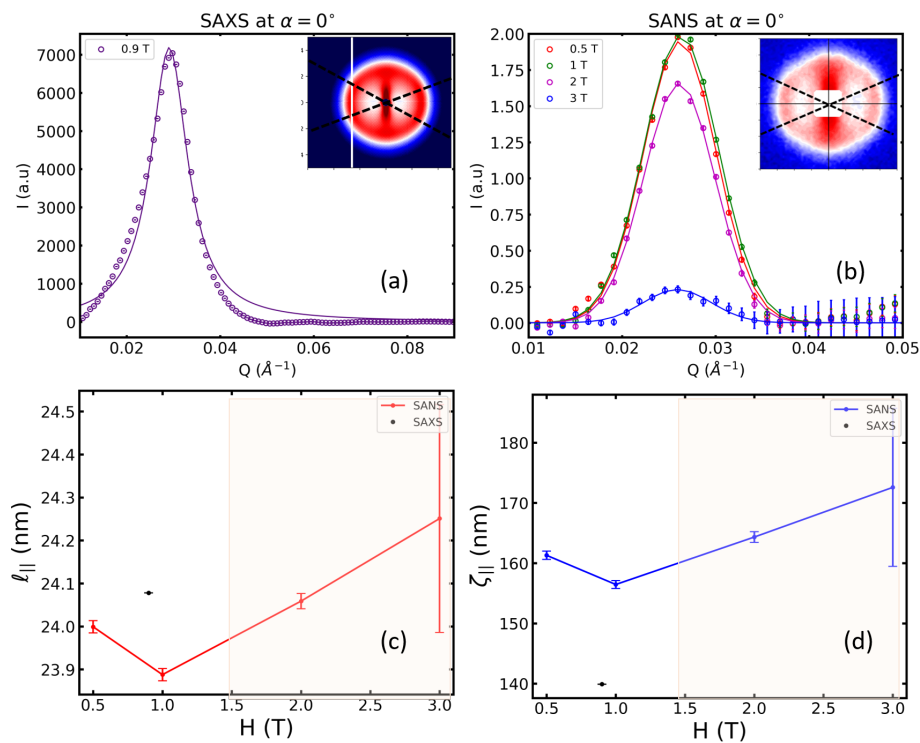


Figure 7.11.: 1D integrated (a) SAXS intensity peak at 0.9 T and (b) SANS intensity peaks at 0.5, 1, 2 and 3 T of A13F14 DBNPs along the sector parallel to the magnetic field. Insets: 2D patterns and parallel sectors depicted as dashed lines. Both (a) and (b) are baseline subtracted and the solid lines are fits to Lorentzian and Gaussian model functions, respectively. (c) The correlation distances $\ell_{||}$ and (d) chain length $\zeta_{||}$ obtained from the peak position and width, respectively plotted as a function of applied field. The shaded region in (c) and (d) indicates high field region with observed drop in intensity due to measurement of supernatant phase.

function and is very low ($\sim 0.02 - 0.08$ nm) due to excellent fit of the peak function. Thus, the average correlation distance for SAXS and 1 T obtained from SANS at various fields is $\ell_{\parallel} \sim 24.1(1)$ nm. Here, the error value of 0.1 nm is deviation of the average value from correlation distances at various fields. Similarly, the average chain lengths from SANS is $\zeta_{\parallel} = 163.6 \pm 4.8$ nm and longer than chains observed with SAXS $\zeta_{\parallel} = 139.9$ nm. Due to dynamic behaviour of chains in field, the chain lengths may vary and cannot be ascertained absolutely. All parameters from TEM image analysis,

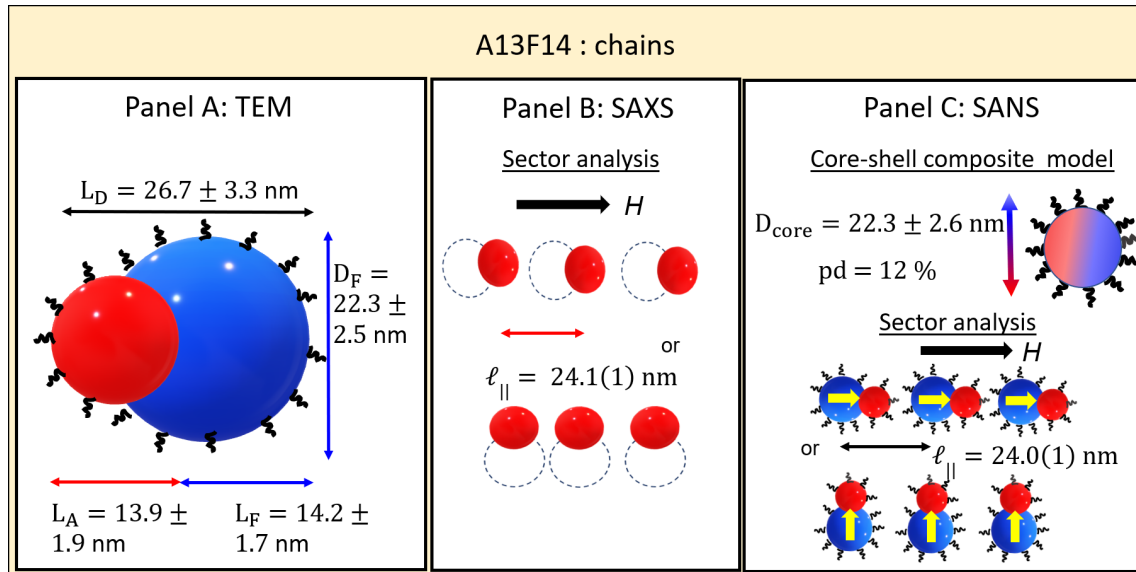


Figure 7.12.: Summary of various geometric parameters of A13F14 DBNPs determined from (Panel A) TEM image analysis, (Panel B) SAXS and (Panel C) SANS analysis.

radial and sectoral analysis of SAXS and SANS data are visualized in Fig. 7.12. The diameter and polydispersity of the composite core-shell model are in close agreement with L_D and size distribution determined from TEM. Comparing the length scales of DBNP from SAXS and SANS sector analysis we note that the $D_F \sim L_D \sim \ell_{\parallel}$. Thus, we cannot distinguish between head-to-tail and side-by-side arrangement of particles.

7.7. Category I: 1D chains

The analysis of the stripe pattern observed from SAXS (Fig. 7.4 (c-d)) and SANS (Fig. 7.5 (b1-b5)) of A9F11 DBNPs are discussed in this section.

7.7.1. Radial analysis

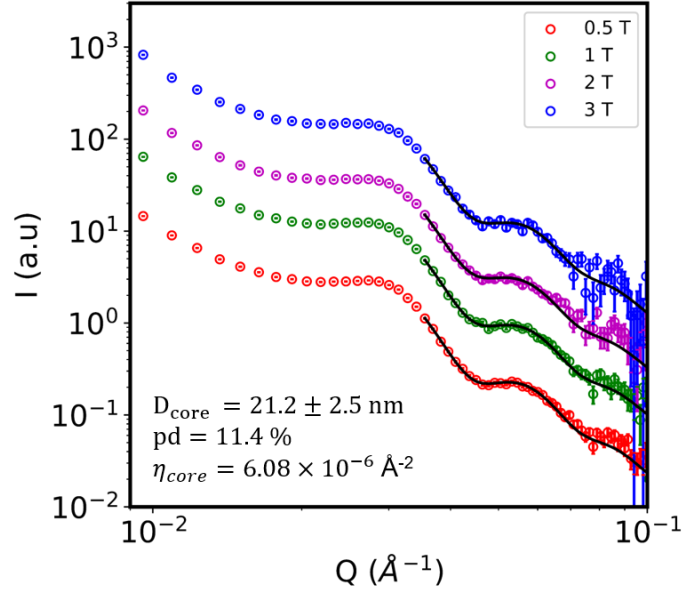


Figure 7.13.: (a) SANS 1D data of A9F11 at 0.5, 1, 2 and 3 T fit to composite core-shell model constrained to high Q . Black solid lines are fits to data and are scaled for visualization. The result of the fits are given in the appendix.

The composite core-shell model adapted from the previous section to A9F11 DBNPs results in $\eta_{core} = 6.08 \times 10^{-6} \text{ \AA}^{-2}$ and $\eta_{shell} = -0.0475 \times 10^{-6} \text{ \AA}^{-2}$. The radially integrated SANS intensities are fit to the composite core-shell model as shown in Fig. 7.13. The average of refined diameters obtained from such composite core-shell model at various fields is $D_{core} = 21.2 \pm 2.5 \text{ nm}$ with 11.4 % polydispersity index. The average diameter and polydispersity is in fair agreement to the overall length of the DBNP L_D and size distribution obtained from TEM image analysis.

7.7.2. Sectoral analysis

The analysis of the SANS and SAXS sector integrated intensities along the applied field for A9F11 DBNPs is summarized in the Fig. 7.14. The 2D pattern resembles the pattern observed for single phase IONPs. In chapter 5, the increase in correlation distance with field is attributed to the bending and straightening of chains. Such field dependent changes are difficult to separate due to phase separation in DBNPs. For chains made of DBNPs, the average correlation distance is $\ell_{\parallel} \sim 19.4(1) \text{ nm}$ and

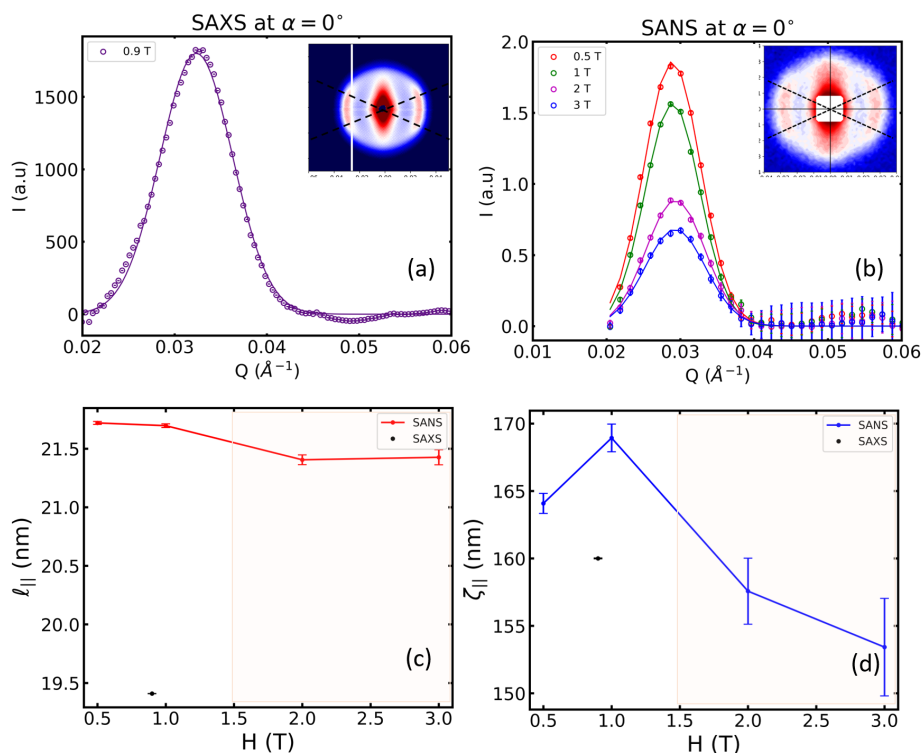


Figure 7.14.: 1D integrated (a) SAXS intensity peak at 0.9 T and (b) SANS intensity peaks at 0.5, 1, 2 and 3 T of A9F11 DBNPs along the sector parallel to the magnetic field. Insets: 2D patterns and parallel sectors depicted as dashed lines. Both (a) and (b) are baseline subtracted and the solid lines are fits to Gaussian model function. (c) The correlation distances $\ell_{||}$ and (d) chain length $\zeta_{||}$ obtained from the peak position and width, respectively plotted as a function of applied field. The shaded region in (c) and (d) indicates high field region with observed drop in intensity due to measurement of supernatant phase.

21.6(1) nm from SAXS and SANS, respectively. This closely corresponds to the L_D value from TEM. The correlation distances confirm that A9F11 DBNPs are arranged in a head-to-tail configuration as summarized in Fig. 7.15. The average length of chains in these DBNPs obtained from SANS ($\zeta_{||} = 161.0 \pm 5$ nm) is in agreement with value obtained from SAXS.

7.8. Category II: 2D chain assemblies

Among all the self-assembling DBNPs, the cross pattern of A10F14, observed in SAXS (Fig. 7.4 (e-f)) and SANS (Fig. 7.5 (c1-c5)), is a unique pattern that has not been

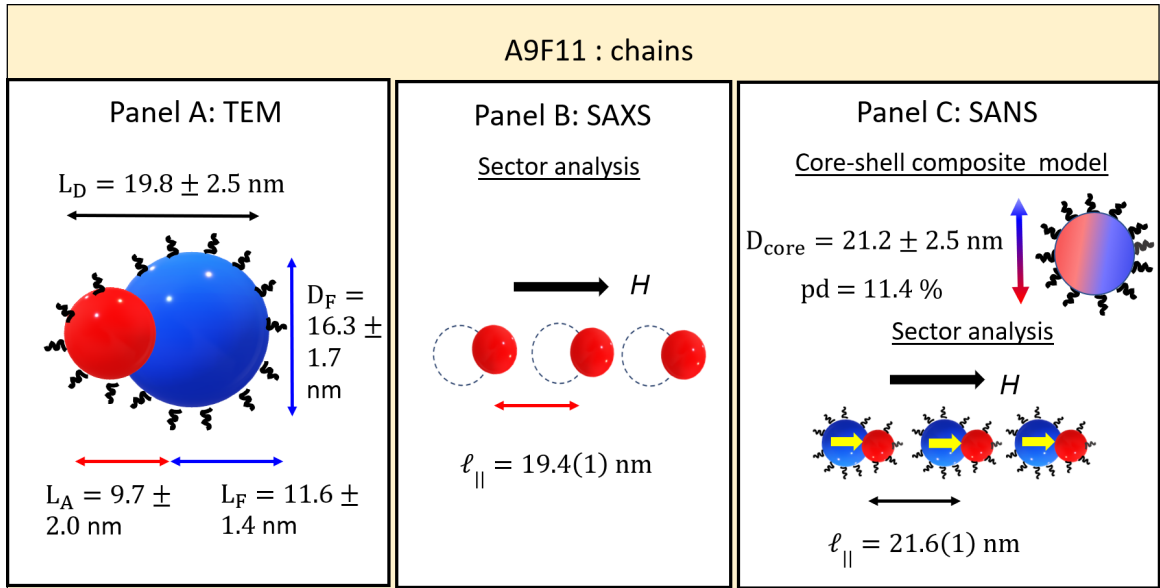


Figure 7.15.: Summary of various geometric parameters of A9F11 DBNPs determined from (Panel A) TEM image analysis, (Panel B) SAXS and (Panel C) SANS analysis.

previously observed in NPs to the best of our knowledge.

7.8.1. Radial analysis

The radially integrated SANS intensities are fit to the composite core-shell model as shown in Fig. 7.16. The core and shell SLD from the calculation is set to $\eta_{core} = 6.15 \times 10^{-6} \text{ \AA}^{-2}$ and $\eta_{shell} = -0.0475 \times 10^{-6} \text{ \AA}^{-2}$, respectively. The diameter of the composite core is refined to $D_{core} = 18.4$ nm with 12 % size distribution. This value corresponds to length D_F obtained from TEM analysis. Details of the fit are provided in the appendix.

7.8.2. Sectoral analysis

The peak positions obtained from sector aligned along field ($\alpha = 0$), as shown in Fig. 7.17 for SAXS and SANS, corresponds to $\ell_{||} = 18.78(7)$ nm and $\ell_{||} = 18.03(7)$ nm, respectively. The numerical results of the fit are provided in the appendix. The errors in parenthesis corresponds to the average of the deviations of mean value from $\ell_{||}$ attained at each field point. These peak positions are in fair agreement to the diameter of the IONP (D_F) determined from TEM. Additionally, in the sector perpendicular to the field, peaks are observed in the case of SANS and is absent in

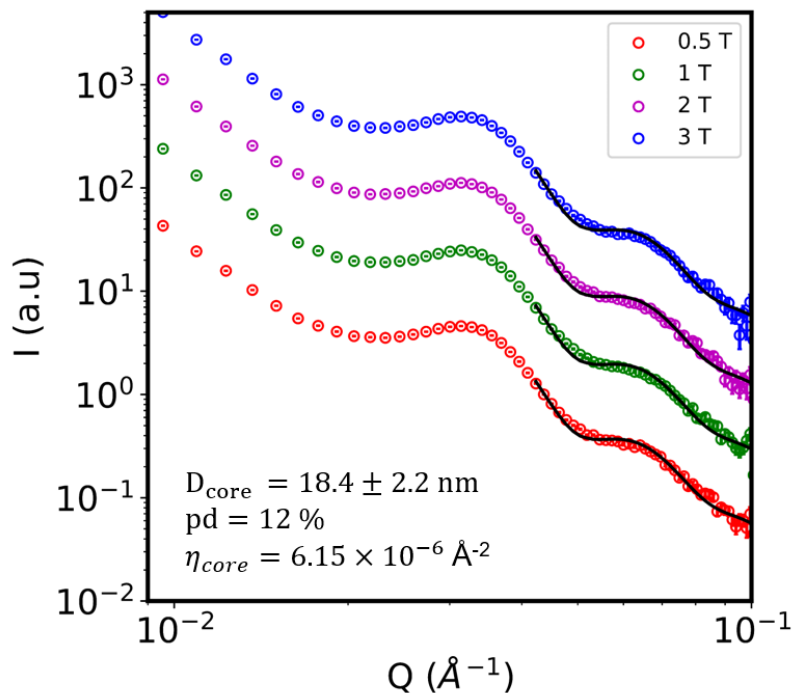


Figure 7.16.: 1D radially integrated SANS intensity of A10F14 at 0.5, 1, 2 and 3 T fit to composite core-shell model constrained to high Q . Black solid lines are fits to data and are scaled for visualization. The result of the fits are given in the appendix.

SAXS (see Fig. 7.18). The average correlation distance is $\ell_{\perp} = 19.82(3)$ nm which is different by 1 nm to the parallel arrangement. The chain lengths in both direction are equivalent $\zeta_{\parallel} \sim \zeta_{\perp} = 158(3)$ corresponds to 8-9 particles in both parallel and perpendicular direction in magnetic field. The cross pattern describes the onset of 2D ordering in these DBNPs, hence such ordering must be present in SAXS. The peaks in direction perpendicular may also have magnetic origin. In this particular DBNPs, for a single contrast variation experiment, the contrast was adjusted by extracting DBNPs and redispersing in solvent containing 78 % d-tol and 22 % h-tol. In this ratio, the solvent matches the contrast of the Au component in the DBNPs. The cross pattern is clearly visible in the SANS pattern at 1 T field as displayed in Fig. 7.19 (a). The peaks from the sector parallel and perpendicular to the applied field results in correlation distances corresponding to 18.1(1) nm and $\ell_{\perp} \sim 19.21(2)$ nm, respectively (see Fig. 7.19 (b-c)). A summary of the various length scales obtained from scattering and image analysis are presented in the Fig. 7.20. The length scales suggest that DBNPs arrange in side-by-side configuration. The peaks in perpendicular

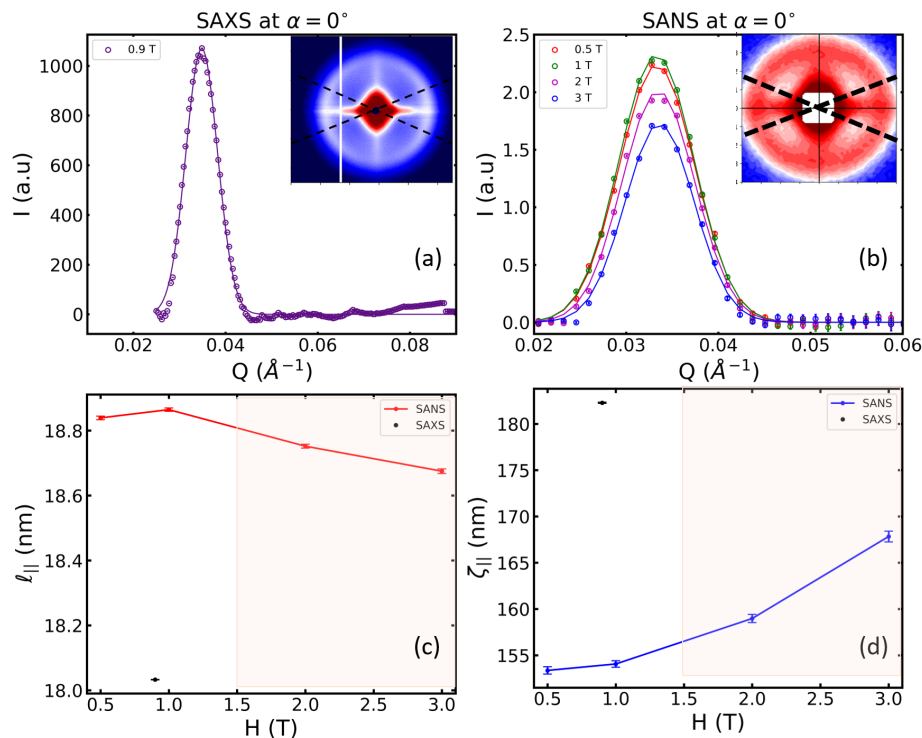


Figure 7.17.: 1D integrated (a) SAXS peak at 0.9 T and (b) SANS peaks at 0.5, 1, 2 and 3 T of A10F14 DBNPs along the sector parallel to the magnetic field. Insets: 2D patterns and parallel sectors depicted as dashed lines. Both (a) and (b) are baseline subtracted and the solid lines are fits to Gaussian model function. (c) The correlation distances $\ell_{||}$ and (d) chain length $\zeta_{||}$ obtained from the peak position and width, respectively plotted as a function of applied field. The shaded region in (c) and (d) indicates high field region with observed drop in intensity due to measurement of supernatant phase.

sector of the 2D SANS data indicates that the arrangement of chains extends in both direction resulting in what we term as 2D chains. In the perpendicular direction, the alignment of magnetic dipoles in side-by-side configuration would result in repulsion possibly leading to unstable structures perpendicular..

7.9. Orientation of Particles

The appearance of cross pattern in A10F14 DBNP requires a more careful treatment of integrated intensities in several directions. Although, sectoral analysis provides quantitative information about distances, there is a need to analyse the entire 2D pattern as done with RMC simulations on IONPs. However, the dumbbell form-

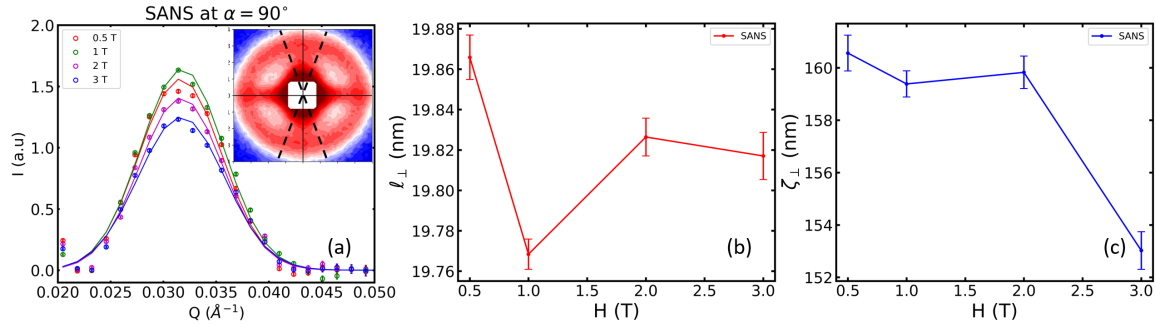


Figure 7.18.: (a) The 1D SANS integrated intensity peak of A10F14 DBNP at 0.5, 1, 2 and 3 T along the sector perpendicular to the applied field. Insets: 2D SANS pattern of A10F14 and sector represented by dashed lines. These peaks are baseline subtracted and the solid lines correspond to the fits using Gaussian peak model. (b) The correlation distances ℓ_{\perp} and (c) chain lengths ζ_{\perp} are plotted as a function of applied field. The shaded region in (b) and (c) indicates high field $H > 1$ T field region with observed drop in intensity due to dynamic nature of the assembly.

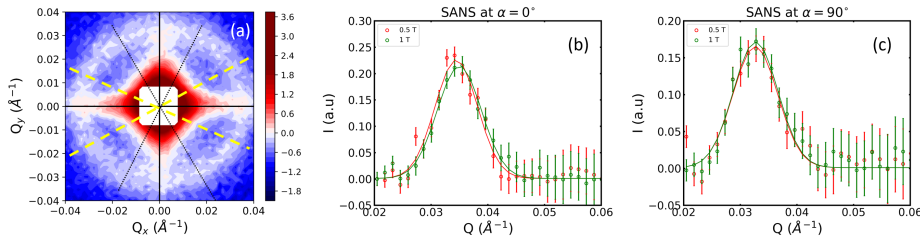


Figure 7.19.: (a) The 2D SANS pattern of A10F14 at 1 T dispersed in 78 % d-toluene. The dashed yellow lines represents the sector along the applied field ($\alpha = 0^{\circ}$) and black dotted line represents the sector perpendicular to the field ($\alpha = 90^{\circ}$). Peak integrated intensity along the sector centered at (b) $\alpha = 0^{\circ}$ and (c) $\alpha = 90^{\circ}$.

factor based on two sphere model does not truly describe the various aspect ratios involved. Based on the particle arrangement information obtained from various MNPs and fundamental principles of scattering outlined in chapter 2, following empirical remarks describe the general features in 2D scattering patterns of assemblies;

- In case of non-interacting randomly oriented IONPs and DBNPs, the 2D SAS pattern is isotropic irrespective of the individual particle form-factor. This resembles the 2D SAS pattern for F05, F10, F20 and F21 IONPs at all fields and A12F10 DBNPs at 0 T. This is schematically shown in Fig. 7.21 (a).
- The vertical stripes pattern is a result of horizontal chains of IONPs and DBNPs.

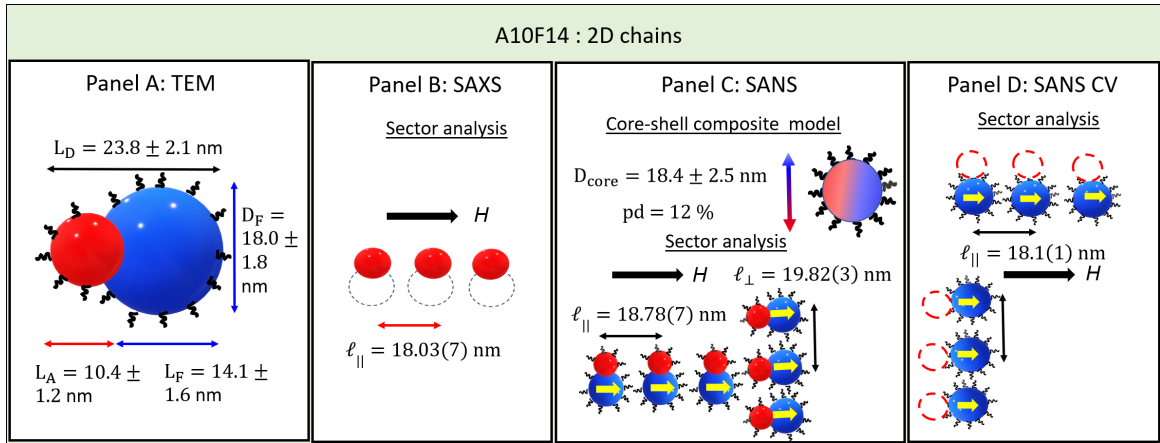


Figure 7.20.: Summary of various geometric parameters of A10F14 DBNP determined from (Panel A) TEM image analysis, (Panel B) SAXS, (Panel C) SANS and (Panel D) SANS with contrast variation analysis.

Such stripe patterns are visible for F27 IONPs, A9F11 and A13F14 DBNPs. The stripes in the direction perpendicular to applied fields are strong indicators of chain formation (see Fig. 7.21 (b)).

- Various orientations of the DBNP have different projection on detector plane. The A12F10 DBNPs in field results in elongated pattern at low Q , These DBNPs orient in the field without forming higher ordered structures (see Fig. 7.21 (c)).
- The stripe patterns F27 IONPs at low fields and A9F11 and A13F14 DBNPs appear as curved strips. This is attributed to misalignment of the particles in the chain (see Fig. 7.21 (d)). The distance between the peaks correspond to the correlation distances.
- Extrapolating from the above observations, one can expect for spherical IONPs arranged in direction parallel and perpendicular to the field results in the 2D SAS pattern sketched in Fig. 7.21 (e). Such 2D assemblies with IONPs are rarely stable and not usually observed with scattering.

Particles with simpler shape such as spherical IONPs, the scattering intensity can be described by analytical or semi analytical expressions [198]. When particles assume complicated shapes, it is not possible to represent scattering merely with simple expressions. To describe the anisotropic particle such as DBNP, the reference orientation of DBNP was to be considered as shown in Fig. 7.22 (a). The incident beam of x-rays or neutrons is along the z-axis. The particle coordinates (a,b and c)

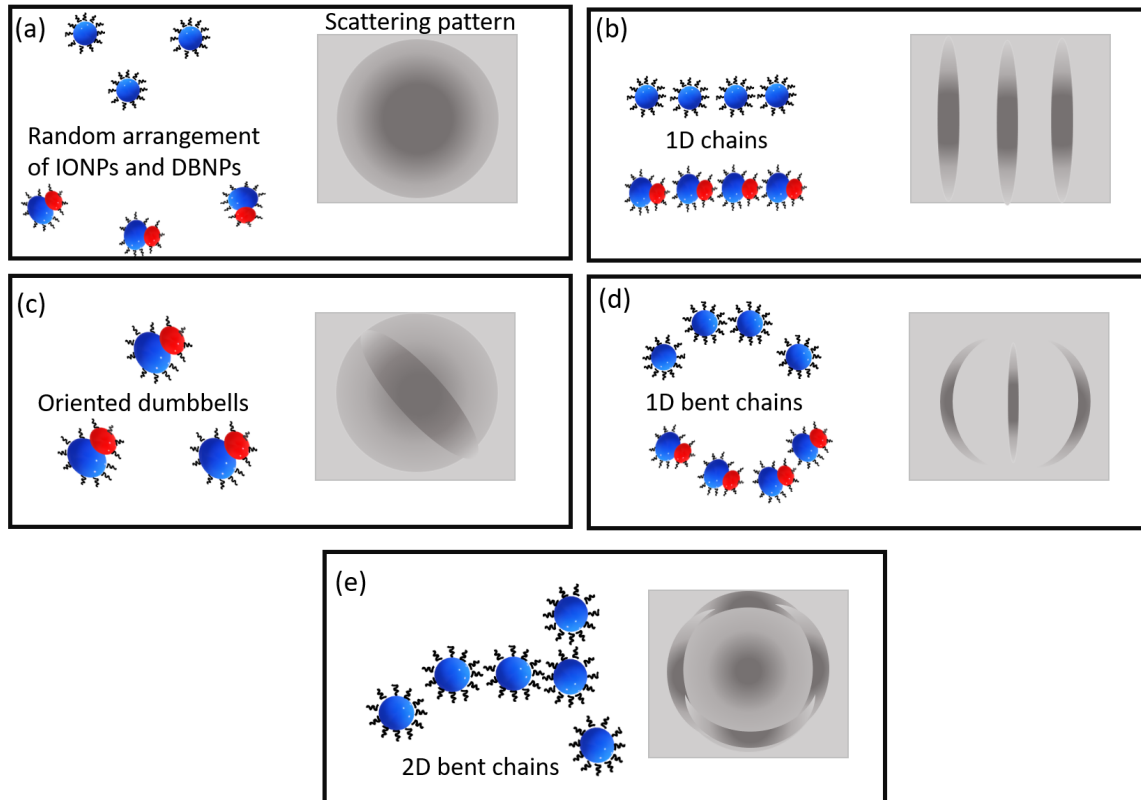


Figure 7.21.: Sketch of expected 2D SAS detector pattern due to scattering from (a) non-interacting ensemble of randomly oriented spheres or dumbbells, (b) IONPs and DBNPs in a chain, (c) oriented dumbbells, (d) misaligned chains containing spherical and dumbbells and (e) spherical particles arranged into chains extending in both directions.

are defined using three angle namely ϕ, θ and ψ . Angles ϕ, θ define orientation of the c -axis of the particle and ψ rotation about c axis. Determination of orientation is obscure when the DBNP axis aligns along the z -axis which is unavoidable. When the particle orientation is changed, the projections change and therefore the 2D scattering pattern also change. In softwares such as *SasView*, while considering form factor of anisotropic objects such as ellipsoids and cylinders, the orientational distribution is fit by performing numerical integrations at these angles. Hence, we could fit the same 1D DBNP data with spherical model. However, they have to be carefully considered while performing 2D fits [199]. The angle θ , initially in the $x-z$ plane, is considered first followed by the rotation ϕ about the z axis. Using this information about oriented particles, the cross pattern in 2D scattering pattern of A10F14 emerges as a result of the inherent anisotropy in the DBNP combined with particle arrangement. The 2D chains formed with these particles have different projection on the detector

plane resulting in the elongation along both directions for the scattering pattern as shown in the Fig. 7.22 (b).

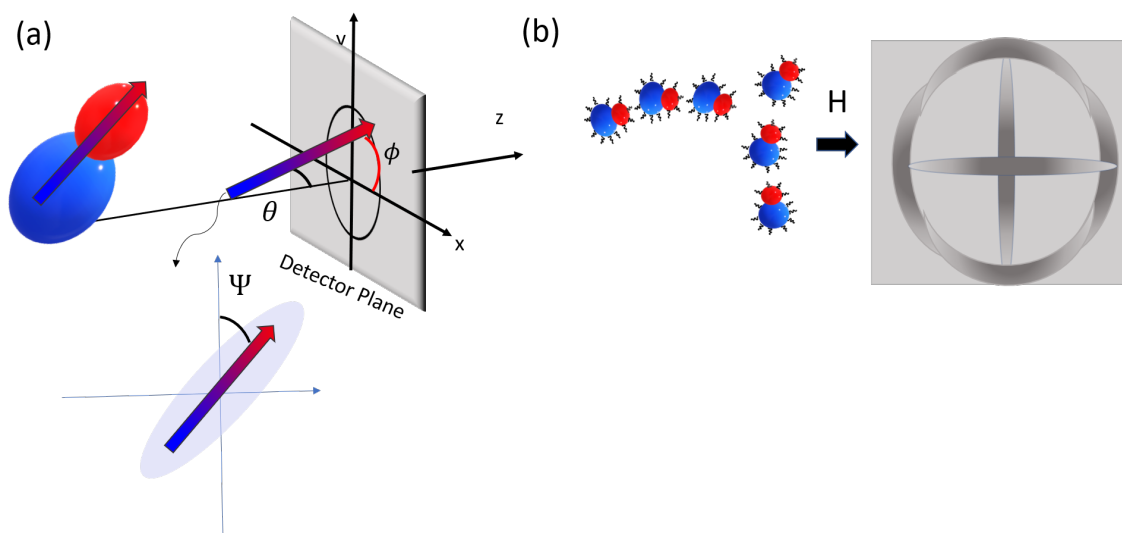


Figure 7.22.: (a) Oriented dumbbell with definitions of θ and ϕ to describe orientation of anisotropic particles when beam is incident along the z-axis. It is noted that θ rotation is performed first followed by the ϕ [140, 199]. The red and blue arrow represents the direction of the dumbbell containing multi-component spherical sub-units (b) Expected 2D scattering pattern expected for DBNPs due to parallel and perpendicular orientation of the anisotropic particles.

7.10. Scattering simulation with BornAgain

BornAgain is a free and open platform targeted for simulation and fit of 2D small angle scattering in grazing incidence based on distorted wave Born approximation (DWBA). BornAgain provides flexible tuning of composite particles made easily accessible with intuitive GUI as shown in the workflow (see Fig. 7.24). As with any grazing incidence scattering mode, the code can be easily modified to transmission mode by rotating the incoming beam and detector location. The geometry is set to transmission mode for SAXS/SANS, which replaces DWBA with ordinary Born approximation [200]. The modifications were done to verify the patterns empirically described in the previous section. The instrument is set to SAXS mode. The scattering patterns for individual spherical IONPs and Au in a non interacting case and in chains are verified (Fig. 7.23). DBNP is created through combination of two spherical sub-units. These composite

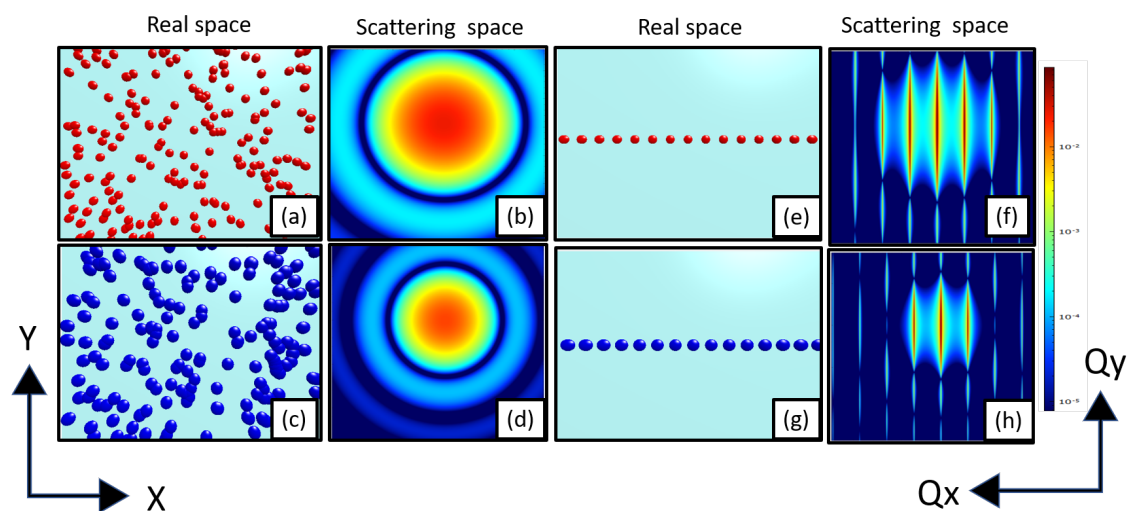


Figure 7.23.: Real space and simulated scattering patterns of spherical (a-b) Au NPs, (c-d) IONPs, (e-f) Au NP chains and (g-h) IONPs chains dispersed in h-toluene.

particles are created by translating the x-coordinate/y-coordinates for center of IONP by the value of Au diameter, they already have a preferential direction inherent to the DBNP for these simulations. DBNPs aligned along x-axis even without any explicit

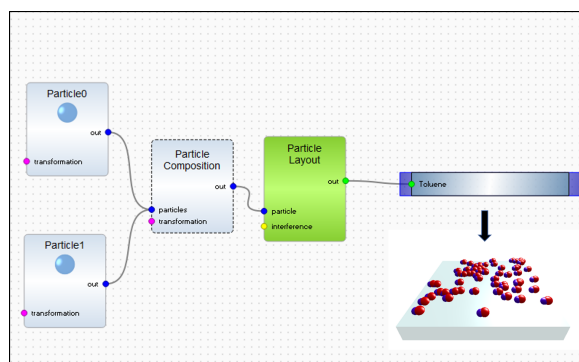


Figure 7.24.: *BornAgain* workflow to create a composite DBNP using spherical sub-units with SLD of the IONP and Au and by translating the origin of IONP to (10,0,0) and setting Au origin to (0,0,0) to realize A10F14 DBNP.

arrangement result in stripe parallel to Q_y of the SAS pattern as shown in Fig. 7.25 (a-b). The broadness of the stripes compared to previously generated chains is the inherent misalignment of these DBNPs. Likewise, for DBNPs aligned along the y axis, resulted in stripes parallel to Q_x (see Fig. 7.25 (c-d)). Orienting the anisotropic

particles such as DBNPs unlike single IONP in both directions result in the cross pattern observed in the Fig. 7.25 (e-f). This further confirms the role of orientation in the observation of anisotropy in 2D patterns. Alves. et. al, have shown the effect of orientation on the 2D scattering pattern model through numerical treatment of oriented particles with spherical subunits, which further indicated such elongation in scattering profile along the center [199].

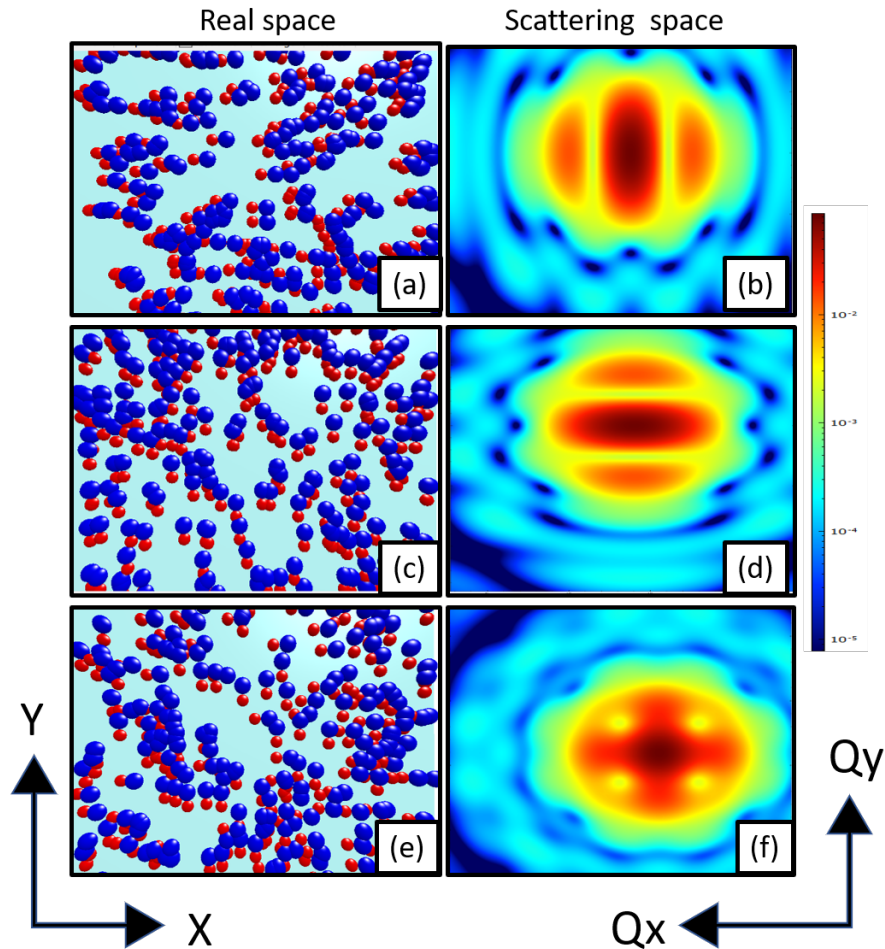


Figure 7.25.: The real space distribution of assemblies on the right and simulated detector image on the left for DBNPs (a-b) aligned along the x-axis (c-d) aligned along the y-axis and (e-f) 50 % distributed in both directions.

7.11. Shape induced mechanisms involved in the assembly formation

The previous sections compared the correlation distances for all DBNPs obtained through scattering data with dimensional parameters acquired via TEM image analysis. Despite the presence of inhomogeneous phase and dynamic assemblies, the average correlation distance remained fairly constant with ± 1 nm fluctuation in applied field. Each DBNPs system is classified in to one of the three broad categories listed below,

- **Category-O: No assemblies** A12F10 DBNPs belongs to this category as these oriented NPs form no assemblies despite the strong applied magnetic field. The dimensional parameters are summarized in Fig. 7.9.
- **Category-I: 1D chains** A13F14 and A9F11 DBNPs that form 1D chains belong to this category with parameters summarized in the Fig. 7.12 and 7.15, respectively. The difference between the two chains is the presence of additional disorder in the A13F14.
- **Category-II: 2D chains** A10F14 DBNPs form 1D chains oriented in two direction to the applied magnetic field. The correlation parameters are summarized in Fig. 7.20.

Together, the present findings has also identified two different chain configurations for DBNPs in category -I and II namely,

1. **head-to-tail:** [(Au₁-IONP₁)-(Au₂-IONP₂)-..]
2. **side-by-side:** [..(Au₁-Au₂) (IONP₁-IONP₂) ...]

7.11.1. Energy estimates

Since the IONP grown on Au is no longer spherical in a DBNP, two length scales L_F and D_F are used to define the sphericity of the IONP. The minimum dipolar energy $E_{dd}(min)$ is calculated assuming a magnetized sphere of diameter L_F . Likewise, $E_{dd}(max)$, is calculations assuming a magnetic sphere of diameter D_F . The magnetization M_s determined from chapter 6 in emu/g for iron oxide is converted to A/m following a simple conversion given by

$$M_s[\text{A/m}] \rightarrow M_s[\text{emu/g}] \times \text{density} [\text{g/cc}] \times 1000 \quad (7.6)$$

The calculations of dipolar and Zeeman energies following eqn. (2.70) and (2.69), respectively are detailed in the appendix. The calculated dipolar energies and Zeeman energies at 1 T applied magnetic field are summarized in the table 7.1 for all the DBNPs.

Table 7.1.: Comparison of dipolar E_{dd} and Zeeman energies E_z calculated using the dimension of IONPs in the DBNP and their respective saturation magnetization M_s

Assembly category	Sample ID	L_F ^(a) (nm)	D_F ^(a) (nm)	M_s ^(b) $\times 10^5$ (A/m)	$E_{dd}(\text{min})$ ^(c) (meV)	$E_{dd}(\text{max})$ ^(d) (meV)	$E_z(\text{min})$ ^(c) @ 1 T (meV)	$E_z(\text{max})$ ^(d) @ 1 T (meV)
O	A12F10	10.9	22.9	1.75	13	126	740	6870
I	A13F14	14.2	22.3	5.27	272	1055	4928	19088
I	A9F11	11.6	16.3	2.45	32	89	1250	3468
II	A10F14	14.1	18.0	3.84	141	294	3515	7814

^(a) Mean values obtained from TEM analysis in chapter 6, ^(b) Saturation magnetization in (emu/g) obtained from chapter 6 converted to A/m using eqn.(7.6), ^(c) estimated energies assuming magnetized sphere of diameter L_F and ^(d) estimated energies assuming magnetized sphere of diameter D_F .

Moreover, the shape anisotropy can not be ignored in such non-spherical IONPs. In general, calculating demagnetizing tensor for an arbitrary body is complicated. Nonetheless, "prolate" and "oblate" type ellipsoids shown in Fig. 7.26 are artificially constructed to perform preliminary estimates using well established theories of ellipsoids outlined in chapter 2 [36, 37]. The "prolate" ellipsoid has the long axis corresponding to L_D and short axis to L_A . The colour gradient in the figure represents the multicomponent nature of the DBNP. The "oblate" ellipsoids represent the IONPs in DBNPs with long axis corresponding to D_F and short axis to L_F . The loss of sphericity in IONPs is most profound in the category-O type and least in category-II type DBNPs. For a body of arbitrary shape, demagnetization energies is generally nonuniform inside the body even with uniform \vec{M} . Therefore, no single demagnetizing field can be associated with the body [37].

Recapitulating eqn. (2.39), $E_{sh} = \frac{1}{2}\mu_o V M_s^2 (\mathcal{N}_\perp - \mathcal{N}_\parallel)$, the shape anisotropy energy $E_P(\parallel)$ for prolate ellipsoid is calculated using demagnetizing factor \mathcal{N} from eqn. (2.40) for preferred magnetization alignment along long axis L_D . Along the similar lines, the energy of IONP ellipsoid $E_o\parallel$ is calculated assuming magnetization along the long axis D_F and $E_o\perp$ for preferred alignment along the growth axis L_F . The details of the calculation can be found in the appendix and estimations are tabulated in Table 7.2.

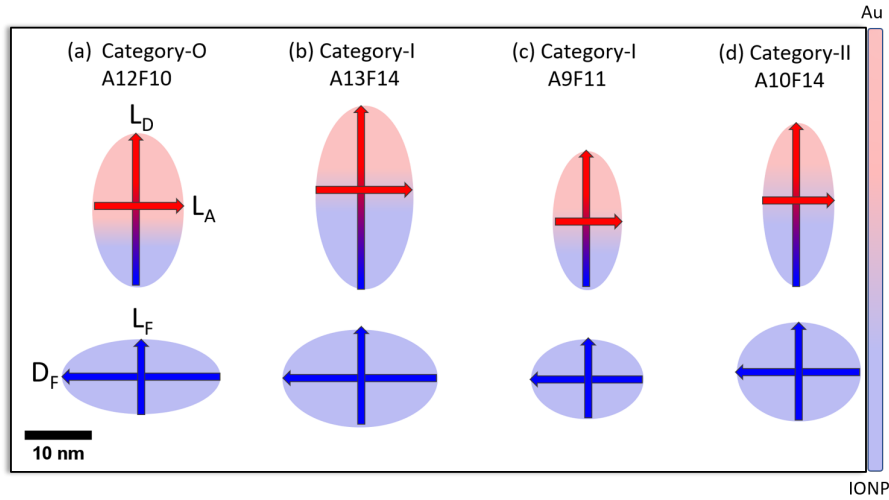


Figure 7.26.: Construction of "prolate" and "oblate" type ellipsoids for shape anisotropy energy calculations with aspect ratio A_1 and A_2 , respectively. The ellipsoids are constructed to scale.

Table 7.2.: Comparison of shape anisotropy energies calculated through artificial construction of ellipsoids. Here $E_p(\parallel)$ and $E_o(\parallel)$ are magnetostatic energies calculated when demagnetizing field is along the long axis of DBNPs and IONPs, respectively. For the demagnetizing field along the growth axis of the IONP, the corresponding energy is $E_o(\perp)$

Assembly category	Sample Id	$V_p(\parallel)$ ^(a) (nm ³)	$E_p(\parallel)$ ^(b) (meV)	$V_o(\parallel)$ ^(c) (nm ³)	$E_o(\parallel)$ ^(d) (meV)	$V_o(\perp)$ ^(e) (nm ³)	$E_o(\perp)$ ^(f) (meV)
O	A12F10	1925	44	1424	43	2992	112
I	A13F14	2701	671	2354	425	3697	759
I	A9F11	975	56	1148	34	1613	53
II	A10F14	1347	215	1873	101	2392	139

^(a) volume of ellipsoid $V = \frac{4}{3}\pi abc$ where $c = L_D/2$ and $b = a = L_A/2$, ^(b) is calculated using eqn (2.39), (2.40) and the volume $V_p(\parallel)$, ^(c) volume of the IONPs where $c = D_F/2$, $b = a = L_F/2$, ^(d) energy calculated using volume $V_o(\parallel)$, ^(e) volume of ellipsoid where $c = b = D_F/2$, $a = L_F/2$, ^(f) energy calculated using $V_o(\perp)$.

The aspect ratio $A_1 = \frac{L_D}{L_A}$ is associated with the overall shape of the DBNP and $A_2 = \frac{D_F}{L_F}$ corresponds to the IONP grown on the Au seed. The range of calculated Zeeman, dipolar and energies associated to the shape anisotropy are plotted as a function of A_2 shown in Fig. 7.27. The Zeeman energies at 1 T are large to saturate the moment in all DBNPs, the type of assembly formed depends on the anisotropy and the dipolar energies. Ideally, assuming equal bulk magnetization ($M_s = 4.46 \times 10^5$ A/m) of IONP for all DBNPs, the energies are expected to converge to a single

value as $A_2 \rightarrow 1$. As shown in Fig. 7.27 (a), the area of shaded green region decreases at low A_2 . However in reality, we have found enhanced magnetization resulting in large grey region in some cases despite low A_2 . This explains the monotonically increasing and decreasing energy range. The range of dipolar energies have decreased substantially for high values of A_2 in category-0 (A12F10) DBNPs (Fig. 7.27 (b)). Previously it has been shown how shape play a critical role in determining magnetic properties, on one hand by inducing anisotropy and the other by stabilizing the single domain state in much larger particles [201]. Reduced magnetization is associated with the internal spin and crystal structure which is further connected to shape of the nanoparticle. Previous studies using simulation methods and experimental studies have confirmed the effect of shape on magnetization of MNPs and other magnetic properties [201, 202]. Computationally expensive simulations are required to model such DBNPs precisely. However, with preliminary estimates of various dipolar and shape anisotropy energies described above and plotted in Fig. 7.27 (b), the net dipolar energy $E_{dd} = E_{dd}(max) - E_{dd}(min)$ is equal to net shape associated energy $E_{sh} = E_{p||} + E_{o\perp} - E_{o||} = 113$ meV, only in category-O DBNPs. In category-I (A9F11), despite the improved magnetization, the smaller sizes in A9F11 results in net dipolar energy $E_{dd} = 75$ meV lower than A12F10. Nevertheless, these DBNPs arrange in head-to-tail fashion to form chains due imbalance with associated net shape energy $E_{sh} = 18$ meV. Similarly the imbalance suggests the formations of chains in category-1 and II DBNPs. In category-I and II, due to improved spherical nature of IONPs the magnetic dipole moments within the IONP attempts to align and attract the neighbouring dipoles strongly resulting in chains. Among the DBNPs, category-II has the lowest value of A_2 and largest value of A_1 indicating improved spherical and dumbbell nature, respectively. This presumably favours the alignment of the whole DBNP in direction parallel and perpendicular to the field to ensure close contact of IONPs, resulting in side-by-side 2D arrangement. Since particles are well separated, the exchange energy between the DBNPs suspended in liquid may be neglected due to short range of interaction. Monte Carlo simulations have shown that uniaxial particles randomly oriented in a 2D array are sensitive to anisotropy, dipolar and Zeeman energies in the presence of the field. Due to competition between these energies several variety of magnetic orientations are expected to be present. For example, in these numerical treatments they have shown antiferromagnetic perpendicular alignment when anisotropy energy dominated and antiferromagnetic inplane alignment for dominating dipolar energies [203]. Steric hindrance may also play a role, however

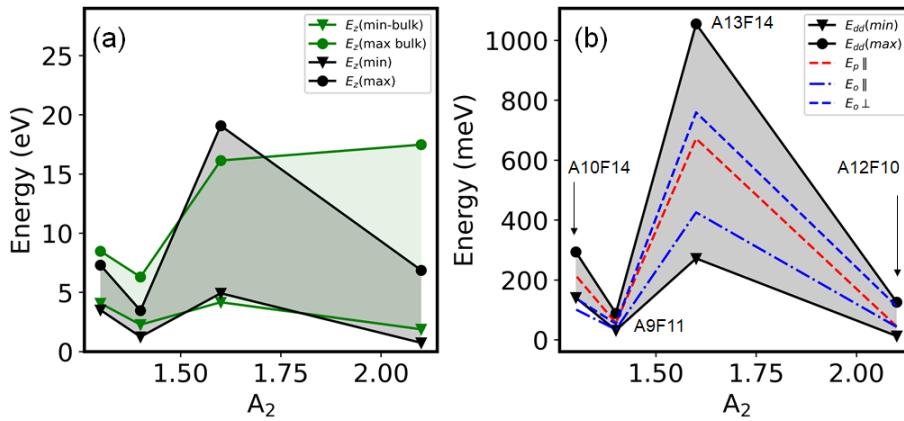


Figure 7.27.: The range of calculated (a) Zeeman (b) dipolar and various shape associated demagnetization energies plotted as a function of aspect ratio A_2 . In (a) and (b) the grey region of energies is plotted using values in Table 7.1 and green region in (a) represents the calculated energy assuming equal bulk magnetization $M_s = 4.46 \times 10^5$ A/m of IONPs in all DBNPs.

preliminary estimates of the surfactant shell reveals no such untoward repulsion in Category-O DBNPs preventing assemblies.

7.11.2. Differences between IONPs and DBNPs

Comparing the results from single phase IONPs, we aim to determine why such varied assemblies exist in DBNPs. Qualitative analysis of complete 2D scattering patterns reveals that although similar assemblies are formed in IONPs and DBNPs, orientation factors inherent in multicomponent DBNPs result in varied 2D scattering patterns. Self-assembly of IONPs into 1D chains was found due to the field-induced dipolar interactions that align the particle. Several intrinsic and external factors influence the assembly formation, such as the diameter of the IONP, composition, thickness of surfactant coating and concentration. These systems are coated with OA ligands to prevent irreversible interactions due to vdW forces. Large ligand density distribution around particles may hinder the dipolar forces, as seen in certain IONPs. Dipolar forces further depend on the magnetic structure of the IONP. The magnetic structure is interconnected to size, composition, crystallinity, and several structural-dependent factors. The blocking temperature T_B scales with volume of the particle for all the IONPs as expected. Additionally, the deviation in the measured T_B from the calculated values for the single-phase IONPs was attributed to the dominant dipolar interactions of the neighbouring particles [14, 204, 205, 206]. However, in the DB-

NPs, the large increase in T_B cannot be merely accounted from the additional dipolar interactions. We introduce two relevant geometric parameters A_1 and A_2 to describe the morphology of DBNPs. Analogous to diameter in spherical IONP counterparts, we can now arrange DBNPs as a function of aspect ratio A_2 . The larger deviation of this ratio from 1 indicates loss of spherical nature of IONP. From the SW model, the energy barrier is associated with the anisotropy energy E_a (including MCA, shape and surface anisotropy). The shape induced anisotropy along with dipolar interaction must indeed affect the energy barrier of the IONPs in DBNPs compared to individual IONPs resulting in shifted T_B . Further, the anisotropy within the DBNP governs the orientation of the magnetic dipole moment. The strong saturating field orients these dipole moments along the field. In both single IONPs and DBNPs, the attraction between neighbouring dipoles are governed by dipole-dipole interactions. The dipoles arrange in head-to-tail fashion in individual IONPs and DBNPs. However due to anisotropic nature of the whole DBNP, the structural subunits can align perpendicular or parallel to the field resulting in the so called "head-to-tail" and "side-by-side" arrangement. The literature on assemblies have predicted that individual IONPs can be tuned with magnetic field to form first 1D chains that coalesce into 2D and later 3D assemblies [94, 92]. However, stable intermediate 2D structures are rarely observed experimentally in dispersion of IONPs. Now with DBNPs, we demonstrate both 1D and 2D assemblies can exist and are tuned as a consequence of the aspect ratio. The enhanced anisotropy in DBNPs are a consequence of the particle aspect ratio which in turn affects magnetic behaviour and the assemblies formed as shown in the schematic Fig. 7.28.

7.12. Conclusion

To summarize, the DBNPs are analyzed through model independent (Guinier-Porod) and dependent (composite core-shell) approaches. Geometric length scales of the DBNP from these approaches concur with values obtained via microscopy. Further based on the type of assemblies formed the DBNPs are classified into one the three categories. In category-O, where ($A_1 \lesssim 2$ and $A_2 \gtrsim 2$), no assemblies were observed despite large external magnetic fields. Further, to analyse the assemblies in category-I and II type DBNPs, shape independent peak functions are used to model the sectoral intensities to obtain correlation distances and lengths. In category-I type, 1D chains aligned in direction of the field are in head-to-tail configuration. In category-II, 2D

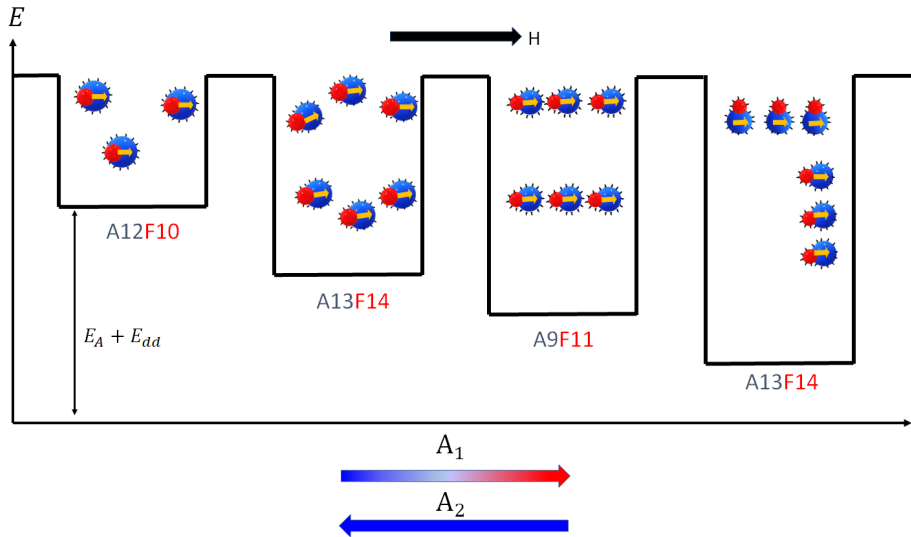


Figure 7.28.: Schematic of shape induced mechanisms governing self-assembly.

chains result in side-by-side configurations. The unique cross pattern in category-II type DBNPs in the 2D SAXS/SANS pattern is a consequence of inherent orientation in the DBNPs combined with formation of 2D chains. This is qualitatively realized through 2D simulations using *BornAgain*. To conclude, chain formation in DBNPs is found as a consequence of the competing tendencies between magnetic-dipolar, anisotropy and Zeeman energies in the presence of magnetic field. In particular, the shape induced anisotropy contributes dominantly to the anisotropy energy. Shape factor in DBNPs arises due to a combination of asymmetric DBNPs characterized by A_1 and non spherical IONPs by A_2 . The shape anisotropic energies of the system are analysed through artificial construction of ellipsoids with aspect ratio A_1 and A_2 . In the limited set of samples, DBNPs are expected to form higher ordered assemblies as $\frac{A_1}{A_2} \rightarrow 2$ and is absent when $\frac{A_1}{A_2} < 1$. A potential way forward to designing and tuning assemblies with field in any hybrid magnetic structures is through attributing a key dimensionless parameter that can describe the shape.

8. Conclusion and outlook

8.1. Conclusion

The spatial organisations of hybrid Au-iron oxide dumbbell nanoparticles (DBNPs) in the presence of magnetic field are investigated in the present thesis using a multiscale experimental approach including imaging and advanced scattering methods. Despite long standing focus on inherently local and spatially confined imaging techniques to observe assemblies, these scattering results provide invaluable information about the predominant order present in such dispersions. In order to gain perspective on the DBNPs, separate investigations were carried out on its spherical magnetic counterparts namely iron-oxide nanoparticles (IONPs). Based on the comparative studies between the IONPs and DBNPs, the observed spatial organizations are broadly classified into three categories.

- **Category-O:** IONPs and DBNPs that do not form any assemblies, despite the external stimuli, belongs to this category. Size, concentration and field dependent studies, within the constraints of the sample space, reveal that IONPs with diameters less than 24 nm do not form any assemblies. While there is a size dependent effect, in some cases, assemblies are inhibited by steric repulsion from the surfactant shell coating around the particle. Analogous to diameters in the spherical counterparts, two aspect ratios A_1 and A_2 are introduced to account for the multicomponent and non-spherical nature of DBNPs. Without loss of generality, $A_1 = A_2 = 1$ in IONPs. In DBNPs that do not form assemblies, $A_1 \lesssim 2$ and $A_2 \gtrsim 2$. Compared to other DBNPs, these particles form the most stable suspension with no evidence of phase separation.
- **Category-I:** IONPs and DBNPs in this category form 1D chains. As mentioned, there is a profound size effect in the observation of chains. IONPs, in particular with diameters equal to 27 nm form 1D chains that are bent at low fields and straighten in the presence of strong magnetic fields. The chain forma-

tion in the IONPs was further visualized using microscopy when deposited on templates and 2D SAXS/SANS data analysis with RMC simulations when dispersed in a suspension. Similar anisotropic scattering patterns were observed in DBNPs, with aspect ratio $A_1 \gtrsim 2$ and $A_2 \lesssim 2$. Using constraints and assumptions from several experiments, model dependent and independent analysis reveal the presence of 1D chains. This category also includes 1D chains that are highly disordered and do not completely align with the field. In this category a head-to-tail arrangement of chains are preferred.

- **Category-II:** Chains that align in two directions with magnetic field belong to this category. In the limited sample space, we have no IONPs that fall into this category. In fact such 2D assemblies in IONPs are considered meta stable [7, 94] and may not be stable in the dispersion. However, such 2D chains are observed in DBNPs with aspect ratio $A_1 \gtrsim 2$ and $A_2 \lesssim 2$. Compared to other DBNPs, this category of particles have the highest mean value of A_1 and the lowest A_2 . The novel scattering pattern observed are a consequence of the DBNP being an anisotropic particle and presence of 2D arrangement. The chains in this category seem to arrange in a side-by-side configuration.

The stability and the assemblies formed in dispersions are topics of considerable research activity. The first step in approaching problems in this area is to study the origin and the nature of the interparticle forces. The main forces include exchange forces, van der Waals (vdW), electrostatic (ES), steric, gravitational and magnetic forces. The steric stabilized organic coating around the surface of the DBNPs and IONPs prevent irreversible aggregation due to vdW forces and considerably reduce any ES type interactions. Exchange forces maybe neglected since these particles are not in contact and are separated by solvent and polymer coating. In IONPs, the suspensions remain more stable compared to DBNPs which are heavier and undergo phase separation almost instantaneously. The predominant magnetic and steric forces most likely affect the assembly formation in our DBNPs and IONPs systems. Macroscopic magnetic properties are driven by dipolar interactions that cause a shift in the blocking temperature T_B of spherical IONPs. The magnetic and steric forces further depends on the diameter of the IONP, composition, thickness of the ligand shell, concentration, magnetic structure and magnetic field. The rich parameter space explored in IONPs provides a foundation for extending more complex DBNPs. Thus, we can infer that the loss of sphericity in IONP of the DBNP accompanied with constrained

growth on Au's curved surface influences the structural and magnetic properties of DBNPs as opposed to its spherical counterparts. The dipolar interactions in combination with anisotropy energy affects the T_B in DBNP. The unique morphology and multi-component nature of DBNPs offers an additional degree of freedom absent in spherical IONPs which further affects the type of assembly. By combining various sets of anisotropy dimensions through definition of aspect ratios, following conclusions about the field induced self-assembly phenomenon in Au-Fe₃O₄ can be made

1. **Spherical IONPs** ($A_1 = A_2 = 1$)

In monodisperse spherical IONPs of high crystalline quality, there are no additional contributions to the shape anisotropy energy. The assemblies formed in IONPs are a result of the competing tendencies between the magnetic dipolar, steric and Zeeman energies.

2. **DBNPs** ($A_1 \lesssim 2$ and $A_2 \gtrsim 2$)

DBNPs explored in this regime indicated no sign of assemblies even in the presence of strong fields. There are no evident indications of dominating steric repulsion in these DBNPs that prevent such formation. Loss of sphericity of the IONP is maximum in these DBNPs indicating a strong influence of the shape induced anisotropy. Calculations of demagnetization energy for arbitrary shape such as dumbbell is done through artificial construction of "prolate" and "oblate" ellipsoids. Additional contribution of shape anisotropy in the energy term results in competition with magnetic dipolar energies which further inhibits formation of assemblies in these DBNPs. Thus, one may predict the likelihood of assemblies by identifying the limits of the geometric aspect ratios.

3. **DBNPs** ($A_1 \gtrsim 2$ and $A_2 \lesssim 2$)

The formation of chains in DBNPs are the result of competing magnetic dipolar and anisotropic contributions arising primarily from the shape induced anisotropy. DBNPs in this regime assembled into 1D and 2D chains. The chains exist in one of the two configurations: "head to tail" or "side by side". The 2D chains are a result of improved size distribution and the ratio $\frac{A_1}{A_2}$ fast approaching 2. This indicates that the probability of assemblies are the highest when the overall DBNP and the individual magnetic component has the maximum and minimum deviation from the spherical nature, respectively.

Importantly, our results provide evidence for inducing pattern formation with magnetic field in DBNP dispersions. These results adds to a growing corpus of research

showing the use of anisotropic building blocks. Analysis methods and identification of a geometric aspect proposed can be generalized to study any hybrid dumbbell system.

8.2. Scope for future developments

Monodisperse DBNPs

There is a continuous need for scalable, economic and large scale production of bio-compatible anisotropic particles due to interest in designing next generation medical nanorobotics. Our studies indicate that assemblies can be tuned with geometric aspect ratio which implies that synthesis route of DBNPs are important and that results may vary for DBNPs designed with Fe_3O_4 as seeds rather than Au. Although the last two decades have improved synthesis methods, further research require large quantity monodisperse DBNPs for experiments. Crystal defects in individual IONPs are explained as possible causes for reduced magnetization in IONPs. Similarly internal crystal structure of DBNPs may be correlated to the macroscopic enhanced magnetization in certain DBNPs. Improved total scattering experiments and RMC modelling schemes have to be adopted to ascertain the crystal and interface structure of the such multicomponent DBNPs.

Analytical form-factor of DBNP:

In the context of self-assembly, collective behaviour were investigated through shape independent functions and models constructed based on *a priori* information. A full theoretical treatment would involve modelling with form-factors of dumbbells. One way to obtain form-factor is to define the SLD function and perform discrete Fourier transform. However in multicomponent non-centrosymmetric particles, the SLD function is dependent further on the orientation of the particle. It is clear, that such an oriented particle have various projections on the scattering plane resulting in different scattering patterns along different orientations. In the case of an ensemble of dumbbells that are randomly oriented, the detector pattern may be indistinguishable from patterns generated by its spherical sub-units. Since the thesis focused on such ensembles, the analysis with assumptions and simpler models are fairly valid. However, in dilute limits and to obtain magnetization distribution within the DBNP particle, description of form-factor of dumbbells may be critical. The closest description to dumbbells existing in the current database of form-factors by *SasView* is the barbell

model. However, the barbell is symmetric and has uniform SLD within the particle and based on our findings, we know the aspect ratios' are critical to the dumbbells. Taking a digression from the current body of literature in DBNPs, analytical formulation of a form-factor was established to describe formation of nonane and water aerosol droplets. These droplets are indeed phase separated and closely resemble the dumbbell particle [207, 208, 209], The analytical formulation of form-factor developed by these authors could be adapted to describe the dumbbells. A brief derivation of the form-factor is presented in the appendix.

RMC simulations with DBNPs

The development of RMC with single phase IONPs reveals the presence of chains through real space visualizations. The RMC models can be easily adapted to visualise novel assemblies formed with isotropic particles with no prior assumptions about the energies involved in the system. However, with anisotropic particles there is an additional degrees of freedom associated with orientation or rotation (see Fig. 8.1). Without including the complex form-factor of the DBNP the problem is simplified by

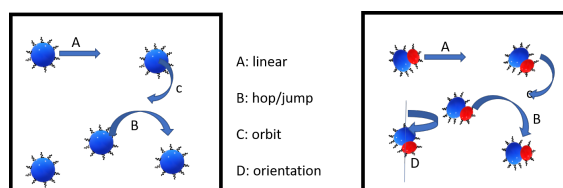


Figure 8.1.: The various motions associated with IONPs and DBNPs distributed in the box.

assuming two spheres Au(red) and IONPs(blue) distributed in the box. The dumbbell morphology is achieved by constraining one sphere to follow the random motion of the other. The preliminary results was simulated for 100 particles in 50 steps took 10hrs to converge are detailed in appendix.

Magnetic structure of IONPs in DBNPs

From macroscopic magnetic measurements, we observe enhanced magnetization in larger DBNPs. Several factors including shared interface with Au, role of Au's conduction electrons and oxygen content may be responsible for such observations. Previous SANS POL experiments on the magnetic structure of individual IONPs have indicated canted shell and magnetic dead layer to explain reduced magnetization.

The microscopic magnetization distribution is correlated with the magnetic nanoparticle form factor of DBNPs and is accessible with polarized scattering cross-sections. Similar SANSPOL experiments at 1 T on different DBNPs classified into their category are as shown in Fig. 8.2. Analysis of SANSPOL patterns as seen with single phase IONPs on its assemblies are not trivial.

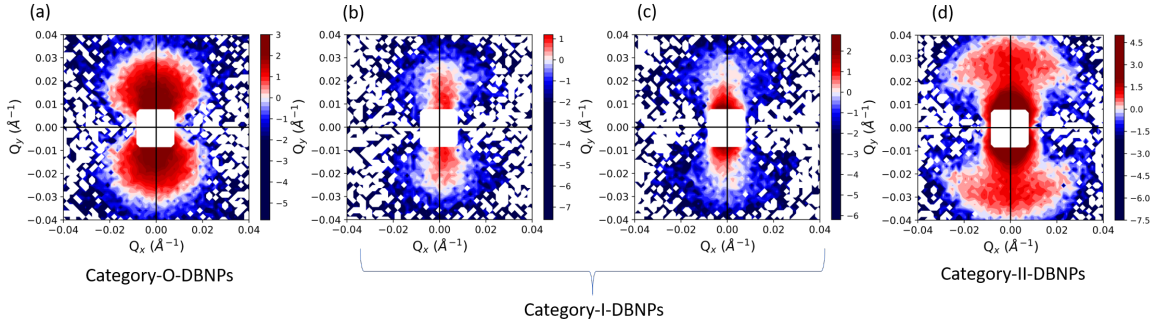


Figure 8.2.: The difference in SANSPOL patterns ($I^- - I^+$) obtained at 1 T for (a) category-O DBNPs (A12F10), (b) (A13F14) and (c) (A9F11) belongs to category-I A. (d) category-II DBNPs (A13F14). A saturating field of 1 T is applied along the horizontal direction.

8.3. Outlook

With advances in particle synthesis, there is growing availability of such anisotropic and complex particles. Research on these colloidal assemblies is relatively in an infant stages and there is still no common nomenclature or general classification scheme to describe the building blocks and assemblies. With increasing complexity of the particles, modern techniques and complementing multiscale approaches must be employed to ascertain their functionality. This work sheds light on the possibility of such classifications and the current findings in the thesis open doors to more advanced analysis of such assemblies.

Appendices

A. Structural parameters

A.1. Image analysis results

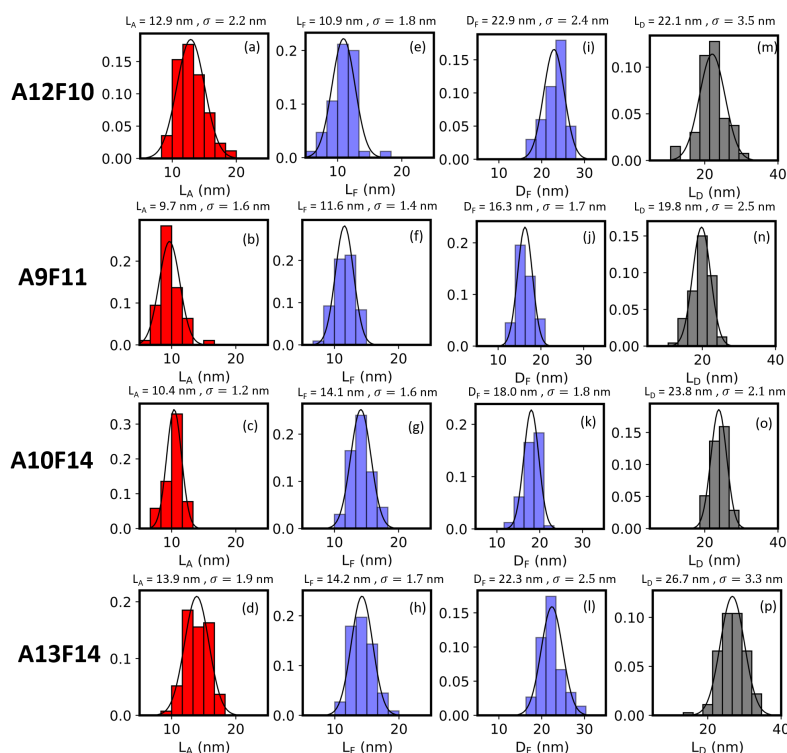


Figure A.1.: Size distributions obtained from TEM image analysis where the red histograms represent diameter of the Au nanoparticles L_A (a-d), the blue histograms represents dimension along the growth axis L_F (e-h) and D_F (i-l) and black represents the whole diameter of the DBNP L_D (m-p). An average of ~ 50 -100 particle were measured for all DBNPs.

The several length scales of **DBNPs** are extracted by fitting normal distribution to statistical data from TEM image analysis using *ImageJ*. The performance specification for our TEM is 0.27 nm point resolution or better and 0.14 nm for a lattice. The values are obtained by measuring 50-100 particles.

The TEM images of F05 and F10 particles. In this image, it is clearly visible how two size ranges exist in F10 IONPs. The initial selected images mainly contained larger particles, however due to lowered diameter with SAXS. All the images were reconsidered.

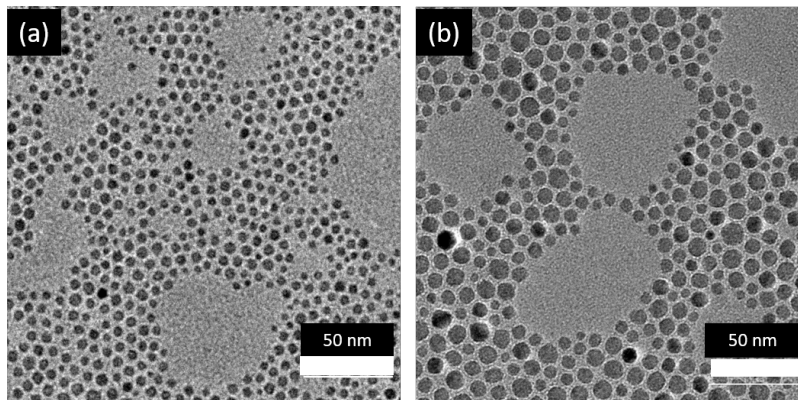


Figure A.2.: TEM images of (a) F05 and (b) F10 IONPs.

A.2. Total scattering refinements

The phase composition and lattice constants for **IONPs** and **DBNPs** are obtained with total scattering experiments. The results of the refinements are as presented below. It should be noted that the errors obtained with refinement using *PDFgui* are ambiguous. The problem lies in integrating the 2D data, which does not produce uncertainty on any data point resulting in unreliable and non-realistic uncertainties in *PDFgui*. It remains an issue in all the parameters refined by *PDFgui*. One way is to take several measurements on the same sample with no condition changing and refine parameters for each measurement and observe the deviation. Due to limited beamtime, we estimate the error based on the stability of the refined point with several iterations of the fit. Based on the expectation of the phase, a structural model is loaded as the phase and parameters are refined to produce R_w which is weighted R value that describes how well the chosen model correspond to the experimental data. The program also includes parameters δ_1 and δ_2 to account for the correlated motion between atoms. At short distances correlated motion this results in sharp peaks and broadening at large distances. The δ_2 is associated often with low temperature and it is sufficient to refine one parameter. Alternative methods to account for correlated motion is through use of *sratio* and *rcut*. Do not use both methods simultaneously.

A. Structural parameters

The Q_{damp} and Q_{broad} parameter is obtained by refining the standard calibrants like CeO_2 , Ni. However, it is fairly valid to fix this value also using a standard reference sample with excellent structural fit. This was done in the case of DBNPs using Au and CeO_2 . This value is fixed during refinement of the data from a single beamtime. Other parameters available for refinement include the $spdiameter$ and $stepcut$. The former is associated with diameter of the NP and the latter truncates PDF to zero at values greater than $stepcut$. The least square fitting is adopted in both cases.

Table A.1.: Summary of the xPDF refinement fits of reference Au and bulk reference iron oxide powdered samples measured at APS. The fits yield lattice constants a , δ_1 , atomic displacement factors U_{iso} .

Sample : Au powder	$Q_{max} \text{ \AA}^{-1}$	Atom label	Atom label	x	y	z	U_{iso}	$Q_{damp} (\text{ \AA}^{-1})$	$Q_{broad} (\text{ \AA}^{-1})$
Fm-3m (ICSD-52249)	24.09	Au ₁	4a	0	0	0	0.0089(2)	0.0377(7)	0.007(2)
a = b = c (\AA)	4.0792(3)								
scale	0.445(7)								
δ_1	1.43								
R_w	0.065								
Sample : Bulk Fe(II and III) oxide	$Q_{max} \text{ \AA}^{-1}$	Atom label	Atom label	x	y	z	$U_{iso} \text{ \AA}^2$	$Q_{damp} (\text{ \AA}^{-1})$	$Q_{broad} (\text{ \AA}^{-1})$
Fd-3m (ICSD-65339)	24.09	Fe ₁	8a	0	0	0	0.0047(3)	0.0377	0.007
		Fe ₂	16d	0.625	0.625	0.625	0.0090(4)		
		O ₁	32e	0.3798	0.3798	0.3798	0.017(1)		
a = b = c (\AA)	8.3901(7)								
scale	0.426(7)								
δ_1	1.54(12)								
R_w	0.127								

The values with errors in parenthesis are refined parameters.

Table A.2.: Summary of the xPDF refinement fits of A12F10 and A13F14 at APS. The fits yield lattice constants a , δ_1 , scale, atomic displacement factors U_{iso} .

Sample : A12F10	$Q_{max} \text{ \AA}^{-1}$	Atom label	Atom label	x	y	z	U_{iso}	a = b = c (\AA)	spdiameter (nm)	Mass (%)
Fm-3m (ICSD-52249)	24.09	Au ₁	4a	0	0	0	0.0124(5)	8.42(3)	6(2)	22
Fd-3m (ICSD-65339)	24.09	Fe ₁	8a	0	0	0	0.5(3)	4.0499(7)	5.4(2)	78
		Fe ₂	16d	0.625	0.625	0.625	0.08(1)			
		O ₁	32e	0.3798	0.3798	0.3798	0.27(7)			
scale-phase Au	0.45(2)	scale-phase Fe ₃ O ₄	0.55							
δ_1	1.94									
R_w	0.218									
Sample : A13F14	$Q_{max} \text{ \AA}^{-1}$	Atom label	Atom label	x	y	z	U_{iso}	a = b = c (\AA)	spdiameter (nm)	Mass (%)
Fm-3m (ICSD-52249)	24.09	Au ₁	4a	0	0	0	0.0119(5)	4.054(1)	7.6	61
Fd-3m (ICSD-65339)	24.09	Fe ₁	8a	0	0	0	0.02(1)	8.40(1)	14.5	39
		Fe ₂	16d	0.625	0.625	0.625	0.007(3)			
		O ₁	32e	0.3798	0.3798	0.3798	0.02(1)			
scale-phase Au	0.274(7)	scale-phase Fe ₃ O ₄	0.04(2)							
δ_1	2.3									
R_w	0.425									

Table A.3.: Summary of the xPDF refinement fits of reference F50 and bulk reference iron oxide powdered samples measured at DESY. The fits yield lattice constants a , δ_1 , atomic displacement factors U_{iso} .

Sample : F50	$Q_{max}\text{\AA}^{-1}$	Atom label	Atom label	x	y	z	$U_{iso}\text{\AA}^2$	$Q_{damp}(\text{\AA}^{-1})$	$Q_{broad}(\text{\AA}^{-1})$
Fd-3m (ICSD-65339)	28.27	Fe ₁	8a	0	0	0	0.0045(5)	0.0322	0.008(2)
		Fe ₂	16d	0.625	0.625	0.625	0.0075(5)		
		O ₁	32e	0.3798	0.3798	0.3798	0.015(2)		
a = b = c (Å)	8.372(1)								
scale	0.335(9)								
δ_1	1.9(3)								
R_w	0.135								
Sample : Bulk Fe(II and III) oxide	$Q_{max}\text{\AA}^{-1}$	Atom label	Atom label	x	y	z	$U_{iso}\text{\AA}^2$	$Q_{damp}(\text{\AA}^{-1})$	$Q_{broad}(\text{\AA}^{-1})$
Fd-3m (ICSD-65339)	28.27	Fe ₁	8a	0	0	0	0.0048(6)	0.0322	0.008
		Fe ₂	16d	0.625	0.625	0.625	0.0079(6)		
		O ₁	32e	0.3798	0.3798	0.3798	0.016(2)		
a = b = c (Å)	8.379(1)								
scale	0.306(9)								
δ_1	1.45(12)								
R_w	0.117								

Table A.4.: Summary of the xPDF refinement fits of reference F20 and F27 IONPs samples measured at DESY. The fits yield lattice constants a , δ_1 , atomic displacement factors U_{iso} .

Sample : F20	$Q_{max}\text{\AA}^{-1}$	Atom label	Atom label	x	y	z	U_{iso}	a = b = c (Å)	mass (%)
Fd-3m (ICSD-65339)	23.0	Fe ₁	8a	0	0	0	0.004(1)	8.34(3)	70
		Fe ₂	16d	0.625	0.625	0.625	0.009(1)		
		O ₁	32e	0.3798	0.3798	0.3798	0.011(2)		
P4332 (ICSD-79196)	23.0	Fe ₁	8c	0.9921	0.9921	0.9921	0.009(1)	8.37(6)	30
		Fe ₂	12d	0.8650	0.6150	0.8750	0.007(2)		
		Fe ₃	4b	0.3750	0.1250	0.8750	0.011(6)		
		O ₁	8c	0.8610	0.8610	0.8610	0.018(7)		
		O ₂	24e	0.3720	0.3770	0.8760	0.1(5)		
scale (phase-1)	0.02(1)	scale (phase-2)	0.01(1)						
spdiameter (nm)	20								
δ_1	1.9(3)								
R_w	0.21	for Q from 5-50 Å							
Sample : F27	$Q_{max}\text{\AA}^{-1}$	Atom label	Atom label	x	y	z	U_{iso}	a = b = c (Å)	mass (%)
Fd-3m (ICSD-65339)	23.0	Fe ₁	8a	0	0	0	0.004(2)	8.349(6)	66
		Fe ₂	16d	0.625	0.625	0.625	0.010(3)		
		O ₁	32e	0.3798	0.3798	0.3798	0.03(2)		
P4332 (ICSD-79196)	23.0	Fe ₁	8c	0.9921	0.9921	0.9921	0.002(3)	8.355(7)	34
		Fe ₂	12d	0.8650	0.6150	0.8750	0.005(6)		
		Fe ₃	4b	0.3750	0.1250	0.8750	0.01(4)		
		O ₁	8c	0.8610	0.8610	0.8610	0.002(1)		
		O ₂	24e	0.3720	0.3770	0.8760	0.002(1)		
scale (phase-1)	0.12(5)	scale (phase-2)	0.06(2)						
spdiameter (nm)	27								
δ_1	0.48								
R_w	0.169	for Q from 0-50 Å							

A.3. SAXS refinement parameter

SAXS data of DBNPs is associated with phase separation. This results in focused beam experiments at different parts of the capillary. The following tables present

various refined parameters and their fits. The quality of fits is identified visually, monitoring the residuals from the fitting functions and when reduced $\chi^2 < 0.01$. Summary of the radially integrated SAXS data fit parameters of DBNPs.

Table A.5.: Summary of the A12F10 SAXS radial fit parameters

	Guinier-Porod model				Gold sphere model			
H (T)	scale	s	P	R_g (nm)	$\eta_{core} \times 10^{-6} \text{Å}^{-2}$	$\eta_{solvent} \times 10^{-6} \text{Å}^{-2}$	R_{core} (nm)	pd (%)
0	3769(12)	0	4	10.9	123	8.03	5.6 ± 2.2	48
0.9	1923(7)	0	4	9.8	123	8.03	6.4 ± 2.2	35

Following the similar analysis protocol from A12F10, a Guinier-Porod and Au sphere model fit to SAXS 1D data at 0 T reveal $R_g \sim 8$ nm and $D_{core} = 10(2)$ nm (see Fig. A.3). However, as discussed in section 7.2, sedimentation affects the scattering from particle phase at 0 T, which means there is an increased possibility of measuring residual particles of the supernatant. To ensure we extract the parameters associated with particle phase, the SAXS 1D data collected at 0.9 T is fit to Au-sphere model by constraining the model to $0.034 \text{Å}^{-1} < Q < 0.147 \text{Å}^{-1}$ limits, so that the structural peak at $Q = 0.0267 \text{Å}^{-1}$ is avoided (Fig. A.3 (b)). The results of the fit indicate large polydispersity for this choice of model with a mean diameter $D_{core} = 12$ nm lying within the expected range of Au diameter determined from TEM .

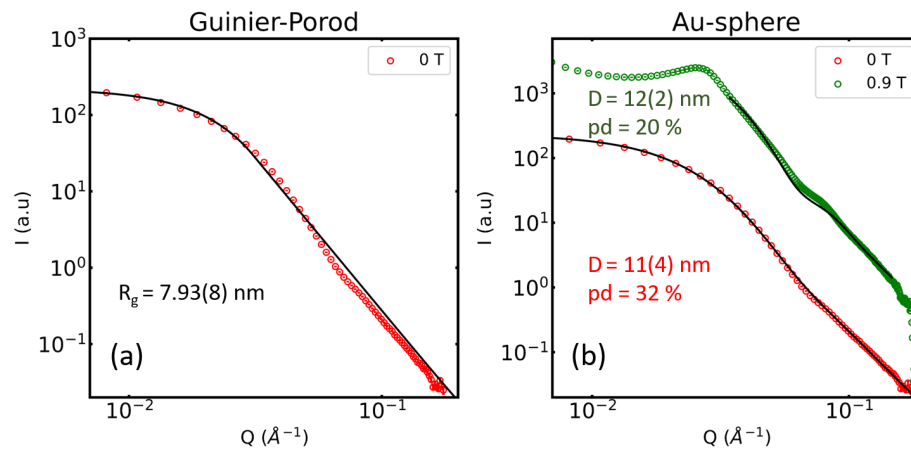


Figure A.3.: SAXS fits of A13F14 ; radially integrated SAXS intensities of A13F14 at 0 T (red) and 0.9 T (green) fit to (a) Guinier-Porod model and (b) a gold sphere model. The intensities are scaled for visualization.

The SAXS at 0 T is dominated by the supernatant and thus lowered intensity.

Table A.6.: Summary of the A13F14 SAXS radial fit parameters

	Guinier-Porod model				Gold sphere model			
H (T)	scale	s	P	R_g (nm)	$\eta_{core} \times 10^{-6} \text{Å}^{-2}$	$\eta_{solvent} \times 10^{-6} \text{Å}^{-2}$	R_{core} (nm)	pd (%)
0	221	0	4	7.9	123	8.03	5.2 ± 1.8	32
0.9	-	-	-	-	123	8.03	6.3 ± 1.2	20

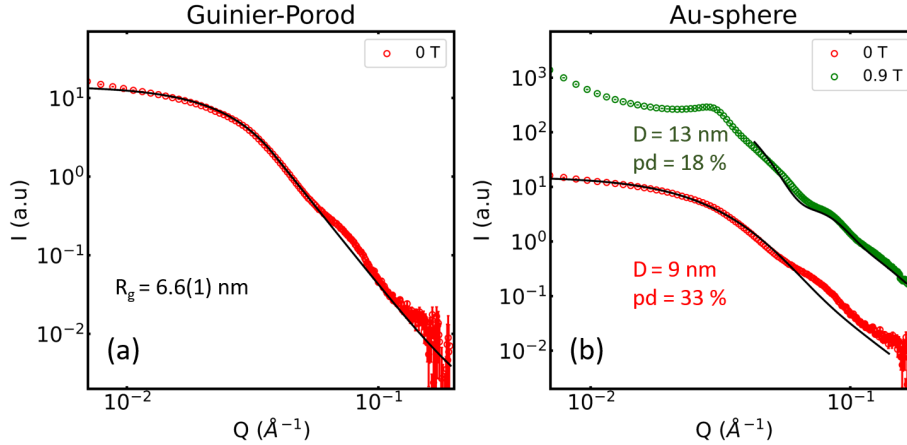


Figure A.4.: SAXS fits of A9F11; radially integrated SAXS intensities of A9F11 at 0 T (red) and 0.9 T (green) fit to (a) Guinier-Porod model and (b) a gold sphere model. The intensities are scaled for visualization.

Table A.7.: Summary of the A9F11 SAXS radial fit parameters

	Guinier-Porod model				Gold sphere model			
H (T)	scale	s	P	R_g (nm)	$\eta_{core} \times 10^{-6} \text{Å}^{-2}$	$\eta_{solvent} \times 10^{-6} \text{Å}^{-2}$	R_{core} (nm)	pd (%)
0	15.6	0	4	6.6(1)	123	8.03	4.5 ± 1.4	33
0.9	-	-	-	-	123	8.03	6.5 ± 1.2	18

Table A.8.: Summary of the A10F14 SAXS radial fit parameters

	Guinier-Porod model				Gold sphere model			
H (T)	scale	s	P	R_g (nm)	$\eta_{core} \times 10^{-6} \text{Å}^{-2}$	$\eta_{solvent} \times 10^{-6} \text{Å}^{-2}$	R_{core} (nm)	pd (%)
0	24	0	4	5.6	123	8.03	4.5 ± 1.2	28
0.9	-	-	-	-	123	8.03	5.5 ± 0.9	18

The following tables are associated with SAXS data collected for IONPs and can be reproduced using these parameters.

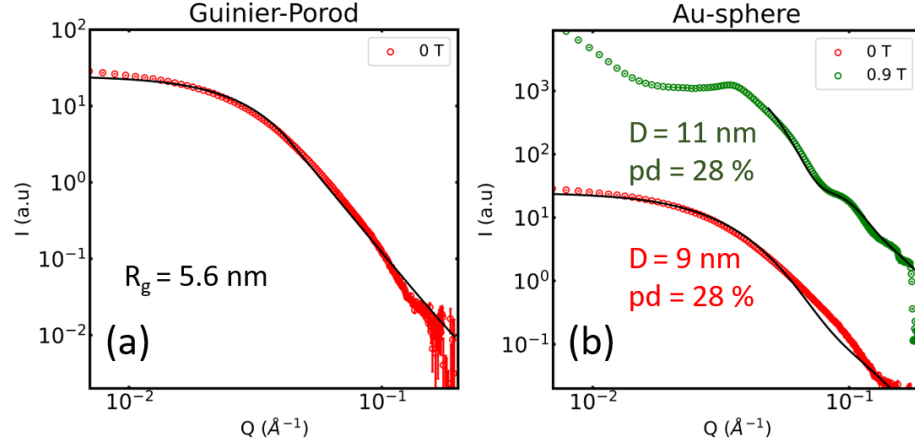


Figure A.5.: SAXS fits of A10F14; radially integrated SAXS intensities of A10F14 at 0 T (red) and 0.9 T (green) fit to (a) Guinier-Porod model and (b) a gold sphere model. The intensities are scaled for visualization.

Table A.9.: SAXS fits for the spherical model at 0 T and 0.9 T

Sample ID	Spherical model		Refined parameters @ 0T			Refined Parameters @ 0.9 T		
	$\eta_c = \times 10^{-6} \text{Å}^{-2}$	$\eta_s = \times 10^{-6} \text{Å}^{-2}$	Scale	Diameter (nm)	Polydispersity (%)	Scale	Diameter (nm)	Polydispersity (%)
F05	41.4	8.03	0.016377	4.7 ± 0.7	14.5	85.839	5.78 ± 0.8	14.5
F10	41.4	8.03	0.01618	5.3 ± 0.7	14.5	79.325	6.6 ± 0.9	14.5
F20	41.4	8.03	0.00023986	20.7 ± 1.2	6	0.25364	20.8 ± 1.2	6
F21	41.4	8.03	1.7037e-05	21.0 ± 1.5	7	0.40535	21.0 ± 1.7	7
F24	41.4	8.03	2.3759	23.0 ± 2.5	11.5	1.9633	21.0 ± 1.7	11.5
F27	41.4	8.03	1.0196	26.4 ± 2.0	8	1.1466	27.2 ± 2.1	8

Table A.10.: SAXS of F24 and F27 IONPs

Sample Id	Linear pearl model		$H = 0 \text{ T}$			$H = 0.9 \text{ T}$		
	$\eta_{core} \times 10^{-6} \text{Å}^{-2}$	$\eta_{solvent} \times 10^{-6} \text{Å}^{-2}$	D (nm)	Polydispersity (%)	$d_{ETE}(nm)$	D (nm)	Polydispersity (%)	$d_{ETE}(nm)$
F24	41.4	8.03	-	-	-	25.2 ± 2	11.5	7.7 ± 0.8
F27	41.4	8.03	27.3 ± 1.9	7	10.67 ± 0.7	27.4 ± 1.9	7	10 ± 0.7

The linear pearl model is taken originally from [166] and adapted in *SasView* [140].

$$P(Q, \alpha) = \frac{scale}{V} \left[\eta_p^2 \left(N + 2 \sum_{n=1}^{N-1} \frac{\sin(qnL)}{qnl} \right) \left(3(\Delta\eta) \frac{\sin(QR) - QR \cos(QR)}{(QR)^3} \right)^2 \right] \quad (\text{A.1})$$

where $\eta_p = (\eta_{pearl} - \eta_{solvent}) * (\text{volume of } N \text{ pearls})$

A.4. SANS fits and parameters

SANS radially integrated data of DBNPs fit to core-shell composite model. The most straightforward way to analyze 2D SAS patterns is to radially integrate to obtain 1D SAS spectra. While this remains a valid choice of analysis for isotropic patterns such as A12F10, there is a loss of valuable information for anisotropy patterns. The analysis of the 1D SAXS data usually begins with form-factor analysis to understand physical properties as described in the case of spherical IONP particles in Chapter 5. Often, such an analyses requires some *a priori* sample knowledge to impart constraints, given the possibility of multiple solutions to describe the SAXS data. Typically to determine the size and shape of a particle, a model dependent approach is considered, one that assumes a particular form-factor scattering. Determining the characteristics is fairly straightforward for geometrically simple particles such as spherical IONPs whose center of mass is at origin given by eqn. (2.121). The scattering from a sphere is only isotropic and mainly depends on the scattering vector, \vec{Q} . In the case of anisotropic object like a cylinder with center of mass at origin oriented parallel to the z axis, the form-factor is calculated as

$$F(Q) = 2\Delta V_{cy} J_1(Q_{\parallel}, R) \text{sinc}\left(\frac{Q_z L}{2}\right) \quad (\text{A.2})$$

and $V_{cy} = \pi R^2 L$, where R and L are the radius and length of the cylinder, respectively. The quantity J_1 is the first order Bessel function, $\text{sinc}(x) = \frac{\sin(x)}{x}$, $Q_{\parallel} = \sqrt{Q_x^2 + Q_y^2}$ where Q_x , Q_y and Q_z are the components of \vec{Q} along x , y and z directions, respectively. The anisotropic cylinder results in a different radial and axial scattering. For randomly aligned particles, the orientational average is applied to eqn. (A.2). A close resemblance to DBNP is the barbell model function derived from cylinder model with spherical caps where L is set to zero [210]. However, barbell model describes two spheres of equal radii and similar SLD.

Table A.11.: SANS core-shell and Guinier-Porod model of A12F10 DBNP

Field	Guinier-Porod model				Core-shell model						
	s	P	scale	R_g (nm)	η_{core} $\times 10^{-6}\text{\AA}^{-2}$	η_{shell} $\times 10^{-6}\text{\AA}^{-2}$	$\eta_{solvent}$ $\times 10^{-6}\text{\AA}^{-2}$	scale	R_{core} (nm)	pd (%)	thickness (nm)
0	0	4	36(4)	11.3 ± 1.7	5.75	-0.0475	0.94	0.005(2)	11.3 ± 1.7	16.5	3.3
0.5	0	4	33(3)	11.4 ± 1.6	5.75	-0.0475	0.94	0.006(2)	11.4 ± 1.6	15.3	3.9
1	0	4	30(3)	11.3 ± 1.6	5.75	-0.0475	0.94	0.005(2)	11.3 ± 1.6	15.2	3.7
2	0	4	28(3)	11.4 ± 1.7	5.75	-0.0475	0.94	0.004(1)	11.4 ± 1.7	15.4	3.6
3	0	4	27(3)	11.4 ± 1.8	5.75	-0.0475	0.94	0.004(1)	11.4 ± 1.8	15.5	3.6

Table A.12.: SANS core-shell fits of A13F14

Field (T)	η_{core} $\times 10^{-6}\text{\AA}^{-2}$	η_{shell} $\times 10^{-6}\text{\AA}^{-2}$	$\eta_{solvent}$ $\times 10^{-6}\text{\AA}^{-2}$	scale	R_{core} (nm)	thickness (nm)	pd (%)
0.5	5.88	-0.0475	0.94	0.00527(3)	11.1 ± 1.3	7.3	12
1	5.88	-0.0475	0.94	0.00522(3)	11.2 ± 1.3	7.2	12
2	5.88	-0.0475	0.94	0.00454(3)	11.2 ± 1.3	6.6	12

Table A.13.: SANS core-shell fits of A9F11

Field (T)	η_{core} $\times 10^{-6}\text{\AA}^{-2}$	η_{shell} $\times 10^{-6}\text{\AA}^{-2}$	$\eta_{solvent}$ $\times 10^{-6}\text{\AA}^{-2}$	scale	R_{core} (nm)	thickness (nm)	pd (%)
0.5	6.08	-0.0475	0.94	0.011(2)	10.6 ± 1.2	3.1	11.4
1	6.08	-0.0475	0.94	0.011(2)	10.6 ± 1.2	3.0	11.6
2	6.08	-0.0475	0.94	0.010(2)	10.7 ± 1.3	3.1	12.0
3	6.08	-0.0475	0.94	0.009(2)	10.6 ± 1.3	3.4	12.0

Table A.14.: SANS core-shell fits of A10F14

Field (T)	η_{core} $\times 10^{-6}\text{\AA}^{-2}$	η_{shell} $\times 10^{-6}\text{\AA}^{-2}$	$\eta_{solvent}$ $\times 10^{-6}\text{\AA}^{-2}$	scale	R_{core} (nm)	thickness (nm)	pd (%)
0.5	6.15	-0.0475	0.94	0.010	9.2 ± 1.1	1.3	12
1	6.15	-0.0475	0.94	0.011	9.2 ± 1.1	1.2	12
2	6.15	-0.0475	0.94	0.011	9.2 ± 1.1	1.0	12
3	6.15	-0.0475	0.94	0.008	9.2 ± 1.1	1.1	12

A.5. Sector fits

Table A.15.: Refined parameters from fitting peak functions to sector integrated peaks for category-1 DBNPs

$\alpha = 0^\circ$	A13F14		A9F11	
field	ℓ_{\parallel} (nm)	ζ_{\parallel} (nm)	ℓ_{\parallel} (nm)	ζ_{\parallel} (nm)
0.5	23.99 ± 0.01	161.3 ± 0.7	21.72 ± 0.01	164.1 ± 0.7
1	23.89 ± 0.01	156.5 ± 0.7	21.70 ± 0.02	168.9 ± 1.0
2	24.06 ± 0.02	164.3 ± 0.9	21.40 ± 0.04	157.6 ± 2.5
3	24.25 ± 0.2	172.5 ± 13.1	21.43 ± 0.06	153.4 ± 3.6
average	24.0 ± 0.1	163.6 ± 4.8	21.6 ± 0.1	161.0 ± 5
SAXS @ 0.9 T	24.0781 ± 0.0001	139.912 ± 0.004	19.4093 ± 0.0004	159.99 ± 0.03

Table A.16.: Refined parameters from fitting peak function models to sector integrated peaks of A10F14 DBNPs

A10F14	$\alpha = 0^\circ$				$\alpha = 90^\circ$			
field	ℓ_{\parallel} (nm)	ζ_{\parallel} (nm)	$\ell_{\parallel-cv}$ (nm)	$\zeta_{\parallel-cv}$ (nm)	ℓ_{\perp} (nm)	ζ_{\perp} (nm)	$\ell_{\perp-cv}$ (nm)	$\zeta_{\perp-cv}$ (nm)
0.5	18.839 ± 0.005	153.4 ± 0.5	18.23 ± 0.1	167 ± 8	19.87 ± 0.01	160.6 ± 0.7	19.23 ± 0.16	159 ± 11.4
1	18.864 ± 0.005	154.0 ± 0.3	18.0 ± 0.1	161.6 ± 9	19.77 ± 0.01	159.4 ± 0.5	19.19 ± 0.16	159.2 ± 11.0
2	18.752 ± 0.006	159.0 ± 0.4			19.83 ± 0.01	159.8 ± 0.6		
3	18.675 ± 0.007	167.8 ± 0.6			19.82 ± 0.01	153.0 ± 0.7		
average	18.8 ± 0.3	158.6 ± 4.8	18.1 ± 0.1	164.5 ± 3	19.82 ± 0.03	158 ± 3	19.21 ± 0.2	159.4 ± 0.1
SAXS @ 0.9 T	18.0328 ± 0.0005	182.28 ± 0.06						

B. Magnetic properties

Macroscopic magnetization

Table B.1.: The diamagnetic corrections for the M-H data of DBNPs, exchange bias (H_{EB}) fields @ 5 K and coercive fields (H_{c1} and H_{c2}) at 5 K and 300 K

Sample ID	Slope correction @5K	Slope correction @300K	H_{EB} (Oe) @5K ± 28 Oe	H_{c1} (Oe) @5K ± 20 Oe	H_{c2} (Oe) @5K ± 20 Oe	H_{c1} (Oe) @300K ± 20 Oe	H_2 (Oe) @300K ± 20 Oe
A12F10	0	-4.450e-05	-7	299	-314	21	-22
A9F11	-6.116e-5	-7.072e-05	-15	480	-490	0	-3
A10F14	0	0	-15	475	-505	36	-41
A13F14	-0.0001	-9.623e-05	-17	388	-423	18	-19

The masses obtained from ICP-OES are tabulated below and used to calculate the saturation magnetization M_s . The details of the experiment are mentioned in the chapter 4.

Table B.2.: Mass of the Fe and Au component in DBNPs determined using ICP-OES

Sample Id	Mass of Fe (μg)	Mass of Au (μg)
A12F10	41.6 ± 0.6	39.8 ± 0.7
A9F11	35.8 ± 1.6	25.7 ± 1.2
A10F14	288 ± 6	175 ± 2
A13F14	11.0 ± 0.3	16.1 ± 0.6

Table B.3.: The diamagnetic corrections for the M-H data of IONPs, exchange bias (H_{EB}) fields @ 5 K and coercive fields (H_{c1} and H_{c2}) at 5 K and 300 K

Sample ID	Slope correction @5K	Slope correction @300K	H_{EB} (Oe) @5K ± 28 Oe	H_{c1} (Oe) @5K ± 20 Oe	H_{c2} (Oe) @5K ± 20 Oe	H_{c1} (Oe) @300K ± 20 Oe	H_{c2} (Oe) @300K ± 20 Oe
F05	-9.330e-05	-0.0001	-4	16	-26	21	-23
F10	-9.181e-05	-9.516e-05	-27	70	-125	20	-26
F20	0	-1.692e-05	-43	513	-601	4	-40
F21	-7.721e-05	-9.795e-05	-1240	824	-3306	22	-24
F24	-0.00012	-0.0001	-90	561	-742	1	-3
F27	-3.059e-06	-1.094e-05	-11	523	-546	181	-156
F50	0	0	-1	220	-223	94	-96

C. Energy calculation

These equations are used for energy calculation based on equations obtained from [39, 211, 212, 213, 36]. Here, $\mu_o = 4\pi \times 10^{-7}$, $M_s = 4.46 \times 10^5$ A/m for bulk magnetite. The M_s from magnetometer is in emu/g is converted to A/m using equation eqn. (7.6). Given $\mu = M_s V$, then for a sphere of diameter D is

$$\mu = \frac{M_s \pi D^3}{6} \quad (\text{C.1})$$

Then the Zeeman energy, where $H = 1 \text{ T} = 7.9 \times 10^5 \text{ A/m}$, is

$$E_z = \mu_o \mu H \quad (\text{C.2})$$

The dipolar energy when in an head-to tail arrangement is

$$E_{dd} = -\frac{\mu_o \mu^2}{2\pi r^3} = -\frac{\mu_o \pi M_s^2 D^6}{72r^3} \quad (\text{C.3})$$

where r is the centre to centre distance between two spheres and δ is the edge to edge separation so that $r = D + \delta$. Then,

$$E_{dd} = -\frac{\mu_o \pi M_s^2}{9} \frac{D^3}{(\Delta + 2)^2} \quad (\text{C.4})$$

where $\Delta = \frac{2\delta}{D}$. This energy is plotted as function of edge to edge separation. The maximum dipolar energy is calculated by setting $\Delta = 0$

The simplified vDW energy for two spheres can be written and calculated as follows [53].

$$E_{vdW} = -\frac{A}{6} \left[\frac{2}{\Delta^2 + 4\Delta} + \frac{2}{(\Delta + 2)^2} + \ln \frac{(\Delta^2 + 4\Delta)}{(\Delta + 2)^2} \right] \quad (\text{C.5})$$

where A is the Hamaker constant.

Calculation of steric energy may be more complex for a general arbitrary shape,

however for spheres it is calculated and given by [53]

$$E_{steric} = -\frac{k_B T \pi D^2 \zeta}{2} \left[2 + \frac{\Delta + 2}{t_{eq}} \ln \frac{(1 + t_{eq})}{1 + \Delta/2} + \frac{\Delta}{t_{eq}} \right] \quad (C.6)$$

where ζ is the surface density, $t_{eq} = 2t/D$ where t is thickness of the surfactant.

D. Extended dumbbell analysis

Form-factor of DBNPs

In this section, the form-factor of a realistic dumbbell model (Fig. D.2) is analytically derived using the formulation of the form-factor developed previously for D₂O-nonane aerosol droplets [207, 208, 209]. This form-factor could be potentially used to model the dumbbell results. Consider the DBNP structure as depicted in Fig. D.2 where the radius of the spherical Au seed (shaded region) is given by R_2 while R_1 is the radius of the iron oxide sphere (unshaded region). The scattering length density for the IONP sphere is η_1 , for the seed is η_2 , and that of the surrounding is η_3 . The scattering length density difference is then given by

$$\Delta\eta_1 = \eta_1 - \eta_3 \quad (\text{D.1})$$

$$\Delta\eta_2 = \eta_2 - \eta_3 \quad (\text{D.2})$$

for each of the IONP and Au seed, respectively. Also consider θ_c to be the contact angle between the Au seed and the IONP sphere. The DBNPs exist in form of a number of possible structures which is broadly classified by their corresponding contact angle as presented in Fig. D.1.

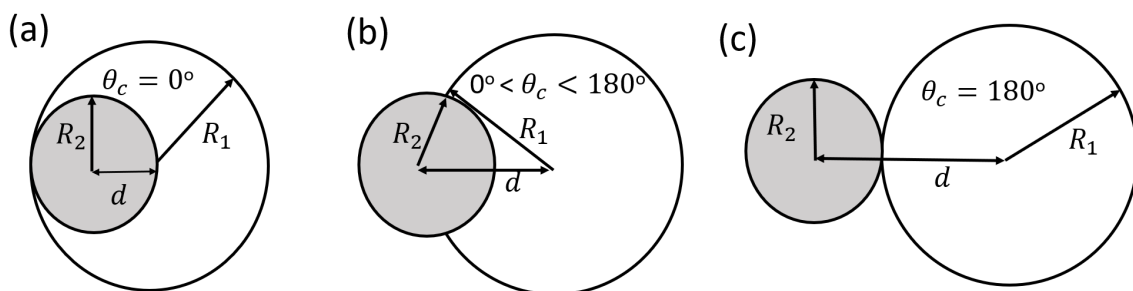


Figure D.1.: Possible structures of the DBNP where (a) $\theta_c = 0^\circ$, (b) $0^\circ < \theta_c < 180^\circ$ and (c) $\theta_c = 180^\circ$, adapted from [208].

The distance between the centers of the two spheres is defined by the quantity d such that

$$d^2 = R_1^2 + R_2^2 - 2R_1R_2\cos\theta_c \quad (\text{D.3})$$

where d is a function of the radius of the two spheres and their mutual contact angle. Formally, the form-factor amplitude for the entire particle assuming constant

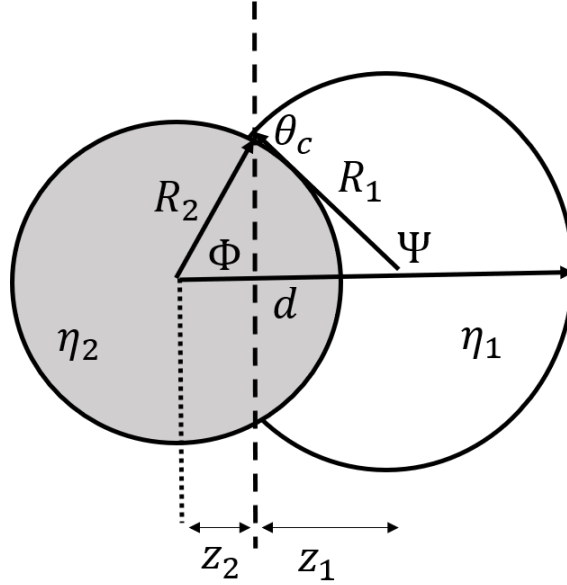


Figure D.2.: Illustration of dumbbell length scales and angles. Here, θ_C is the contact angle while d is the distance between the centers i.e. $z_1 + z_2$.

scattering length density in each component is written as

$$F(Q, \Delta\eta_1, \Delta\eta_2, R_1, R_2) = F_1(Q, \Delta\eta_1, R_1) + F_2(Q, \Delta\eta_2, R_2) \quad (\text{D.4})$$

where F_1 and F_2 are the form-factors of IONP and Au, respectively. The form-factor of the Au seed, i.e., F_2 , is given by the spherical form-factor obtained using eqn. (2.121),

$$F_2(Q) = 3\Delta\eta_2 V_2 \frac{(\sin(QR_2) - QR_2\cos(QR_2))}{(QR)^3} \quad (\text{D.5})$$

and here $V_2 = 4\pi R_2^3/3$ is the volume of the seed. Fütterer, Vliegthart and Lang (FVL model) developed the form-factor of the hemispherical cap of uniform density [214]. Thus, the IONP sphere grown on Au seed can be apprehended as the difference between form amplitudes of hemispherical caps sharing the same base indicated by

the dashed line in Fig. D.2. Thus, form amplitude of the IONP sphere is given by

$$F_1 = \Delta\eta_1 \left(\int_{V_1^{SC}} \exp(i\vec{Q}\cdot\vec{r}) d^3r - \int_{V_2^{SC}} \exp(i\vec{Q}\cdot\vec{r}) d^3r \right) \quad (D.6)$$

where V_1^{SC} and V_2^{SC} are the volumes of the spherical caps with radius R_1 and R_2 , respectively. The integrals are evaluated by extending the FVL method on Janus particles. The volume of the hemisphere with radius R_2 has the integration limits ranging from 0 to R_2 . Here, the cap origin is conceived as shifted from 0 to $z_2 = d + R_1 \cos\psi$. The angle ψ as portrayed in Fig. D.2 is introduced by Fletcher [209]. Therefore, the integration limits for V_2^{SC} is now z_2 to R_2 . FVL results on the cap with radius R_1 is then applied by changing the lower limits to $z_1 = R_1 \cos\psi$. Thus, eqn (D.6) is rewritten as

$$F_1(Q) = \Delta\eta_1 [F_1^{(1)}(Q) - F_1^{(2)}(Q)] \quad (D.7)$$

where the superscript index denotes the cap volume used in integration

$$F_1^n(Q) = \int_{V_n^{sc}} \exp\{iQ\cdot r\} d\vec{r} \quad (D.8)$$

Based on FVL results this integral is then expressed as

$$F_1^{(2)}(Q) = \frac{2\pi}{Q\sqrt{1-\mu^2}} \int_{z_2}^{R_2} \sqrt{R_2^2 - z^2} J_1(u_2) \exp(iQ\mu z) dz \quad (D.9)$$

where J_1 is the Bessel function of the first order, while

$$\mu = \cos\theta \quad (D.10)$$

and θ is the angle between the scattering vector \vec{Q} and the z-axis. To evaluate $F_1^{(1)}$,

$$F_1^{(1)}(Q) = \frac{2\pi}{Q\sqrt{1-\mu^2}} \int_{z_1}^{R_1} \sqrt{R_1^2 - z^2} J_1(u_1) \exp(iQ\mu[z+d]) dz \quad (D.11)$$

where

$$u_1 = Q\sqrt{1-\mu^2}\sqrt{R_1^2 - z^2} \quad (D.12)$$

$$u_2 = Q\sqrt{1-\mu^2}\sqrt{R_2^2 - z^2} \quad (D.13)$$

To complete the construction of the particle form factor $P(Q) = \langle F^2(Q) \rangle$, the square

of $F(Q)$ is written as

$$F^2(Q) = F_2^2 + \Delta\eta_1 F_2 [F_1^{(1)}(Q) + F_1^{(1)*}(Q) - F_1^{(2)}(Q) - F_1^{(2)*}(Q)] \quad (\text{D.14})$$

$$+ \Delta\eta_1^2 [F_1^{(1)}(Q) - F_1^{(2)}(Q)] [F_1^{(1)*}(Q) - F_1^{(2)*}(Q)]$$

where * indicates complex conjugation. Then the expression is explicitly written in a more compact form as

$$F^2(Q) = F_2^2(Q) + 2\pi\Delta\eta_1 [C_1(\mu, d) - C_2(\mu, 0)]$$

$$+ (2\pi\Delta\eta_1)^2 [(C_1(\mu, d) - C_2(\mu, 0))^2$$

$$+ ((S_1(\mu, d) - S_2(\mu, 0))^2] \quad (\text{D.15})$$

where C_i and S_i are defined as follows,

$$C_1(\theta) = \frac{1}{Q\sqrt{1-\mu^2}} \int_{Z_1}^{R_1} \sqrt{R_1^2 - z^2} J_1(u_1) \cos[Q\mu(z+d)] dz \quad (\text{D.16})$$

$$C_2(\theta) = \frac{1}{Q\sqrt{1-\mu^2}} \int_{Z_2}^{R_2} \sqrt{R_1^2 - z^2} J_1(u_2) \cos[Q\mu z] dz \quad (\text{D.17})$$

$$S_1(\theta) = \frac{1}{Q\sqrt{1-\mu^2}} \int_{Z_1}^{R_1} \sqrt{R_1^2 - z^2} J_1(u_1) \sin[Q\mu(z+d)] dz \quad (\text{D.18})$$

$$S_2(\theta) = \frac{1}{Q\sqrt{1-\mu^2}} \int_{Z_2}^{R_2} \sqrt{R_1^2 - z^2} J_1(u_2) \sin[Q\mu z] dz \quad (\text{D.19})$$

To complete the calculation, the orientational average over the angle θ is performed.

$$P(Q) = F_2^2 + 2\pi\Delta\eta_1 \int_0^\pi [C_1(\theta) - C_2(\theta)] \sin\theta d\theta$$

$$+ (2\pi\Delta\eta_1)^2 \int_0^\pi [(C_1(\theta) - C_2(\theta))^2 + ((S_1(\theta) - S_2(\theta))^2] \sin\theta d\theta$$

Preliminary RMC simulation on DBNPs

The preliminary results was simulated for 100 particles in 50 steps took 10hrs to converge. Although, the result do not currently satisfactorily replicate the 2D pattern, there are early indications of 2D chains present in A10F14 and 1D chains in A9F11. Fits have to be further optimised based on the above analytical or numerical

descriptions of dumbbells. Preliminary results show chains arrange in head-to-tail 1D arrangement for A9F11 and 2D arrangements in A10F14.

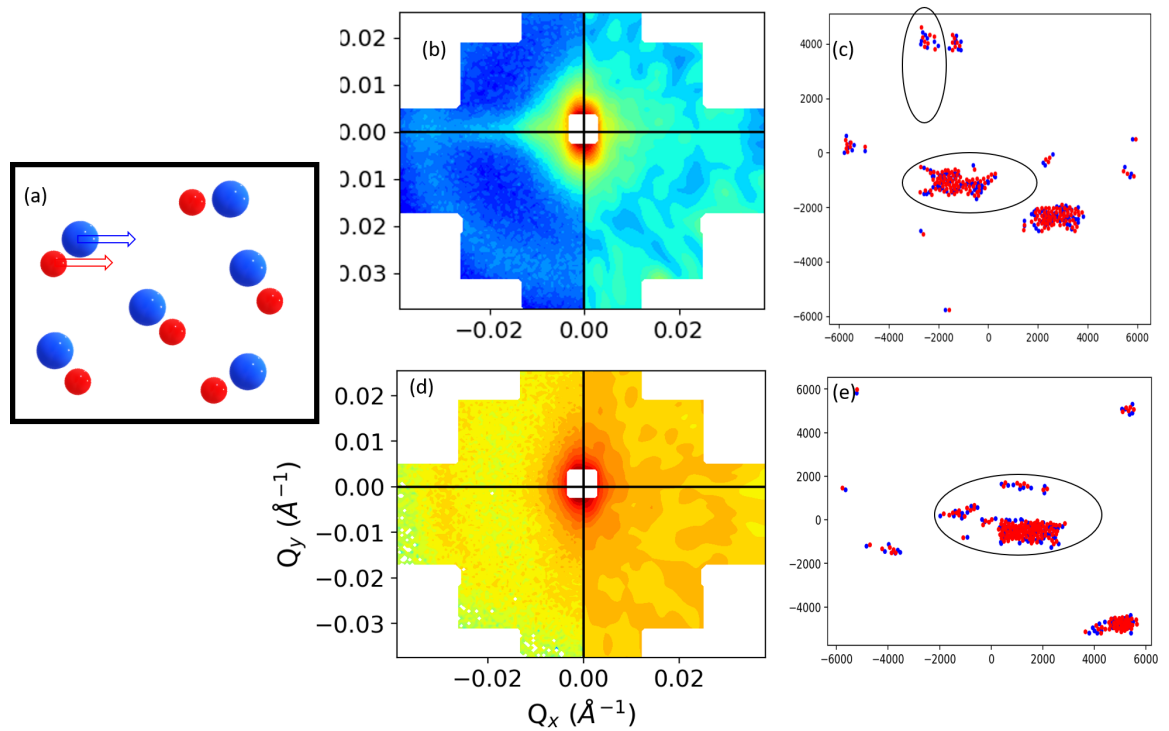


Figure D.3.: (a) The scheme of simplified RMC. (b) 2D Simulated patterns on right half and experimental data on the left (c) corresponding real space assembly of A10F14. (d) 2D Simulated patterns on right half and experimental data on the left (e) corresponding real space assembly of A9F11.

List of Abbreviations

NP	nanoparticle
MNP	magnetic nanoparticle
IONP	iron oxide nanoparticle
DBNP	dumbbell nanoparticle
ZFC	zero field cooling
FC	field cooling
PPMS	physical property measurement system
SW	Stoner-Wohlfarth
SOC	spin-orbit coupling
FM	ferromagnet
AF	antiferromagnet
FiM	ferrimagnet
MCA	magnetocrystalline anisotropy
SW	Stoner-Wohlfarth
SPM	superparamagnetism
vdW	van der Waals
xPDF	x-ray pair distribution function
SAS	small-angle scattering
SLD	scattering length density
SAXS	small-angle x-ray scattering
SANS	small-angle neutron scattering
RMC	reverse Monte-Carlo

List of Symbols

m_e	mass of electron	9.109×10^{-31} kg
m_n	mass of neutron	1.675×10^{-27} kg
μ_B	Bohr magneton	$1\mu_B = 9.27 \times 10^{-24}$ Am ²
μ_o	magnetic permeability in free space	$4 \pi \times 10^{-7}$ H/m
k_B	Boltzmann constant	1.381×10^{-23} J/K
\mathcal{J}	Exchange integral	J
$\vec{\mu}$	magnetic moment	Am ²
M_s	saturation magnetization	A/m
M_r	remanent magnetization	A/m
\vec{B}	magnetic field	T
\vec{H}	magnetic field strength	1 T = 795 kA/m
H_c	coercive field	T
χ	magnetic susceptibility	
C	Curie constant	K
T_C	Curie temperature	K
T_N	Néel temperature	K
T_B	Blocking temperature	K
E_a	anisotropy energy	J
E_{mca}	magnetocrystalline anisotropy energy	J
E_{sh}	shape anisotropy energy	J
E_z	Zeeman energy	J
E_{ex}	exchange energy	J
E_m	magnetostatic energy	J
E_{me}	magnetoelastic energy	J
K_{eff}	effective anisotropy constant	J/m ³
K_1	crystalline anisotropy constant	J/m ³
K_{sh}	shape anisotropy constant	J/m ³

K_s	surface anisotropy constant	J/m ²
K_V	anisotropy constant macroscopic sample	J/m ³
\mathcal{N}_{ij}	demagnetizing tensor	
E_{vdW}	van der Waals energy	J
E_{ES}	electrostatic energy energy	J
E_{dd}	magnetic dipole energy	J
E_{steric}	steric energy	J
\vec{Q}	scattering vector	Å ⁻¹
V	volume	m ³
V	interaction potential	
$A(\vec{Q})$	scattering amplitude	
$P(\vec{Q})$	particle form-factor	
$S(\vec{Q})$	structure factor	
$\mathcal{S}(\vec{Q})$	scattering function	
\mathcal{H}	general Hamiltonian	

Bibliography

- [1] George M Whitesides and Bartosz Grzybowski. “Self-assembly at all scales”. In: *Science* 295.5564 (2002), pp. 2418–2421.
- [2] Quentin A Pankhurst, J Connolly, Stephen K Jones, and JJJopDAp Dobson. “Applications of magnetic nanoparticles in biomedicine”. In: *Journal of physics D: Applied physics* 36.13 (2003), R167.
- [3] Joan Estelrich, Elvira Escribano, Josep Queralt, and Maria Antònia Busquets. “Iron oxide nanoparticles for magnetically-guided and magnetically-responsive drug delivery”. In: *International journal of molecular sciences* 16.4 (2015), pp. 8070–8101.
- [4] Hira Fatima and Kyo-Seon Kim. “Iron-based magnetic nanoparticles for magnetic resonance imaging”. In: *Advanced Powder Technology* 29.11 (2018), pp. 2678–2685.
- [5] Ziba Hedayatnasab, Ali Dabbagh, Faisal Abnisa, and Wan Mohd Ashri Wan Daud. “Polycaprolactone-coated superparamagnetic iron oxide nanoparticles for in vitro magnetic hyperthermia therapy of cancer”. In: *European Polymer Journal* 133 (2020), p. 109789.
- [6] RH Kodama. “Magnetic nanoparticles”. In: *Journal of magnetism and magnetic materials* 200.1-3 (1999), pp. 359–372.
- [7] Zhendong Fu, Yinguo Xiao, Artem Feoktystov, Vitaliy Pipich, Marie-Sousai Appavou, Yixi Su, Erxi Feng, Wentao Jin, and Thomas Brückel. “Field-induced self-assembly of iron oxide nanoparticles investigated using small-angle neutron scattering”. In: *Nanoscale* 8.43 (2016), pp. 18541–18550. ISSN: 2040-3364.
- [8] Mark Klokkenburg, Chantal Vonk, Eva M. Claesson, Johannes D. Meeldijk, Ben H. Ern , and Albert P. Philipse. “Direct imaging of zero-field dipolar structures in colloidal dispersions of synthetic magnetite”. In: *Journal of the American Chemical Society* 126.51 (2004), pp. 16706–16707.

-
- [9] Sergey P Gubin. *Magnetic nanoparticles*. John Wiley & Sons, 2009.
- [10] S Bedanta, A Barman, W Kleemann, O Petravic, and T Seki. “Magnetic nanoparticles: a subject for both fundamental research and applications”. In: *Journal of nanomaterials* 2013 (2013).
- [11] Sabrina Disch. *The spin structure of magnetic nanoparticles and in magnetic nanostructures*. Vol. 21. Forschungszentrum Jülich, 2010.
- [12] Dominika Zákutná, Daniel Nižňanský, Lester C Barnsley, Earl Babcock, Zahir Salhi, Artem Feoktystov, Dirk Honecker, and Sabrina Disch. “Field dependence of magnetic disorder in nanoparticles”. In: *Physical Review X* 10.3 (2020), p. 031019.
- [13] Mark Klokkenburg, Ben H. Ern , Johannes D. Meeldijk, Albrecht Wiedemann, Andrei V. Petukhov, Roel P.A. Dullens, and Albert P. Philipse. “In situ imaging of field-induced hexagonal columns in magnetite ferrofluids”. In: *Physical Review Letters* 97.18 (2006), pp. 4–7.
- [14] Nileena Nandakumaran, Lester Barnsley, Artem Feoktystov, Sergei A Ivanov, Dale L Huber, Lisa S Fruhner, Vanessa Leffler, Sascha Ehlert, Emmanuel Kentzinger, Asma Qdemat, et al. “Unravelling Magnetic Nanochain Formation in Dispersion for In Vivo Applications”. In: *Advanced Materials* (2021), p. 2008683.
- [15] Prashant K Jain, Xiaohua Huang, Ivan H El-Sayed, and Mostafa A El-Sayed. “Review of some interesting surface plasmon resonance-enhanced properties of noble metal nanoparticles and their applications to biosystems”. In: *Plasmonics* 2.3 (2007), pp. 107–118.
- [16] Heng Yu, Min Chen, Philip M Rice, Shan X Wang, RL White, and Shouheng Sun. “Dumbbell-like bifunctional Au- Fe₃O₄ nanoparticles”. In: *Nano letters* 5.2 (2005), pp. 379–382.
- [17] Chao Wang, Hideo Daimon, and Shouheng Sun. “Dumbbell-like Pt- Fe₃O₄ nanoparticles and their enhanced catalysis for oxygen reduction reaction”. In: *Nano letters* 9.4 (2009), pp. 1493–1496.
- [18] Elvira Fantechi, Alejandro G Roca, Borja Sep lveda, Pau Torruella, Sonia Estrad , Francesca Peir , Emerson Coy, Stefan Jurga, Neus G Bast s, Josep Nogu s, et al. “Seeded growth synthesis of Au–Fe₃O₄ heterostructured nanocryst-

- tals: rational design and mechanistic insights”. In: *Chemistry of Materials* 29.9 (2017), pp. 4022–4035.
- [19] P Guardia, S Nitti, ME Materia, G Pugliese, N Yaacoub, J-M Greneche, C Lefevre, L Manna, and T Pellegrino. “Gold–iron oxide dimers for magnetic hyperthermia: the key role of chloride ions in the synthesis to boost the heating efficiency”. In: *Journal of Materials Chemistry B* 5.24 (2017), pp. 4587–4594.
- [20] Natalie A Frey, Sanyadanam Srinath, Hariharan Srikanth, Chao Wang, and Shouheng Sun. “Static and Dynamic Magnetic Properties of Composite Au-Fe₃O₄ Nanoparticles”. In: *IEEE transactions on magnetics* 43.6 (2007), pp. 3094–3096.
- [21] E Umut, Francesco Pineider, P Arosio, C Sangregorio, M Corti, F Tabak, A Lascialfari, and P Ghigna. “Magnetic, optical and relaxometric properties of organically coated gold–magnetite (Au–Fe₃O₄) hybrid nanoparticles for potential use in biomedical applications”. In: *Journal of Magnetism and Magnetic Materials* 324.15 (2012), pp. 2373–2379.
- [22] Mikhail Feygenson, John C Bauer, Zheng Gai, Carlos Marques, Meigan C Aronson, Xiaowei Teng, Dong Su, Vesna Stanic, Volker S Urban, Kevin A Beyer, et al. “Exchange bias effect in Au-Fe₃O₄ dumbbell nanoparticles induced by the charge transfer from gold”. In: *Physical Review B* 92.5 (2015), p. 054416.
- [23] Dmitri V Talapin, Elena V Shevchenko, Maryna I Bodnarchuk, Xingchen Ye, Jun Chen, and Christopher B Murray. “Quasicrystalline order in self-assembled binary nanoparticle superlattices”. In: *Nature* 461.7266 (2009), pp. 964–967.
- [24] Guido Avvisati, Teun Vissers, and Marjolein Dijkstra. “Self-assembly of patchy colloidal dumbbells”. In: *The Journal of Chemical Physics* 142.8 (2015), p. 084905.
- [25] Emanuela Bianchi, Ronald Blaak, and Christos N Likos. “Patchy colloids: state of the art and perspectives”. In: *Physical Chemistry Chemical Physics* 13.14 (2011), pp. 6397–6410.
- [26] Liang Hong, Angelo Cacciuto, Erik Luijten, and Steve Granick. “Clusters of amphiphilic colloidal spheres”. In: *Langmuir* 24.3 (2008), pp. 621–625.

-
- [27] Fei Liu, Shailja Goyal, Michael Forrester, Tao Ma, Kyle Miller, Yasmeen Mansoorieh, John Henjum, Lin Zhou, Eric Cochran, and Shan Jiang. “Self-assembly of Janus dumbbell nanocrystals and their enhanced surface plasmon resonance”. In: *Nano Letters* 19.3 (2018), pp. 1587–1594.
- [28] Javier Reguera, Tatjana Flora, Naomi Winckelmans, José C Rodríguez-Cabello, and Sara Bals. “Self-assembly of Janus Au: Fe₃O₄ branched nanoparticles. From organized clusters to stimuli-responsive nanogel suprastructures”. In: *Nanoscale Advances* 2.6 (2020), pp. 2525–2530.
- [29] Davit Jishkariani, Yaoting Wu, Da Wang, Yang Liu, Alfons Van Blaaderen, and Christopher B Murray. “Preparation and self-assembly of dendronized Janus Fe₃O₄-Pt and Fe₃O₄-Au heterodimers”. In: *ACS nano* 11.8 (2017), pp. 7958–7966.
- [30] Maximilian Niehues, Sabrina Engel, and Bart Jan Ravoo. “Photo-Responsive Self-Assembly of Plasmonic Magnetic Janus Nanoparticles”. In: *Langmuir* 37.37 (2021), pp. 11123–11130.
- [31] John MD Coey. *Magnetism and magnetic materials*. Cambridge university press, 2010.
- [32] Alberto P Guimarães and Alberto Passos Guimaraes. *Principles of nanomagnetism*. Vol. 7. Springer, 2009.
- [33] Stephen Blundell. *Magnetism in condensed matter*. 2003.
- [34] E. P. Wohlfarth. “Magnetic properties of single domain ferromagnetic particles”. In: *Journal of Magnetism and Magnetic Materials* 39.1-2 (1983), pp. 39–44. ISSN: 03048853.
- [35] Kurt Heinz Jürgen Buschow, Frank R Boer, et al. *Physics of magnetism and magnetic materials*. Vol. 7. Springer, 2003.
- [36] AD Shine and RC Armstrong. “The rotation of a suspended axisymmetric ellipsoid in a magnetic field”. In: *Rheologica Acta* 26.2 (1987), pp. 152–161.
- [37] JA Osborn. “Demagnetizing factors of the general ellipsoid”. In: *Physical review* 67.11-12 (1945), p. 351.
- [38] L Berger, Y Labaye, M Tamine, and JMD Coey. “Ferromagnetic nanoparticles with strong surface anisotropy: Spin structures and magnetization processes”. In: *Physical Review B* 77.10 (2008), p. 104431.

- [39] Ronald E Rosensweig. “Heating magnetic fluid with alternating magnetic field”. In: *Journal of magnetism and magnetic materials* 252 (2002), pp. 370–374.
- [40] Satoshi Ota and Yasushi Takemura. “Characterization of Néel and Brownian relaxations isolated from complex dynamics influenced by dipole interactions in magnetic nanoparticles”. In: *The Journal of Physical Chemistry C* 123.47 (2019), pp. 28859–28866.
- [41] Nguyen TK Thanh. “Magnetic nanoparticles: from fabrication to clinical applications”. In: (2012).
- [42] Kyle JM Bishop, Christopher E Wilmer, Siowling Soh, and Bartosz A Grzybowski. “Nanoscale forces and their uses in self-assembly”. In: *small* 5.14 (2009), pp. 1600–1630.
- [43] Byoung Har Hwang, Han Jin Ahn, Soon Joon Rho, Soo Sang Chae, and Hong Koo Baik. “Vertical alignment of liquid crystals with negative dielectric anisotropy on an inorganic thin film with a hydrophilic surface”. In: *Langmuir* 25.14 (2009), pp. 8306–8312.
- [44] V Adrian Parsegian. *Van der Waals forces: a handbook for biologists, chemists, engineers, and physicists*. Cambridge university press, 2005.
- [45] Bertrand Faure, German Salazar-Alvarez, and Lennart Bergstrom. “Hamaker constants of iron oxide nanoparticles”. In: *Langmuir* 27.14 (2011), pp. 8659–8664.
- [46] Dmitri V Talapin, Jong-Soo Lee, Maksym V Kovalenko, and Elena V Shevchenko. “Prospects of colloidal nanocrystals for electronic and optoelectronic applications”. In: *Chemical reviews* 110.1 (2010), pp. 389–458.
- [47] Silvina M Gatica, Milton W Cole, and Darrell Velegol. “Designing van der Waals forces between nanocolloids”. In: *Nano letters* 5.1 (2005), pp. 169–173.
- [48] AJ Stone. “Intermolecular forces”. In: *Molecular Liquids*. Springer, 1984, pp. 1–34.
- [49] Bertrand Faure. “Particle interactions at the nanoscale: From colloidal processing to self-assembled arrays”. PhD thesis. Department of Materials and Environmental Chemistry (MMK), Stockholm University, 2012.
- [50] EJW Verwey and J Th G Overbeek. “Theory of the stability of lyophobic colloids. Elsevier, Amsterdam.” In: *Theory of the stability of lyophobic colloids*. Elsevier, Amsterdam. (1948).

-
- [51] Boris Derjaguin and Lev Landau. “Theory of the stability of strongly charged lyophobic sols and of the adhesion of strongly charged particles in solutions of electrolytes”. In: *Progress in Surface Science* 43.1-4 (1993), pp. 30–59.
- [52] S Alexander. “Adsorption of chain molecules with a polar head a scaling description”. In: *Journal De Physique* 38.8 (1977), pp. 983–987.
- [53] Stefan Odenbach. *Colloidal magnetic fluids: basics, development and application of ferrofluids*. Vol. 763. Springer, 2009.
- [54] PG De Gennes. “Polymers at an interface; a simplified view”. In: *Advances in colloid and interface science* 27.3-4 (1987), pp. 189–209.
- [55] Donald H Napper. *Polymeric stabilization of colloidal dispersions*. Vol. 3. Academic Press, 1983.
- [56] Max Mason and Warren Weaver. “The settling of small particles in a fluid”. In: *Physical Review* 23.3 (1924), p. 412.
- [57] Devidirjit Singh Sivia. *Elementary scattering theory: for X-ray and neutron users*. Oxford University Press, 2011.
- [58] Thomas Brückel, Gernot Heger, Dieter Richter, Reiner Zorn, and Georg Roth. *Laboratory Course Neutron Scattering: Lectures*. PreJuSER-16299. Streumethoden, 2011.
- [59] Thomas Brückel. *Neutron Scattering Lectures of the JCNS Laboratory Course held at Forschungszentrum Jülich and at the Heinz Maier-Leibnitz Zentrum Garching In cooperation with RWTH Aachen and University of Münster*. Vol. 63. Forschungszentrum Jülich, 2013.
- [60] Ta-You Wu and Takashi Ohmura. *Quantum theory of scattering*. Courier Corporation, 2014.
- [61] Stefan Blugel. “A 2 Scattering Theory: Born Series”. In: (2012).
- [62] Roger Pynn. “LECTURE 1: Introduction & Neutron Scattering “Theory””. In: *Los Alamos Neutron Science Center, Los Alamos Science* (1989).
- [63] Th Zemb and Peter Lindner. *Neutron, X-rays and light. Scattering methods applied to soft condensed matter*. North Holland, 2002.
- [64] B Hammouda. “Probing Nanoscale Structures: The SANS Toolbox (2009)”. In: *NIST Center for Neutron Research* (2008).

- [65] Boualem Hammouda. “A new Guinier–Porod model”. In: *Journal of Applied Crystallography* 43.4 (2010), pp. 716–719.
- [66] A. Hoell, A. Wiedenmann, U. Heyen, and D. Schüler. “Nanostructure and field-induced arrangement of magnetosomes studied by SANSPOLE”. In: *Physica B: Condensed Matter* 350.1-3 SUPPL. 1 (2004), pp. 309–313. ISSN: 09214526.
- [67] M Kammel, A Wiedenmann, and A Hoell. “Nuclear and magnetic nanostructure of magnetite ferrofluids studied by SANSPOLE”. In: *Journal of magnetism and magnetic materials* 252 (2002), pp. 89–91.
- [68] Robert E Dinnebier and Simon JL Billinge. *Powder diffraction: theory and practice*. Royal society of chemistry, 2008.
- [69] Simon JL Billinge. “The rise of the X-ray atomic pair distribution function method: a series of fortunate events”. In: *Philosophical Transactions of the Royal Society A* 377.2147 (2019), p. 20180413.
- [70] Takeshi Egami and Simon JL Billinge. *Underneath the Bragg peaks: structural analysis of complex materials*. Elsevier, 2003.
- [71] Xuelong Wang, Sha Tan, Xiao-Qing Yang, and Enyuan Hu. “Pair distribution function analysis: Fundamentals and application to battery materials”. In: *Chinese Physics B* 29.2 (2020), p. 028802.
- [72] Ralph A Sperling, Pilar Rivera Gil, Feng Zhang, Marco Zanella, and Wolfgang J Parak. “Biological applications of gold nanoparticles”. In: *Chemical Society Reviews* 37.9 (2008), pp. 1896–1908.
- [73] C Sönnichsen, T Franzl, T Wilk, G Von Plessen, and J Feldmann. “Plasmon resonances in large noble-metal clusters”. In: *New Journal of Physics* 4.1 (2002), p. 93.
- [74] Rajesh Sardar, Alison M Funston, Paul Mulvaney, and Royce W Murray. “Gold nanoparticles: past, present, and future”. In: *Langmuir* 25.24 (2009), pp. 13840–13851.
- [75] Da-Ren Chen, Christine H Wendt, and David YH Pui. “A novel approach for introducing bio-materials into cells”. In: *Journal of Nanoparticle Research* 2.2 (2000), pp. 133–139.
- [76] Erik C Dreaden, Megan A Mackey, Xiaohua Huang, Bin Kang, and Mostafa A El-Sayed. “Beating cancer in multiple ways using nanogold”. In: *Chemical Society Reviews* 40.7 (2011), pp. 3391–3404.

- [77] Jennifer L West and Naomi J Halas. “Engineered nanomaterials for biophotonics applications: improving sensing, imaging, and therapeutics”. In: *Annual review of biomedical engineering* 5.1 (2003), pp. 285–292.
- [78] Lev Dykman and Nikolai Khlebtsov. “Gold nanoparticles in biomedical applications: recent advances and perspectives”. In: *Chemical Society Reviews* 41.6 (2012), pp. 2256–2282.
- [79] Nikolai Khlebtsov and Lev Dykman. “Biodistribution and toxicity of engineered gold nanoparticles: a review of in vitro and in vivo studies”. In: *Chemical Society Reviews* 40.3 (2011), pp. 1647–1671.
- [80] M Mohapatra and S Anand. “Synthesis and applications of nano-structured iron oxides/hydroxides—a review”. In: *International Journal of Engineering, Science and Technology* 2.8 (2010).
- [81] Li Li, Wen Jiang, Kui Luo, Hongmei Song, Fang Lan, Yao Wu, and Zhongwei Gu. “Superparamagnetic iron oxide nanoparticles as MRI contrast agents for non-invasive stem cell labeling and tracking”. In: *Theranostics* 3.8 (2013), p. 595.
- [82] Ruirui Qiao, Chunhui Yang, and Mingyuan Gao. “Superparamagnetic iron oxide nanoparticles: from preparations to in vivo MRI applications”. In: *Journal of Materials Chemistry* 19.35 (2009), pp. 6274–6293.
- [83] Zahra Bakhtiary, Amir Ata Saei, Mohammad J Hajipour, Mohammad Raoufi, Ophir Vermesh, and Morteza Mahmoudi. “Targeted superparamagnetic iron oxide nanoparticles for early detection of cancer: Possibilities and challenges”. In: *Nanomedicine: Nanotechnology, Biology and Medicine* 12.2 (2016), pp. 287–307.
- [84] Peter Wust, B Hildebrandt, G Sreenivasa, B Rau, J Gellermann, H Riess, R Felix, and PM Schlag. “Hyperthermia in combined treatment of cancer”. In: *The lancet oncology* 3.8 (2002), pp. 487–497.
- [85] Damien Faivre and Dirk Schuler. “Magnetotactic bacteria and magnetosomes”. In: *Chemical reviews* 108.11 (2008), pp. 4875–4898.
- [86] Farheen N Sayed and Vivek Polshettiwar. “Facile and sustainable synthesis of shaped iron oxide nanoparticles: effect of iron precursor salts on the shapes of iron oxides”. In: *Scientific reports* 5.1 (2015), pp. 1–14.

- [87] Alexey Shavel and Luis M Liz-Marzán. “Shape control of iron oxide nanoparticles”. In: *Physical Chemistry Chemical Physics* 11.19 (2009), pp. 3762–3766.
- [88] Damien Faivre. *Iron oxides: from nature to applications*. John Wiley & Sons, 2016.
- [89] Seyed Mohammadali Dadfar, Karolin Roemhild, Natascha I Drude, Saskia von Stillfried, Ruth Knüchel, Fabian Kiessling, and Twan Lammers. “Iron oxide nanoparticles: Diagnostic, therapeutic and theranostic applications”. In: *Advanced drug delivery reviews* 138 (2019), pp. 302–325.
- [90] Gang Liu, Jinhao Gao, Hua Ai, and Xiaoyuan Chen. “Applications and potential toxicity of magnetic iron oxide nanoparticles”. In: *Small* 9.9-10 (2013), pp. 1533–1545.
- [91] Attarad Ali, Muhammad Zia Hira Zafar, Ihsan ul Haq, Abdul Rehman Phull, Joham Sarfraz Ali, and Altaf Hussain. “Synthesis, characterization, applications, and challenges of iron oxide nanoparticles”. In: *Nanotechnology, science and applications* 9 (2016), p. 49.
- [92] Zhendong Fu, Yinguo Xiao, Artem Feoktystov, Vitaliy Pipich, Marie-Sousai Appavou, Yixi Su, Erxi Feng, Wentao Jin, and Thomas Brückel. “Field-induced self-assembly of iron oxide nanoparticles investigated using small-angle neutron scattering”. In: *Nanoscale* 8.43 (2016), pp. 18541–18550.
- [93] Delphine Toulemon, Mircea V Rastei, David Schmool, José Sáiz Garitaonandia, Luis Lezama, Xavier Cattoën, Sylvie Bégin-Colin, and Benoit P Pichon. “Enhanced collective magnetic properties induced by the controlled assembly of iron oxide nanoparticles in chains”. In: *Advanced Functional Materials* 26.15 (2016), pp. 2454–2462.
- [94] Mingsheng Wang, Le He, and Yadong Yin. “Magnetic field guided colloidal assembly”. In: *Materials Today* 16.4 (2013), pp. 110–116.
- [95] L-S Zhong, J-S Hu, H-P Liang, A-M Cao, W-G Song, and L-J Wan. “Self-Assembled 3D flowerlike iron oxide nanostructures and their application in water treatment”. In: *Advanced materials* 18.18 (2006), pp. 2426–2431.
- [96] Chao Wang, Hongfeng Yin, Sheng Dai, and Shouheng Sun. “A general approach to noble metal- metal oxide dumbbell nanoparticles and their catalytic application for CO oxidation”. In: *Chemistry of Materials* 22.10 (2010), pp. 3277–3282.

-
- [97] Yanqiu Li, Qiang Zhang, Arto V Nurmiikko, and Shouheng Sun. “Enhanced magneto-optical response in dumbbell-like Ag-CoFe₂O₄ nanoparticle pairs”. In: *Nano letters* 5.9 (2005), pp. 1689–1692.
- [98] Hongwei Gu, Zhimou Yang, Jinhao Gao, CK Chang, and Bing Xu. “Heterodimers of nanoparticles: formation at a liquid-liquid interface and particle-specific surface modification by functional molecules”. In: *Journal of the American Chemical Society* 127.1 (2005), pp. 34–35.
- [99] Kwan-Wook Kwon and Moonsub Shim. “ γ -Fe₂O₃/II-VI sulfide nanocrystal heterojunctions”. In: *Journal of the American Chemical Society* 127.29 (2005), pp. 10269–10275.
- [100] Rui Hao, Ruijun Xing, Zhichuan Xu, Yanglong Hou, Song Gao, and Shouheng Sun. “Synthesis, functionalization, and biomedical applications of multifunctional magnetic nanoparticles”. In: *Advanced materials* 22.25 (2010), pp. 2729–2742.
- [101] Zhenan Bao, Linda Chen, Marcus Weldon, Edwin Chandross, Oksana Chernavskaya, Yong Dai, and Jeffery B-H Tok. “Toward controllable self-assembly of microstructures: selective functionalization and fabrication of patterned spheres”. In: *Chemistry of materials* 14.1 (2002), pp. 24–26.
- [102] DH Reich, M Tanase, A Hultgren, LA Bauer, CS Chen, and GJ Meyer. “Biological applications of multifunctional magnetic nanowires”. In: *Journal of Applied Physics* 93.10 (2003), pp. 7275–7280.
- [103] Chao Wang, Chenjie Xu, Hao Zeng, and Shouheng Sun. “Recent progress in syntheses and applications of dumbbell-like nanoparticles”. In: *Advanced materials* 21.30 (2009), pp. 3045–3052.
- [104] S Banerjee, SO Raja, M Sardar, N Gayathri, B Ghosh, and A Dasgupta. “Iron oxide nanoparticles coated with gold: Enhanced magnetic moment due to interfacial effects”. In: *Journal of Applied Physics* 109.12 (2011), p. 123902.
- [105] AM Clogston. “Range of a static spin perturbation in palladium”. In: *Physical Review Letters* 19.10 (1967), p. 583.
- [106] JJ Hauser. “Magnetic proximity effect”. In: *Physical Review* 187.2 (1969), p. 580.

- [107] Paul Zakalek. “Magnetic Interface Effects in Thin Film Heterostructures”. Dissertation, RWTH Aachen, 2015. Dissertation. RWTH Aachen, 2015, 150 p. URL: <https://juser.fz-juelich.de/record/818161>.
- [108] Ton VW Janssens, Bjerne S Clausen, Britt Hvolbæk, Hanne Falsig, Claus H Christensen, Thomas Bligaard, and Jens K Nørskov. “Insights into the reactivity of supported Au nanoparticles: combining theory and experiments”. In: *Topics in Catalysis* 44.1 (2007), pp. 15–26.
- [109] Chengjun Kang and Andrei Honciuc. “Influence of geometries on the assembly of snowman-shaped Janus nanoparticles”. In: *ACS nano* 12.4 (2018), pp. 3741–3750.
- [110] Stoyan K Smoukov, Sumit Gangwal, Manuel Marquez, and Orlin D Velev. “Reconfigurable responsive structures assembled from magnetic Janus particles”. In: *Soft Matter* 5.6 (2009), pp. 1285–1292.
- [111] Andreas Walther and Axel HE Muller. “Janus particles: synthesis, self-assembly, physical properties, and applications”. In: *Chemical reviews* 113.7 (2013), pp. 5194–5261.
- [112] Chengjun Kang and Andrei Honciuc. “Versatile triblock Janus nanoparticles: synthesis and self-assembly”. In: *Chemistry of Materials* 31.5 (2019), pp. 1688–1695.
- [113] Liang Hong, Angelo Cacciuto, Erik Luijten, and Steve Granick. “Clusters of charged Janus spheres”. In: *Nano letters* 6.11 (2006), pp. 2510–2514.
- [114] Qian Chen, Sung Chul Bae, and Steve Granick. “Directed self-assembly of a colloidal kagome lattice”. In: *Nature* 469.7330 (2011), pp. 381–384.
- [115] Jie Zhang, Bartosz A Grzybowski, and Steve Granick. “Janus particle synthesis, assembly, and application”. In: *Langmuir* 33.28 (2017), pp. 6964–6977.
- [116] Fangfang Chu. “Dumbbell-shaped colloids: equilibrium and nonequilibrium phase behaviour”. PhD thesis. Berlin, Humboldt Universität zu Berlin, Diss., 2014, 2014.
- [117] Jibin Song, Binghui Wu, Zijian Zhou, Guizhi Zhu, Yijing Liu, Zhen Yang, Lisen Lin, Guocan Yu, Fuwu Zhang, Guofeng Zhang, et al. “Double-layered plasmonic–magnetic vesicles by self-assembly of Janus amphiphilic gold–iron (II, III) oxide nanoparticles”. In: *Angewandte Chemie International Edition* 56.28 (2017), pp. 8110–8114.

- [118] Hayato Takahashi, Daisuke Nagao, Kanako Watanabe, Haruyuki Ishii, and Mikio Konno. “Magnetic field aligned assembly of nonmagnetic composite dumbbells in nanoparticle-based aqueous ferrofluid”. In: *Langmuir* 31.20 (2015), pp. 5590–5595.
- [119] Tinghua Wang, Jun Liu, Xue Li, and Xiaokai Zhang. “Arrays of Dumbbell-like Au-Fe₃O₄ Nanoparticles via Block Copolymer Self-Assembly”. In: *Integrated Ferroelectrics* 152.1 (2014), pp. 51–59.
- [120] Jianyu Liu, Xinxin Wang, and Wenke Zhang. “Atomic Force Microscopy Imaging Study of Aligning DNA by Dumbbell-like Au-Fe₃O₄ Magnetic Nanoparticles”. In: *Langmuir* 34.49 (2018), pp. 14875–14881.
- [121] Chenjie Xu, Jin Xie, Don Ho, Chao Wang, Nathan Kohler, Edward G Walsh, Jeffrey R Morgan, Y Eugene Chin, and Shouheng Sun. “Au-Fe₃O₄ dumbbell nanoparticles as dual-functional probes”. In: *Angewandte Chemie International Edition* 47.1 (2008), pp. 173–176.
- [122] Hassan Arkaban, Reza Karimi Shervedani, Fatemeh Yaghoobi, Amirhosein Kefayat, and Fatemeh Ghahremani. “Imaging and therapeutic capabilities of the AuNPs@ MnCO₃/Mn₃O₄, coated with PAA and integrated with folic acid, doxorubicin and propidium iodide for murine breast cancer”. In: *Journal of Drug Delivery Science and Technology* 67 (2022), p. 102818.
- [123] AI Figueroa, Juan Bartolomé, LM Garcia, Fernando Bartolomé, A Arauzo, A Millán, and Fernando Palacio. “Magnetic anisotropy of maghemite nanoparticles probed by RF transverse susceptibility”. In: *Physics Procedia* 75 (2015), pp. 1050–1057.
- [124] Stefanie Klein, Julia Otto, Christina Harreiß, Luitpold VR Distel, Angelika Leistner, Winfried Neuhuber, Erdmann Spiecker, and Carola Kryschi. “Pt-Fe₃O₄, Pd-Fe₃O₄, and Au-Fe₃O₄ Nanoheterodimers and Their Efficacy as Radiosensitizers in Cancer Therapy”. In: *ACS Applied Bio Materials* 4.11 (2021), pp. 7879–7892.
- [125] Lisa Landgraf, Carolin Christner, Wiebke Storck, Isabel Schick, Ines Krumbein, Heidi Dähring, Katja Haedicke, Karl Heinz-Herrmann, Ulf Teichgräber, Jürgen R Reichenbach, et al. “A plasma protein corona enhances the biocompatibility of Au@ Fe₃O₄ Janus particles”. In: *Biomaterials* 68 (2015), pp. 77–88.

- [126] Lisa Landgraf, Peter Ernst, Isabel Schick, Oskar Köhler, Hartmut Oehring, Wolfgang Tremel, and Ingrid Hilger. “Anti-oxidative effects and harmlessness of asymmetric Au@ Fe₃O₄ Janus particles on human blood cells”. In: *Biomaterials* 35.25 (2014), pp. 6986–6997.
- [127] Fang-hsin Lin, Hsu-Hsia Peng, Ya-Han Yang, and Ruey-an Doong. “Size and morphological effect of Au–Fe₃O₄ heterostructures on magnetic resonance imaging”. In: *Journal of nanoparticle research* 15.12 (2013), pp. 1–13.
- [128] Mika Valden, Xiaofeng Lai, and D Wayne Goodman. “Onset of catalytic activity of gold clusters on titania with the appearance of nonmetallic properties”. In: *science* 281.5383 (1998), pp. 1647–1650.
- [129] Qin Wei, Zhi Xiang, Jing He, Gaolei Wang, He Li, Zhiyong Qian, and Minghui Yang. “Dumbbell-like Au-Fe₃O₄ nanoparticles as label for the preparation of electrochemical immunosensors”. In: *Biosensors and Bioelectronics* 26.2 (2010), pp. 627–631.
- [130] Yu Zhang, Mingfu Gong, Xiang Li, Hongyu Liu, Penghui Liang, Shuhua Cui, Liang Zhang, Chunyu Zhou, Tao Sun, Maosheng Zhang, et al. “Au-Fe₃O₄ heterodimer multifunctional nanoparticles-based platform for ultrasensitive naked-eye detection of Salmonella typhimurium”. In: *Journal of Hazardous Materials* (2022), p. 129140.
- [131] Andres Kaech. *Introduction to electron microscopy*. 2011.
- [132] Frank Krumeich. “Properties of electrons, their interactions with matter and applications in electron microscopy”. In: *Laboratory of Inorganic Chemistry* (2011), pp. 3–08.
- [133] Peter J Goodhew, John Humphreys, and Richard Beanland. *Electron microscopy and analysis*. CRC press, 2000.
- [134] Ray F Egerton et al. *Physical principles of electron microscopy*. Vol. 56. Springer, 2005.
- [135] PR Willmott, D Meister, SJ Leake, M Lange, A Bergamaschi, M Böge, M Calvi, C Cancellieri, N Casati, A Cervellino, et al. “The materials science beamline upgrade at the swiss light source”. In: *Journal of synchrotron radiation* 20.5 (2013), pp. 667–682.

-
- [136] Ann Christin Dippel, Hanns Peter Liermann, Jan Torben Delitz, Peter Walter, Horst Schulte-Schrepping, Oliver H. Seeck, and Hermann Franz. “Beamline P02.1 at PETRA III for high-resolution and high-energy powder diffraction”. In: *Journal of Synchrotron Radiation* 22 (2015), pp. 675–687.
- [137] Xiangyun Qiu, Jeroen W. Thompson, and Simon J.L. Billinge. “PDFgetX2: A GUI-driven program to obtain the pair distribution function from X-ray powder diffraction data”. In: *Journal of Applied Crystallography* 37.4 (2004), p. 678.
- [138] Xiaohao Yang, Pavol Juhas, Christopher L Farrow, and Simon JL Billinge. “xPDFsuite: an end-to-end software solution for high throughput pair distribution function transformation, visualization and analysis”. In: *arXiv preprint arXiv:1402.3163* (2014).
- [139] Emmanuel Kentzinger, Margarita Krutyeva, and Ulrich Rücker. “GALAXI: Gallium anode low-angle x-ray instrument”. In: *Journal of large-scale research facilities JLSRF* 2 (2016), p. 61.
- [140] Mathieu Doucet, Jae Hie Cho, Gervaise Alina, Jurrian Bakker, Wim Bouwman, Paul Butler, Kieran Campbell, Miguel Gonzales, Richard Heenan, Andrew Jackson, et al. “SasView Version 4.1”. In: *Zenodo and <http://www.sasview.org>* (2017).
- [141] Artem V Feoktystov, Henrich Frielinghaus, Zhenyu Di, Sebastian Jaksch, Vitaliy Pipich, M-S Appavou, Earl Babcock, Romuald Hanslik, Ralf Engels, Günther Kemmerling, et al. “KWS-1 high-resolution small-angle neutron scattering instrument at JCNS: current state”. In: *Journal of applied crystallography* 48.1 (2015), pp. 61–70.
- [142] Dafne Musino, Anne-Caroline Genix, Thomas Chaussée, Laurent Guy, Natalia Meissner, Radoslaw Kozak, Thomas Bizien, and Julian Oberdisse. “Aggregate formation of surface-modified nanoparticles in solvents and polymer nanocomposites”. In: *Langmuir* 34.9 (2018), pp. 3010–3020.
- [143] Younjin Min, Mustafa Akbulut, Kai Kristiansen, Yuval Golan, and Jacob Israelachvili. “The role of interparticle and external forces in nanoparticle assembly”. In: *Nanoscience and Technology: A Collection of Reviews from Nature Journals*. World Scientific, 2010, pp. 38–49.

- [144] Armin Hoell, A Wiedenmann, U Heyen, and Dirk Schüler. “Nanostructure and field-induced arrangement of magnetosomes studied by SANS POL”. In: *Physica B: Condensed Matter* 350.1-3 (2004), E309–E313.
- [145] Mark Klokkenburg, Ben H Ern e, Johannes D Meeldijk, Albrecht Wiedenmann, Andrei V Petukhov, Roel PA Dullens, and Albert P Philipse. “In situ imaging of field-induced hexagonal columns in magnetite ferrofluids”. In: *Physical review letters* 97.18 (2006), p. 185702.
- [146] Erika C Vreeland, John Watt, Gretchen B Schober, Bradley G Hance, Mariah J Austin, Andrew D Price, Benjamin D Fellows, Todd C Monson, Nicholas S Hudak, Lorena Maldonado-Camargo, et al. “Enhanced nanoparticle size control by extending LaMer’s mechanism”. In: *Chemistry of Materials* 27.17 (2015), pp. 6059–6066.
- [147] Xiaolian Sun, Natalie Frey Huls, Aruna Sigdel, and Shouheng Sun. “Tuning exchange bias in core/shell FeO/Fe₃O₄ nanoparticles”. In: *Nano Letters* 12.1 (2012), pp. 246–251. ISSN: 15306984.
- [148] S. K. Sharma, J. M. Vargas, K. R. Pirota, Shalendra Kumar, C. G. Lee, and M. Knobel. “Synthesis and ageing effect in FeO nanoparticles: Transformation to core-shell FeO/Fe₃O₄ and their magnetic characterization”. In: *Journal of Alloys and Compounds* 509.22 (2011), pp. 6414–6417. ISSN: 09258388.
- [149] D. W. Kavich, J. H. Dickerson, S. V. Mahajan, S. A. Hasan, and J. H. Park. “Exchange bias of singly inverted FeO/Fe₃O₄ core-shell nanocrystals”. In: *Physical Review B - Condensed Matter and Materials Physics* 78.17 (2008), pp. 1–6. ISSN: 10980121.
- [150] Zaneta Swiatkowska-Warkocka, Kenji Kawaguchi, Hongqiang Wang, Yukiko Katou, and Naoto Koshizaki. “Controlling exchange bias in Fe₃O₄/FeO composite particles prepared by pulsed laser irradiation”. In: *Nanoscale Research Letters* 6.1 (2011), pp. 1–7. ISSN: 1556276X.
- [151] Franz X. Redl, Charles T. Black, Georgia C. Papaefthymiou, Robert L. Sandstrom, Ming Yin, Hao Zeng, Christopher B. Murray, and Stephen P. O’Brien. “Magnetic, electronic, and structural characterization of nonstoichiometric iron oxides at the nanoscale”. In: *Journal of the American Chemical Society* 126.44 (2004), pp. 14583–14599. ISSN: 00027863.

-
- [152] J. Nogués and Ivan K. Schuller. “Exchange bias”. In: *Journal of Magnetism and Magnetic Materials* 192.2 (1999), pp. 203–232. ISSN: 03048853.
- [153] Katharine Page, Thomas Proffen, Markus Niederberger, and Ram Seshadri. “Probing local dipoles and ligand structure in BaTiO₃ nanoparticles”. In: *Chemistry of Materials* 22.15 (2010), pp. 4386–4391.
- [154] F Fabris, Kun-Hua Tu, CA Ross, and WC Nunes. “Influence of dipolar interactions on the magnetic properties of superparamagnetic particle systems”. In: *Journal of Applied Physics* 126.17 (2019), p. 173905.
- [155] MJ Benitez, O Petravic, H Tüysüz, F Schüth, and H Zabel. “Fingerprinting the magnetic behavior of antiferromagnetic nanostructures using remanent magnetization curves”. In: *Physical Review B* 83.13 (2011), p. 134424.
- [156] G. F. Goya, T. S. Berquó, F. C. Fonseca, and M. P. Morales. “Static and dynamic magnetic properties of spherical magnetite nanoparticles”. In: *Journal of Applied Physics* 94.5 (2003), pp. 3520–3528. ISSN: 00218979.
- [157] Murtaza Bohra, Nishit Agarwal, and Vidyadhar Singh. “A short review on Verwey transition in nanostructured Fe₃O₄ materials”. In: *Journal of Nanomaterials* 2019 (2019).
- [158] Arijit Mitra, J Mohapatra, SS Meena, CV Tomy, and M Aslam. “Verwey transition in ultrasmall-sized octahedral Fe₃O₄ nanoparticles”. In: *The Journal of Physical Chemistry C* 118.33 (2014), pp. 19356–19362.
- [159] Taehun Kim, Sangwoo Sim, Sumin Lim, Midori Amano Patino, Jaeyoung Hong, Jisoo Lee, Taeghwan Hyeon, Yuichi Shimakawa, Soonchil Lee, J Paul Attfield, et al. “Slow oxidation of magnetite nanoparticles elucidates the limits of the Verwey transition”. In: *Nature communications* 12.1 (2021), pp. 1–6.
- [160] J. P. Chen, C. M. Sorensen, K. J. Klabunde, and G. C. Hadjipanayis. “of Nanoscale Colloidal Cobalt Particles”. In: *Physical Review B* 51.17 (1995), pp. 527–533.
- [161] “Models for the dynamics of interacting magnetic nanoparticles”. In: *Journal of Magnetism and Magnetic Materials* 184.3 (1998), pp. L262–274. ISSN: 03048853.
- [162] Christophe Petit, Abdelhafed Taleb, and Marie Paule Pileni. “Self-Organization of Magnetic Nanosized Cobalt Particles”. In: *Chemical Engineering and Technology* 21.8 (1998), pp. 679–681. ISSN: 09307516.

- [163] Ji Sung Lee, Reasmey P Tan, Jun Hua Wu, and Young Keun Kim. “Effect of interparticle interactions and size dispersion in magnetic nanoparticle assemblies: A static and dynamic study”. In: *Applied Physics Letters* 99.6 (2011), p. 062506.
- [164] Jordi S. Andreu, Juan Camacho, and Jordi Faraudo. “Aggregation of superparamagnetic colloids in magnetic fields: The quest for the equilibrium state”. In: *Soft Matter* 7.6 (2011), pp. 2336–2339. ISSN: 17446848. arXiv: 1011.4819.
- [165] Jordi Faraudo, Jordi S. Andreu, and Juan Camacho. “Understanding diluted dispersions of superparamagnetic particles under strong magnetic fields: A review of concepts, theory and simulations”. In: *Soft Matter* 9.29 (2013), pp. 6654–6664. ISSN: 1744683X.
- [166] Andrey V Dobrynin, Michael Rubinstein, and Sergei P Obukhov. “Cascade of transitions of polyelectrolytes in poor solvents”. In: *Macromolecules* 29.8 (1996), pp. 2974–2979.
- [167] “Chain formation in a magnetic fluid under the influence of strong external magnetic fields studied by small angle neutron scattering”. In: *Soft Matter* 7.14 (2011), pp. 6678–6683. ISSN: 1744683X.
- [168] K. Butter, P. H.H. Bomans, P. M. Frederik, G. J. Vroege, and A. P. Philipse. “Direct observation of dipolar chains in iron ferrofluids by cryogenic electron microscopy”. In: *Nature Materials* 2.2 (2003), pp. 88–91.
- [169] Konstantin I. Morozov and Mark I. Shliomis. “Magnetic Fluid as an Assembly of Flexible Chains”. In: (2002), pp. 162–184.
- [170] MR Fitzsimmons and CF Majkrzak. “Application of polarized neutron reflectometry to studies of artificially structured magnetic materials”. In: ().
- [171] Andreas Michels and Jörg Weissmüller. “Magnetic-field-dependent small-angle neutron scattering on random anisotropy ferromagnets”. In: *Reports on Progress in Physics* 71.6 (2008), p. 066501.
- [172] M. Klokkenburg, B. H. Ern e, A. Wiedenmann, A. V. Petukhov, and A. P. Philipse. “Dipolar structures in magnetite ferrofluids studied with small-angle neutron scattering with and without applied magnetic field”. In: 75.5 (2007), pp. 1–9.

- [173] Sanjib Paul and Harish Vashisth. “Self-assembly behavior of experimentally realizable lobed patchy particles”. In: *Soft Matter* 16.35 (2020), pp. 8101–8107.
- [174] José M Vargas, Leandro M Socolovsky, Marcelo Knobel, and Daniela Zanchet. “Dipolar interaction and size effects in powder samples of colloidal iron oxide nanoparticles”. In: *Nanotechnology* 16.5 (2005), S285.
- [175] Hiroaki Mamiya, Hiroya Fukumoto, Jhon L Cuya Huaman, Kazumasa Suzuki, Hiroshi Miyamura, and Jeyadevan Balachandran. “Estimation of magnetic anisotropy of individual magnetite nanoparticles for magnetic hyperthermia”. In: *ACS nano* 14.7 (2020), pp. 8421–8432.
- [176] Gleyggestone Lopes, José M Vargas, Surender K Sharma, Fanny Béron, Kleber R Pirota, Marcelo Knobel, Carlos Rettori, and Roberto D Zysler. “Ag- Fe₃O₄ dimer colloidal nanoparticles: synthesis and enhancement of magnetic properties”. In: *The Journal of Physical Chemistry C* 114.22 (2010), pp. 10148–10152.
- [177] NA Frey, MH Phan, H Srikanth, S Srinath, C Wang, and S Sun. “Interparticle interactions in coupled Au-Fe₃O₄ nanoparticles”. In: *Journal of applied physics* 105.7 (2009), 07B502.
- [178] Kai Wu, Jinming Liu, Renata Saha, Chaoyi Peng, Diqing Su, Yongqiang Andrew Wang, and Jian-Ping Wang. “Investigation of Commercial Iron Oxide Nanoparticles: Structural and Magnetic Property Characterization”. In: *ACS omega* 6.9 (2021), pp. 6274–6283.
- [179] Jun Wang, Jingjun Sun, Qian Sun, and Qianwang Chen. “One-step hydrothermal process to prepare highly crystalline Fe₃O₄ nanoparticles with improved magnetic properties”. In: *Materials research bulletin* 38.7 (2003), pp. 1113–1118.
- [180] B Martinez, X Obradors, Ll Balcells, A Rouanet, and C Monty. “Low temperature surface spin-glass transition in γ -Fe₂O₃ nanoparticles”. In: *Physical Review Letters* 80.1 (1998), p. 181.
- [181] T Jean Daou, Jean-Marc Greneche, Seong-Joo Lee, Soonchil Lee, Christophe Lefevre, Sylvie Bégin-Colin, and Genevieve Pourroy. “Spin canting of maghemite studied by NMR and In-Field Mossbauer spectrometry”. In: *The Journal of Physical Chemistry C* 114.19 (2010), pp. 8794–8799.

- [182] Kathryn L Krycka, Ryan A Booth, Charles R Hogg, Y Ijiri, Julie A Borchers, WangChun Chen, SM Watson, M Laver, Thomas R Gentile, Liv R Dedon, et al. “Core-shell magnetic morphology of structurally uniform magnetite nanoparticles”. In: *Physical review letters* 104.20 (2010), p. 207203.
- [183] Tobias Köhler, Artem Feoktystov, Oleg Petravic, Emmanuel Kentzinger, Tanvi Bhatnagar-Schöffmann, Mikhail Feygenson, Nileena Nandakumaran, Joachim Landers, Heiko Wende, Antonio Cervellino, et al. “Mechanism of magnetization reduction in iron oxide nanoparticles”. In: *Nanoscale* 13.14 (2021), pp. 6965–6976.
- [184] Lingyan Wang, Lingyan Wang, Jin Luo, Quan Fan, Masatsugu Suzuki, Itsuko S Suzuki, Mark H Engelhard, Yuehe Lin, Nam Kim, Jian Q Wang, et al. “Monodispersed core-shell Fe₃O₄@ Au nanoparticles”. In: *The Journal of Physical Chemistry B* 109.46 (2005), pp. 21593–21601.
- [185] Susmita Pal, Marienette Morales, Pritish Mukherjee, and Hariharan Srikanth. “Synthesis and magnetic properties of gold coated iron oxide nanoparticles”. In: *Journal of Applied Physics* 105.7 (2009), 07B504.
- [186] P Esquinazi, D Spemann, R Höhne, A Setzer, K-H Han, and T Butz. “Induced magnetic ordering by proton irradiation in graphite”. In: *Physical Review Letters* 91.22 (2003), p. 227201.
- [187] Koichi Kusakabe and Masanori Maruyama. “Magnetic nanographite”. In: *Physical Review B* 67.9 (2003), p. 092406.
- [188] Petri O Lehtinen, Adam S Foster, Yuchen Ma, AV Krashennnikov, and Risto M Nieminen. “Irradiation-induced magnetism in graphite: a density functional study”. In: *Physical review letters* 93.18 (2004), p. 187202.
- [189] M Venkatesan, CB Fitzgerald, Coey, and JMD. “Unexpected magnetism in a dielectric oxide”. In: *Nature* 430.7000 (2004), pp. 630–630.
- [190] H Hori, T Teranishi, Y Nakae, Y Seino, M Miyake, and S Yamada. “Anomalous magnetic polarization effect of Pd and Au nano-particles”. In: *Physics Letters A* 263.4-6 (1999), pp. 406–410.
- [191] P Crespo, R Litrán, TC Rojas, M Multigner, JM De la Fuente, JC Sánchez-López, MA Garcia, A Hernando, S Penadés, and A Fernández. “Permanent magnetism, magnetic anisotropy, and hysteresis of thiol-capped gold nanoparticles”. In: *Physical review letters* 93.8 (2004), p. 087204.

-
- [192] T Taniyama, Eiji Ohta, and Tetsuya Sato. “Observation of 4d ferromagnetism in free-standing Pd fine particles”. In: *EPL (Europhysics Letters)* 38.3 (1997), p. 195.
- [193] T Shinohara, Tetsuya Sato, and T Taniyama. “Surface ferromagnetism of Pd fine particles”. In: *Physical Review Letters* 91.19 (2003), p. 197201.
- [194] W-H Li, SY Wu, CC Yang, SK Lai, KC Lee, HL Huang, and HD Yang. “Thermal contraction of Au nanoparticles”. In: *Physical review letters* 89.13 (2002), p. 135504.
- [195] P De la Presa, M Multigner, J De la Venta, MA Garcia, and ML Ruiz-González. “Structural and magnetic characterization of oleic acid and oleylamine-capped gold nanoparticles”. In: *Journal of applied physics* 100.12 (2006), p. 123915.
- [196] JJ Shen, WB Mi, ZQ Li, P Wu, EY Jiang, and HL Bai. “Enhancement of magnetization in sputtered polycrystalline Fe₃O₄/Al bilayers”. In: *Journal of Physics D: Applied Physics* 39.17 (2006), p. 3726.
- [197] J Canet-Ferrer, P Albella, A Ribera, JV Usagre, and SA Maier. “Hybrid magnetite–gold nanoparticles as bifunctional magnetic–plasmonic systems: three representative cases”. In: *Nanoscale horizons* 2.4 (2017), pp. 205–216.
- [198] André Guinier, Gérard Fournet, and Kenneth L Yudowitch. *Small-angle scattering of X-rays*. Wiley New York, 1955.
- [199] Cassio Alves, Jan Skov Pedersen, and Cristiano LP Oliveira. “Calculation of two-dimensional scattering patterns for oriented systems”. In: *Journal of Applied Crystallography* 50.3 (2017), pp. 840–850.
- [200] Gennady Pospelov, Walter Van Herck, Jan Burle, Juan M Carmona Loaiza, Céline Durniak, Jonathan M Fisher, Marina Ganeva, Dmitry Yurov, and Joachim Wuttke. “BornAgain: software for simulating and fitting grazing-incidence small-angle scattering”. In: *Journal of applied crystallography* 53.1 (2020), pp. 262–276.
- [201] RP Cowburn. “Property variation with shape in magnetic nanoelements”. In: *Journal of Physics D: Applied Physics* 33.1 (2000), R1.
- [202] Winnie M Kiarie, Dylan Sitarski, and David C Jiles. “Study of effective particle shape-dependent magnetization behavior of soft magnetic polymeric composites”. In: *AIP Advances* 12.3 (2022), p. 035115.

- [203] C Xu, YQ Ma, and PM Hui. “Equilibrium magnetic moment configurations in magnetic nanoparticle films: Effects of anisotropy, dipolar interaction, and Zeeman energy”. In: *Journal of applied physics* 98.8 (2005), p. 084303.
- [204] GF Goya, TS Berquo, FC Fonseca, and MP Morales. “Static and dynamic magnetic properties of spherical magnetite nanoparticles”. In: *Journal of applied physics* 94.5 (2003), pp. 3520–3528.
- [205] R Řezníček, V Chlan, H Štěpánková, P Novák, and M Maryško. “Magnetocrystalline anisotropy of magnetite”. In: *Journal of Physics: Condensed Matter* 24.5 (2012), p. 055501.
- [206] Horng-Tay Jeng and GY Guo. “First-principles investigations of the electronic structure and magnetocrystalline anisotropy in strained magnetite Fe_3O_4 ”. In: *Physical review B* 65.9 (2002), p. 094429.
- [207] Harshad Pathak, Abdalla Obeidat, Gerald Wilemski, and Barbara Wyslouzil. “The structure of D₂O-nonane nanodroplets”. In: *The Journal of chemical physics* 140.22 (2014), p. 224318.
- [208] A Obeidat, Fawaz Hrahsheh, and Gerald Wilemski. “Scattering Form Factors for Russian Doll Aerosol Droplet Models”. In: *The Journal of Physical Chemistry B* 119.29 (2015), pp. 9304–9311.
- [209] Neville H Fletcher. “Size effect in heterogeneous nucleation”. In: *The Journal of chemical physics* 29.3 (1958), pp. 572–576.
- [210] Håkon Kaya and N-R de Souza. “Scattering from capped cylinders. Addendum”. In: *Journal of Applied Crystallography* 37.3 (2004), pp. 508–509.
- [211] Stefan Odenbach and Steffen Thurm. “Magnetoviscous Effects in Ferrofluids”. In: *Ferrofluids: Magnetically Controllable Fluids and Their Applications*. Ed. by Stefan Odenbach. Berlin, Heidelberg: Springer Berlin Heidelberg, 2002, pp. 185–201. ISBN: 978-3-540-45646-9.
- [212] Nicusor Iacob, Andrei Kuncser, Cezar Comanescu, Petru Palade, and Victor Kuncser. “Optimization of magnetic fluid hyperthermia with respect to nanoparticle shape-related parameters: case of magnetite ellipsoidal nanoparticles”. In: *Journal of Nanoparticle Research* 22.6 (2020), pp. 1–10.
- [213] Fernando Vereda, Juan de Vicente, and Roque Hidalgo-Álvarez. “Physical properties of elongated magnetic particles: magnetization and friction coefficient anisotropies”. In: *ChemPhysChem* 10.8 (2009), pp. 1165–1179.

- [214] Tobias Fütterer, Gerrit A Vliegenthart, and Peter R Lang. “Particle scattering factor of Janus micelles”. In: *Macromolecules* 37.22 (2004), pp. 8407–8413.

List of Figures

2.1.	(a) The current carrying loop with moment $\vec{\mu}$ in direction of $d\vec{A}$. (b) The Bohr's atom where the electron moves in a circular orbit where its $\vec{\ell}$ and $\vec{\mu}$ are in opposite directions and (c) the spin-orbit interaction from the viewpoint of electron.	5
2.2.	(a) Spatially symmetric and (b) anti-symmetric wave function. (c) Splitting of spin-singlet and triplet states for H_2 molecule.	10
2.3.	The sign of exchange integral \mathcal{J} resulting in various interactions in a solid	12
2.4.	Types of magnetic materials: temperature dependent susceptibility (red) and magnetization (black) curves for (a) an ideal paramagnet, (b) Pauli paramagnet and diamagnets, (c) ferromagnet, (d) antiferromagnet and (e) ferrimagnet ; adapted from [35].	14
2.5.	Magnetization along (a) the long axis in a prolate and (b) short axis in oblate shaped ellipsoids with aspect ratio c/a	16
2.6.	Magnetic spin configurations in FM nanoparticles simulated with (a) no surface anisotropy, (b) and (c) with perpendicular surface anisotropy of increasing strength and (d) in-plane surface anisotropy. Reprinted (abstract/excerpt/figure) with permission from [38] ©(2008) by the American Physical Society.	18
2.7.	Effect of size on magnetic properties of magnetic material: (a) multidomain bulk FM, (b) ferromagnetic sphere (c) single domain and (d) superparamagnet.	20
2.8.	Magnetization in small NP with (a) low anisotropy (b) high anisotropy in cubic crystal and (c) uniaxial system.	21
2.9.	The initial state of the magnetic moment is the ellipsoid with magnetic moment (black arrow) pointing along the long axis. (a) Néel rotation, when the magnetic moment rotates in the ellipsoid and (b) Brownian rotation where the particle itself rotates.	22

2.10. Single domain ellipsoidal particle in a magnetic field \vec{H} with relevant angles between this field, anisotropy z-axis and magnetization \vec{M}	23
2.11. (a) Longitudinal and (b) transverse hysteresis loops for various angles ψ of the field $h = H/H_A$ with the anisotropy axis; reprinted with permission [41].	24
2.12. (a) The energy barrier of the single domain ellipsoid at $H = 0$ for a spin flip. Switching of magnetization of a single domain ellipsoid particles across the energy barrier under the action of an external magnetic field H (b) pointing upward and (c) pointing downward; adapted from [41].	25
2.13. Sketch showing overlap of ionic clouds around positively charged particles (blue spheres). The surface charge is balanced by excess of counterions (red spheres) with depletion of co-ions (green region). This electric double layer is formed when particles are dispersed in a polar solvent.	29
2.14. Steric repulsion caused by surfactants or polymers on the surface: (a) when particles have a separation distance larger than twice thickness of surfactant layer $s > 2t$, no repulsion interaction exist and (b) when surfactants are interdigitated $s < 2t$ results in steric repulsion.	31
2.15. Magnetic dipolar interactions between magnetic nanoparticles: (a) schematic of random orientation of magnetic moments (represented by white arrows) in weakly interacting spherical magnetic nanoparticles when no field is applied and in (b) chain like aggregates are formed when field is applied.(c) The attraction (blue) and repulsive region (red) in between dipoles based on the position of the dipoles; adapted from [42]	31
2.16. The sketch of the elastic scattering process in the Fraunhofer approximation with a monochromatic source; the sketch is adapted from [58] .	34
2.17. (a) Scattering geometry for calculation of the far field limit at the detector. (b) Diagrammatic form of multiple scattering effects included in the Born approximation.	36
2.18. Various interactions mechanisms between atoms and incident radiation; adapted from [62].	38
2.19. Schematic illustration of dipolar field and the scattering vector \vec{Q} . (a) For $\vec{M} \perp \vec{Q}$, magnetic dipole interaction show constructive interference and (b) $\vec{M} \parallel \vec{Q}$ results in destructive interference; adapted from	40
2.20. Transmission geometry set-up for small-angle scattering (SAS).	42

2.21. (a) The intensity associated with particle form-factor $P(Q)$ for various shapes averaged over all orientations. (b) The scattering intensity (in blue) includes product of particle form-factor of sphere (red) and structure factor associated with hard sphere potential (green).	45
2.22. (a) and (b) represents the Rg for particles of different types of particle (adapted from [64]) (c) Porod constants for different objects; taken from [64])	47
2.23. (a) Schematic illustration of eqn. (2.118) where grey is the matrix in which anisotropic particle are embedded. (b) The concept of contrast variation in core-shell particles in natural contrast, (c) shell contrast; $\eta_o = \eta_{shell}$ and (d) core contrast; where $\eta_o = \eta_{core}$; adapted from ref [57]	49
2.24. (a) Schematic of the SANS experimental setup including velocity selector for selection of wavelength and (b) SANS POL setup includes velocity selectors along with a polarizer to polarize the neutron beam and flipper to reverse the polarization on the neutron beam.	51
2.25. (a) 2D scattering pattern obtained for particles in a matrix are corrected and integrated radially (in general) to obtain (b) $I(Q)$	54
2.26. Radially averaged SAS intensity $I(Q)$ smeared due polydispersity (2%, 5% and 10%) in NPs.	55
2.27. (a) Atomic planes with a vector normal \hat{n} and interplanar spacing d . (b) Ewald sphere with crystal at origin of the sphere and radius $2\pi/\lambda$. The beam of x-rays/neutrons strikes the crystal and are diffracted along directions passing through the atoms. The origin of the reciprocal lattice is indicated by O.	57
2.28. Conventional x-ray diffraction of (a) crystalline and (b) nanocrystalline sample indicating broad and diffuse peaks; taken from [69]	59

- 2.29. (a) Total scattering experiment geometry with x-rays. Data treatment steps followed to obtain pair distribution function: (b) Calibration of the sample-to-detector distance by fitting the powder rings of the calibrant (CeO_2 for x-rays). Here the colored rings are the fit to the powder rings. (c) 2D data in usual scattering experiments are centred using values in (b) and integrated to obtain (d) Debye scattering intensities $I(Q)$. Normalized and corrected $I(Q)$ is further analyzed to obtain (e) total scattering function $\mathcal{S}(Q)$ (using eqn. (2.156)), (f) reduced scattering function $\mathcal{F}(Q)$ as a function of Q (using eqn. (2.157)). (g) Finally a real spaced pair distribution function $G(r)$ is obtained by Fourier transform of the $\mathcal{F}(Q)$ 62
- 2.30. Analysis of $G(r)$ functions: (a) Peak position, area under peak and width (FWHM) of the peaks in the PDF corresponds to various structural aspects of the nanostructure. (b) The crystallite size is denoted by the peak cut-off in the PDF. (c) Schematic process for modelling the PDF considers the atom at the origin and (d) Fit of $G(r)$ data with experimental data in blue open circles and calculated pattern is the red curve based on the modelling described in (c) and difference between calculated and experimental data is the green difference curve. 63
- 3.1. (a) $\text{Au-Fe}_3\text{O}_4$ (b) $\text{Ag-Fe}_3\text{O}_4$ (c) $\text{AuAg-Fe}_3\text{O}_4$ and (d) $\text{Ag-CoFe}_2\text{O}_3$ DB-NPs. (a-c) Reprinted (adapted) with permission from [96] ©2010 American Chemical Society and (d) reprinted (adapted) with permission from [97] ©2005 American Chemical Society. 66
- 3.2. Sketch representing the heterogeneous nucleation and homogeneous nucleation of one component (blue) on the preformed seed of other (red). Homogeneous nucleation results in composite system containing two disjoint particles. Heterogeneous nucleation results in dumbbell, core-shell and flower nanoparticle; Figure adapted from [18]. 67

3.3.	(a) Micrometer sized dumbbells containing organic compounds forming vesicles, reprinted (adapted) with permission from [109] ©2018 American Chemical Society. (b) and (c) Non magnetic DBNPs in ferrofluid dispersion forming chains with simultaneous application of magnetic and electric field, reprinted (adapted) with permission from [118], ©2015 American Chemical Society. (d) Scheme of surface functionalization of Au-Fe ₃ O ₄ with hydrophilic and hydrophobic ligand to induce assembly, reprinted (adapted) with permission from [29] ©2017 American Chemical Society. (e) Vesicle formation as result of the surface functionalization of Au- Fe ₃ O ₄ DBNPs, reprinted with permission from [27] ©2018 American Chemical Society. (f) The photo activated self-assembly in Au-Fe ₃ O ₄ surface functionalized DBNPs, reprinted with permission from [30] ©2021 American Chemical Society.	71
4.1.	Different electron interactions in an electron microscope; inspired from several sources [131, 132].	74
4.2.	(a) The working principle of TEM involves imaging thin samples in transmission mode. (b) Principal components of the TEM setup; adapted from [131, 132].	76
4.3.	(a) The working principle of a SEM involves imaging samples in scanning mode and can be thicker than TEM samples. (b) Principal components of the SEM setup; adapted from [131, 132].	77
4.4.	(a) Schematic of the magnetometer in VSM mode. (b) The PPMS-DynaCool system and (c) VSM module from Quantum Design at Forschungszentrum Jülich GmbH.	79
4.5.	(a) VSM capsule loaded with sample. (b) The teflon covered capsule loaded on the brass sample holder and aligned for VSM measurement.	79
4.6.	(a) The NETZCH TG 209 F1 Libra at Forschungszentrum Jülich GmbH in which (b) the aluminium crucible loaded with sample is placed in nitrogen atmosphere to obtain TGA curves.	81
4.7.	xPDF setup: (a) schematic and (b) actual Mythen-II point detector at PSI, SLS. (c) Schematic and (d) actual 2D detector at DESY, Hamburg.	82
4.8.	(a) The quartz capillaries used at SLS and (b) kapton capillaries used at APS and DESY.	82

4.9.	(a) Schematic of GALAXI setup with its components, here the x-ray source is on the far right separated by the wall to the other components including optics to align the beam, evacuated detector tube and 2D position detector on the left. (b) Photograph of the GALAXI setup at JCNS, Forschungszentrum Jülich GmbH.	84
4.10.	(a) The magnetic field setup includes magnet of 0.9 T on (left) and the holder on (right) to insert capillary of about 4 cm vertically. (b) The sample holder setup to load capillaries for zero field measurements. . .	85
4.11.	(a) Schematic of the SANS setup at (b) KWS-1 at MLZ, Garching, adapted from [141] and (c) Hellma cells in which dispersions are filled. .	86
4.12.	(a) 2D SANS simulated patterns (top) and experimental (bottom) patterns. (b) The initial configuration of the box with particles and random motions described as A, B and C. (c) Particles after fitting experimental 2D pattern.	89
4.13.	Summary of the multiscale experiments and range of parameters probed with experiments.	90
5.1.	TEM and normal size distribution of (a and g) F05, (b and h) F10, (c and i) F20, (d and j) F21, (e and k) F24 and (f and l) F27 IONPs. The high resolution TEM micrographs in the bottom inset.	93
5.2.	High resolution TEM micrographs of (a) F20 and (b) F27 IONPs. The crystalline lattice spacing corresponds to $\langle 111 \rangle$ crystal plane.	93
5.3.	The best refinements of PDF data for (a) F20 (b) F27 (c) F50 MNPs and (d) magnetite powdered bulk, with experimental data in open circles, calculated pattern in red and difference curve in green.	95
5.4.	ZFC (●) and FC (▲) magnetization in an applied field of 0.01 T as a function of temperature for (a) F05 (b) F10 (c) F20 (d) F21 (e) F24 (f) F27 IONPs.	97
5.5.	(a) ZFC (●) and FC (▲) magnetization at 100 Oe as a function of temperature for F50. (b) The experimental T_B (●) plotted as a function of particle diameter. The blue (magnetite) and red (maghemite) solid lines are calculated T_B using K . (c) H_{EB} plotted as function of diameter at 5 K and (d) H_{c1} as a function of particle diameter at 5 K (●) and 300 K (▼). Solid lines are guides for the eye.	99

5.6.	DC magnetization as a function of applied magnetic field at (a) 5 K (b) 300 K. Inset shows the same (a) and (b) but expanded to show lower fields.	100
5.7.	(a) The dipolar coupling strength and (b) Bjerrum length plotted as a function of diameter. The aggregation parameter N^* plotted as a function of concentration for (c) F05, F10, F20, F21, F24 and F27 samples. Solid lines are guides for the eye.	101
5.8.	(a) Dipole-dipole energies (b) van der Waal's (c) Zeeman energies calculated for F05, F10, F20, F21, F24 and F27 IONPs, and (d) steric energies calculated for F27 IONP with varying shell thickness ranging from (0.8 nm to 1.9 nm). All energies are plotted as a function of edge to edge separation between IONPs in assemblies.	101
5.9.	2D SAXS patterns at applied magnetic field, $H = 0.9$ T and in concentration of 25 mg/ml for (a) F05, (b) F10, (c) F20, (d) F21, (e) F24 and (f) F27 IONPs. The intensities are in log scale. The black vertical line in the pattern is the gap between two detectors which is masked during reduction of the data.	103
5.10.	The radially averaged SAXS data at (a),(b) 0T and (c)(d) 0.9 T for F05,F10, F20, F21, F24 and F27. The IONPs are fixed to concentration 25(2) mg/ml. The intensities are therefore scaled for easy visualizations. The open circle in respective colours are experimental data and solid black lines are fits to form-factor models as described.	104
5.11.	The radially averaged SAXS data measured in applied field of 0.9 T for (a) F24 (b) F27 samples in a concentration of 22(2) mg/mL(\circ), 5.9(1) mg/mL(\circ), 1.9(9) mg/mL(\circ) with the experimental data as open symbols and linear pearl model fit as solid black lines. The bottom insets show the structure factors and the top inset shows the 2D pattern at 0.66 mg/mL. (c) The edge separation parameter l as a function of concentration for F27 (\blacktriangledown) and F24 (\bullet) samples. Solid lines are guides for the eye.	105
5.12.	2D SANS patterns of F27 MNPs in solution in applied magnetic field of (a) 0 T, (b) 0.004 T, (c) 0.008 T, (d) 0.02 T, (e) 0.5 T and (f) 2.2 T. The magnetic field was applied perpendicular to the incident neutron beam as indicated by the black arrow. The colour scale is in units of scattering cross section (cm^{-1}) and represented in the log-scale.	106

- 5.13. (a) 1D sector integrated intensities of F27 IONPs along the sector centered at $\alpha = 0^\circ$, where α is the angle between \vec{H} and \vec{Q} for fields ranging from 0 - 2.2 T, inset: The sector of width 15° , in 2D SANS pattern. (b) The peaks from (a) are zoomed in for further visualization. The solid lines are the fits to Gaussian functions. 107
- 5.14. (a) The projected distance between nanoparticles ℓ_{\parallel} and (b) the correlation length ζ plotted as a function of the magnetic field. Schematic representation of the change in (c) ℓ_{\parallel} and (d) ζ in IONPs as they respond to low field (left) and strong field (right). 108
- 5.15. SEM image of F27 IONPs when (a) drop-casted (b) spin-coated. 108
- 5.16. (a) SANS of F20 at two different contrasts, in (100 %) h-tol (blue) and (100 %) d-tol (red) measured at SNS. The black lines are fit to core-shell model (b) SANS of F27 prepared in four different contrasts (100 %, 78%, 54 % and 0% d-tol) measured at KWS-1, here the solid lines are fit to core-shell model. (c) Calculated SLD (black) and refined SLD (red dots and dashed line) as function of diameter. (d) Weight loss plotted as a function of temperature obtained via TGA for F05, F10, F20, F21, F24 and F27. 111
- 5.17. 2D SANSPOL scattering patterns of F20 at 1 T (a) I^- (b) I^+ (c) $(I^- + I^+)/2$ and (d) $I^- - I^+$, (e) Intensity of (d) plotted as a function of α where solid lines are the fit to $\sin^2\alpha$ for different values of Q. (f) Q-dependence of the nuclear and magnetic form factors, where solid lines are fit to spherical form factor. 112
- 5.18. 2D SANSPOL scattering patterns of F27 at 1 T (a) I^- (b) I^+ (c) $(I^- + I^+)/2$ and (d) $I^- - I^+$, the colour scale is in units of scattering cross section (cm^{-1}) and represented in logscale. (e) Integrated intensity of $I^-(\circ)$ and $I^-(\nabla)$ of sectors 15° in width, with sector centers at $\alpha = 0^\circ$ (f) 30° (g) 60° (h) 90° . Solid lines are guides for the eye. 113
- 5.19. Simulated and experimental halves of the 2D SANS patterns and real space distribution of IONPs in space at (a-b) 0 T (c-d) 0.006 T (e-f) 2.2 T. 114

-
- 6.1. The morphology of DBNP and its length scales. The red sphere represents the Au seed of diameter L_A . The blue non-spherical structure represents the IONP with diameter D_F that is grown on Au. The length of IONP along symmetry axis is L_F such that length of DBNP, $L_D = L_A + L_F$. The surface is coated with ligands of thickness t 117
 - 6.2. Steps involved in seed mediated growth of Au-Fe₃O₄. The primary steps include: formation of Au seeds, decomposition of iron pentacarbonyl on the surface of Au and oxidation of grown Fe. 118
 - 6.3. TEM (left) and high resolution (right) TEM micrographs of (a-b) A12F10 (c-d) A9F11 (e-f) A10F14 and (g-h) A13F14. The crystal plane spacing is shown with yellow lines in each case. 119
 - 6.4. The best refinements of xPDF data for (a) bulk iron oxide Fe₃O₄, (b) bulk Au, (c) A12F10 and (d) A13F14 with experimental data in open blue circles, calculated pattern in red curve and difference curve in green. 122
 - 6.5. G(r) function plotted for DBNPs in the range of (a) 1 - 50 Å and (b) 1 - 20 Å. (c) The simulated G(r) plotted for bulk gold (red), magnetite (blue) and 50 % mix fraction of gold and magnetite (black). The red and blue dashed lines extending through (b) and (c) represents the corresponding Au- Au and Fe - Fe, peaks found in simulated and experiments data. 123
 - 6.6. ZFC (black) and FC (red) magnetization as function of temperature in an applied field of 100 Oe for (a) A12F10 (b) A9F11 (c) A10F14 (d) A13F14. 125
 - 6.7. (a) Calculated T_B corresponding to energy barrier E_{min} (blue) and E_{max} (red), plotted as a function of IONPs' aspect ratio (A_2). (b) Schematic representing the energy barrier increase as a result of the anisotropy in the DBNPs. 126
 - 6.8. Field-cooled DC magnetization M(H) curves as a function of magnetic field at (a) 5 K and (b) 300 K with 1 T cooling field, inset; M(H) is zoomed in at low fields to indicate the waist shaped curved for A9F11(green) and A10F14(red) 128
 - 6.9. TGA curve representing the mass loss as a function of temperature for (a) A12F10, (b) A13F14 (c) A9F11 and (d) A10F14 131

-
- 7.1. Scattering length density of various components in a surfactant coated Au-Fe₃O₄ DBNP system suspended in h-toluene with (a) x-rays and (b) neutrons. 134
- 7.2. Sedimentation of DBNPs: Hellma cells filled with A10F14 DBNPs in toluene dispersion (a) before and (b) after sedimentation, the supernatant is the solution phase containing residual particles above the dark sedimented particles collected at bottom of the cell. (c) The same DBNPs in the presence of 200 Oe hand held in inhomogeneous field, here the DBNPs clearly separate out of dispersion to form macroscopic structures. 135
- 7.3. (a) The capillaries are held horizontally for zero field and (b) vertically for magnetic field SAXS measurements on DBNPs at GALAXI. In (b) due to phase separation and magnetic field response, the x-ray beam is focused at two different positions on the capillary represented by blue and red arrow. The direction of applied field \vec{H} is given by the black arrow. (c) The SAXS patterns of A9F11 DBNP collected from top (red outline) and bottom (blue outline) of the capillary. Note the capillaries in the figure are just representative and do not contain the actual DBNPs samples. 136
- 7.4. The 2D SAXS patterns of (a-b) A12F10 (c-d) A13F14 (e-f) A9F11 and (g-h) A10F14 DBNPs collected at $H = 0.9$ T (top panel) and 0 T (bottom panel). The black area represents the insensitive part of the detector. The DBNPs with similar 2D SAXS pattern are classified into same category. 137
- 7.5. 2D SANS patterns of (a1-a5) A12F10, (b1-b5) A13F14, (c1-c5) A9F11, and (d1-d5) A10F14 DBNPs in the field ranging from 0 T to 3.3 T. The horizontal panels from left to right displays the 2D pattern collected at 0, 0.5, 1, 2 and 3 T for respective sizes. 138

7.6. The loss of intensity in the 2D SANS patterns at low and high fields is due to the inhomogeneous sample and the limited size of the neutron beam (shown by the yellow region). (a) At low fields, magnetic forces compete with phase separation and sedimentation forces. (b) In the intermediate field region, magnetic forces lift the particle phase to displace the supernatant. (c) Strong fields further tear apart the assemblies to pull the DBNPs to the edge of the cells resulting in lowered intensities. 139

7.7. SAXS fits of A12F10 ; radially integrated SAXS intensities of A12F10 at 0 T (red) and 0.9 T (green) fit to (a) Guinier-Porod model to fit asymptotic limits and (b) a gold sphere model. The intensities are scaled for visualization. 141

7.8. (a) Radially integrated SANS intensities of A12F10 DBNP in fields ranging from 0-3 T, where the solid black lines are fits to Guinier-Porod model, bottom inset: The isotropic 2D SANS pattern of A12F10 DBNP at 1 T. The intensities integrated along the black ring represents the intensity at a single Q value. The integrated intensities are plotted as function of Q for radial analysis. (b) The blue solid line is the neutron SLD of the original DBNP system and the black solid line is the calculated SLD of the composite core-shell model used to describe A12F10. (c) SANS 1D data of A12F10 at various fields fit to a composite core-shell model described in (b). 142

7.9. Summary of various geometric parameters of A12F10 DBNP determined from (Panel A) TEM image analysis, (Panel B) SAXS and (Panel C) SANS analysis. 144

7.10. SANS 1D data of A13F14 at 0.5, 1 and 2 T fit to composite core-shell model constrained to high Q . Black solid lines are fits to data. The result of the fits are given in the appendix. 145

7.11. 1D integrated (a) SAXS intensity peak at 0.9 T and (b) SANS intensity peaks at 0.5, 1, 2 and 3 T of A13F14 DBNPs along the sector parallel to the magnetic field. Insets: 2D patterns and parallel sectors depicted as dashed lines. Both (a) and (b) are baseline subtracted and the solid lines are fits to Lorentzian and Gaussian model functions, respectively. (c) The correlation distances ℓ_{\parallel} and (d) chain length ζ_{\parallel} obtained from the peak position and width, respectively plotted as a function of applied field. The shaded region in (c) and (d) indicates high field region with observed drop in intensity due to measurement of supernatant phase.	146
7.12. Summary of various geometric parameters of A13F14 DBNPs determined from (Panel A) TEM image analysis, (Panel B) SAXS and (Panel C) SANS analysis.	147
7.13. (a) SANS 1D data of A9F11 at 0.5, 1, 2 and 3 T fit to composite core-shell model constrained to high Q . Black solid lines are fits to data and are scaled for visualization. The result of the fits are given in the appendix.	148
7.14. 1D integrated (a) SAXS intensity peak at 0.9 T and (b) SANS intensity peaks at 0.5, 1, 2 and 3 T of A9F11 DBNPs along the sector parallel to the magnetic field. Insets: 2D patterns and parallel sectors depicted as dashed lines. Both (a) and (b) are baseline subtracted and the solid lines are fits to Gaussian model function. (c) The correlation distances ℓ_{\parallel} and (d) chain length ζ_{\parallel} obtained from the peak position and width, respectively plotted as a function of applied field. The shaded region in (c) and (d) indicates high field region with observed drop in intensity due to measurement of supernatant phase.	149
7.15. Summary of various geometric parameters of A9F11 DBNPs determined from (Panel A) TEM image analysis, (Panel B) SAXS and (Panel C) SANS analysis.	150
7.16. 1D radially integrated SANS intensity of A10F14 at 0.5, 1, 2 and 3 T fit to composite core-shell model constrained to high Q . Black solid lines are fits to data and are scaled for visualization. The result of the fits are given in the appendix.	151

- 7.17. 1D integrated (a) SAXS peak at 0.9 T and (b) SANS peaks at 0.5, 1, 2 and 3 T of A10F14 DBNPs along the sector parallel to the magnetic field. Insets: 2D patterns and parallel sectors depicted as dashed lines. Both (a) and (b) are baseline subtracted and the solid lines are fits to Gaussian model function. (c) The correlation distances ℓ_{\parallel} and (d) chain length ζ_{\parallel} obtained from the peak position and width, respectively plotted as a function of applied field. The shaded region in (c) and (d) indicates high field region with observed drop in intensity due to measurement of supernatant phase. 152
- 7.18. (a) The 1D SANS integrated intensity peak of A10F14 DBNP at 0.5, 1, 2 and 3 T along the sector perpendicular to the applied field. Insets: 2D SANS pattern of A10F14 and sector represented by dashed lines. These peaks are baseline subtracted and the solid lines correspond to the fits using Gaussian peak model. (b) The correlation distances ℓ_{\perp} and (c) chain lengths ζ_{\perp} are plotted as a function of applied field. The shaded region in (b) and (c) indicates high field $H > 1$ T field region with observed drop in intensity due to dynamic nature of the assembly. 153
- 7.19. (a) The 2D SANS pattern of A10F14 at 1 T dispersed in 78 % d-toluene. The dashed yellow lines represents the sector along the applied field ($\alpha = 0^{\circ}$) and black dotted line represents the sector perpendicular to the field ($\alpha = 90^{\circ}$). Peak integrated intensity along the sector centered at (b) $\alpha = 0^{\circ}$ and (c) $\alpha = 90^{\circ}$ 153
- 7.20. Summary of various geometric parameters of A10F14 DBNP determined from (Panel A) TEM image analysis, (Panel B) SAXS, (Panel C) SANS and (Panel D) SANS with contrast variation analysis. 154
- 7.21. Sketch of expected 2D SAS detector pattern due to scattering from (a) non-interacting ensemble of randomly oriented spheres or dumbbells, (b) IONPs and DBNPs in a chain, (c) oriented dumbbells, (d) misaligned chains containing spherical and dumbbells and (e) spherical particles arranged into chains extending in both directions. 155

7.22. (a) Oriented dumbbell with definitions of θ and ϕ to describe orientation of anisotropic particles when beam is incident along the z-axis. It is noted that θ rotation is performed first followed by the ϕ [140, 199]. The red and blue arrow represents the direction of the dumbbell containing multi-component spherical sub-units (b) Expected 2D scattering pattern expected for DBNPs due to parallel and perpendicular orientation of the anisotropic particles.	156
7.23. Real space and simulated scattering patterns of spherical (a-b) Au NPs, (c-d) IONPs, (e-f) Au NP chains and (g-h) IONPs chains dispersed in h-toluene.	157
7.24. <i>BornAgain</i> workflow to create a composite DBNP using spherical sub-units with SLD of the IONP and Au and by translating the origin of IONP to (10,0,0) and setting Au origin to (0,0,0) to realize A10F14 DBNP.	157
7.25. The real space distribution of assemblies on the right and simulated detector image on the the left for DBNPs (a-b) aligned along the x-axis (c-d) aligned along the y-axis and (e-f) 50 % distributed in both directions.	158
7.26. Construction of "prolate" and "oblate" type ellipsoids for shape anisotropy energy calculations with aspect ratio A_1 and A_2 , respectively. The ellipsoids are constructed to scale.	161
7.27. The range of calculated (a) Zeeman (b) dipolar and various shape associated demagnetization energies plotted as a function of aspect ratio A_2 . In (a) and (b) the grey region of energies is plotted using values in Table 7.1 and green region in (a) represents the calculated energy assuming equal bulk magnetization $M_s = 4.46 \times 10^5$ A/m of IONPs in all DBNPs.	163
7.28. Schematic of shape induced mechanisms governing self-assembly.	165
8.1. The various motions associated with IONPs and DBNPs distributed in the box.	170
8.2. The difference in SANS POL patterns ($I^- - I^+$) obtained at 1 T for (a) category-O DBNPs (A12F10), (b) (A13F14) and (c) (A9F11) belongs to category-I A. (d) category-II DBNPs (A13F14). A saturating field of 1 T is applied along the horizontal direction.	171

A.1.	Size distributions obtained from TEM image analysis where the red histograms represent diameter of the Au nanoparticles L_A (a-d), the blue histograms represents dimension along the growth axis L_F (e-h) and D_F (i-l) and black represents the whole diameter of the DBNP L_D (m-p). An average of ~ 50 -100 particle were measured for all DBNPs.	174
A.2.	TEM images of (a) F05 and (b) F10 IONPs.	175
A.3.	SAXS fits of A13F14 ; radially integrated SAXS intensities of A13F14 at 0 T (red) and 0.9 T (green) fit to (a) Guinier-Porod model and (b) a gold sphere model. The intensities are scaled for visualization.	178
A.4.	SAXS fits of A9F11; radially integrated SAXS intensities of A9F11 at 0 T (red) and 0.9 T (green) fit to (a) Guinier-Porod model and (b) a gold sphere model. The intensities are scaled for visualization.	179
A.5.	SAXS fits of A10F14; radially integrated SAXS intensities of A10F14 at 0 T (red) and 0.9 T (green) fit to (a) Guinier-Porod model and (b) a gold sphere model. The intensities are scaled for visualization.	180
D.1.	Possible structures of the DBNP where (a) $\theta_c = 0^\circ$, (b) $0^\circ < \theta_c < 180^\circ$ and (c) $\theta_c = 180^\circ$, adapted from [208].	188
D.2.	Illustration of dumbbell length scales and angles. Here, θ_C is the contact angle while d is the distance between the centers i.e. $z_1 + z_2$	189
D.3.	(a) The scheme of simplified RMC. (b) 2D Simulated patterns on right half and experimental data on the left (c) corresponding real space assembly of A10F14. (b) 2D Simulated patterns on right half and experimental data on the left (c) corresponding real space assembly of A9F11.	192

Eidesstattliche Erklärung

Declaration of Authorship

I, *Nileena Nandakumaran*

declare that this thesis and the work presented in it are my own and has been generated by me as the result of my own original research.

Hiermit erkläre ich an Eides statt / I do solemnly swear that:

1. This work was done wholly or mainly while in candidature for the doctoral degree at this faculty and university;
2. Where any part of this thesis has previously been submitted for a degree or any other qualification at this university or any other institution, this has been clearly stated;
3. Where I have consulted the published work of others or myself, this is always clearly attributed;
4. Where I have quoted from the work of others or myself, the source is always given. This thesis is entirely my own work, with the exception of such quotations;
5. I have acknowledged all major sources of assistance;
6. Where the thesis is based on work done by myself jointly with others, I have made clear exactly what was done by others and what I have contributed myself;
7. Parts of this work have been published before as: Nandakumaran, Nileena, et al. "Unravelling Magnetic Nanochain Formation in Dispersion for In Vivo Applications." *Advanced Materials* 33.24 (2021): 2008683. <https://doi.org/10.1002/adma.202008683>

Date: 08.06.2022

Signature:



